Synthesis and Characterization of Calcium Phosphate Silicate Bio-Cements

by

SHUXIN ZHOU

A THESIS SUBMITTED IN PARTIAL FULFUILLMENT OF
THE REQUIREMENTS FOR THE DEGREE OF

DOCTOR OF PHILOSOPHY

in

THE FACULTY OF GRADUATE AND POSTDOCTORAL STUDIES
(Materials Engineering)

THE UNIVERSITY OF BRITISH COLUMBIA
(Vancouver)

April 2014

Abstract

Calcium phosphate silicate cement (CPSC) describes a family of materials in which the powder component is composed of the mixture of hydraulic calcium silicates and calcium phosphates. CPSC was developed and characterized in this work with the broad goal to address, and possibly overcome, the disadvantages of calcium silicate and calcium phosphate cements used in medical and dental fields. The main objective of this work was to synthesize and characterize CPSC, focusing particularly on the hydration process of CPSC. The cements consisting of various amounts of triclacium silicate (C_3S) and calcium phosphate monobasic (CPM), were synthesized by the sol-gel process, followed by heat treatment at 1550ºC and planetary ball-milling. It has been determined that after mixing with water, C_3S hydrates to calcium silicate hydrates (C-S-H) and calcium hydroxide (CH); within 10 min CPM reacts with CH to form dicalcium phosphate dihydrate (DCPD), which further reacts with CH and precipitates hydroxyapatite (HAP). It is proposed that the phosphate ions incorporate into C-S-H to form another type of hydrates C-S-P-H. The morphology of the hydrates depends on the process of hydration and the composition of CPSC. At the early stages of hydration, the hydration products form "almond-shaped" particles that serve as a nucleation site for the hydrates. The hydrates take tubular shape and form bundles clustered along the radial direction of the tubes. CPM influences the hydration kinetics of C_3S by increasing the duration of the hydration acceleration period rather than increasing the hydration rate, especially for the higher content of CPM in CPSC. CPM also increases the porosity of CPSC and reduces the content of CH, thought to be the "weak link" in the set CPSC. As a compromise between the two effects, the optimal content of CPM appears to exist at about 10 wt% of CPM in CPSC. After immersion in simulated body fluid, HAP forms on the surface of CPSC indicating that CPSC is bioactive *in vitro*. Cytotoxicity assay and cell adhesion assay against human gingival fibroblast indicated that the biocompatibility of CPSC is significantly enhanced.

Preface

This research work is collaboration between the University of British Columbia and Innovative BioCeramix Inc. of Vancouver and partially supported by Natural Sciences and Engineering Research Council of Canada. This dissertation is an original intellectual product of the author, Shuxin Zhou. The published journal paper listed below has been prepared based on the work presented in the dissertation, with co-authors contribution limited to guidance, suggestions and editorial comments.

1. **Zhou S**, Ma J, Shen J, Haapasalo M, Ruse ND, Yang Q, Troczynski T. In vitro studies of calcium phosphate silicate bone cements. J Mater Sci Mater Med. 2013;24:335-64.

The delay between the patents submission dates (2005) and this thesis publication, including respective journal and conference publications (2012-13) relates to the disclosure limitations during the patenting process, as well as technology commercialization by Innovative BioCeramix Inc., of Vancouver BC, Canada.

Table of Contents

List of Tables

List of Figures

Lists of Symbols and Abbreviations

Symbols

α	Degree of hydration
λ	Wavelength of the radiation
$(\mu/\rho)_c$	Absorption coefficient of the poly-phase specimens
ρ_a	Density of phase *a*
B	Dry weight
b	Width of the specimen
d	Distance of the crystal planes
D	Diameter of the specimen
F	Maximum load
h	Height of the specimen
$I_{(hkl)a}$	Peak intensity of the (*hkl)* diffraction plane for phase *a*
$I_{(hkl)a}/I_{(hkl)'s}$	Intensity ratio of phases *a* and *s*
I_c/I_s	Intensity ratio of C_3S to quartz in area
k	Slope of the plot of $I_{(hkl)a}/I_{(hkl)'s}$.vs. X_a/X_s
$K_{(hkl)a}$	Constant for the *(hkl)* diffraction line of phase *a* in a mixture
k_d	Reaction rate constant for a diffusion-controlled process
K_e	Constant for a particular experimental system
k_n	Reaction rate constant for a nucleation-controlled process
k_r	Rate constant
K_{sp}	Solubility product constant
L	Distance between the supports
L_{CaO}	Volume of 0.1 N HCl for standard CaO
L_{cem}	Volume of 0.1 N HCl for cement
m	Molar ratio of H_2O/SiO_2 in hydrates C-S-H
q	Constant, $q = [(u/v) + w]$
M_{C3S}	Molar weight of C_3S
M_{CaO}	Weight of standard CaO
M_{cem}	Weight of cement
M_{CH}	Molar weight of CH
M_{H2O}	Molar weight of water
n	Molar ratio of CaO/SiO_2 in hydrates C-S-H

n_i	Integer
P	Apparent porosity
P_{C3S}	Percentage of C_3S to W_I
P_{CH}	Percentage of CH to W_I
P_I	Percentage of the ignited weight to W_I
pK_{sp}	-logarithm of K_{sp}
t	Time
P_I	Percentage of the ignited weight to W_I
S	Suspended weight
u	Factor related to the morphology of the growing phase
V	Exterior volume of the specimen
v	Factor related to the rate–limiting process
W	Saturated weight
w	Factor related to the rate of nucleation
w/c	Weight ratio of water to cement
$W_{B\text{-}H2O}$	Amount of bond water
W_{C3S}	Weight of unhydrated C_3S
W_{CH}	Weight of calcium hydroxide
W_{dc}	Weight loss during decarbonation
W_{dh}	Weight loss during dehydration
W_{dx}	Weight loss during dehydroxylation
W_I	Ignited weight at 1100 ºC
X_a	Weight fraction of phase a
X_a/X_s	Mass ratio of peak areas of phases a and s
X_c/X_s	Weight ratio of C_3S and quartz
γ	Density of kerosene
$\Delta W_{B\text{-}H2O}$	Percentage of the weight loss of total bond water to W_I
ΔW_{CH}	Percentage of the weight loss of total CH to W_I
ΔW_{dh}	Percentage of the weight loss of total hydrate to W_I
θ	Angle of the diffraction peak

Abbreviations

ACP	Amorphous calcium phosphate
ANOVA	Analysis of variance
ATP	Adenosine triphosphatase
BA	BioAggregate
BET	Brunauer-Emmet-Teller
BSE	Backscatter electrons
C_2S	Dicalcium silicate
C_3S	Tricalcium silicate
Ca/P	Molar ratio of element Ca to P in a calcium phosphate compound
CaO/SiO_2	Molar ratio of Cao/SiO_2 in hydrates
CH	Calcium hydroxide
CPC	Calcium phosphate cement
CPM	Calcium phosphate monobasic
CPP	Calcium polyphosphate
CPSC	Calcium phosphate silicate cement
CSC	Calcium silicate cements
C-S-H	Calcium silicate hydrate
C-S-H (E)	Early stage C-S-H
C-S-H (M)	Middle stage C-S-H
C-S-P-H	Calcium silicate phosphate hydrate
d	Day(s)
DCPA	Dicalcium phosphate anhydrous
DCPD	Dicalcium phosphate dihydrate
DMEM	Dulbecco's modified eagle's medium
DNA	Deoxyribonucleic acid
DTA	Differential thermal analysis
EDX	Energy dispersive X-ray analysis
Eq.	Equation
h	Hour(s)
H_2O/SiO_2	Molar ratio of H_2O/SiO_2 in hydrates
HAP	Hydroxyapatite
M	Monoclinic

MCPM	Monocalcium phosphate monohydrate
MTA	Mineral trioxide aggregate
MTT	3-(4,5-Dimethylthiazol-2-yl)-2,5-diphenyltetrazolium bromide
OCP	Octacalcium phosphate
OPC	Ordinary Portland cement
PBS	Phosphate buffer solutions
PDF	Powder diffraction file
PEG	Polyethylene glycol
PMMA	Polymethylmethacrylate
QXRD	Quantitative X-ray diffraction
R	Rhombohedral
RH	Relative humidity
RMA	Reference maximum amount
RNA	Ribonucleic acid
SBF	Simulated body fluid
SEI	Secondary electron imaging
SEM	Scanning electron microscopy
T	Triclinic
TCP	Tricalcium phosphate
TEM	Transmission electron microscopy
TEOS	Tetraethyl orthosilicate
TG	Thermogravimetric analysis
TGA	Thermogravimetric analysis
TTCP	Tetracalcium phosphate
XRD	X-ray diffraction

Acknowledgements

I would like to take this opportunity to express my deepest gratitude towards my supervisor, Dr. Tom Troczynski, for his encouragement, guidance, support and patience. This thesis would not have been possible without him.

I am heartily thankful to my co-supervisors and the committee members, Dr. Dorin N Ruse, Dr. Quanzu Yang, and Dr. Rizhi Wang for their support and guidance and the Natural Sciences and Engineering Research Council of Canada for partial financial support. I would also like to acknowledge the support from the Department of Materials Engineering at UBC.

I specially thank my friends Nigel Todd and Bill Reimer, who took their time to proofread this thesis and make it readable.

In addition, I would like to thank my family, my wife Jin and daughter Penny and my parents for their love, trust, patience and support and everyone else who gave their assistance and support in any way during my studies at UBC.

1 INTRODUCTION

1.1 Background

Since its invention by Brown and Chow in 1986 [1, 2], calcium phosphate cement (CPC) has been an interesting, useful and widely studied material. Upon being mixed with water, CPC self-sets and forms hydroxyapatite (HAP) for Brown & Chow's formulation. CPC can only have three different end-products: apatite, brushite [the mineral of dicalcium phosphate dihydrate (DCPD)], and amorphous calcium phosphate (ACP) [3]. The study on ACP showed that the cement is rapidly converted to HAP [4]. Therefore, all CPC formulations can be divided into two categories: apatite CPC and brushite CPC in according with their end-products [3]. Brushite CPC can only set at a pH value lower than about 6, when the pH is higher, the cement transforms into HAP [3]. The advantages of set CPC include the mineral similarity to the composition of natural bone [5, 6], good biocompatibility [7-9], and excellent bioactivity and osteoconductivity [10-13]. Calcium phosphate cements have therefore been used for a variety of orthopaedic and dental applications, including repair of craniofacial defects [14, 15] and periodontal bone defects [16], reconstruction of alveolar bone defects [17], and other dental applications [8, 11]. The drawback of CPC is its relatively low strength; thus it can only be used for non load-bearing applications [18]. The average compressive strength of the calcium phosphate cement (the Brown and Chow's formula) was reported to be about 36 MPa after completion of the setting reactions in 24 h [19], which is significantly lower than the average compressive strength of human cortical bone (greater than 100 MPa [20]). The main reasons for the relatively low strength are (i) low fracture toughness, reported generally below 0.3 MPa $m^{1/2}$ [21, 22], and (ii) their porosity, which is about 43 vol% after cement sets and the connected pores form relatively large flaws and thus weaken the cement [20, 23]. The diameter of pores was about 8 to 12 microns [20, 23]. Therefore, many researchers have been trying to reduce the flaw sizes and to increase fracture

toughness, leading to different strategies to improve the mechanical properties of CPC [21, 24, 25].

Calcium silicate-based cements (i.e. similar to Portland cement, with hydraulic phases of tricalcium silicate and dicalcium silicate, with or without calcium aluminate) are another type of cements, which are also used in biomedical applications. For example, Mineral Trioxide Aggregate (MTA) and BioAggregate (BA) are two commercially available calcium silicate-based cements for dental applications, such as pulp capping, pulpotomy dressing, root perforation repair, and root-end sealing [26-29]. Calcium silicate cements have reasonably good mechanical properties. For example MTA can reach 58 MPa in compression after 3 d of setting [30]. Such calcium silicate cements (CSC) are also biocompatible and bioactive [31-34]. During setting, calcium silicates react with water and form calcium silicate hydrate (C-S-H) gel and calcium hydroxide [$Ca(OH)_2$, abbreviated to CH]. CH is slightly soluble in water (pK_{sp} = 5.26 at 20 ºC [35], equivalent to 0.83 g of CH soluble in 1 liter water at 20 ºC), resulting in a high pH of 12 to 13 in the setting solution. The disadvantage of CSC as bone cements is therefore their high setting pH. This high pH, however, imparts CSC antibacterial properties and is therefore beneficial in some dental applications (e.g. as root canal fillers) but may be detrimental in others. Due to CH solubility in water, its presence in the set cements is considered as a “weak link”, resulting in decreased mechanical properties [36]. Therefore, it would be desirable to decrease CH content in set cements in order to increase their strength and, possibly, also decrease the setting pH. A number of investigators have reported improvement of the compressive strength of Portland cement by adding "silica fume" (silicon oxide particles, generally smaller than one micron [37]) in order to decrease CH content in hydrated cements [38, 39], wherein the silica fume reacts with part of CH during setting, leading to the formation of C-S-H.

In order to overcome the drawbacks of CSC biological cements as per above, the present author and Lu [40-43], in 2005, were first worldwide to propose a novel calcium phosphate silicate cement (CPSC), which consists of phosphate salts in addition to hydraulic calcium silicates. The motivation for the development of such formulations was the expectation that during CPSC setting, along with the formation of C-S-H and CH resulting from calcium silicate hydration, the phosphates would react with the CH to precipitate HAP. It was anticipated that this process would enhance the mechanical properties and decrease pH. The present work is largely devoted to verifying these hypotheses.

Polymethylmethacrylate (PMMA) - based bone cements are currently the most common orthopaedic surgical cements, with over one million procedures performed worldwide annually in hip, knee, and other joint replacement [44]. PMMA is an acrylic polymer that is formed by mixing a powered methylmethacrylate polymer and a liquid methylmethacrylate monomer used as an initiator of the radical polymerization. The cement has been used in surgical fixation of artificial joints for over 50 years [45]. The mechanical properties of PMMA cements are good, i.e. tensile strength ~35 MPa, shear strength ~42 MPa, compressive strength ~93 MPa, bending strength ~64 MPa, and bending modulus 2,552 MPa [46]. However, PMMA bone cement has a number of drawbacks [45]. The polymerization of PMMA is an exothermal reaction, increasing temperature at the center of the cement mantle up to 124 ºC *in vivo* (depending on the cement formulation) [45]. This may be responsible to the thermal necrosis of bone, impaired local blood circulation, and predisposition to membrane formation at the cement-bone interface. The second drawback is the toxicity of the unreacted liquid monomer, which may also cause chemical necrosis of the bone due to the release or leakage of the monomer before polymerization of the cement [45]. The third problem is that the cement cannot chemically bond to bone (i.e. the acceptable bond strength is achieved mainly due to interlocking of the bone tissue and the

prosthesis surface). The cement acts therefore like a mortar or grout filling the voids between the surface of the prosthesis and the interstitial spaces in the surrounding bone.

1.2 Research Hypothesis and Motivation

CPSC consists of hydraulic calcium silicates such as tricalcium silicate (C_3S, Ca_3SiO_5) and dicalcium silicate (C_2S, Ca_2SiO_4) and phosphate salts, such as calcium phosphate monobasic [CPM, $Ca(H_2PO_4)_2$]. It is hypothesized that during CPSC setting, CH resulting from the hydration of calcium silicates reacts with the phosphates and thus precipitates HAP, in the process largely removing CH from the set cement and reducing pH of the cement paste. Meanwhile, the resulting C-S-H would form a composite structure *in-situ* with the precipitating HAP crystals. The schematic of the expected hydration route of CPSC is given in Figure 1.1. If this hypothesis is true, CPSC would be expected to have enhanced biocompatibility, bioactivity (at lower setting pH), and improved mechanical strength, in comparison to the pure CSC.

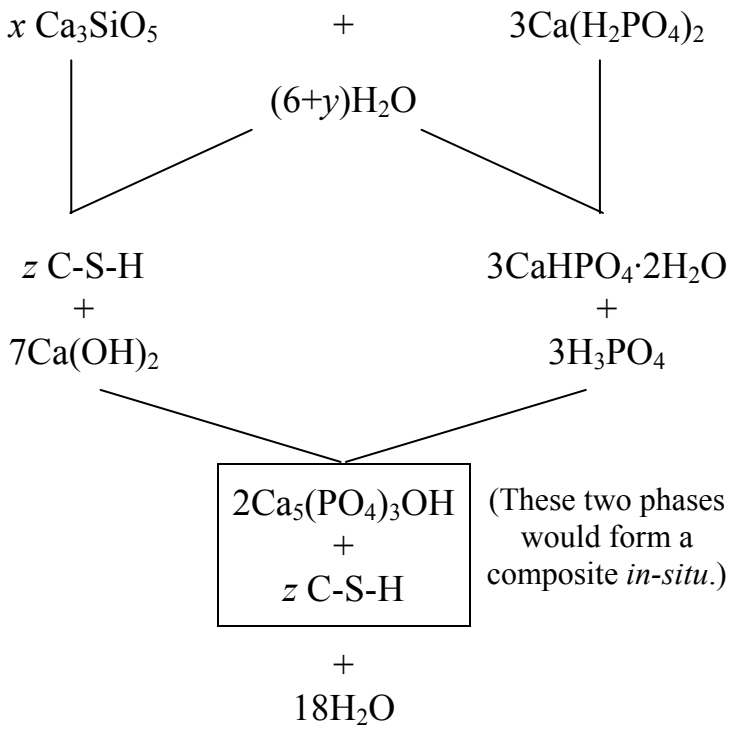

Figure 1.1 Schematic of the expected hydration route of CPSC. Ca_3SiO_5 and $Ca(H_2PO_4)_2$ are used as pure calcium silicate cement and phosphate salt, respectively, in this study. (Note: *x* and *z* are the coefficients related to Ca_3SiO_5 and C-S-H, respectively; *y* is the number of molecules of H_2O required for the complete hydration of Ca_3SiO_5. Because C-S-H is non-stoichiometric and has variable composition, *x, y* and *z* cannot be precisely determined at this stage. It is believed however that $1.7CaO{\cdot}SiO_2{\cdot}4.0H_2O$ is the best representation of C-S-H resulting from C_3S hydration [47]; therefore the best estimation of *x,* y, and *z* would be around 5.4, 28.5 and 5.4, respectively.)

1.3 Objectives and Scope

The overall goal of this research is to synthesize and characterize the novel CPSC as the next generation bio-cement for medical applications. The particular focus is to investigate and understand the hydration process of CPSC, including the microstructure development during the cement hydration, to evaluate the physical, and chemical and biological properties of CPSC, and to compare the results with those of pure calcium silicate cement (CSC), so that the research hypotheses could be verified.

As mentioned above, CPSC is a novel cement for medical and dental applications. Accordingly, there is no existing knowledge regarding its hydration mechanism, mechanical and biological properties. The purpose of the present work is to systematically study CPSC processing, hydration mechanism, and correlate them with the set cement properties. This information may then be used to decide the specific formulations of the cements for specific applications *in vivo*.

The specific objectives of this research were as follows:

1) To explore and develop practical methods for CPSC cement synthesis;

2) To identify the CPSC hydration products, to characterize their morphologies and to investigate the cement microstructure during the hydration process at/near the physiological temperature;

3) To characterize set CPSC, including its mechanical properties, bioactivity, and biocompatibility;

4) Based on the new knowledge generated in objectives 2 and 3, to propose and verify the hydration mechanism of CPSC and test the main research hypothesis of this thesis;

5) To determine the optimal composition of CPSC that may provide a combination of both good mechanical properties and good biological properties.

Calcium silicate-based cements, such as mineral trioxide aggregate (MTA) and CPSC, once set, are believed to be non-resorbable (or poorly-resorbable) and practically insoluble [48-50], thus have good resistance to corrosion in biological environment. Therefore, they are different from calcium phosphate cements (and bioglasses), which are not stable in biological environments [23]. The degradability of these materials provides favourable bio-chemical environment benefitting growth of new tissues [23]. However, many applications, such as orthograde and retrograde filling treatments in endodontics, require the cements to be relatively stable in biological environments [51], i.e. non/slowly resorbable, and the calcium silicate-based cements containing calcium phosphates fit these requirements.

CPM was used in CPSC as a phosphate provider and a consumer of CH produced from the hydration of calcium silicate by an acid-base reaction during cement setting. CPM is one of the most soluble calcium phosphates (solubility of about 18 g/l in water at 25 ºC) with the lowest pH of the resulting solution (the stability range of pH = 0.0 – 2.0 in aqueous solution at 25 ºC) [52]; therefore, the adoption of CPM in the formulation of CPSC should benefit the neutralization of the high setting pH.

Since CPSC is a novel cement, it is important to understand its synthesis process, the properties of set cement and its microstructure development during the setting reactions. As mentioned above, because CPSC consists of hydraulic calcium silicates (including tricalcium silicate, dicalcium silicate, or a mixture of the two) and calcium phosphates or their combinations, the CPSC system is a complex system. Therefore, this work is limited to one

particular variant of CPSC, including C_3S and CPM as the hydraulic calcium silicate and a phosphate salt, respectively. The mixture of C_3S and CPM was used as powder components of CPSC and distilled water was the setting liquid component. In order to achieve well-defined reactants, a sol-gel process was used to synthesize pure C_3S. CPSC powders were then obtained by ball-milling C_3S and up to 25 wt% of CPM powders. To understand the hydration process, the microstructure of the CPSC with 10 and 20 wt% CPM was investigated in detail and compared with that of pure C_3S cement, as a function of the progress of the hydration process. The analytical methods used included scanning electron microscopy (SEM), X-ray diffraction (XRD), differential thermal analysis and thermogravimetric analysis (DTA-TGA).

Since the hydration of CSC is a complex process, the precise mechanism of tricalcium silicate hydration is still unclear and the detailed structure of C-S-H, one of the main products of the hydration, is not completely known even though the cement hydration has been extensively investigated for more than one century [53]. Therefore, the present work is an attempt to incrementally add knowledge and understanding regarding the hydration of the new composite cement of tricalcium silicate and CPM.

To find suitable applications for the cements in medical fields, it is necessary to understand their physical, chemical and biological properties. Therefore, in this research the compressive strength and three-point flexural strength of set CPSC were evaluated. The biological properties, such as *in vitro* bioactivity and biocompatibility, were evaluated as well. The research work included the following tasks:

1. Prepare CPSC by ball-milling various mixtures of CPM and C_3S that was synthesized through a sol-gel process.

2. Compare, at pre-set time points, the microstructure development during the hydration process between CPSC and CSC (i.e. containing only C_3S)
3. Identify the hydration mechanism and products of CPSC, utilizing different analytical techniques, such as DTA-TGA and XRD.
4. Determine the influence of the addition of CPM into C_3S on the mechanical properties, specifically compressive strength and flexural strength.
5. Investigate the behaviour of CPSC in simulated body fluid (SBF).
6. Demonstrate the *in vitro* response of human gingival fibroblasts to CPSC.

2 LITERATURE REVIEW

2.1 Introduction

This literature review overviews previous work on hydration models of tricalcium silicate with/without phosphate compounds and the effects of different calcium phosphates which could occur during the CPSC hydration. After reviewing previous work, an overview of *in vitro* bioactivity and biocompatibility of bio-cements is also presented.

2.2 Tricalcium Silicate as Hydraulic Cement

2.2.1 Hydration of tricalcium silicate

Tricalcium silicate is the major hydraulic cementitious component known to humanity and consists of up to 70% of Portland cement [54]. The hydration of C_3S controls the setting and development of early age strength of Portland cement, and primarily takes place within 28 days and completes to a large degree in about one year [54]. The hydration of C_3S is rather complex, and has not been fully understood [53]. The products of C_3S hydration are CH and C-S-H. C-S-H is of non-stoichiometry and poor crystallinity and also of variable compositions; therefore, there is no certain formula for C-S-H and the structure of C-S-H was not fully clear [54]. The hydration reaction of C_3S with water can be described by the following equation [53]:

$$Ca_3SiO_5 + (3 + m - n)\ H_2O = nCaO{\cdot}SiO_2{\cdot}mH_2O\ \text{(C-S-H)} + (3 - n)\ Ca(OH)_2\ \text{(CH)} \quad (2.1)$$

where nCaO·SiO$_2$·mH$_2$O is the general formula of C-S-H and both n and m may vary over a wide range, i.e. n = 1.4 to 2.0 and m = 1.3 to 4.0, depending on the hydration conditions [53, 54]. Tricalcium silicate dissolves in water; for example, a C_3S sample with a specific area of 310 m^2/kg was stirred in pure water at w/c (the weight ratio of water to cement) of 5000 and it dissolved completely in about 30 min [55]. The dissolution rate was at least 1.4 x 10^{-5} mol per second per square meter of the surface area. Under most experimental conditions, due to a protective surface hydrate coating, the dissolution rate of C_3S is much reduced. For example, at the "normal" w/c = 0.3 to 0.6 (i.e. values typically used to set the cement), the reaction of 70% of C_3S in Portland cement with water needs about 28 days and of all C_3S needs one year [54]. At room temperature, an initial w/c of about 0.42 is necessary for a complete reaction [54]. If w/c is less than 0.42, either some of C_3S will not hydrate, or hydrates will be of low water content. Extreme values of w/c are reported in literature in experiments evaluating the hydration products and their solubility in water. For example, if w/c is greater than about 280, the CaO/SiO$_2$ ratio in C-S-H will be less than 1.7 [55]. If w/c exceeds 2200, all of the hydration products will dissolve completely [55].

Due to the differences in preparation of C_3S and in experiment conditions, there is considerable divergence of the opinions in literature on the mechanisms of C_3S hydration. According to the calorimeter curves, it is generally agreed that upon mixing with water, C_3S hydrates in five stages, Figure 2.1 [56, 57]. The processes taking place at different stages can be summarized as follows:

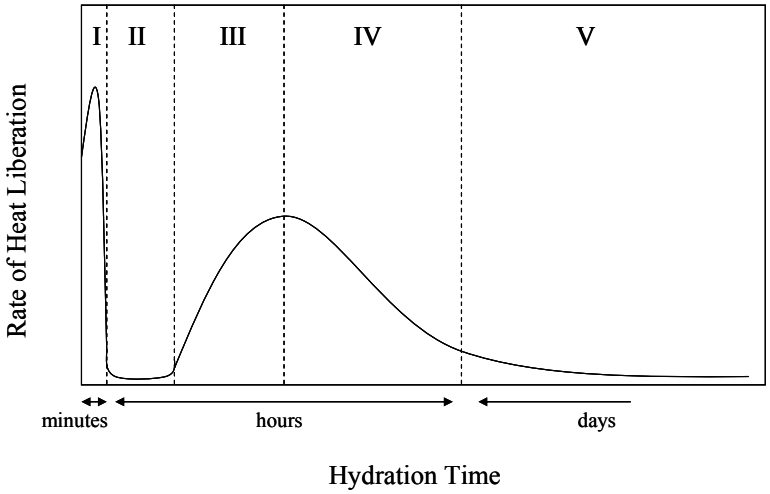

Figure 2.1 Schematic representation of the different stages taking place during the hydration of C_3S (w/c < 1.0) [56]

Stage I (Pre-induction period): marked by rapid heat liberation. C_3S hydrolyzes and Ca^{2+}, OH^-, and $H_2SiO_4^{2-}$ ions immediately dissolve in the solution followed by the formation of a C-S-H coating on the anhydrous C_3S surface, which retards its dissolution [55]. The duration of this period is typically a few minutes.

Stage II (Induction period): a period of relative inactivity, in which heat evolution is low and Ca^{2+} slowly continues passing into solution. The mechanisms causing this slow period are still debatable and two broad groups of theories have been proposed: protective layer theories and delayed nucleation theories. The protective layer theories postulate that the formation of a protective layer, which might be a layer of hydrated product [58-62] or an electric double layer of SiO_2-rich layer with adsorbed Ca^{2+} ions [57, 63, 64], acts as a barrier to significantly slow down the transport of water to the anhydrous surface and/or that of Ca^{2+}, OH^-, and silicate ions into the liquid phase. Towards the end of the induction period, the initially formed layer becomes more permeable, which makes a renewed fast hydration possible [59]. The layer may undergo

changes in composition and /or morphology, adsorb water, or breakdown due to osmotic pressure generated between the layer and anhydrous phase; and the renewed acceleration of the hydration continues when this layer is disrupted.

Alternatively, delayed nucleation theories suggested the induction period is caused by delayed nucleation of CH and /or C-S-H. Initial hydration of C_3S releases Ca^{2+} into liquid phase and causes supersaturation of the liquid phase with respect to CH, due to a poisoning of the surface of the CH nuclei by silicate ions [61, 65, 66]. The supersaturation slows down the formation of the "first-stage" C-S-H and stops further rapid dissolution of C_3S [66-68]. Eventually, the concentration of $Ca(OH)_2$ in liquid phase becomes high enough to overcome the poisoning effect and to precipitate CH. In other words, the induction period terminates when a "second-stage" C-S-H begins to nucleate and grow in a large number. This period lasts typically a few hours.

Stage III (Acceleration period): crystal $Ca(OH)_2$ precipitates from solution and C-S-H forms in the water-filled space. Typically this period begins at a few hours after mixing with water and reaches a maximum within about 5-10 h. The detailed process of the acceleration period is not precisely known, but one of the most acceptable models follows the Avrami equation [53]:

$$-\ln(1 - \alpha)^{1/3} = k_n t \qquad (2.2)$$

where α is the degree of hydration, t is the time, and k_n is the reaction rate constant for a nucleation-controlled process. During this period, setting takes place.

Stage IV (Deceleration period): hydration products continue to form into large empty spaces and decrease the porosity of the system and the paths of ionic transportation between liquid and solid. In the deceleration period the most commonly used equation to describe the kinetics of the C_3S hydration is the Jander equation (2.3) [53]

$$[1 - (1 - \alpha)^{1/3}]^2 = k_d t \qquad (2.3)$$

where (as before) α is the degree of hydration, t is the time, and k_d is the reaction rate constant for a diffusion-controlled process.

Stage V (Final slow period): a diffusion process with a rapid increase in the mean diffusion distance due to the overlap of the hydrated coating of neighbouring grains caused by the decreased porosity as a consequence of stage IV.

These stages determined by studying calorimeter curves roughly correspond to the stages defined by Jennings et al [69] based on microstructural studies of the products in C_3S pastes: stages I and II linking to the early stage of hydration; stages III and IV to the middle stage, and stage V to the late stage [54].

2.2.2 Microstructure of C-S-H in C_3S paste

Of over 30 crystalline calcium silicate hydrates known, afwillite ($3CaO{\cdot}SiO_2{\cdot}3H_2O$) is the thermodynamically stable phase in the environment of water and CH at room temperature [54]. The product of hydration of C_3S and cement pastes, nCaO·SiO_2·$m$$H_2O$, is a poorly crystalline phase. The value of the n (the molar ratio of CaO/SiO_2) ranges from 1.4 to 2.0, and the most

reported value for *n* is near 1.7 when formed under saturated or near saturated conditions, regardless of the water content of the preparation [47].

Due to the indistinctness of the boundaries between pores and solid C-S-H particles, the value of *m* (the molar ratio of H_2O/SiO_2) can only be defined in relation to the hydration conditions and /or specified drying conditions. For example *n* =1.7 and *m* = 4 were obtained in nearly saturated C_3S pastes (the pores are totally filled with water), and *n* = 1.7 and *m* = 2.1 at 11% RH (the interlayer spaces are presumed saturated) [70]. After "D-drying" (the partial pressure of the water vapour = 5 x 10^{-4} torr), *n* = 1.7 and *m* = 1.3 to 1.5 [71]. These values are approximately equivalent to the drying to constant mass at 105 ºC [54]. Except at the very beginning of hydration, the H_2O/SiO_2 ratio of C-S-H in C_3S pastes does not change with the hydration process, but slightly increases as the initial mixing of the w/c ratio increases [53].

The detailed structure of C-S-H is not completely known, however, it is generally agreed that it consists of condensed silicate tetrahedral sharing oxygen atoms with a central, calcium hydroxide-like CaO_2 sublayer [53]. The silicate tetrahedral forms linear chains that are kinked and repeat at the interval of three SiO_4, of which two of them (called "paired" SiO_4) share two of their oxygens with the CaO_2 sublayer and a third one (called "bridging" SiO_4) connects two pairs of paired SiO_4 to form a continuous SiO_4 chain. Such arrangement is called "dreierkette". If some or all of the bridging tetrahedral are missing, the SiO_4 chain splits into fragments containing 2, 5, …(3*n*-1) tetrahedral. On the nano-scale level, the C-S-H formed from C_3S pastes at room temperature are structurally related to two crystalline phases: 1.4 nm tobermorite ($[Ca_4(Si_3O_9H)_2]Ca{\cdot}8H_2O$) and jennite ($[Ca_8(Si_3O_9H)_2(OH)_8]Ca{\cdot}6H_2O$); both having the dreierketten layer structure. In 1.4 nm tobermorite, the "1.4 nm" is the layer thickness and the central O-Ca-O sublayer of each layer share all the oxygen atoms with the Si-O in SiO_4

tetrahedral chains on both sides. The interlayer space between the individual layers is filled with Ca^{2+} ions and water molecules. On the other hand, the structure of jennite is very similar with that of 1.4 nm tobermorite, and the main difference is that only one side of O-Ca-O sublayer links to SiO_4 tetrahedral chains and on the other side the SiO_4 tetrahedral is replaced by OH group and silicate chains alternate with rows of OH groups on both side of the layer.

Several models [72-78] have been suggested for the structure of C-S-H from C_3S and cement pastes. Of all the models, a mixed tobermorite-jennite model proposed by Taylor is worth mentioning here [72, 79]. The model suggested that C-S-H phase from C_3S and cement pastes contained elements of both 1.4 nm tobermorite and jennite structures, and the elements perhaps merged into each other with individual dreierketten layers. It is assumed that each bridging tetrahedron carries one H atom and one of the two end-group tetrahedra of each anion also carries an H atom. The ranges of the CaO/SiO_2 ratios of 1.4 nm tobermorite and jennite are from 0.83 to 1.25 and from 1.5 to 2.25 respectively. The CaO/SiO_2 ratio of C-S-H depends on the ratio of 1.4 nm tobermorite to jennite and the length of silicate chains.

At the early stage of the hydration of tricalcium silicate paste, C-S-H hydrate consists mainly of monomeric orthosilicate (SiO_4^{4-}) and some amount of dimeric silicate ($Si_2O_7^{6-}$). During the middle stage, C-S-H contains primarily dimeric silicates and later dimmers polymerize to give pentamers, octomers, etc. This process can be described as the monomer silicates progressively inserting and bridging dimmers to form the '*dreierkette*' structure. After a long hydration time, hydrates become more tightly packed. Figure 2.2 shows the changing of the silicate ion content with hydration time by trimethylsilylation methods [80].

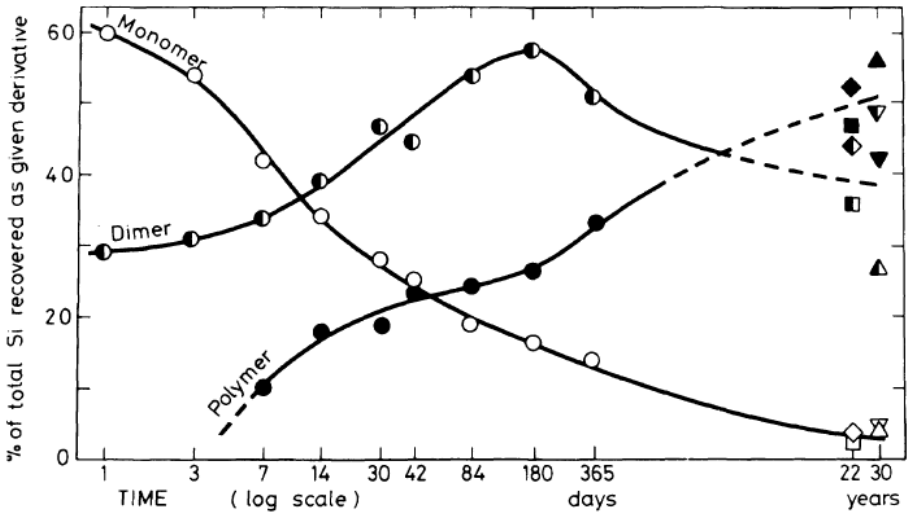

Figure 2.2 Percentage of recovered monomer (open symbols), dimmer (half-open symbols), and polymer (closed symbols) in the total silicon of C_3S or alite pastes by a trimethylsilylation method. Different shaped symbols denote different C_3S or alite specimens. (Reproduced with permission [80])

C-S-H can be divided into two types on the micro-scale level in mature paste, i.e. so-called "outer product" and "inner product". "Outer product" forms early and mostly outside the original boundaries of the anhydrous particles and contributes to setting and hardening. This type of C-S-H is less dense and has a prevailing fibre-like texture. In contrast, "inner product" forms later and is mostly within the original particle volume, as the result of slow, diffusion – controlled mass transfer. This type of C-S-H is dense, compact and featureless and contributes to later hardening. With the hydration process, C-S-H phases have different morphologies. According to the observations by SEM [81] and TEM (transmission electron microscopy) [69], two major classifications of types of C-S-H during various stages have been suggested and are listed in Table 2.1.

Table 2.1 C-S-H morphology observed by SEM and TEM during different stages of CSC hydration [69, 81]

Stage	SEM	TEM
I and II (Early stage)	Type I: Fibrous particles	Type E: Thin flakes or foils which become tubes like cigars when dried
III and IV (Middle stage)	Type II: Reticular network (interlock or honeycomb structure)	Type 0: Amorphous Type 1 and 1': Needle shape radiating from C_3S grain Type 3: Partly crumpled foils
V (Late stage)	Type III: small, irregular flattened grain. Type IV: Agglomerate	Type 3: Crumpled foils Type 4: Dense gel

2.2.3 Techniques to investigate hydration

2.2.3.1 X-ray diffraction

X-ray diffraction (XRD) is a powerful technique used to study crystalline materials. The diffraction pattern includes information about peak positions and intensity, and it is unique for each crystalline material. The positions of the peaks are indicative of the crystal structure and symmetry of the contributing phase. The positions are determined by the spacing of the crystallographic planes according to Bragg's law:

$$n_i\lambda = 2d \sin\theta \qquad (2.4)$$

where n_i is an integer,

λ is the wavelength of the radiation used,

d is the distance of the crystal planes, and

θ is the angle of the diffraction peak.

The peak intensities are related to both the structure and composition of this phase. For a particular experimental system, the peak intensity $I_{(hkl)a}$ from a phase a can be written [82]:

$$I_{(hkl)a} = \frac{K_e K_{(hkl)a} X_a}{\rho_a (\mu/\rho)_c} \tag{2.5}$$

where K_e is a constant for a particular experimental system,

$K_{(hkl)a}$ is a constant for the *(hkl)* diffraction line of phase a in a mixture,

X_a is the weight fraction of phase a,

ρ_a is the density of phase a;

$(\mu/\rho)_c$ is the absorption coefficient of the poly-phase specimens.

The ratio of the intensity of phase a to that of phase s in one specimen can be written as Equation 2.6 to eliminate the absorption factor $(\mu/\rho)_c$.

$$\frac{I_{(hkl)a}}{I_{(hkl)'s}} = k \frac{X_a}{X_s} \tag{2.6}$$

The linear relationship between the intensity ratio $(I_{(hkl)a}/I_{(hkl)'s})$ and the mass ratio (X_a/X_s) of phases a and s establishes a basis of the internal standard method of quantitative analysis. This method requires a well-known standard, s and a variety of diffraction patterns run on prepared samples in which the varied ratios of X_a/X_s are pre-known. The k (a constant) can be obtained

from the slope of the internal standard calibration curve by plotting X_α/X_s vs. the corresponding $I_{(hkl)\alpha}/I_{(hkl)'s}$. The addition of a known amount, X_s, of an internal standard to a mixture of phases (which may include amorphous material) allows the quantitative analysis of each of the components of the mixture. The substances such as rutile (TiO_2), corundum (Al_2O_3), Si, KBr, CaF_2, and quartz (SiO_2) have been used as the internal standard for the quantitative analysis of the cement samples [54, 83]. A satisfactory analysis using this method requires the sample with a particle sizes that is uniform and small (normally below 5 μm) and adequate mixing with an internal standard.

The kinetics of the hydration of C_3S is normally determined by monitoring the consumed C_3S (α) with time. The internal standard method is widely used to determine the unreacted C_3S, though the precision is low for values of α below about 10%. Conventionally, a single peak of the reference standard and of the phase was determined, such as the X-ray peak of 41.3 ° 2θ CuKα for C_3S [84]. Also, with increases in computing power, wider ranges of 2θ are used to improve precision and accuracy [54].

2.2.3.2 Scanning electron microscopy (SEM)

SEM can provide information of specimens on surface topography and surface films with secondary electron imaging (SEI). Backscatter electrons (BSE) can give average atomic number information (also crystallographic information on surface). SEM is equipped with an energy dispersive X-ray (EDX) spectrometer to enable the chemical analysis of bulk specimens. For quantitative analysis, a flat, polished surface is essential. On fracture surfaces of cement and calcium silicate pastes, four morphological types of C-S-H gel were distinguished by SEM [81]. Type I, prominent at early stage, was the fibrous shape, the fibres being up to about 2 μm long

and less than 0.2 μm across. Type II was described as forming reticular networks or honeycomb structure. Type III, prominent in mature pastes, was small, irregular flattened morphology and appeared to be more massive and inconspicuous in character, typically 0.3 μm across. Type IV, also prominent in mature pastes, was the inner product and showed a dimpled appearance due to having packed small grains or regular pores, which were 0.1 μm in size.

2.2.3.3 Differential thermal analysis – thermogravimetric analysis (DTA – TGA)

In the differential thermal analysis (DTA) technique, the temperature difference (termed differential temperature) between the sample and a reference material, associated with physical or chemical changes, is continuously recorded as either a function of the temperature of the furnace, reference material or of time as the sample is heated at a uniform rate. The method has been used to study cement chemistry both qualitatively and quantitatively. Thermogravimetric analysis (TG or TGA) allows the determination of weight changes that take place when a sample is continuously heated at a uniform rate. The first derivative of change of mass (DTG) can also be used for the purpose of identification due to its sharp peaks. However, TGA cannot detect crystalline transitions as they do not involve weight losses. A combination of DTA and TGA has been widely used to study cement systems, including the transition between polymorphisms of clinkers, the hydration process, and hydration products. The polymorphisms of C_3S and the transition temperature are showed below [54]:

$$T_1 \overset{620°C}{\Leftrightarrow} T_2 \overset{920°C}{\Leftrightarrow} T_3 \overset{980°C}{\Leftrightarrow} M_1 \overset{990°C}{\Leftrightarrow} M_2 \overset{1060°C}{\Leftrightarrow} M_3 \overset{1070°C}{\Leftrightarrow} R$$

where T_1 = the first triclinic, T_2 = the second triclinic, T_3 = the third triclinic, M_1 = the first monoclinic, M_2 = the second monoclinic, M_3 = the third monoclinic, R = rhombohedral.

In the DTA of cementitious materials, thermal effects are normally reported in terms of the peak temperature, the range of the peak temperatures, peak width, peak height, and peak area [85]. Many factors such as the instrument system, rate of heating, degree of dryness of the sample, the amount of the sample, particle size and crystallinity, packing density and more affect the results. On a DTA curve of a hydrated C_3S paste, endothermal effects for calcium silicate hydrates, CH, and calcium carbonate are below 200 ºC, 450 – 550 ºC, and 750 – 900 ºC, respectively [86] (This graph is shown in Figure 2.3). Under normal conditions of hydration, it is difficult to prevent the reaction of CH with CO_2 in air. From the TG plots at 105-1007 ºC, the amount of bound water in hydrating cement has been calculated by El-Jazairi and Illston [87, 88] by accounting for the weight losses during dehydration (W_{dh}), dehydroxylation (W_{dx}), and decarbonation (W_{dc}). The amount of bond water ($W_{B\text{-}H2O}$) and CH (W_{CH}) can be obtained from Equations (2.7) and (2.8), respectively [87,88]:

$$W_{B\text{-}H2O} = W_{dh} + W_{dx} + 0.41\ W_{dc} \qquad (2.7)$$

where the factor 0.41 corrects for the water loss equivalent to that of decarbonation, assuming that the carbonate is formed by the carbon dioxide reaction with CH from hydration.

$$W_{CH} = 4.11\ W_{dx} + 1.68\ W_{dc} \qquad (2.8)$$

where the factors 4.11 and 1.68 are stoichiometeric factors for dehydroxylation and dehydration.

The CaO/SiO_2 ratio (the molar ratio of CaO to SiO_2 in hydrates C-S-H) of the C-S-H produced in the hydration of C_3S has been determined using a combination of DTA and TG [89]. For a known amount of vacuum-dried paste, TG determined the percentage of the ignited weight

(P_I) and the percentage of CH formed (P_{CH}) at different periods of hydration. DTA was used to estimated the amount of unhydrated C_3S (P_{C3S}; the percentage of unhydrated C_3S) remaining in the sample. The CaO/SiO_2 ratio was calculated by Equation (2.9a) [89]:

$$CaO/SiO_2 = 3.000 - 3.081\ P_{CH} / (P_I - P_{C3S}) \qquad (2.9a)$$

In the same way, the CaO/SiO_2 ratio can also be calculated by Equation (2.9b) if the ignited weight (W_I), the weight of CH formed (W_{CH}) and the weight of unhydrated C_3S (W_{C3S}) are known,

$$CaO/SiO_2 = 3.000 - 3.081\ W_{CH} /(W_I - W_{C3S}) \qquad (2.9b)$$

Both methods of DTA and TGA have been used to follow the hydration of C_3S as a function of time [86, 90]. In Figure 2.3 [86] the small endothermal effect below 200 ºC, which was caused by the removal of loosely bounded water and firmly held water from the C-S-H gel, was the evidence of the onset of hydration.

The endothermal effect at about 480 ºC was attributed to the hydration of $Ca(OH)_2$. Ramachandran [90] compared the relative amounts of CH formed at different times of hydration using DTA and chemical methods and gave the curves of the amounts of CH vs. the time of the hydration of C_3S (Figure 2.4). The higher values derived from the chemical analysis compared to those from the thermal method may be due to the attack of the C-S-H phase by the solvents used in the chemical method.

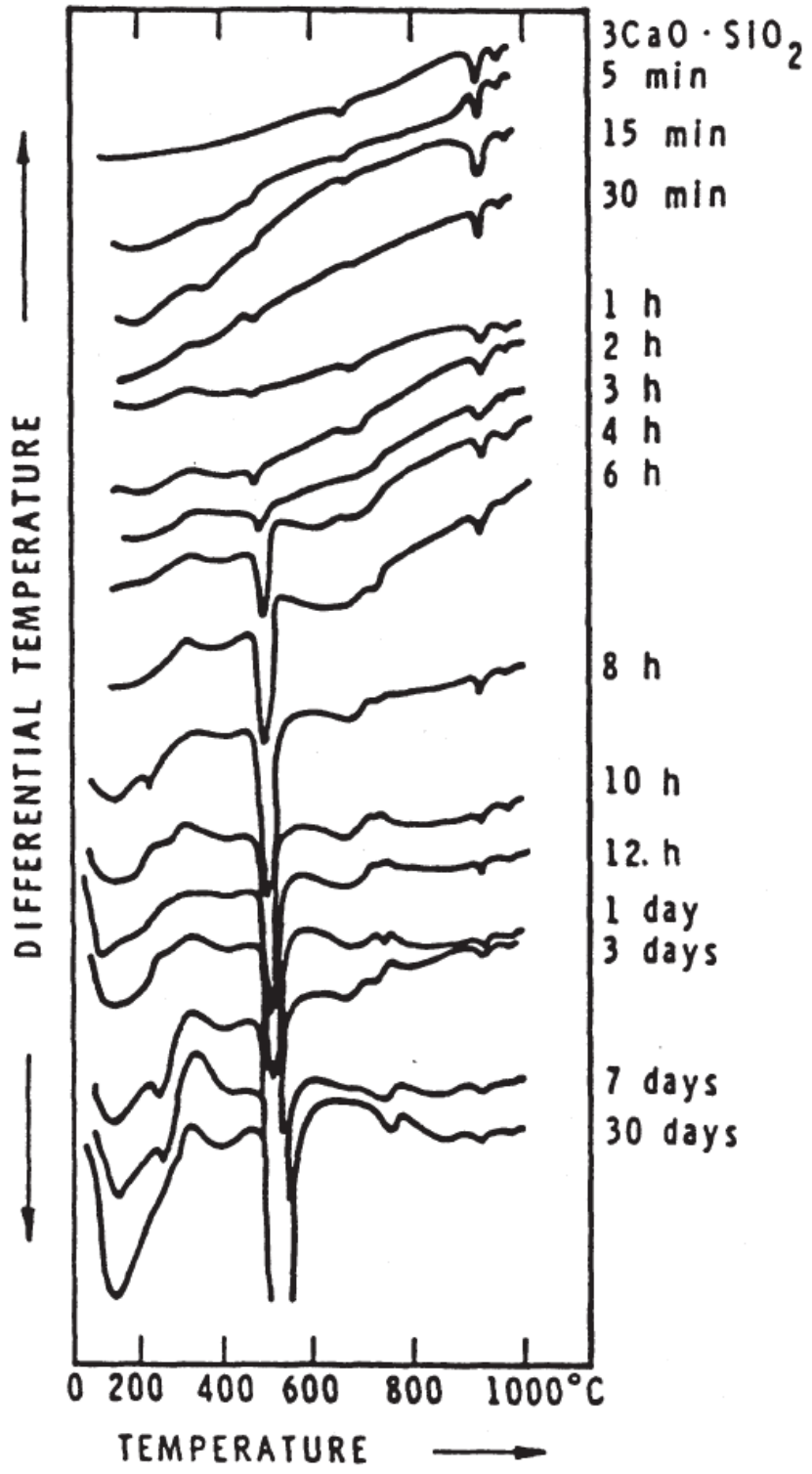

Figure 2.3 DTA curves of tricalcium silicate hydrated in water (Reproduced with permission [86])

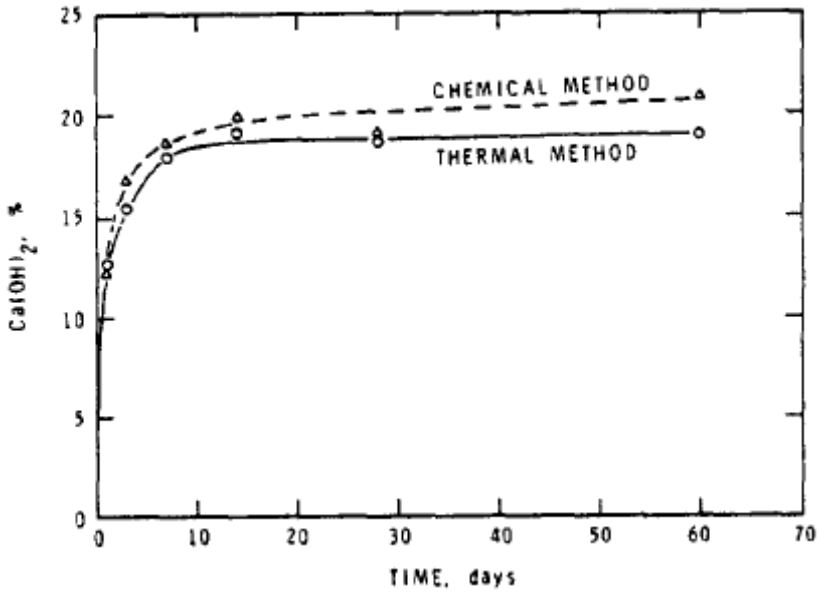

Figure 2.4 Amounts of CH vs. the time of the hydration of C_3S (Reproduced with permission [90])

2.3 Calcium Phosphates

Calcium phosphates (in this review phosphate means orthophosphate, i.e. containing PO_4 groups) are the most important inorganic constituents of biological hard tissues, of which the mineral phase is carbonated hydroxyapatite. In the ternary system $Ca(OH)_2 – H_3PO_4 – H_2O$, there are eleven known non-ion-substituted calcium phosphates [52]. In this review, only calcium phosphates possibly related to this research will be discussed, refer to Table 2.2 below. They include monocalcium phosphate monohydrate (MCPM), CPM, DCPD, dicalcium phosphate anhydrous (DCPA), octacalcium phosphate (OCP), ACP, and HAP. The important parameters, such as Ca/P ratio (the molar ratio of element Ca to P in a calcium phosphate compound), basicity – acidity and solubility, of the calcium phosphates are strongly affected by

the solution pH. Table 2.2 lists the solubility product constants for the calcium phosphate compounds at 25 and 37 ºC [52, 91, 92]. Calcium phosphates are easily soluble in acids but insoluble in alkaline solution [52]. The solubility of these compounds in water depends on the molar ratio of Ca/P. The lower the Ca/P ratio, the more acidic and water-soluble the calcium phosphate is.

Table 2.2 Ca/P ratio and solubility of some calcium phosphates at 25 and 37 ºC [52, 91 - 93]

Compound	Ca/P ratio	Formula	-logK_{sp} at 25ºC	-logK_{sp} at 37ºC
MCPM	0.50	$Ca(H_2PO_4)_2 \cdot H_2O$	1.14	-
CPM	0.50	$Ca(H_2PO_4)_2$	1.14	-
DCPD	1.00	$CaHPO_4 \cdot 2H_2O$	6.59	6.63
DCPA	1.00	$CaHPO_4$	6.90	7.02
OCP	1.33	$Ca_8H_2(PO_4)_6 \cdot 5H_2O$	96.6	98.6
ACP	1.20-2.20	$Ca_xH_y(PO_4)_z \cdot nH_2O$ n=3-4.5; 15-20% H_2O	~	~
HAP	1.67	$Ca_{10}(PO_4)_6(OH)_2$	116.8	117.2

(~ Cannot be measured precisely.). [a] Stable at temperatures above 100ºC.

The solubility phase diagrams of the ternary system $Ca(OH)_2 – H_3PO_4 – H_2O$ at 37 ºC are demonstrated in Figures 2.5(a) and 2.5(b) [94]. They show the logarithm of the total calcium concentration (log [Ca]) and of the total phosphate concentration (log [P]) of the saturated solutions as a function of pH for seven calcium phosphate compounds: tetracalcium phosphate (TTCP), DCPD, DCPA, OCP, α-tricalcium phosphate (α-TCP), β-tricalcium phosphate (β-TCP),

and HAP. The diagrams indicate that these compounds are soluble when pH ≤ 7, and in the alkaline regions the concentration of Ca increases as the pH increases. Except for DCPD and DCPA, the concentration of P decreases as pH increases [94]. In general, at a given pH any compound whose isotherm lies below another is relatively less soluble and more stable. Although MCPM and CPM are not included in the diagrams, in according to their data of *Ksp* (Table 2.2), it would be reasonable to assume that the MCPM and CPM isotherms lie above DCPC and DCPA. From these solubility phase diagrams it can be seen that at 37 ºC HAP is the least soluble salt among all calcium phosphates in a solution pH above about 4.2, where DCPD becomes the least soluble salt at pH below 4.2 [94]. Therefore, in the pH above 4.2, other calcium phosphate compounds suspended in an aqueous solution tend to dissolve and re-precipitate as HAP. The reaction equations of CPM and DCPD in the solution of the pH above 4.2 would be:

$$5Ca(H_2PO_4)_2 + H_2O = Ca_5(PO_4)_3OH + 7H_3PO_4 \qquad (2.10a)$$

$$5CaHPO_4{\cdot}2H_2O = Ca_5(PO_4)_3OH + 2H_3PO_4 + 9H_2O \qquad (2.10b)$$

For all calcium phosphate compounds except TTCP and TCP, the ratios of Ca/P are lower than that of HAP, resulting in the production of H_3PO_4 in the solution as a by-product. The accumulation of H_3PO_4 in the solution would decrease the pH value of the calcium phosphate solution to a point (the singular point) that the solution becomes saturated with respect to both compounds, i.e. the calcium phosphate compound and HAP. When an alkali, such as $Ca(OH)_2$, is

introduced into the solution, the alkali neutralizes H_3PO_4 and the reactions (2.10a) and (2.10b) shift to the direction to form HAP. Due to the triprotic equilibrium existing in the phosphate-containing solution, the effect of pH on the formation of calcium phosphates is linked to the relative concentrations of the four protonated forms of phosphate acid (Figure 2.6) [95].

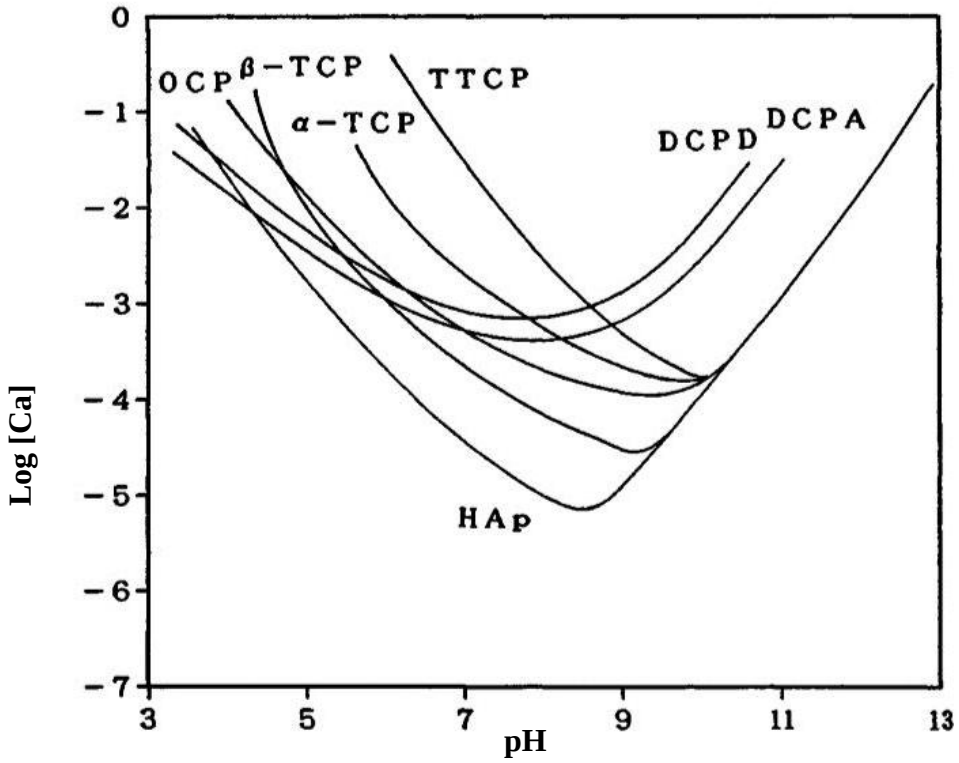

(a)

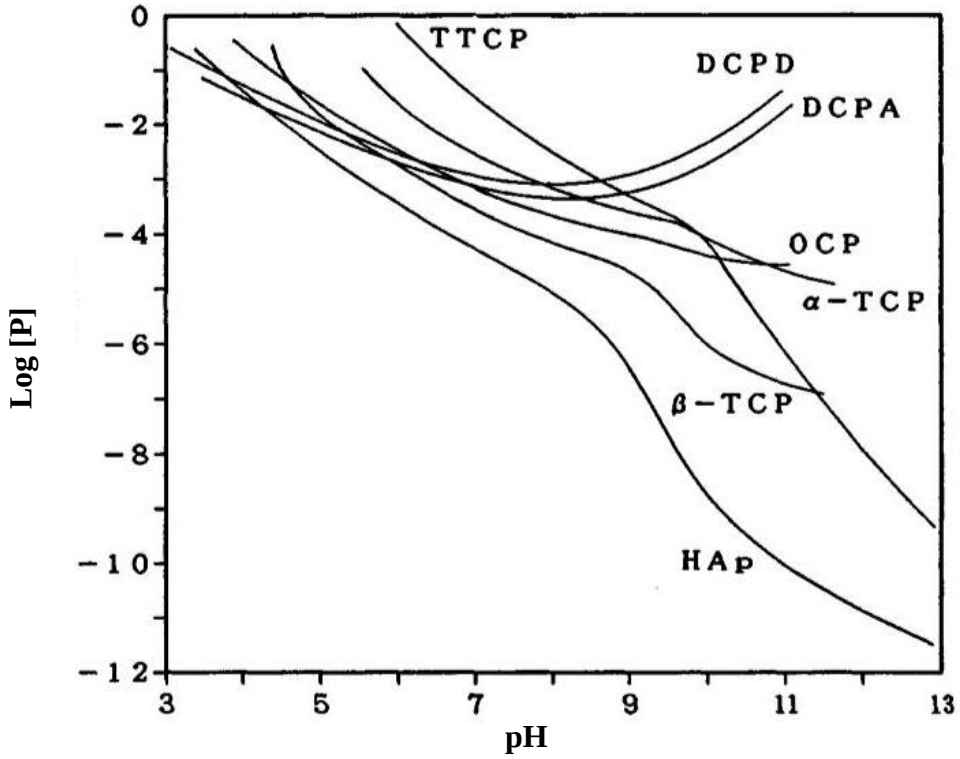

(b)

Figure 2.5 Solubility isotherms of various calcium phosphate salts in equilibrium with their solutions for the ternary system $Ca(OH)_2$-H_3PO_4-H_2O at 37 ºC. (a) log [Ca] versus pH of the solutions and (b) log[P] versus pH of the solutions (Reproduction with permission [94]).

$$H_3PO_4 \overset{K_I}{\Leftrightarrow} H_2PO_4^- \overset{K_{II}}{\Leftrightarrow} HPO_4^{2-} \overset{K_{III}}{\Leftrightarrow} PO_4^{3-}$$

$K_I = 7.50 \times 10^{-3}$, $K_{II} = 6.20 \times 10^{-8}$, $K_{III} = 1.70 \times 10^{-12}$

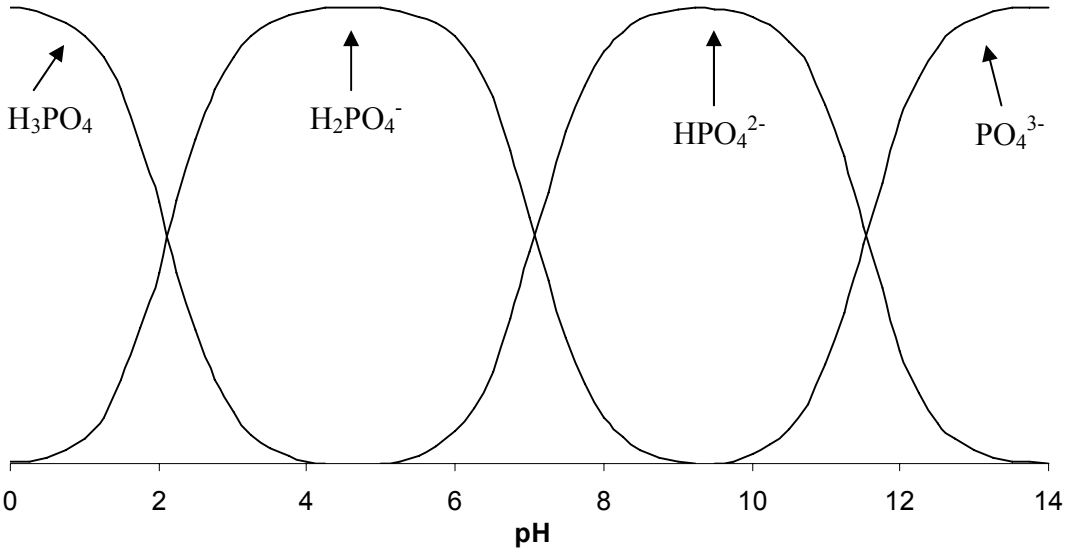

Figure 2.6 pH variations of ionic concentrations in triprotic equilibrium for phosphoric acid solutions. Variations in pH alter the relative concentrations of the four protonated forms of phosphoric acid (Redrawn from [95]).

2.3.1 MCPM and CPM

MCPM [$Ca(H_2PO_4)_2 \cdot H_2O$] and CPM [$Ca(H_2PO_4)_2$, also named monocalcium phosphate anhydrous], are the most acidic and water-soluble calcium phosphate compounds. The Ca/P molar ratio is 0.5; and pH of the saturated aqueous solution is less than 2.0 [52]. Due to their acidity, both MCPM and CPM are not biocompatible; however, either material can be used in medicine as a component of biomaterials.

2.3.2 Dicalcium phosphate dihydrate (DCPD)

DCPD ($CaHPO_4 \cdot 2H_2O$; the mineral brushite) easily precipitates from aqueous solutions and converts to DCPA by drying. DCPA can be precipitated from aqueous solution but at above 60ºC [96]. DCPD crystals consist of paralleled $CaPO_4$ chains, between which crystal water molecules are interlayered [52]. Due to the absence of water inclusions in its structure, DCPA is less soluble than DCPD. Thermodynamically, DCPD is more stable than OCP and HAP below pH 4.2 at ambient temperature and 37 ºC [93]. However, DCPD is in its predominant phase up to pH 6.5, resulting from the effect of kinetic factors, where above this pH ACP and OCP form more easily [97]. They are thermodynamically metastable with respect to HAP and serve as precursor phases.

2.3.3 Octacalcium phosphate (OCP)

OCP ($Ca_8H_2(PO_4)_6 \cdot 5H_2O$) has a triclinic structure; however, a portion of OCP displays remarkable similarities to the hexagonal structure of HAP. This portion of OCP has been referred to as the 'apatite layers', in which atomic arrangements of calcium and phosphate ions are similar to those in HAP. Another portion of OCP containing water molecules is referred to as the 'hydrated layers,' in which atomic arrangements of calcium and phosphate ions and water molecules are similar to those in DCPD. Alternating apatite and hydrated layers, which are parallel to the face (100), consist of the structure of OCP [96, 98, 99]. The closeness in crystal structure between OCP and HAP is one reason that the epitaxial growth and the formation of lamellar mixtures by these two phases are observed.

OPC is an important biological mineral component because it plays a significant role as a possible precursor during the formation of carbonated apatite in the skeletal tissues. OCP was first proposed to be essential in the mineral-forming process of hard tissue as an intermediate

phase with a unique intracrystalline relationship with the final HAP-like phase [100, 101]. A "central dark line" often seen by transmission electron microscopy in the hexagonal cross-sections of mature enamel crystallites is possibly a remnant of the initial OCP template [102, 103]. OCP is an unstable transient phase and tends to transform to HAP through dissolution and re-precipitation, as other calcium phosphates do.

2.3.4 Amorphous calcium phosphate (ACP)

ACP ($Ca_xH_y(PO_4)_z{\cdot}nH_2O$, n = 3 – 4.5; 15-20% H_2O) is characterized by a lack of long-range order and usually may be prepared by rapidly mixing the supersaturated solutions containing calcium and phosphate ions. Thermodynamically, ACP is an unstable phase and easily converts to HAP in aqueous solution, unless stored in dry conditions or stabilized by other molecules or ions [104]. The lifetime of ACP in aqueous solution is influenced by the pH, ions, ionic strength and temperature. Increasing the concentrations of calcium and phosphate ions and the solution pH makes ACP form easily. However, if the solution is sufficiently dilute, such as $[Ca^{2+}]$ = 1.67 mM and $[PO_4^{3+}]$ = 1.00 mM and pH 7.4, HAP is the first solid phase precipitated without forming an amorphous precursor [105]. ACP has a relatively constant chemical composition over the pH range 7.4 – 9.25 and the solid-phase composition is postulated to be $Ca_3(PO_4)_{1.87}(HPO_4)_{0.2}$ i.e. Ca/P = 1.45, about 10% HPO_4^{2-}, no OH^- ions [106]. ACP with a Ca/P ratio as low as 1.18 at pH 6.6, 1.53 at 11.7, even to 2.5 has been reported [52]. Under TEM, dried ACP solids display a curvilinear appearance rather than the faceted and angular shape of crystalline calcium phosphates [107] and the size is about 20 – 300 nm in diameter. The transformation kinetic, which can be described by a "first-order" rate law, is a function only of the pH of the mediating solution at constant temperature. The solution-mediated transformation is controlled by the conditions which govern both the dissolution of ACP and the precipitation of the HAP nuclei [108].

2.3.5 Hydroxyapatite (HAP)

Hydroxyapatite [HAP or OHAP; $Ca_5(PO_4)_3OH$, also written as $Ca_{10}(PO_4)_6(OH)_2$] crystals may have either monoclinic or hexagonal unit cells. HAP is the second most stable and least soluble calcium phosphate after fluorapatite [52]. The detailed HAP structure was described in elsewhere [109] and has been widely accepted as an aggregation of the $Ca_9(PO_4)_6$ cluster (so-called Posner's cluster) [110]. The amorphous clusters hydrolyze almost instantaneously to more stable phases and serve as seeds during HAP crystallization via a stepwise assembly process [111]. The monoclinic form is more stable than the hexagonal one, even though both are very similar; however, in biological apatite the hexagonal form of HAP is a more common [109]. In comparison with the monoclinic HAP, the hexagonal form has more disordered hydroxide ions within each row, pointing either upward or downward in the structure. This causes substitutions or ion vacancies to compensate the induced strains; therefore, hexagonal HAP is rarely the stoichiometric phase [109]. Fluoride, chloride, and carbonate ions can be incorporated into the HAP structure to form substituted HAP very easily.

Generally, HAP synthetic techniques can be divided into solid-state reactions and wet methods [96, 112]. The formation of calcium phosphates from supersaturated solutions is dependent upon the combination of pH and temperature rather than on the initial Ca/P molar ratio of the solution [96]. Table 2.3 lists the dependence of calcium phosphate formation on pH / temperature.

2.3.6 Calcium polyphosphates (CPP)

Calcium polyphosphate (CPP) is one of the condensed phosphates, consisting of PO_4^{3-} tetrahedra linked through oxygen atoms to form three-dimensional networks, ring structures, or linear chain inorganic polymer [113]. CPP decomposes through hydrolytic degradation, during

which water molecules break down the P-O-P bonds resulting in detachment of phosphates from the end of chains or formation of two shorter chains that continue to degrade and eventually form phosphates [114]. The final degradation products of CPP, i.e. phosphate and calcium ions, are important to metabolism, and studies proved that at a suitable degradation rate, CPP is *in vitro* [115] and *in vivo* biocompatible [113, 116]. The degradation rate depends on the sintering condition, microstructure, particle size, and geometry of the implants [116-119]. With suitable synthetic techniques, porous CPP scaffolds with relatively high compressive strength and stiffness have been obtained [113]. CPP is a promising material to fabricate porous bone substitute implants for load-bearing skeletal sites.

Table 2.3 The dependence of calcium phosphate formation on pH/temperature [96]

pH/ temperature, ºC	Calcium phosphate formed
4-6/ 25	DCPD
4-6/ 37	DCPD
6.5/ 37	OCP
7.5-9/ 37	HAP (poorly crystallized)
4/ 60	DCPD
5/ 60	OCP
7-9/ 60	HAP
4/80	OCP
6-9/80	HAP
4-9/ 95-100	HAP

Molar Ca/P = 1; concentration = 10 mM.

The pH/temperature effect is modified in the presence of other ions, e.g. Mg^{2+}, CO_3^{2-}, $P_2O_7^{4-}$.

2.4 Calcium Silicate with Phosphates

Calcium phosphate silicate cement is the next generation biological cement first proposed by Lu and Zhou in 2005 [40-43]. CPSC describes a family of materials, in which the powder component is mainly composed of the mixture of hydraulic calcium silicates and calcium phosphates with/ without crystal water. Hydraulic calcium silicates include C_3S and C_2S, or mixtures thereof. Calcium phosphates include such as CPM, MCPM, DCPD/DCPA, and /or mixtures thereof, etc. The hydration liquid is pure water or aqueous solutions of calcium chloride or sodium phosphates of various types.

In calcium silicate-based cements containing inorganic phosphate ions, the substitution of P^{5+} for Si^{4+} may take place in clinker alites due to the presence of phosphates in the raw material used in producing cement [54]. The concentration of P_2O_5 for most cement is around 0.2 % and higher contents of P_2O_5 cause C_3S to decompose into C_2S and free lime (CaO). During high temperature processing, P_2O_5 and C_2S phases form a solid solution. Therefore, the high content of P_2O_5 in cement reduces its strength development during the cement setting. A study [120] showed that 2.25 % P_2O_5 should be the maximum amount allowed in cement clinker and that for every percent of P_2O_5 present in cement, C_3S was reduced by 9.9 % and C_2S increased 10.9 % in solid solution. On the other hand, phosphate compounds may be included (admixed) in composite cements with hydraulic calcium silicates; such composite cements belong to the CPSC group. However, limited studies on the cements of the CPSC system have been made so far.

A study [121] showed that the addition of MCPM (10 to 30 wt%) to C_3S had a complex effect on the cement setting time. With the addition of 20 wt% of MCPM into C_3S, the initial and final setting times of the cement pastes decreased three times as compared with those of pure

tricalcium silicate paste, i.e. from 90 min to 30 min and from 180 min to 90 min, respectively. When the content of MCPM was 30 wt%, however, the initial and final setting times, i.e. 75 and 150 min, were much higher than those of the cement paste containing 20 wt% of MCPM. The acceleration of the C_3S hydration was expected due to an acid-base reaction between MCPM and CH produced by the hydration of C_3S. With the addition of 30 wt% of MCPM, a lower rate of polymerization of C-S-H gels produced by the hydration of C_3S likely causes the prolongation of setting times. Another study [122] on CPC comprising ACP and DCPD, with the addition of β-C_2S, showed that the setting time decreased with the amount of β-C_2S, i.e. the initial and final setting times changed from 35 min and 50 min for CPC to 23 min and 33 min for CPC with 20 % β-C_2S. However, other studies [123-125] on the varieties of CPSCs showed that the setting times became longer with the addition amounts of calcium silicates in comparison with pure CPCs. These studies also indicated that for CPCs with a low content of calcium silicates, the variation of pH of the cement paste in simulated body fluid (SBF) solution did not change significantly; however, with the addition of more MCPM in C_3S, its pH in SBF was notably reduced. For examples, for pure C_3S and the cement containing 10 wt% MCPM, the pH increased rapidly and reached maximum at 11.5 – 12.0 after 5 h, but for the cements with 20 % and 30 % MCPM, the pH reached the maximum of 10.5 after 8 h and of 9.0 after 10 h, respectively [121]. These studies demonstrated the changes in setting times and the pH of cement pastes during setting. The reactions between calcium silicates and calcium phosphates during cement setting or their hydration products were believed to be responsible to the changes. However, these studies did not provide the solid experiment data to illuminate the reaction mechanisms between calcium silicates and calcium phosphates during setting; and these reactions and their products are crucial to understand the hydration of calcium phosphate silicates cements, in turn to understand the microstructure development of the cements and their properties, to control and/or adjust the hydration processes by using different formulations or

hydration conditions, and further to find suitable applications. The present research work investigates the reaction mechanisms between C_3S and CPM (0 – 25 wt%) with distilled water using DTA-TGA, XRD, and quantitative XRD with quartz as an internal standard.

Mechanical properties are affected by the composition of CPSC. A study [122] on the cements of CPC with 0 to 20 % β-C_2S showed that the compressive strength increased with the addition of 8 wt% of β-C_2S from 26.5 ± 1.5 MPa to about 47.5 ± 2.0 MPa. The enhancement was mainly attributed to the filler effect of the hydrated amorphous C-S-H gel [122]. After investigating the cements of DCPD with 20 – 40 % C_3S, Han and Chang [123] suggested that the formation of hydroxyapate in the cement of DCPD + C_3S was another reason that improved the compressive strength, besides the filler effect of C-S-H phase. However, another study [125] on the compositions of α-TCP + 5 and 10 % C_3S observed that the compressive strength of the cement of α-TCP + 10 % C_3S was lower than that of pure α-TCP after up to 14 days of setting. The authors suggested that the C-S-H phase might coat on the α-TCP particles and reduced its hydration rate and the strength at early stages [125]. The homogeneous distribution of cement components was important to the mechanical property; the appearance of microcracks, due to the non-uniform distribution of MCPM (20 and 30 %) in C_3S matrix, reduced the compressive strength [121]. Although these authors proposed some mechanisms that explained the improved or decreased mechanical properties for CPSC cements, there is still lack of understanding of the microstructure and mechanical property development of CPSC during setting. The present work investigated the microstructure and mechanical properties of CPSC composed of C_3S with 0 – 25 wt% of CPM for various periods of hydration time using SEM/EDX and XRD.

The hydration mechanisms of CPSC systems have not been reported in literature, but some related reactions between calcium phosphates and calcium hydroxide/ oxide, or Portland cement are reviewed here. Generally, calcium phosphate cement consists of one or a mixture of more-acidic components and one or a mixture of more-basic components [3]. Upon being mixed with water or an aqueous solution, it sets and forms a network of crystals of one or more calcium phosphates of intermediate acidity [3]. This occurs around room or body temperature through the process of dissolution and re-precipitation. The solubility and the relative stability vs. pH for crystalline calcium phosphate compounds in solutions at room and /or body temperature are shown in Tables 2.2 and 2.3 and Figure 2.5.

The first discovered CPC [1, 2], consisting of DCPD / DCPA and TTCP [$Ca_4 (PO_4)_2O$] (1:1 molar ratio), forms HAP upon being mixed with water according to the following reactions:

$$2\ CaHPO_4{\cdot}2H_2O + 2\ Ca_4(PO_4)_2O = Ca_{10}(PO_4)_6(OH)_2 + 4\ H_2O \quad (2.11)$$

$$2\ CaHPO_4 + 2\ Ca_4\ (PO_4)_2O = Ca_{10}(PO_4)_6(OH)_2 \quad (2.12)$$

Since then many formulations have been developed, and here are two examples: DCPD + CaO [126] and DCPD + $Ca(OH)_2$ [127]. The reactions are shown below.

$$6\ CaHPO_4{\cdot}2H_2O + 4\ CaO = Ca_{10}(PO_4)_6(OH)_2 + 14\ H_2O \quad (2.13)$$

$$6\ CaHPO_4{\cdot}2H_2O + 4\ Ca(OH)_2 = Ca_{10}(PO_4)_6(OH)_2 + 18\ H_2O \quad (2.14)$$

A study [128] on a cement composed of MCPM and CaO (Ca/P around 1.67) mixed with water or various concentrations of phosphate buffer solutions (PBS) indicated that the hydration reaction of the cement was completed in two steps as follows:

$$3\ Ca(H_2PO_4)_2{\cdot}H_2O + 3\ CaO + 6\ H_2O = 6\ CaHPO_4{\cdot}2H_2O \qquad (2.15)$$

$$6\ CaHPO_4{\cdot}2H_2O + 4\ CaO = Ca_{10}(PO_4)_6(OH)_2 + 14\ H_2O \qquad (2.13)$$

The reaction (2.13), especially when the liquid was PBS, was slower than the reaction (2.15) that took place immediately upon mixing with liquid [128]. When water was used as the liquid phase, the reaction (2.13) produced HAP in less than 24 h [128]. Another study [129] optimized the formulation of the cement consisting of MCPM and CaO and discovered that the most suitable formula was at the molar ratio of Ca/P = 1.35 and the weight ratio of w/c = 0.53; and thus OCP was speculated as the final product of the hydration reaction by the authors. In this case, the maximum values of the compressive strength and the diametral tensile strength were 6 and 1.6 MPa, respectively, within 5 h of setting and the amount of precipitated HAP was about 7 wt% in the set cement. Other formulations of the cements containing MCPM or CPM as starting materials, such as MCPM + β-TCP [β-$Ca_3(PO_4)_2$] [130], MCPM + TTCP + CH [131], MCPM + HAP [132], have been investigated and DCPD was either the final product or the intermediate product, depending on the Ca/P ratio and solution pH.

Hu and his co-workers [133-135] synthesized the materials of different compositions in the system CaO-SiO_2-P_2O_5-H_2O by a sol-gel process, followed by calcining at 700 ºC for 2 h. They found that when mixing the materials with water at different temperatures, the final reaction products were HAP, crystalline and gel phases of C-S-H and C-S-P-H with/ without CH. The

amounts of these phases depended on the composition of the starting material. The following reactions represent the hydration reactions.

$$3\beta\text{-}Ca_3(PO_4)_2 \text{ (from calcining)} + CaO + H_2O \rightarrow Ca_{10}(PO_4)_6(OH)_2 \qquad (2.16)$$

$$CaO + SiO_2 \text{ (gel)} + H_2O \rightarrow \text{C-S-H (crystalline)} + \text{C-S-H (gel)} \qquad (2.17)$$

$$\text{C-S-H (gel)} + \text{amorphous } P_2O_5 \rightarrow \text{C-S-P-H (gel)} \qquad (2.18)$$

The C-S-H and C-S-P-H phases showed fibrous and acicular microstructure and their compositions were $CaO:SiO_2 = 0.6 – 0.8$ for C-S-H gel and $CaO:SiO_2:P_2O_5 = 1:1:0.5$ for C-S-P-H gel. The CH phase formed when the content of CaO in the start materials was more than 58 wt%, which corresponded to the content of CaO in silicocarnotite ($5CaO{\cdot}SiO_2{\cdot}P_2O_5$). The optimal composition for the maximum tensile splitting strength was 59.2 wt% CaO, 17.2 wt% SiO_2 and 23.5 wt% P_2O_5, and the C-S-H phase contributed the strength to the material.

Ordinary Portland cement (OPC) mixed with different phosphates (sodium and calcium phosphates) was studied by Ma et al [136]. The phosphate-modified OPC produced more heat and showed much faster hydration rates than OPC. The faster the hydration reaction is, the more strength the sample exhibits. Generally, the presence of sodium and calcium phosphates resulted in improved flexural strength, but a modest ratio of w/c was needed to achieve high strength for the OPC-phosphate system. The phosphate-containing hydration products formed in this system at room temperature were X-ray amorphous, but SEM shows that the modified OPC developed distinct hydration products morphologically. For example, fibrous, poorly crystalline HAP

formed in the calcium phosphate-modified OPC was observed under SEM. After hydrothermal treatment at 160 ºC, this phase transformed to crystalline HAP.

Although these studies are related to the present work, the hydration mechanisms of CPSC including C_3S and 0 – 25 wt% of CPM and distilled water, have not been reported. Understanding CPSC hydration processes at 37 ºC, in terms of its kinetics, the hydration products, and the microstructure development, is important. Additionally the properties of CPSC as bio-cement including setting, hardening, pH of the cement pastes, the mechanical properties, bioactivity as well as biocompatibility, are very important to find suitable applications. As mentioned above, in the present work, the compositions of CPSC powders consisted of tricalcium silicate and 0, 5, 10, 15, 20, and 25 wt% of CPM. They were synthesized through a sol-gel process followed by sintering and planetary ball-milling. The investigation focuses on such prepared CPSC exposed to distilled water at 37 ºC to understand the hydration mechanisms including the hydration products and hydration kinetics. CPSC cement pastes were studied including the phase compositions, pH, the microstructure development, the mechanical properties development (compressive strength and three – point flexural strength), *in vitro* bioactivity with SBF solution, and *in vitro* biocompatibility against human gingival fibroblasts.

2.5 *In Vitro* Bioactivity

A material is *in vivo* bone bioactive if the material implanted into bone defects develops chemical bonding between the material and living bone instead of being isolated by fibrous tissues from the surrounding bone. Kokubo and his co-workers [137] first proposed that the formation of bonelike apatite on a material's surface is the essential requirement for the material to bond to living bone when implanted in a living body. Also, this *in vivo* apatite formation can be reproduced in simulated body fluid (SBF), in which ion concentrations are nearly equal to

those in human blood plasma [137]. The ability to form bone-like apatite on the surface of a material in SBF has been called *in vitro* bioactivity. The ion concentrations of SBF and human blood plasma are shown in Table 2.4 and the preparation of SBF is described in the reference [137].

Table 2.4 Nominal ion concentrations of SBF in comparison with those in human blood plasma [137]

	Ion concentrations (mM)								
	Na^+	K^+	Mg^{2+}	Ca^{2+}	Cl^-	HCO_3^-	HPO_4^{2-}	SO_4^{2-}	pH
Human blood plasma	142.0	5.0	1.5	2.5	103.0	27.0	1.0	0.5	7.2 7.4
SBF	142.0	5.0	1.5	2.5	147.8	4.2	1.0	0.5	7.40

Many investigations on the mechanisms of the formation of apatite layers have been made with different materials, including those in the CaO-SiO_2-P_2O_5 system [121, 123, 138 – 143]. It was found that a silica hydrogel layer or silanol (Si-OH) groups in Si-containing materials induced apatite nucleation [141]. Once the apatite nuclei are formed, they can spontaneously grow by consuming the calcium and phosphate ions from SBF, since SBF is already highly supersaturated with respect to apatite. Materials without silanol group or silica hydro gel lose their apatite-forming ability, for instance, silica glass and crystalline quartz cannot form apatite layers. Calcium ion released from materials into SBF accelerates apatite formation because calcium ion increases the ionic activity product of apatite in SBF and the pH of SBF, i.e. the concentration of OH^-, since both Ca^{2+} and OH^- are components of apatite. Although studies

showed that CPSC and C_3S are *in vitro* bioactive by immersion into SBF, the comparison of *in vitro* bioactivities of CPSC vs. C_3S is not known. The present work made an attempt to demonstrate the *in vitro* bioactivity of CPSC by studying the layer of HAP formed on CPSC in SBF.

2.6 *In Vitro* Biocompatibility

Biocompatibility is the ability of a material to perform with an appropriate host response in a specific application [144]. The evaluation of biocompatibility is a process conducted on a variety of biomaterials, medical devices, and related products to identify the presence of toxins or any other potentially harmful effects; the safety evaluation includes *in vitro* and *in vivo* studies. Cytotoxicity is a major factor of biocompatibility and is generally determined by *in vitro* cell culture studies [145]. In comparison with *in vivo* studies, cytotoxicity assays provide simple, convenient, controllable, repeatable, and cost-effective means for an initial evaluation of biological response to materials and are useful predictors for the assessment of biomaterial biocompatibility. The tetrazolium salt MTT assay, which measures mitochondrial dehydrogenase activity in living cells, is a sensitive, quantitative, and reliable colorimetric assay and a well-accepted assay to evaluate the cytotoxicity of biomaterials [146]. Cell attachment and spreading on biomaterial surfaces are critical phenomena for successful tissue-biomaterial interaction because the attachment and spreading of cells dominate normal cell growth and protein synthesis, while poor adhesion and lack of spreading will lower cell proliferation rate [147, 148].

A previous study showed that the addition of a small amount (2.5 to 7.5 wt%) of C_3S to an α-$Ca_3(PO_4)_2$ – based cement enhanced *in vitro* biocompatibility in comparison with α-$Ca_3(PO_4)_2$–based cement [125]. The authors explained the improvement of *in vitro* biocompatibility as the stimulation effect of silicate ions in α-$Ca_3(PO_4)_2$ + C_3S on cell

proliferation. Another study [123] demonstrated that *in vitro* biocompatibility of DCPD + 40 wt% C_3S was better than that of DCPD + CaO (Ca/P = 1.67). The high pH (9.5 to 10.2) caused the latter cement for the toxicity, while silicate ions in the former cement stimulated cell proliferation. Although the above investigations showed that CPSC had an enhanced *in vitro* biocompatibility, the hypothesis proposed in Section 1.2, i.e. the improvement of CPSC *in vitro* biocompatibility in comparison with calcium silicate cement, still needed to be verified and constituted one of the objective of the present work. To our knowledge, there is no previous literature on the comparison of the *in vitro* biocompatibility of CPSC with calcium silicate cements. The aim of the bio-properties (*in vitro* bioactivity and biocompatibility) evaluation was to investigate the influence of the addition of CPM on the properties of CPSC cement, consisting of C_3S and CPM, and to compare the results, in terms of *in vitro* bioactivity, cytotoxicity, and cell adhesion and proliferation, with those obtained for C_3S.

3 MATERIALS AND METHODOLOGY

3.1 Material Preparation

3.1.1 Preparation of tricalcium silicate

Tricalcium silicate powder was synthesized through a sol-gel process. The following chemicals were used in the production of C_3S: calcium nitrate tetrahydrate [$Ca(NO_3)_2$ $4H_2O$; Fisher], tetraethyl orthosilicate [TEOS, $Si(OC_2H_5)_4$; Sigma-Aldrich], distilled water, ethanol (denatured; Fisher), and nitric acid (HNO_3; Sigma-Aldrich). The molar ratio of CaO/SiO_2 was 3.0 and nitric acid was used as a catalyst. In the first step of the procedure, $Ca(NO_3)_2$ $4H_2O$ was dissolved in a minimum amount of ethanol under continuous stirring. Then, distilled water (TEOS: distilled water = 1:4 in mol) and nitric acid were added during stirring. After getting a homogeneous solution, the required amount of TEOS diluted with the same weight of ethanol was added into calcium nitrate solution and continuously stirred for another 24 h. Then, the solution was maintained at room temperature for 48 h until a transparent gel formed. The gel was dried at 150 °C and then fired at 1550 °C for 4 h in a platinum crucible to reduce contamination and as-synthesized C_3S powder was obtained. The powder was stored in a desiccator for further experiments.

The phase composition of the as-synthesized C_3S powder was determined by XRD (XRD; Multiflex, Rigaku Co, Japan) using Cu Kα radiation at 40 KV and 20 mA and diffraction data was collected in the range of 10 - 60 ° in 2 theta (θ) at the rate of 2 °/min with a step size of 0.04 degree. The morphology was examined under SEM, equipped with an energy dispersive X-ray spectroscopy analyser (SEM/EDX; Hitachi S-3000N, Electronic System Ltd, Tokyo, Japan).

The content of free CaO in the as-synthesized C_3S powder was determined by the method described in Reference [149]. Briefly, a standard CaO was first prepared by calcining 0.2000 g of dry, primary standard grade calcium carbonate ($CaCO_3$) at 982 ºC for 30 min in a platinum crucible. About 0.1 g (accurate to ± 0.1 mg) of the standard CaO and 2 g of dry standard sand (-50 Mesh) were thoroughly mixed in a dry 250 ml Erlermeyer flask. After 50 ml of ethylene glycol was added, the flask was heated for three min on a hot plate with a surface temperature of 232 ºC. The mixture was filtered under suction through a dry, medium fritted glass filter into a 125 ml Erlenmeyer flask. The residue in the 250 ml flask and the fritted glass were separately washed three times with alcohol. Using 10 drops of phenolphthalein as indicator, the liquid was titrated with 0.1 N hydrochloric acid. The above procedure was repeated with a 1.000 g cement sample instead of the standard CaO. The percentage of free CaO in cement was calculated using the following equation:

$$\text{Percentage of CaO} = \frac{M_{CaO}L_{cem}}{M_{cem}L_{CaO}} \times 100\% \qquad (3.1)$$

where M_{CaO} is the weight of standard CaO, g

L_{CaO} is the volume of 0.1 N HCl for standard CaO, mL

M_{cem} is the weight of cement, g

L_{cem} is the volume of 0.1 N HC for cement, mL.

3.1.2 Preparation of cement powders

CPSC powders were prepared by ball-milling the mixture of as-synthesized C_3S powder and different percentages of CPM (Sigma) in ethanol, with a planetary ball-mill machine

(Pulverisetts 5, Fristsch, Germany) for 20 min, using zirconia jar and Φ 20 mm zirconia balls and the ball to powder weight ratio was 3:1. The CPSC compositions are shown in Table 3.1. After being ground CPSC powders were dried in an oven at 110 ºC for 24 h and characterized under SEM. Four of the cement powders (0CPM, 5CPM, 10CPM and 20CPM) were chosen to measure Brunauer-Emmet-Teller (BET) specific surface area using nitrogen adsorption/ desorption at 77 K using a Quantachrome-1MP BET analyzer equipped with a 1-mm Hg pressure transducer (Quantachrome Instruments, Boynton Beach, Florida USA).

Table 3.1 The CPSC compositions, wt%

Group	0CPM	5CPM	10CPM	15CPM	20CPM	25CPM
C_3S	100	95	90	85	80	75
CPM	-	5	10	15	20	25

3.2 Characterization of the Hydration of CPSC

CPSC powders were mixed with distilled water at w/c = 10. The cement pastes were stored in sealed plastic bottles and stored in a water-bath of 37 ºC for the pre-set periods of time up to 28 days. Then, the pastes were filtered with filter papers [Q2 (1 – 5 μm); Fisher brand quantitative grade circle, Fisher] in a glove box, which was flushed with CO_2-free argon gas to prevent carbonation. The filtered solids were immediately immersed in ethanol for 2 h to stop the hydration and were subsequently air-dried for 24 h, and finally stored in a desiccator for further use. The solid materials were divided and used in the following experiments.

3.2.1 The pH of cement pastes

To measure the pH variations of the cement pastes after being mixed with water, the cement powders were mixed with distilled water in plastic bottles at the ratio of w/c = 10. The plastic bottles with the cement pastes were stored in a 37 ºC water bath during the measurement. The pH was determined and recorded for the first hour with a pH meter (Oakton Acron pH 5 equipped with an Oakton WD-35801 electronic probe, Oakton Instruments, Vernon Hills, IL USA) in air.

3.2.2 Hydration study using XRD

The qualitative and quantitative XRD studies were carried out on the set cement pastes crushed in ethanol using alumina mortar and pestle. The powders were air-dried for 24 h and vacuumed with a rotary pump for 1 h. The XRD data was collected using Cu K_α radiation at 40 kV and 40 mA and the scan range 10 – 60 º in 2θ, scan speed 2.000 º/min, and sample width 0.02 degree. For the quantitative XRD study, an internal standard was used with custom calibration curve. The standard sample mixtures of C_3S and quartz (SiO_2; used as the internal standard) at their weight ratios (X_c/X_s) of 8/92, 15/85, 25/75, 50/50, 70/30, and 90/10 were mixed and XRD scanned at the same conditions as above, except for the scan range 25 – 45 º in 2θ. The slope k from the internal standard calibration curve was obtained by plotting X_c/X_s vs. corresponding I_c/I_s (intensity ratio) of C_3S (at d = 2.19 Å) to quartz (at d = 3.34 Å) calculated in the peak areas. The cement paste samples for quantitative analysis were prepared by mixing the cement pastes, which set for pre-set periods of time, with 10 wt% of quartz (the same quartz sample) in ethanol using alumina mortar and pestle for 10 min, air-drying for 24 h, and vacuuming with a rotary pump for 1 h. The XRD measurements were done on the samples at the same conditions as those for the calibration curves. The percentage of unhydrated C_3S in the cement pastes was calculated using the following equation (3.2):

$$\text{Percentage of unhydrated } C_3S = \frac{100}{9k}(I_c/I_s)\ \% \qquad (3.2)$$

where k is the slope of internal standard calibration curve in Eq. (2.6) and I_c/I_s is the measured intensity ratio of C_3S to quartz calculated in peak area in the tested pastes.

3.2.3 Hydration study using DTA – TG

DTA-TG analysis was employed to determine the hydration products and carried out in helium (99.999%) at a flow rate of 0.5 L/min using a DTA-TG instrument (96 Line TGA-DTA, Setaram Instrumentation, France). The heating rate was 10 ºC/min from room temperature to 1200 ºC. The powder samples of cement pastes were the same as those for the qualitative XRD measurement and the sample weight was about 25 mg in platinum crucibles. The data was processed with the instrument software package (SETSOFT 2000) and expressed as the percentage of the ignited weight at 1100 ºC. The molar ratios of CaO/SiO_2 and H_2O/SiO_2 of C-S-(P-)H hydrates were calculated with Eqs. 3.3(a) and (b) and 3.4 (a) and (b), respectively.

$$CaO/SiO_2 = \frac{\frac{3\alpha}{M_{C_3S}} - \frac{\Delta W_{CH}}{M_{CH}}}{\frac{\alpha}{M_{C_3S}}} \qquad (3.3a)$$

$$H_2O/SiO_2 = \frac{\frac{\Delta W_{dh}}{M_{H_2O}}}{\frac{\alpha}{M_{C_3S}}} \qquad (3.4a)$$

where ΔW_{CH} is the percentage of the weight loss of total CH (W_{CH}, mg) to W_I, %, and calculated by $\Delta W_{CH} = W_{CH} / W_I$, where W_{CH} is obtained by Eq. (2.8), i.e. $W_{CH} = (4.11\ W_{dx} + 1.68\ W_{dc})$,

W_I is the ignited weight of the sample at 1100 ºC, mg,

α is the degree of hydration obtained from the XRD analysis, %,

ΔW_{dh} is the percentage of the weight loss of the hydrate dehydration (W_{dh}, mg) to W_I, %,

W_{dx} is weight loss during dehydroxylation, mg,

W_{dc} is weight loss during decarbonation, mg,

W_{dh} is weight loss during dehydration, mg,

M_{C3S} is the molar weight of C_3S, 228.33 g/mol,

M_{CH} is the molar weight of CH, 74.10 g/mol,

M_{H2O} is the molar weight of water, 18.02 g/mol.

The equations (3.3a) and (3.4a) can be simplified to

$$CaO/SiO_2 = 3.000 - 3.081\ \Delta W_{CH} / \alpha \qquad (3.3b)$$

$$H_2O/SiO_2 = 12.671\ \Delta W_{dh} / \alpha \qquad (3.4b)$$

3.2.4 Hydration study using SEM / EDX

The microstructure and morphology of 0CPM, 10CPM, and 20CPM were examined using SEM. Due to a lack of integrity of the cement specimens with the w/c ratio of 10 at the early hydration stage, the specimens were in powder form. The morphology of the hydration products was not easy to recognize. Another group of samples (0CPM, 10CPM, and 20CPM) with the w/c ratio of 0.5 were prepared and examined under SEM.

3.2.5 Apparent porosity of hydrated cements

After measuring their mechanical properties, the specimens were immersed in ethanol for 2 h, to stop hydration, and then air-dried. The apparent porosity were determined using the test method described in [150] and kerosene was chosen as the saturation liquid instead of water to avoid any reaction with the specimen. The air-dried specimens were dried in an oven at 105 ºC to a constant weight and the dry weight, *B*, was determined (for all the weight, gram was the unit with the accuracy 0.001 g). Then the test specimens immersed in kerosene were vacuumed in a vacuum chamber to an absolute pressure of not more than 6.4 kPa for 60 min. At least three measurements were used for each determination. The suspended weight, *S*, was determined in grams for each test specimen suspended in kerosene after saturation. The saturated weight, *W*, was determined by removing all drops of the liquid with a wet smooth linen from the surface. The exterior volume was calculated by Eq. (3.5) and the apparent porosity of the specimen was calculated by Eq. (3.6).

$$V = (W - S) / \gamma \tag{3.5}$$

$$\begin{aligned} P &= [(W - B) / \gamma / V] \text{ x } 100\ \% \\ &= [(W - B) / (W - S)] \text{ x } 100\ \% \end{aligned} \tag{3.6}$$

where V is the exterior volume of the specimen, cm^3,

W is the saturated weight, g,

S is the suspended weight, g,

γ is the density of kerosene, g/cm^3,

P is the apparent porosity, %,

B is the dry weight, g.

3.3 Mechanical Properties Measurements

After mixing with polyethylene glycol (PEG) as a binder, CPSC – PEG pastes were produced and cast into moulds, which were gently shaken in order to allow air bubbles to escape. The moulds were clamped between glass plates faced with wet cloth and cured in 37 ºC distilled water. For compressive strength, cylinders 6 mm in diameter by 12 mm in height were made; and for three-point flexural strength 25 x 3 x 2 mm bars were made. The clamps were removed after 24 h and the cement specimens were de-moulded after another 48 h; the specimens were still kept in 37 ºC distilled water for pre-set periods of 4, 7, 14, and 28 days, respectively. The compressive strength and three-point flexural strength measurements were carried out with a universal testing machine (Instron 3369, Instron Co., USA), as shown in Figures 3.1 and 3.2. The crosshead speed was 0.5 mm/min for compressive strength and 0.2 mm/min for three-point flexural strength. The fixture span was 20 mm and loading span was 10 mm for the flexural strength. The compressive and three-point flexural strengths were calculated using the following equations, respectively. Eight specimens were used for each determination.

$$\text{Compressive strength (MPa)} = \frac{4F}{\pi D^2} \qquad (3.7)$$

$$\text{Flexural strength (MPa)} = \frac{3FL}{2bh^2} \qquad (3.8)$$

where F is the maximum load, N,

D is the diameter of the specimen, mm,

L is the distance between the supports, mm (= 20 mm),

b is the width of the specimen, mm,

h is the height of the specimen, mm.

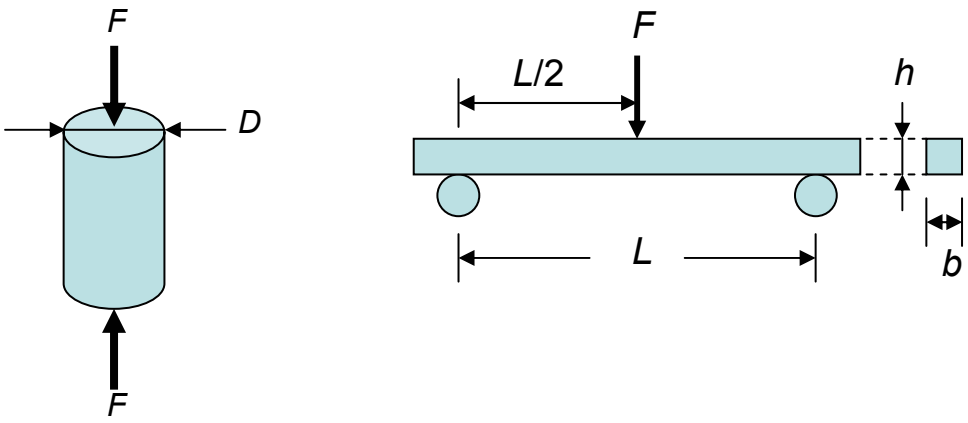

(a) (b)

Figure 3.1 Schematic diagram and conditions of (a) compressive strength test and (b) three-point flexural strength test

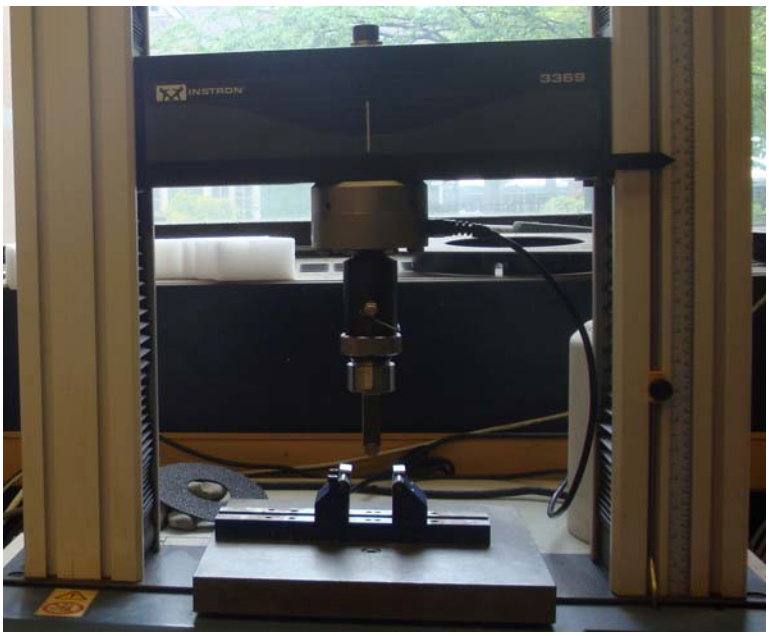

Figure 3.2 The equipment (Instron 3369) to measure compressive strength and flexural strength.

3.4 *In Vitro* Bioactivity Evaluation

To determine the *in vitro* bioactivity of CPSC, 7 day set sample discs (10 mm in diameter by 2 mm thick) were immersed in SBF at 37 ºC for 7 days. The preparation of SBF followed the procedure described elsewhere [137]. The ratio of SBF volume (ml) to the sample surface area (mm^2) was approximately 0.1. The half volume of the SBF solution for immersion was renewed every 24 h during the soaking period. After being soaked for 7 days, the samples were characterized using XRD and SEM equipped with energy dispersive X-ray spectroscopy analyser (SEM/EDX; Hitachi S-3000N, Electronic System Ltd, Tokyo, Japan).

3.5 *In Vitro* Biocompatibility Evaluation

3.5.1 Cytotoxicity assay

Both cytotoxicity and cell adhesion were evaluated with human gingival fibroblasts (seventh to eighth passage), due to the availability of the cells. The cells were obtained from previously established stocks and cultured from healthy patients [151]. Dulbecco's Modified Eagle's Medium (DMEM; Gibco, Grand Island, NY), containing 100 μg/mL penicillin G, 50 μg/mL streptomycin, 0.25 μg/mL fungizone, and 10% fetal bovine serum (Gibco, Grand Island, NY), was used as the cell culture medium. Cytotoxicity is a major factor of biocompatibility and is generally determined by *in vitro* cell culture studies [145]. Considering the resemblance to clinical applications for injectable cements, which set in the body, the cytotoxicity of CPSC cements was evaluated using the extract of freshly mixed cement paste. After mixing at w/c = 0.5, the cement pastes were immediately placed into 24-well tissue culture plates (Sarstedt Inc, Newton, NC) at 300 mg/well and exposed to ultraviolet light for 20 min before 1.5 ml of DMEM was added per well. The extracts were obtained and filtered (0.22 μm) after extraction for 24 h and 3 days at 37 ºC in 100 % RH atmosphere containing 5 % of CO_2. To observe a possible dose-dependant effect, the extracts were serially two-fold diluted using DMEM and each dilution

had five parallel experiment groups and one background group. DMEM served as a negative control. After the extracts were obtained, pH values of the extracts were measured and the ionic concentrations of Ca, Si, and P in the extracts were analyzed with an inductively coupled plasma optical emission spectroscopy (ICP-OES; Vista-PRO, Varian Inc, Palo Alto, CA).

Human gingival fibroblast cells were seeded to 96-well flat-bottomed plates (Nunc, Roskilde, Denmark) at 5×10^3 cells per well and incubated for 24 h to allow the attachment of the cells. Then, the culture medium was removed and replaced by the extracts from different extract groups at 50 μl/well. After incubation for 3 d, cell viability was determined by 3-(4,5-Dimethylthiazol-2-yl)-2,5-diphenyltetrazolium bromide (MTT) assay using a CellTiter 96® assay kit (Promega, Madison, WI) according to the manufacturer's instructions. Optical densities of each well were recorded at 570 nm using a microplate reader (Model 3550, BIO-RAD Laboratories, Hercules, CA). Cell viability was calculated as the percentage of the experiment group to the control group and the background absorbance was subtracted from the experimental ones.

3.5.2 Cell adhesion assay

Cell adhesion on biomaterial surfaces is critical for successful tissue-biomaterial interaction; the attachment and spreading of cells dominate normal cell growth and protein synthesis, while poor adhesion and lack of spreading will lower cell proliferation rate [147, 148]. For cell adhesion assay, two groups of disc samples (5 mm in diameter by 1.6 mm in thickness), of CPSC with w/c of 0.5 were prepared by curing them at 37 ºC and 100 % RH for 3 d. The samples in group 1 were examined under SEM immediately after the three day curing. The samples in group 2 were placed into a 24-well plate with gingival fibroblasts at a density of 5×10^4 cells/ml/well and cultured at 37 ºC in 100 % RH atmosphere containing 5 % of CO_2 for 3

day. For SEM examination, cells attached on the specimens were washed twice with phosphate-buffered saline (PBS, pH 7.4), fixed in 2.5 % glutaraldehyde for 10 min and in 1 % osmium tetroxide for 1 h, and dehydrated in ascending concentrations of ethanol (50 %, 70 %, 80 %, and 100 %) for 5 min at each concentration. The samples were then dried with a critical point drier (Samdri-795, Tousimis Research Corporation, Rockville, MD) and sputter-coated with gold-palladium (Hummer VI, Technics West Inc. CA). Cell morphology and EDX analysis of the sample surfaces were examined using SEM/EDX at 20 kV.

3.6 Statistical Analysis

Univariate analysis of variance (ANOVA) was used to evaluate the obtained data. The results were considered statistically significant at a p-value less than 0.05. When a significant difference was observed, individual comparisons were performed using the Turkey test [152]. The statistical calculation was carried out using the software “IBM SPSS Statistics” Version 19 (IBM Corporation, Armonk, New York, USA).

4 EXPERIMENTAL RESULTS AND DISCUSSION 1: CEMENT SYNTHESIS AND CHARACTERIZATION

4.1 Introduction

This chapter describes the results of the experimental work on process engineering of CPSC. It includes i) the synthesis process of the cements; ii) the characteristics of the hydrated CPSC pastes.

4.2 Synthesis of C_3S and CPSC Powders

The XRD pattern of the as-synthesized C_3S powder showed that the sample contained only Ca_3SiO_5 and free CaO (calcium oxide) in Figure 4.1, as compared with the powder diffraction file (PDF) of Ca_3SiO_5 (PDF Card 00-031-0301) and calcium oxide (PDF Card 00-048-1467). The content of free CaO in the as-synthesized C_3S powder after sintering at 1550 °C was 0.03 %. The procedure to determine free CaO in tricalcium silicate powder was described in Section 3.1.1. The as-synthesized C_3S powder morphology is shown in Figure 4.2. After mixing and planetary ball-milling, the particle sizes of the CPSC powders determined with SEM were less than 5 μm (Figure 4.3). Element mapping demonstrated that calcium, silicon, and phosphorus were uniformly distributed in CPSC (Figure 4.4).

Sol-gel processes are the wet-chemical techniques for making advanced materials including ceramics [153]. The chemistry involved in sol-gel processes is based on the hydrolysis and condensation of the organo-metallic precursor compounds. The chemical processes include the association of solutions and/or the solid colloidal state with a liquid medium. For the mult compound systems, the various elements can be controlled down to the atomic level, therefore sol-gel processes can offer high homogeneity and purity and lower processing temperatures

compared with traditional ceramic powder methods. In addition, the structure of sol-gel powders, including the particle shape, size and size distribution, can be easily controlled [153].

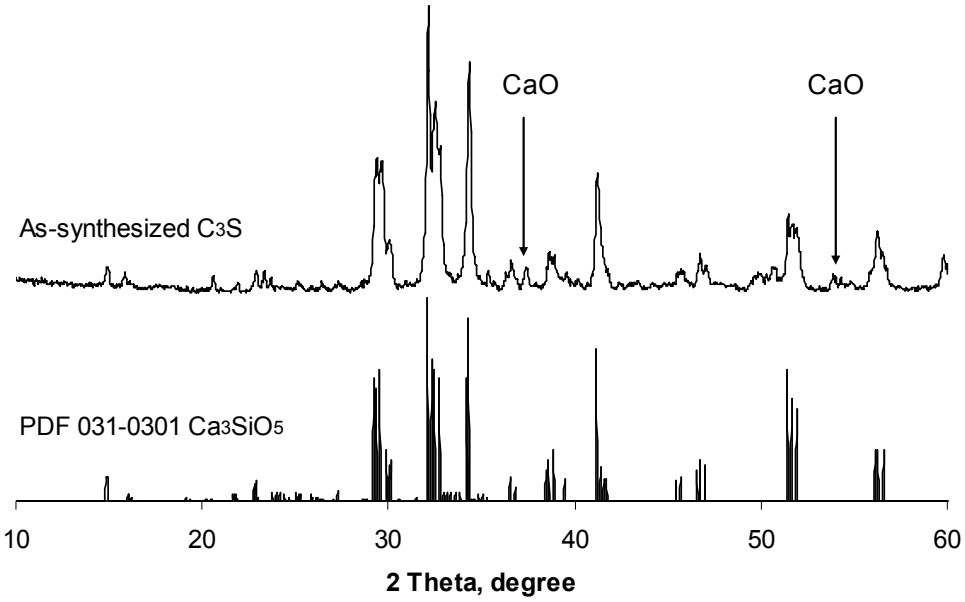

Figure 4.1 XRD pattern of as-synthesized C_3S powder.

In the present work, the C_3S powder was synthesized with a sol-gel process followed by sintering at 1550 ºC for 4 h. From this process the C_3S powder was of high purity (greater than 99.9%) and dense particles and grain size was up to 30 μm. A previous study [34] showed that the sintering temperature to form C_3S with a sol-gel method was higher than 1300 ºC and the content of free lime decreased with the sintering temperature. After sintering at 1550 ºC for 4 h, the synthesized C_3S had 0.03 % free CaO, which was lower than 0.64% [154] and 0.07% [34] obtained when sintered at 1450 ºC. The traditional methods of the solid-phase reaction needed a higher temperature and longer sintering time, up to 1850 ºC for up to 24 h [155-157].

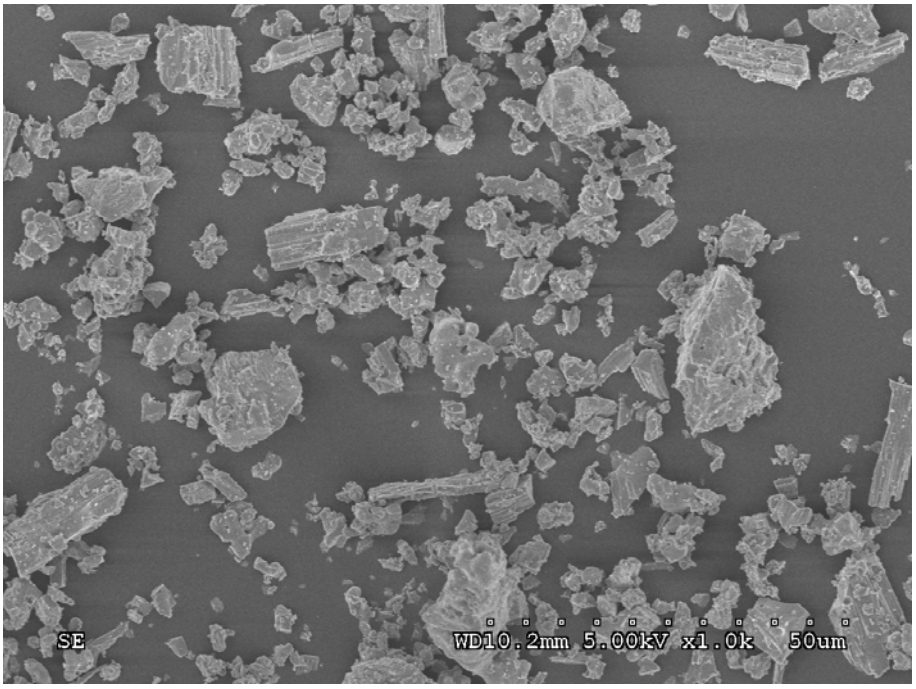

(a)

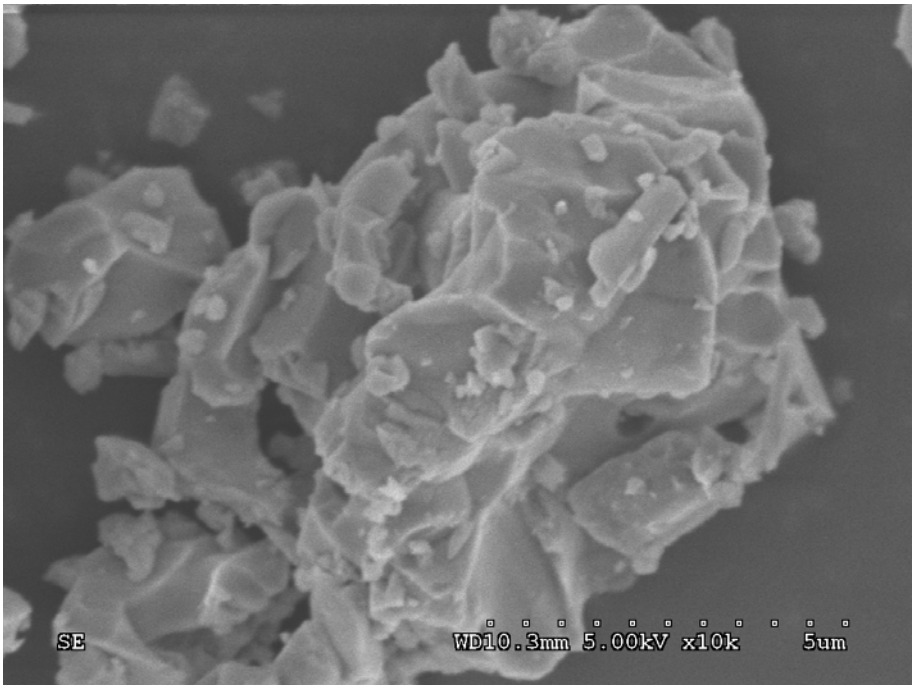

(b)

Figure 4.2 SEM micrograph of as-synthesized C_3S powder: (a) a lower magnification (x1.0k); (b) a higher magnification (x10k).

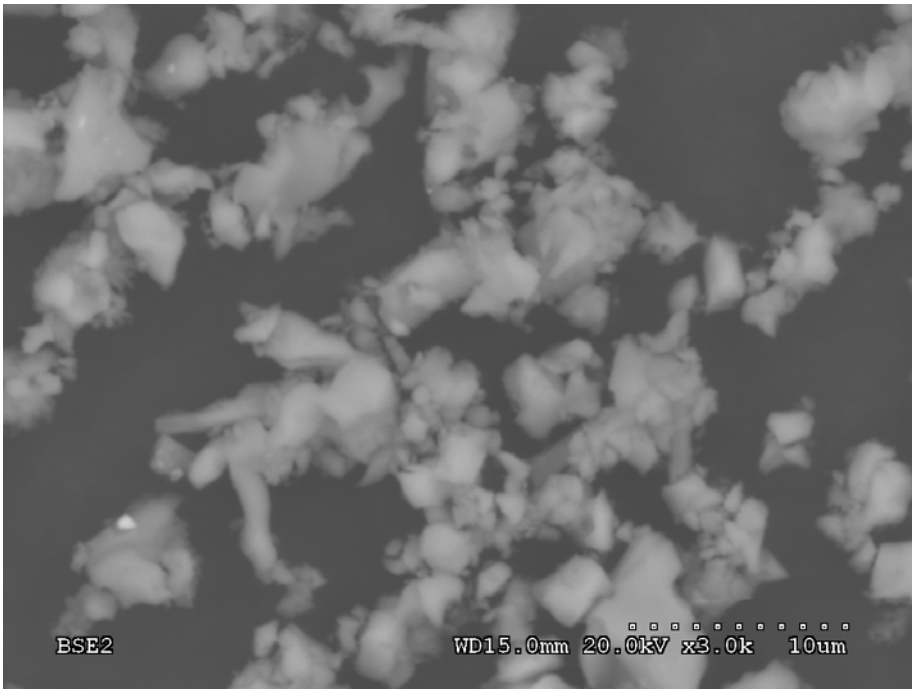

(a)

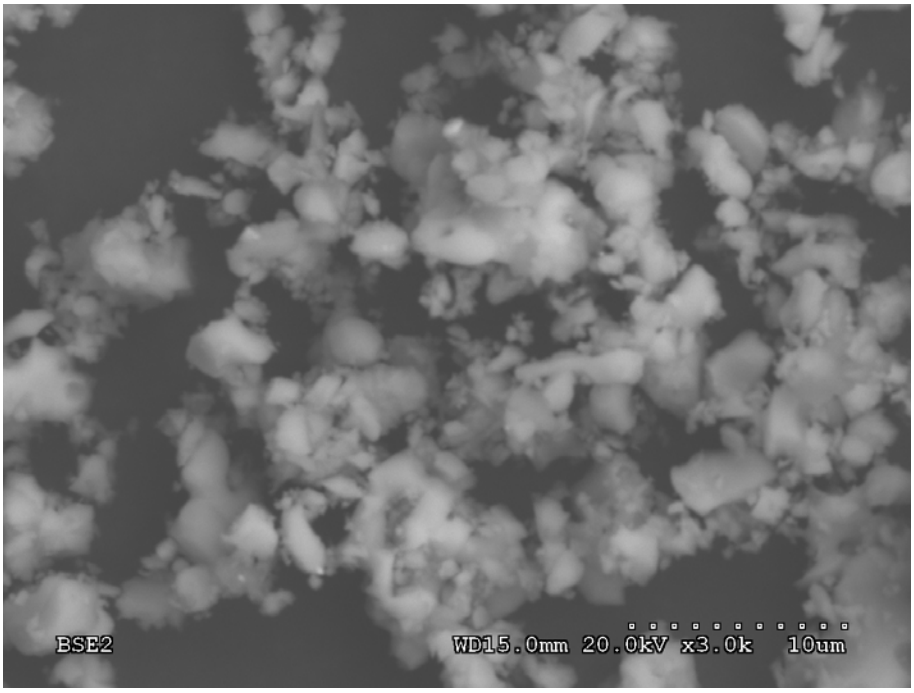

(b)

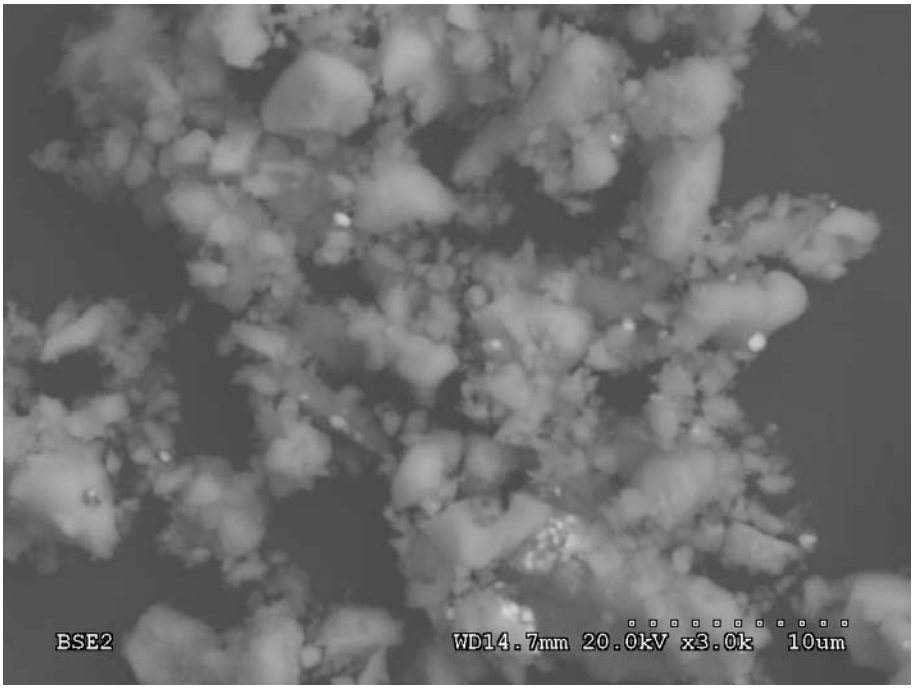

(c)

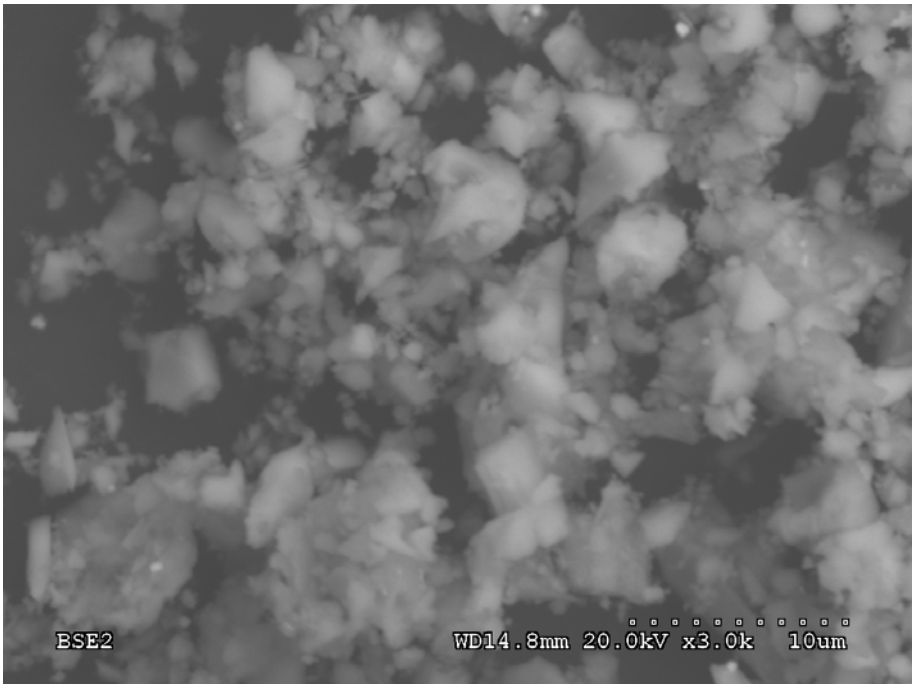

(d)

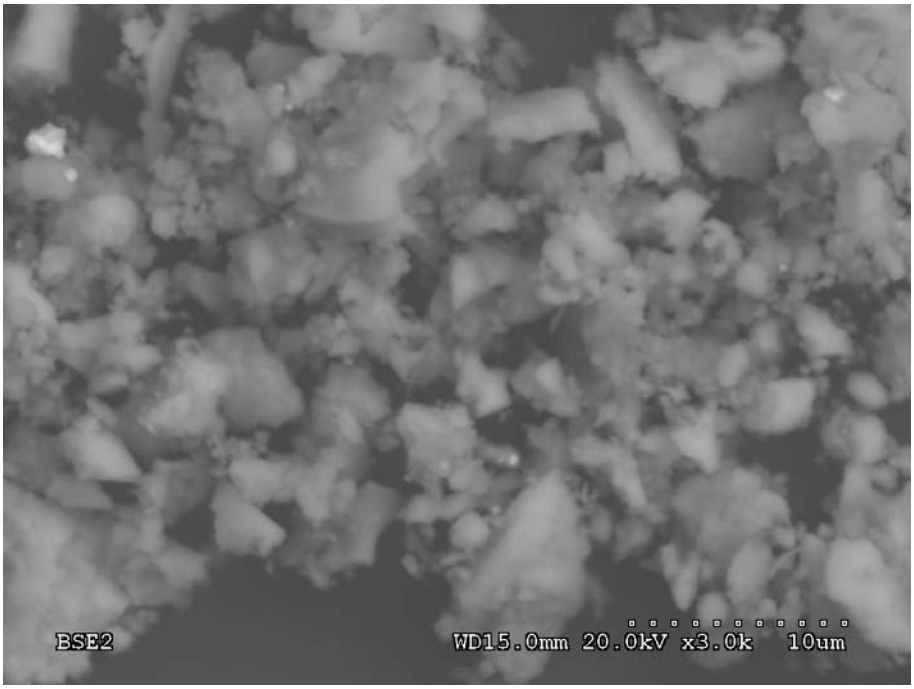

(e)

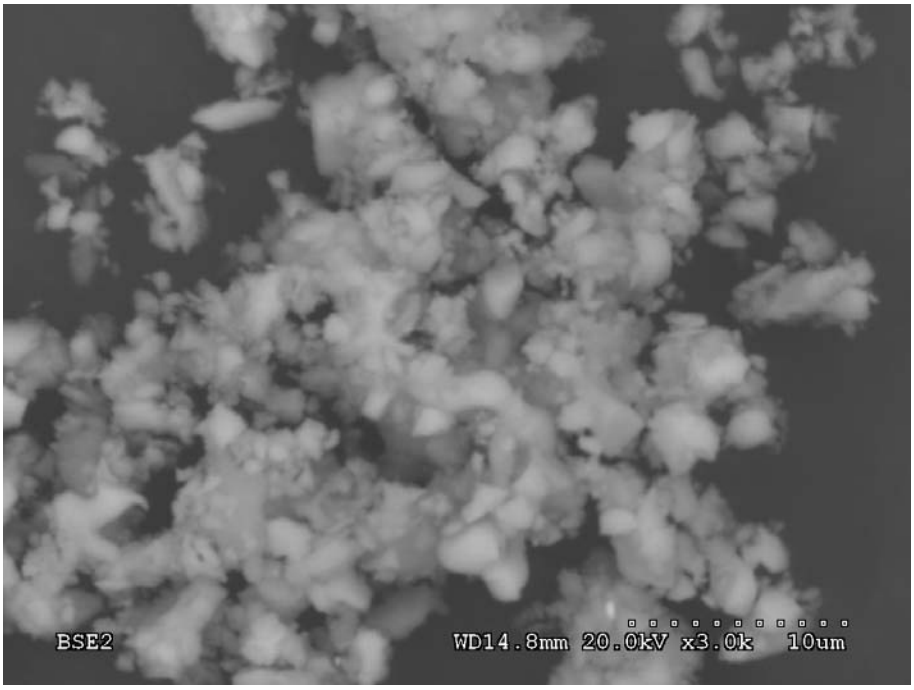

(f)

Figure 4.3 SEM micrographs of cement powders after planetary ball milling for 20 min. (a): 0CPM; (b): 5CPM; (c): 10CPM; (d): 15CPM; (e): 20CPM; (f): 25CPM.

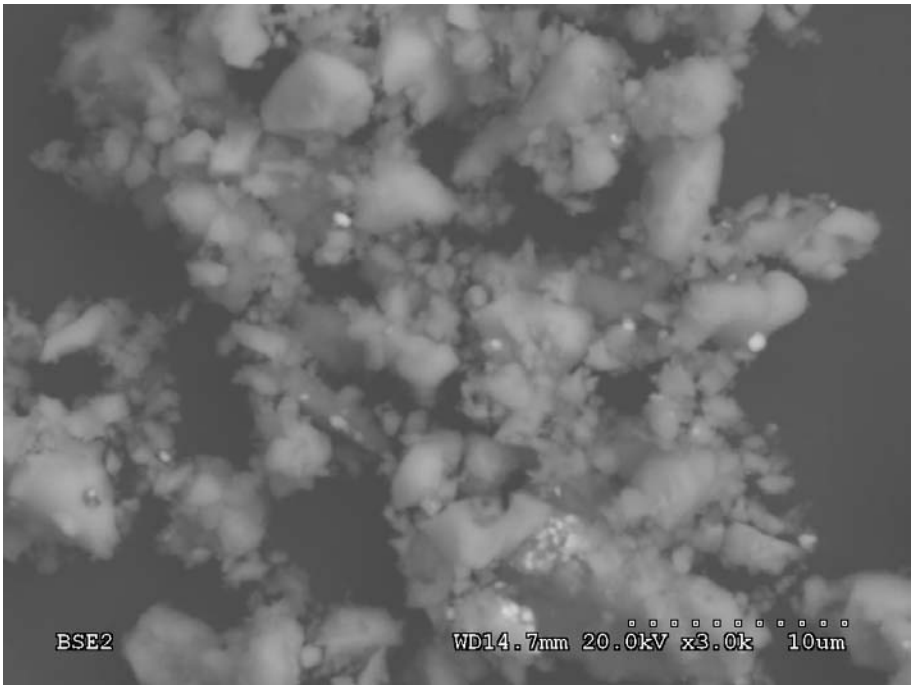

(a)

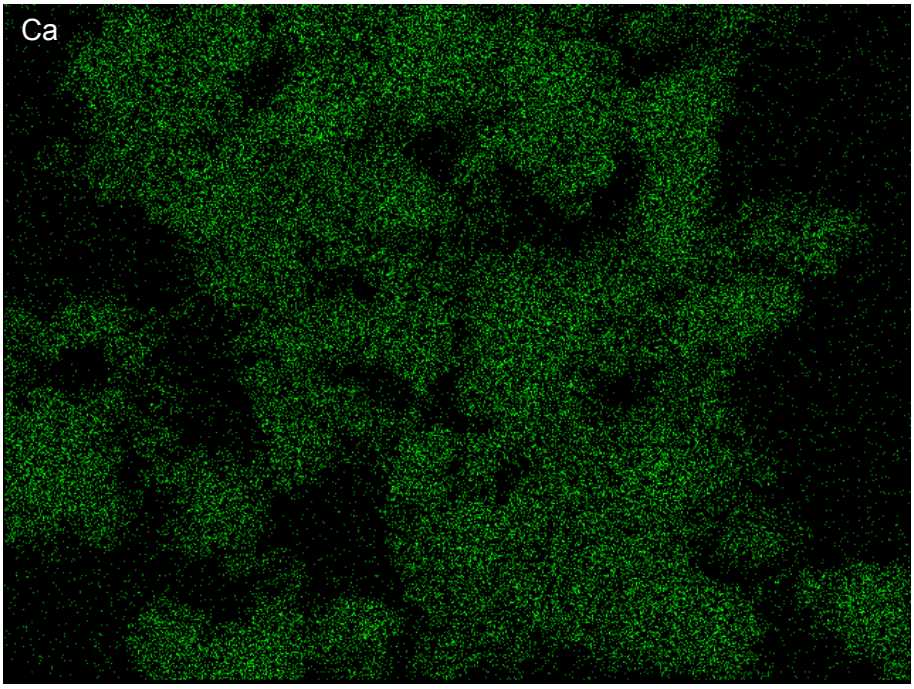

(b)

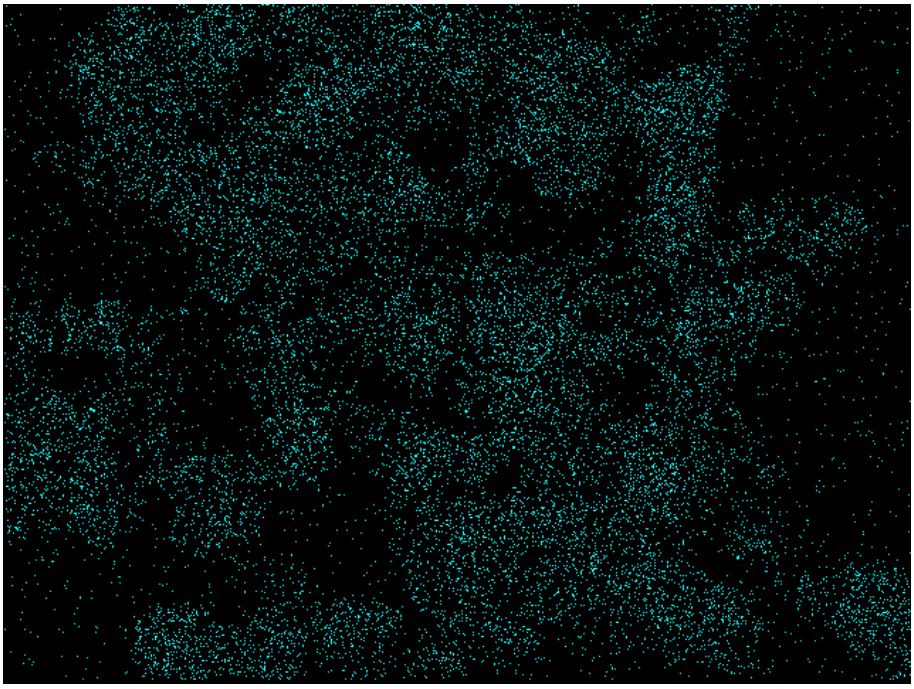

(c)

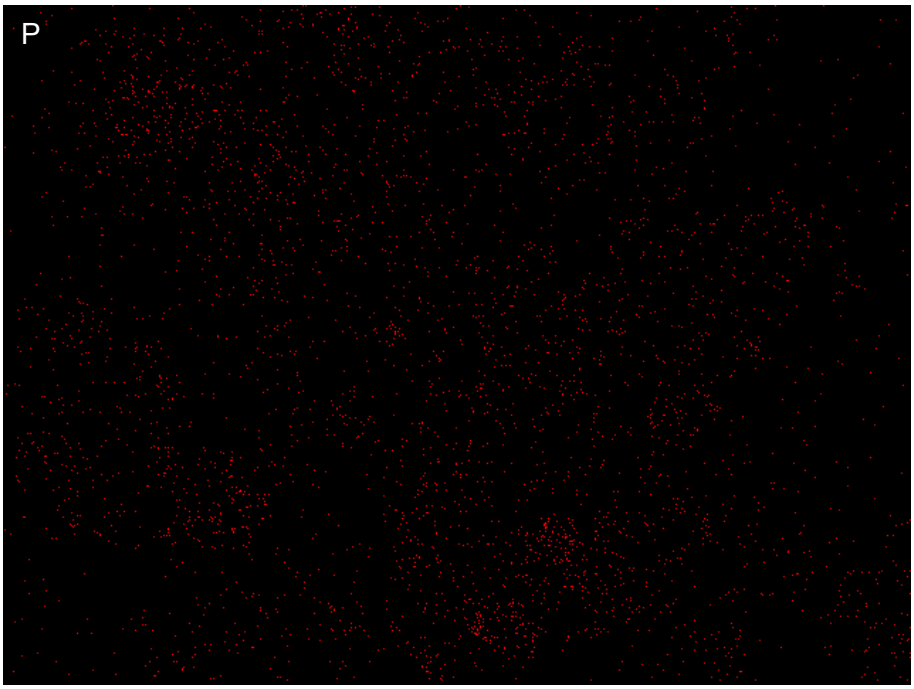

(d)

Figure 4.4 The element mapping images of 10CPM after mixing and grinding. (a) morphology, (b) Calcium, (c) Silicon, and (d) Phosphorus.

Planetary ball mills are high-energy ball mills, which are more efficient than traditional ball mills. After planetary ball-milling for 20 min, CPSC cements were ground to less than 5 μm (Figure 4.3) and the morphology of the powders showed irregular shapes and agglomeration of smaller particles occurred. When the particle size is less than 5 μm, the relative standard deviation of the measured intensity by XRD is less than a few percent [82]. A statistical error of ± 5% for major phases in an intensity-related quantitative analysis should be considered reasonable. Figure 4.4 shows that the elements of calcium, silicon and phosphorus from CPM were uniformly distributed in CPSC cements. The BET data (Table 4.1) of the cement powders indicated that CPM was more easily ground than C_3S, probably due to the lower hardness of CPM. Assuming that the specific surface area of C_3S in CPSC was the same as that in 0CPM, i.e. 3.00 m^2/g, from the data in Table 4.1, the specific surface area of CPM could be calculated in the range of 21.4 to 25.6 m^2/g. With the high purity, low free CaO, high homogeneity, and uniform mixture of CPSC, the synthesis processes, including the sol-gel method to synthesize C_3S and sintering at 1550 ºC for 4 h followed by planetary ball milling to grind the mixture of CPM and C_3S, has been declared as a suitable process to fabricate CPSC cement powders.

The CaO/SiO_2 molar ratio of the C-S-H hydrates produced from the hydration of C_3S was represented by an average value of 1.7 [47]. According to this value, the calculated content of CPM in CPSC would have to be 36.4 wt% so that CH produced from the hydration of C_3S could be completely consumed by CPM to precipitate HAP. The CPM amount of 36.4 wt% in CPSC could be defined as "*Reference Maximum Amount (RMA)*." However, the preliminary results indicated that the addition of CPM over 30 wt% dramatically decreased the mechanical properties of set CPSC. For example, compressive strength of CPSC with 30 wt% CPM was 63.3 % of that for CPSC with 20 wt% and 32.9% of that for CPSC with 10 wt% CPM. The complete

data on compressive strength is in Section 6.4 Therefore, the compositions of 0 – 25 wt% of CPM in CPSC were chosen for further studies in the present work.

Table 4.1 The specific surface area measured with the BET method for cement powders

Cement	0CPM	5CPM	10CPM	20CPM
Specific surface area, m^2/g	3.00	3.92	5.09	7.52

4.3 Characteristics of C_3S and CPSC Cements

4.3.1 The pH of C_3S and CPSC suspensions

In the literature, the studies on the hydration of C_3S have been carried out for different w/c ratios (the ratio of water to cement by weight). For cement paste, w/c is typically 0.3 to 0.6 and many studies have also been done in aqueous suspension (high w/c), termed "bottle hydration" [54]; a w/c ratio up to 500 was used in a previous study [155]. Although the kinetics of C_3S hydration in "bottle hydration" is different from that in C_3S paste, the use of diluted suspensions prolongs the early reaction steps and facilitates the study of the early stages of the reaction. In the present work, the study of the hydration of CPSC was carried out at w/c = 10.

The changes in pH as a function of time for C_3S and CPSC pastes during the first-hour of hydration at 37 ºC are shown in Figure 4.5. For all the cement samples, the pH changes almost followed the same pattern in this period of time, with the exception of the initial pH value of the paste. In the beginning of measurement, pH increased for 2 min and then remained relatively constant for 2 to 4 min, followed by a slight decrease until 10 min of the test, after which it

increased again. 0CPM (pure C_3S) had a highest pH in comparison with CPSC cements during the whole period of measurement and also the pH reached to the highest after the relatively constant periods. After mixing with water, pH of 0CPM was 11.83 ± 0.03 and raised to 12.03 ± 0.04 within less than 2 min. 0CPM kept the pH at 12.03 ± 0.04 until 8 min followed by a slight decrease to 11.98 ± 0.04 at the 10^{th} min before it started to increase again. After hydration for 20 min, 0CPM reached pH 12.35 ± 0.04 , which was higher than those of the CPSC cements, and it remained the highest pH until the end of the measurement. A previous study on hydration of C_3S in stirred suspension solutions (w/c = 500 – 1000) showed that at around pH = 11.5 at 25 ºC, Ca^{2+} and OH^- ions generated from the hydration of C_3S in the solution appeared a "plateau" period, during which an equilibrium was established between one of the calcium silicate hydrates and the solution [158]. Another similar study showed that at 10, 25, and 40 ºC the "plateau" pH values were about 12.0 (i.e at pOH = 2.0) in stirred suspension solutions at w/c = 500 [155] and proposed that two calcium silicate hydrates were produced from the hydration of C_3S. The earlier formed hydrate was fine-grained and grew on C_3S grains to form a hydrate layer. Based on reported data [155, 158], it is expected that the first rapid increasing in pH is due to the hydration of C_3S and formation of CH; at the same time, the earlier hydration product C-S-H formed and precipitated on the surfaces of anhydrous C_3S grains, thus slowing down the increase of pH. After about 10 min C_3S continued to dissolve until the solution was supersaturated with respect to the second C-S-H and the pH of the solution continued to increase.

For 5CPM, the pH increased from 11.83 ± 0.04 to 11.98 ± 0.03 within the first 1.5 min and remained unchanged for about 2 min, then decreased to 11.92 ± 0.04 after 10 min, and increased to 12.07 ± 0.04 after 1 h. 5CPM had a similar pH level to that of C_3S within the first minute of hydration. The pH of 10CPM increased to 11.77 ± 0.04 from 11.72 ± 0.04 in the first 40 seconds of hydration followed by a gradual decrease to 10.70 ± 0.05 after 10 min and then increase to

11.86 ± 0.04 after 1 h. 15CPM, 20CPM, and 25CPM had a similar pattern to 10CPM, but their pH decreased with the content of CPM in cement, suggesting a suppressing effect of CPM on the pH of CPSC pastes at the very early hydration due to its acidity. CPSC cements did not show the second period of fast increase in pH as obviously as 0CPM, indicating that the hydration mechanisms of CPSC after the first 10 min might be different from that of pure C_3S.

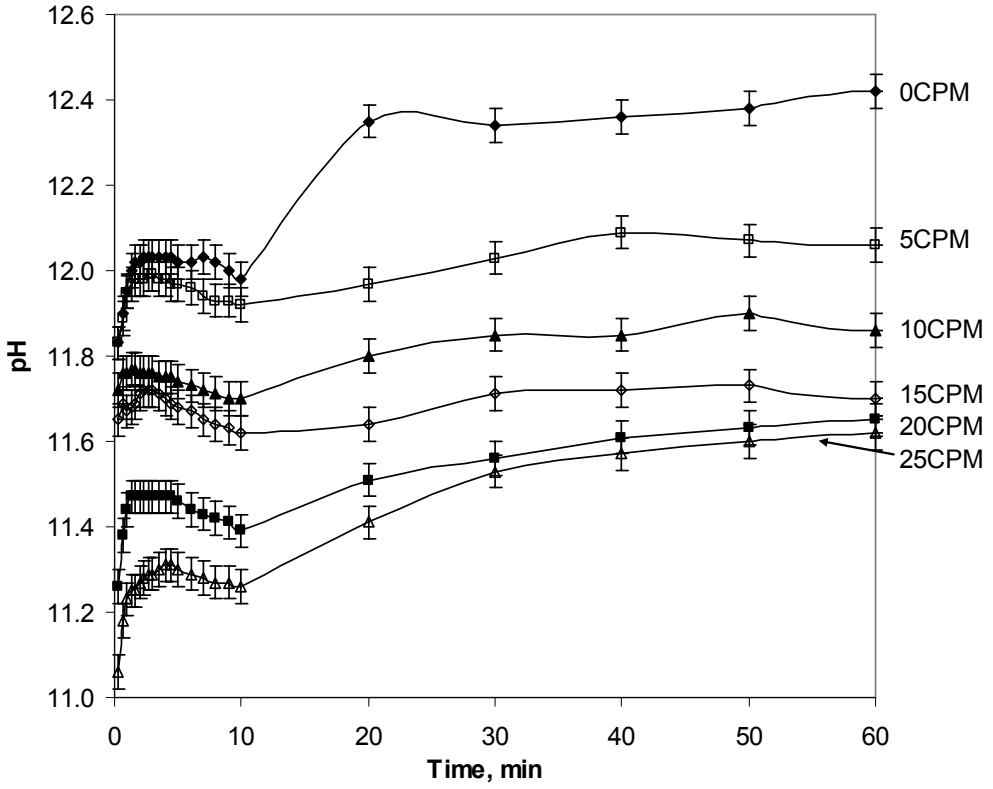

Figure 4.5 The pH variation of C_3S (0CPM) and CPSC pastes at the w/c = 10 during the first hour of hydration at 37ºC.

When CPSC cement, containing C_3S and CPM, is mixed with water, hydration of C_3S and dissolution of CPM take places. Both processes go through liquid phases with dissolution /

precipitation reactions forming intermediate or thermodynamically stable products; therefore, the pH variations of the liquid phase are important to the reaction kinetics and the final products [54, 94]. When the pH of cement suspension increases due to C_3S hydration, the reactions (2.10a) and (2.10b) move to the right so that CPM dissolves in the solution more easily and it is expected that, as a result, more HAP forms.

According to the solubility phase diagram of the ternary system $Ca(OH)_2$-H_3PO_4-H_2O at 37 ºC (Figure 2.5), at the pH values higher than 11.0 in a liquid phase containing calcium phosphate compounds, HAP would be the most stable phase of calcium phosphates. At the pH values recorded for the CPSC cements ($11.0 \leq pH \leq 11.8$ at the very beginning and $11.6 \leq pH \leq 12.1$ after 1 h hydration), HPO_4^{2-} and PO_4^{3-} would be the major species of phosphate ions in the solutions (according to the pH dependence of ion concentrations of phosphorus acid solutions showed in Figure 2.6). Since the pH values of C_3S and CPSC pastes were higher than 11.0, CPSC would be suitable for certain dental applications where high pH would provide the benefit to killing bacteria, for instance, dental root canal filling.

4.3.2 Phase composition of C_3S and CPSC pastes

The XRD patterns of CPSC pastes after hydration for 7 d at 37 ºC in distilled water are shown in Figure 4.6. After 7 d of hydration of 0CPM, the peaks of unhydrated C_3S and C-S-H (located at 2 theta of 29.5, 32.8, and 50.1 degrees) and CH (located at 2 theta of 34.1, 18.0, 47.1, and 50.8 degrees) were observed. For the CPSC cement pastes, HAP appeared beside C-S-H, CH, and unhydrated C_3S; and the peak intensity of HAP increased with the content of CPM in CPSC, but those of CH and C_3S decreased (Figure 4.6).

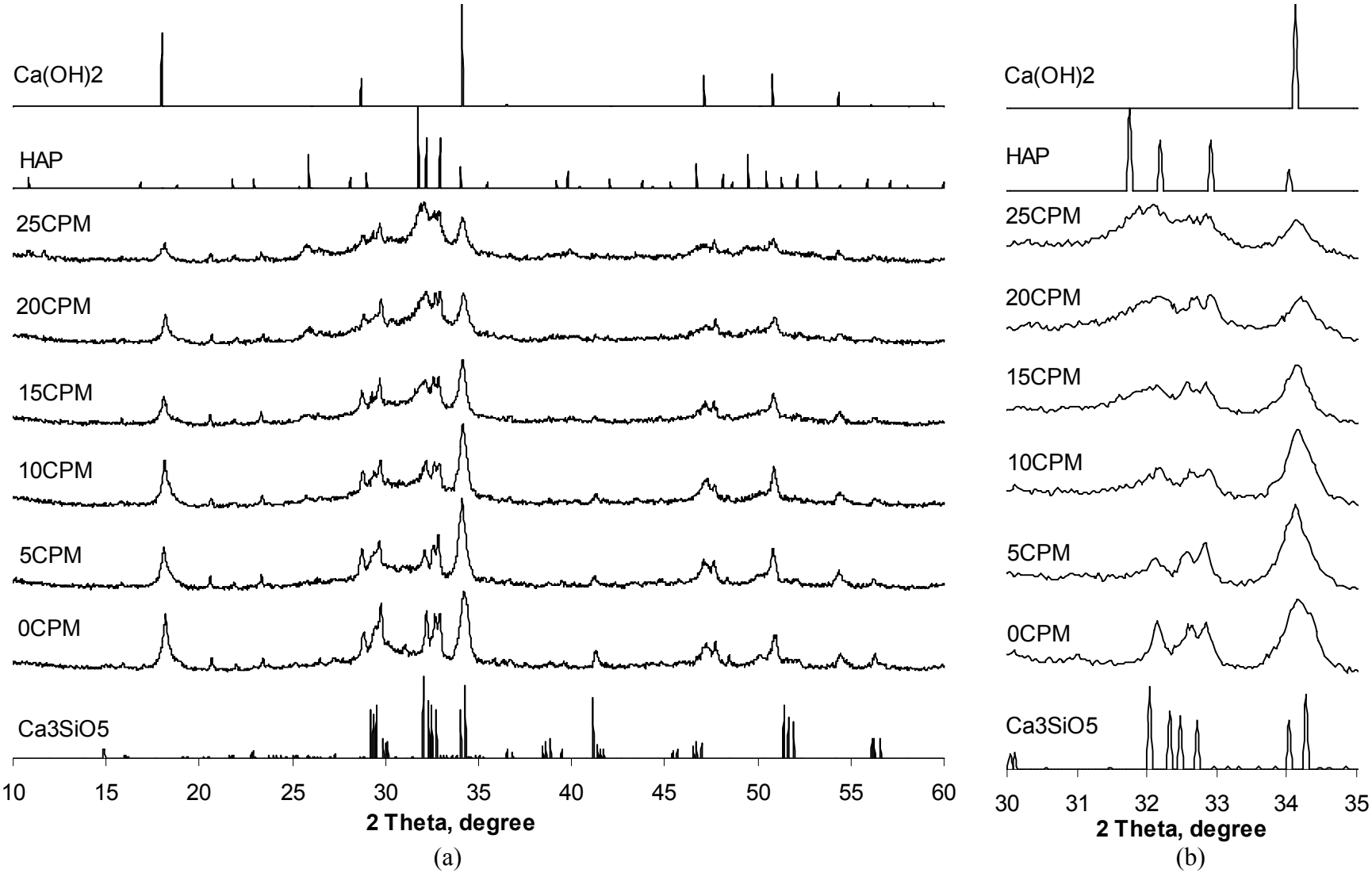

Figure 4.6 XRD patterns of 0CPM, 5CPM, 10CPM, 15CPM, 20CPM, and 25CPM pastes after setting for 7 d at 37ºC and 100% RH. (a) whole range between 10 – 60 degree (2 theta), (b) the enlarged part between 30 to 35 degree (2 theta).

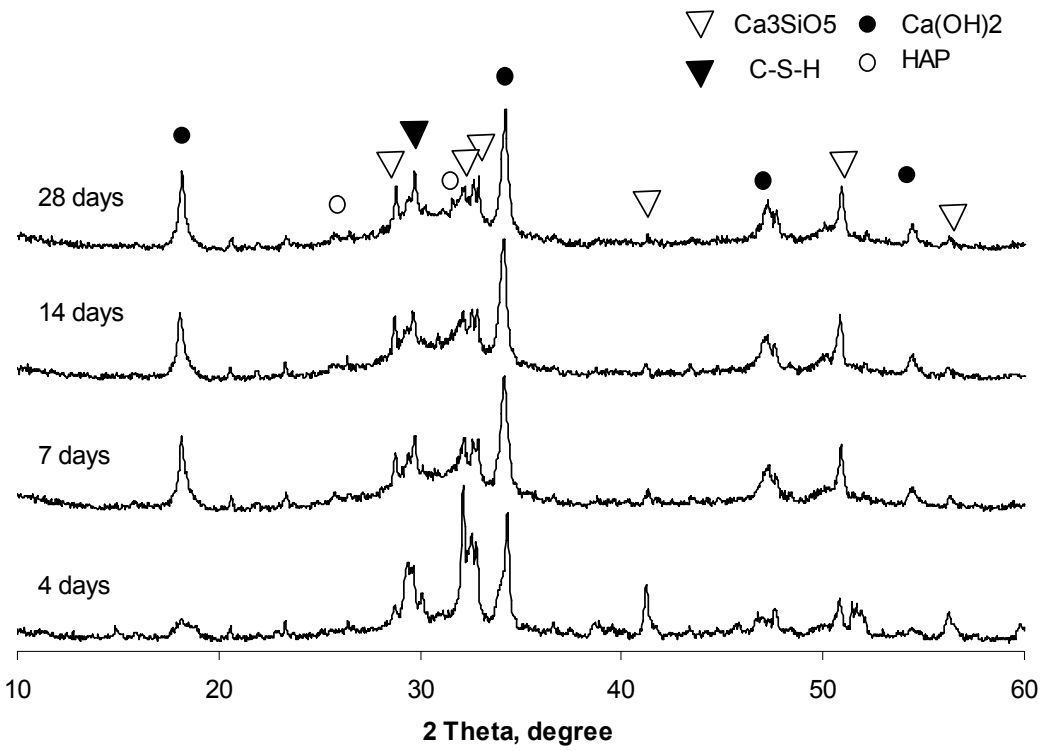

Figure 4.7 XRD patterns of 10CPM after hydration for 4, 7, 14 and 28 d.

The XRD patterns of 10CPM pastes after hydration for 4, 7, 14, and 28 d at 37ºC in distilled water as an example for CPSC are shown in Figure 4.7. The peaks of CH, C-S-H, Ca_3SiO_5, and HAP were observed and with hydration time, the peak intensities of the CH and C-S-H, and HAP phases increased and those of Ca_3SiO_5 decreased. XRD analysis showed that CH decreased and HAP increased with the content of CPM in CPSC, indicating that CPM reacted with CH to form HAP through an acid-base reaction. In the present research, the maximum of 25 wt% of CPM in the cement (i.e. 25CPM samples), was lower than RMA (36.4 wt%). Therefore extra CH was expected to be leftover in the set cement after the CPM was consumed.

4.4 Summary

1. The "best-practice" process developed in this work to prepare CPSC included the following steps:

i) synthesize the precursor for C_3S through a sol-gel process, combining in proper proportions the starting materials including calcium nitrate tetrahydrate, tetraethyl orthosilicate, and distilled water and alcohol as a solvent and nitric acid as a catalyst.

ii) fabricate C_3S by sintering the precursors at 1550 ºC for 4 h; the high purity of the resulting cement powder (i.e. impurities level < 0.1 %) was maintained through the use of high purity starting materials, and well-controlled environment (such as the use of Pt crucibles).

iii) obtain the CPSC powder by planetary ball milling the mix of C_3S with various amounts of CPM for about 20 min, to reduce its average particle size to less than 5 μm.

2. The addition of CPM into CPSC affected pH of CPSC pastes and the phase compositions. CPM reduced pH of the CPSC cement pastes and the content of CH in the set cements and increased the content of HAP, and it also accelerated the consumption of C_3S. These effects were more obvious for the high content of CPM in CPSC.

5. EXPERIMENTAL RESULTS AND DISCUSSION 2: CPSC HYDRATION MECHANISMS

5.1 Introduction

This chapter describes the results of the quantitative XRD of the hydrating CPSC, using quartz as an internal standard, includes the results of DTA-TGA studies of the hydrating CPSC, and discusses the hydration kinetics and hydration products, especially the molar ratios of CaO/SiO_2 and H_2O/SiO_2 in the hydrates.

5.2 Hydration Kinetics

For the quantitative XRD analysis, quartz with the median particle size of 2.75 μm was used as an internal standard. The reasons to choose quartz as internal standard are that its XRD peaks do not overlap with those for C_3S and it does not react with other compounds in the system studied [83]. The reference peak was 26.6 deg 2θ CuKα (d = 3.34 Å) for quartz, which is the strongest one in the XRD pattern of quartz, and 41.1 deg 2θ CuKα (d = 2.19 Å) for C_3S, which is the relatively strong one in the XRD pattern of C_3S, moreover, these peaks do not overlap with others. An internal standard calibration curve was produced from the compositions of 8/92, 15/85, 25/75, 50/50, 70/30, and 90/10 (ratio of C_3S to quartz in weight) and is shown in Figure 5.1.

The relationship between the weight ratio of C_3S to quartz and the intensity ratio of the corresponding peak areas was represented by the following equations ($R^2 = 0.9999$):

$$I_c/I_s = 0.0933\ (X_c/X_s) + 0.0027 \qquad (5.1a)$$

or

$$X_c/X_s = 10.715(I_c/I_s) - 0.0286 \qquad (5.1b)$$

where X_c/X_s = the weight ratio of C_3S to quartz in the mixed cement pastes,

I_c/I_s = the intensity ratio of the peak area of C_3S (at $2\theta = 41.1$ º) to quartz (at $2\theta = 26.6$ º).

The peak areas were calculated by the software MDI JADE 7 provided with the XRD machine.

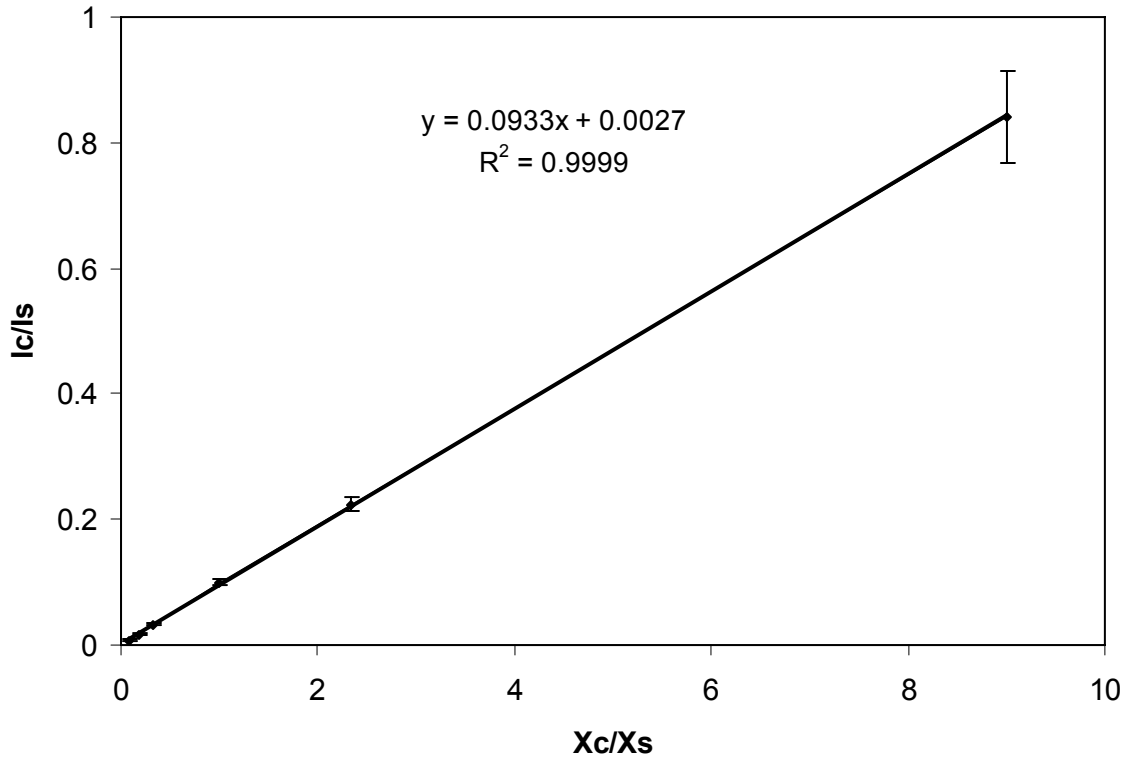

Figure 5.1 The internal standard calibration curve. X_c/X_s is the weight ratio of C_3S to quartz and I_c/I_s is the intensity ratio of the peak area of 41.1 degree for C_3S to that of 26.6 degree for quartz.

The cements of 0CPM, 5CPM, 10CPM, and 20CPM at w/c = 10 hydrated for pre-set times at 37 ºC were mixed with the 10 wt% of the standard quartz. C_3S that remained unreacted in the

hydrated pastes was determined with Equation (3.2) from the XRD data and the plot of the percentage of hydrated C_3S (the hydration degree, α) against the hydration time is shown in Figure 5.2(a). Each piece of data was derived from an average of no less than 12 measurements. The average hydration rate (the hydration degree per hour) with the hydration time was calculated and is shown in Figure 5.2(b). The complete data and data processing for quantitative XRD analysis and the procedures for generation of Figures 5.2(a) and 5.2(b) can be found in Appendix.

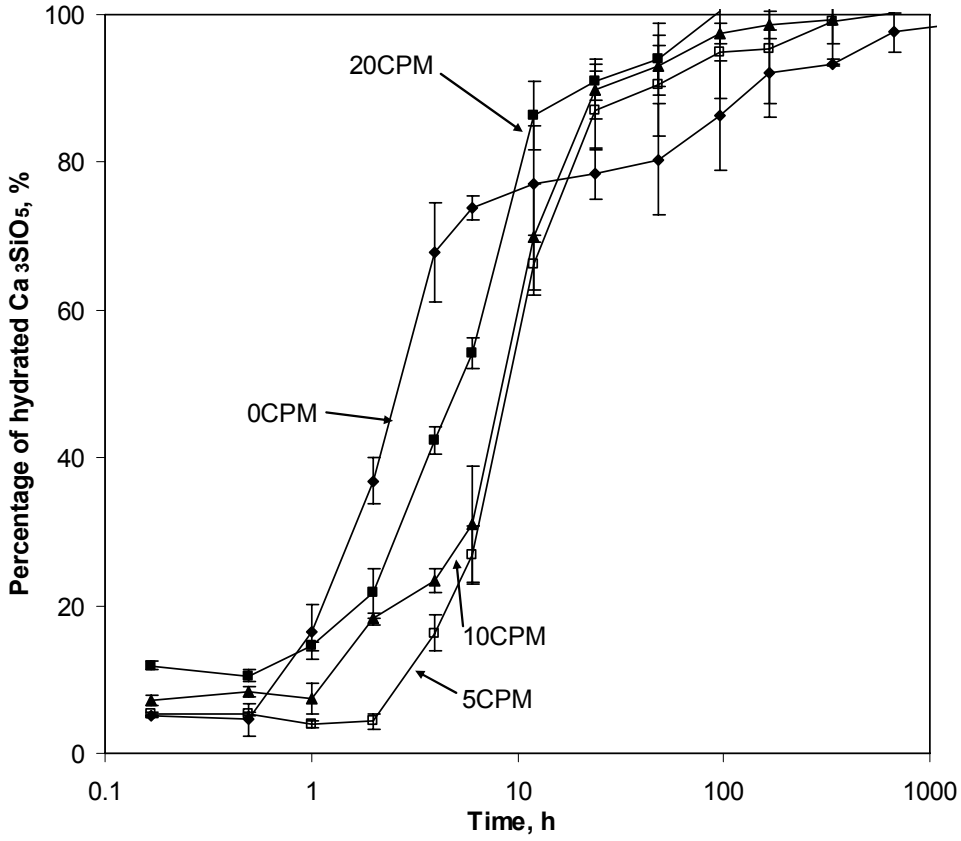

(a)

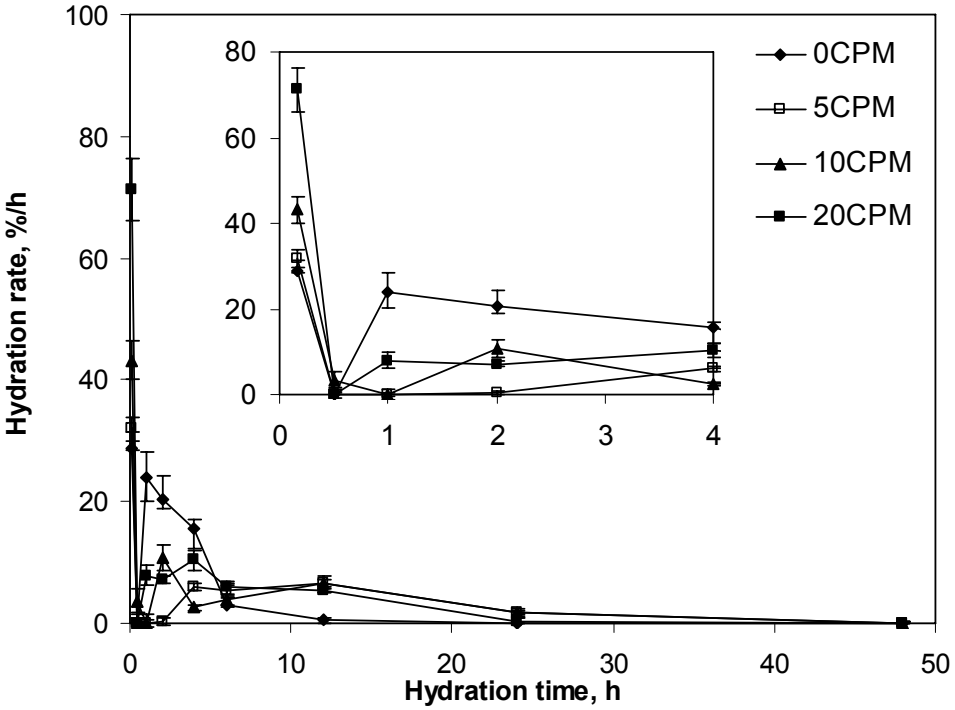

(b)

Figure 5.2 (a) The percentage of hydrated C_3S (α) with hydration time and (b) the average hydration rate (the first derivative of the hydration degree to hydration time) with hydration time for the cements of 0CPM, 5CPM, 10CPM, and 20CPM at w/c = 10 at 37 ºC.

For 0CPM, hydration started to accelerate at about 30 min, which may be the end of the induction period, and the hydration degree was 4.5 ± 0.1%. Up to about 6 h, the degree of hydration, α, reached 73.8 ± 6.7% and the hydration was relatively fast between 30 min and 6 h. The hydration rate reached the maximum at one hour [Figure 5.2(b)] and then decreased over time. With hydration longer than 6 h, the hydration slowed down considerably and after 28 d, C_3S hydrated almost completely.

For 5CPM, 10CPM, and 20CPM, the induction periods ended later than that of pure C_3S, i.e. at between 1 and 2 h for 5CPM, 1 h for 10CPM, and 30 min for 20CPM, respectively. However, the periods of the fast hydration lasted longer than that of pure C_3S; afterwards hydration degrees were higher than that of pure C_3S. The beginning and end of the periods of the fast hydration, the degree of hydration, the duration of the fast hydration, and the calculated average hydration rates are listed in Table 5.1 (For comparison purpose, the fast hydration was defined as the hydration rate greater than 1 %/h).

Table 5.1 Hydration degree and rate at the beginning and end of the fast hydration periods for various samples of CPSC cements

	Time, h		Hydration degree, %		Duration of the fast hydration,	Average hydration rate	Total % of hydrated C_3S,
	Beginning	End	Beginning	End	h	%/h	%
0CPM	0.5	6	4.5 ± 0.1	73.8 ± 6.7	5.5	12.6	69.3
5CPM	2	24	4.3 ± 0.5	87.1 ± 4.1	22	3.8	82.8
10CPM	1	24	7.4 ± 0.7	89.9 ± 7.2	23	3.6	82.5
20CPM	0.5	12	10.5 ± 0.6	86.4 ± 2.1	11.5	6.6	75.9

For any isothermal solid phase reactions, the product – time (α - t) curves (Figure 5.3) can be generally divided into the following five stages [159], which are similar to the stages observed from the calorimeter curves shown in Figure 2.1. A, an initial stage, during which the chemical reaction starts to take place; B, the induction stage, during which the stable nuclei are developed (at low α); C, the acceleration stage, during which the nuclei grow and new nuclei

may also form; D, the maximum point of the reaction rate; E, the deceleration stage, which continues until completion of the reaction [159]. The rate-determining step can be either (i) a chemical reaction, i.e. one or more bond redistribution steps, which generally takes place at a reaction interface, or (ii) diffusion, i.e. the migration of participants to, or from, a zone of preferred reaction. In most cases, a transition regions or intermediate behaviour takes place as well [159]. According to the stages described above, the different stages for the hydration of 0CPM, 5CPM, 10CPM, and 20CPM were divided and listed in Table 5.2.

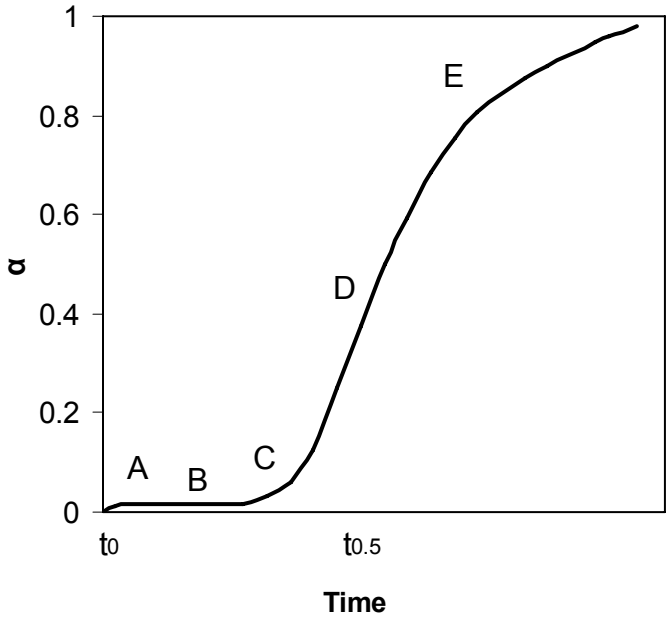

Figure 5.3 The general plot of the isothermal product – time ($\alpha - t$) curve from the start point to the completion point of a reaction. The reaction is divided into different stages described by letters. A, initial stage; B, induction stage; C, acceleration stage; D, the maximum point of the reaction rate; E deceleration stage [159].

Table 5.2 The different stages for the hydration of 0CPM, 5CPM, 10CPM, and 20CPM

	Induction stage	Acceleration stage	Transition zone between accel. and decel.	Deceleration stage	Completion stage
0CPM	10 to 30 min	30 min to 4 h	4 to 12 h	12 h to 2 d	After 2 d
5CPM	10 min to 2 h	2 to 12 h	12 to 24 h	24 to 4 d	After 4 d
10CPM	10 min to 1 h	1 to 12 h	12 to 24 h	24 to 4 d	After 4 d
20CPM	10 to 30 min	30 min to 12 h	-	12 to 2 d	After 2 d

The detailed kinetics to describe cement hydration is still debated [55]. Various models have been proposed to explain the process of hydration. One of the most acceptable models follows the Avrami equation, i.e. Eq. (2.2). More general form of Eq. (2.2) is the equation (5.2a) [160]:

$$-\ln(1 - \alpha) = k_r t^q \qquad (5.2a)$$

where k_r is the rate constant; q is a constant, which depends on the three factors in Eq. (5.2b) [160]:

$$q = [(u/v) + w] \qquad (5.2b)$$

where u is the factor related to the morphology of the growing phase, i.e. u = 1 for growth as needle, 2 for sheets, and 3 for isotropic growth;

v is the factor related to the rate – limiting process, i.e. v = 1 for pure phase-boundary control and 2 for pure diffusion control;

w is the factor related to the rate of nucleation, i.e. w = 0 for no nucleation and 1 for continuous nucleation at constant rate.

The q-parameters values in the rate law Eq. (5.2a) are summarized in Table 5.3 [159].

Table 5.3 The q values for the equation (5.2a) [159]

Model	Nucleation rate	Phase boundary control	Diffusion control
Three – dimensional growth (Spherical particles of reactant)	(1) Constant	4	2.5
	(2) Zero (instantaneous)	3	1.5
	(3) Deceleration	3 – 4	1.5 – 2.5
Two – dimensional growth (Laminar particles of reactant)	(1) Constant	3	2.0
	(2) Zero	2	1.0
	(3) Deceleration	2 – 3	1.0 – 2.0
One – dimensional growth (Lath-shaped particles of reactant)	(1) Constant	2	1.5
	(2) Zero	1	0.5
	(3) Deceleration	1 – 2	0.5 – 1.5

When applying Eq. (5.2a), if a given kinetic process becomes rate controlling at $t = t_0$ (where $\alpha = \alpha_0$), Eq. (5.2a) can be transformed to Eq. (5.2c) [161]:

$$-\ln[1-(\alpha-\alpha_0)] = k_r(t-t_0)^q \qquad (5.2c)$$

If the kinetics of a given hydration process conforms to the equation (5.2c), a plot of $\ln\ln[1/1-(\alpha-\alpha_0)]$ against $\ln(t-t_0)$ will be linear over the range of α. The plots for the acceleration of the hydration of 0CPM, 5CPM, 10CPM, and 20CPM are shown in Figure 5.4. The slope of the plot is the exponent q and the intercept is $\ln(k_r)$ and both are listed in Table 5.4.

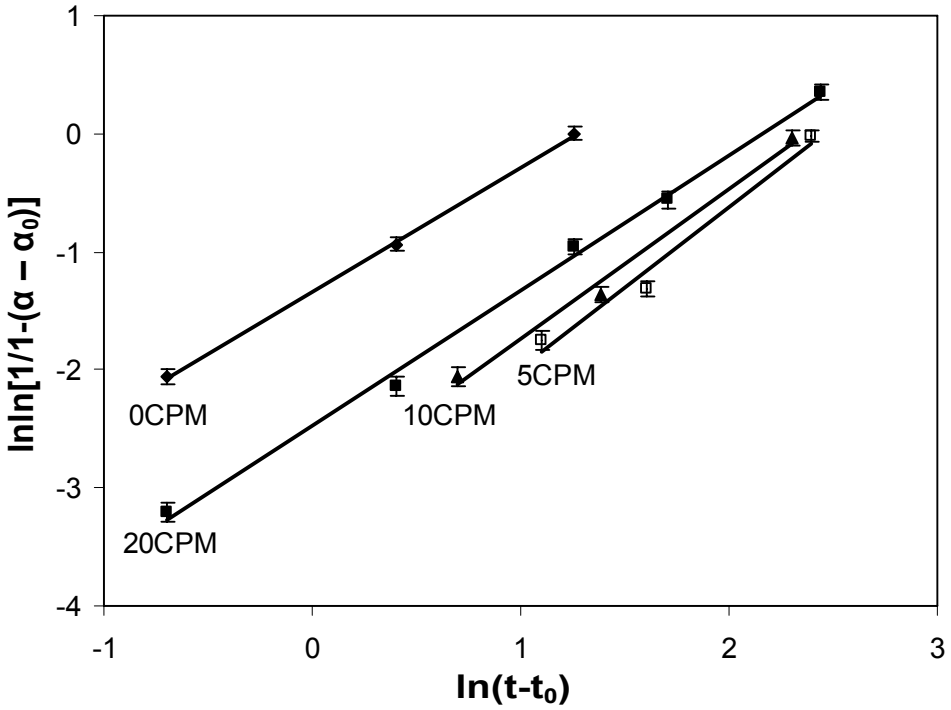

Figure 5.4 The plot of Eq. (5.2c), i.e. $\ln\ln[1/1-(\alpha-\alpha_0)]$ against $\ln(t-t_0)$, for the acceleration stage of the hydration of 0CPM, 5CPM, 10CPM, and 20CPM. α (%) is the degree of hydration and t (h) is the hydration time.

Table 5.4 The values of the exponent q and rate constant $\ln(k_r)$ of the acceleration stage for the hydration of 0CPM, 5CPM, 10CPM, and 20CPM

	t_0, h	α_0, %	q	$\ln(k_r)$	k_r, calculated	R squared
0CPM	0.5	4.5 ± 0.1	1.06 ± 0.03	-1.34 ± 0.02	$2.62 \pm 0.05 \times 10^{-1}$	0.9994
5CPM	2	4.3 ± 0.3	1.36 ± 0.21	-3.33 ± 0.38	$3.58 \pm 1.5 \times 10^{-2}$	0.9758
10CPM	1	7.4 ± 0.7	1.27 ± 0.12	-3.00 ± 0.20	$4.98 \pm 1.0 \times 10^{-2}$	0.9904
20CPM	0.5	10.5 ± 0.6	1.15 ± 0.04	-2.47 ± 0.06	$8.64 \pm 0.5 \times 10^{-2}$	0.9963

The hydration kinetics of 0CPM, i.e. pure C_3S, includes several distinct rate controlling steps. The first such step is the dissolutions of C_3S; however as C_3S dissolves into water very easily [55], this step is rapidly followed by the formation of a layer of C-S-H on C_3S. The dissolution of C_3S is therefore not the rate controlling step [161]. The hydration data for 0CPM indicated that two kinetically distinct stages controlled the rate of hydration after the induction stage. The first one, phase boundary control, initiated during the induction stage and prevailed through the acceleration stage and the second one, diffusion control, started at the onset of deceleration stage.

The value of q obtained from Eq. (5.2c) was near unity (1.06 ± 0.03) for the acceleration stage of the hydration of 0CPM. The microstructure of the hydrated 0CPM paste observed by SEM (Section 6.2) showed that the C-S-H, which formed during this stage, was essentially fibre shape, i.e. nearly one-dimensional. This indicated that $u = 1$ in Eq. (5.2b) for the hydration of C_3S during this stage and predicted that v and w would, respectively, be 1 and 0, i.e. one-dimensional phase boundary controlled growth at zero nucleation rate. This was probably because the nuclei rapidly formed and occupied the nucleation sites during the formation of the

C-S-H layer in the pre-induction stage, resulting in the elimination of the sites of nucleation, leading to the zero nucleation rates through the course of subsequent hydration (the acceleration and deceleration stages). The rate of growth of the needle-shaped C-S-H hydrates (one dimension) was previously predicted to control the hydration after the induction stage. An investigation by Brown et al. [161] showed similar results and these authors also discussed the possible reasons for the value of q in Eq. (5.2a) near unity rather than near 3, as predicted from calorimetric data. Based on the integration of the rate of heat liberation, the effects of C_3S dissolution, C-S-H formation, CH formation, and any subsequent solid-state transformations would be included in the exponents [161].

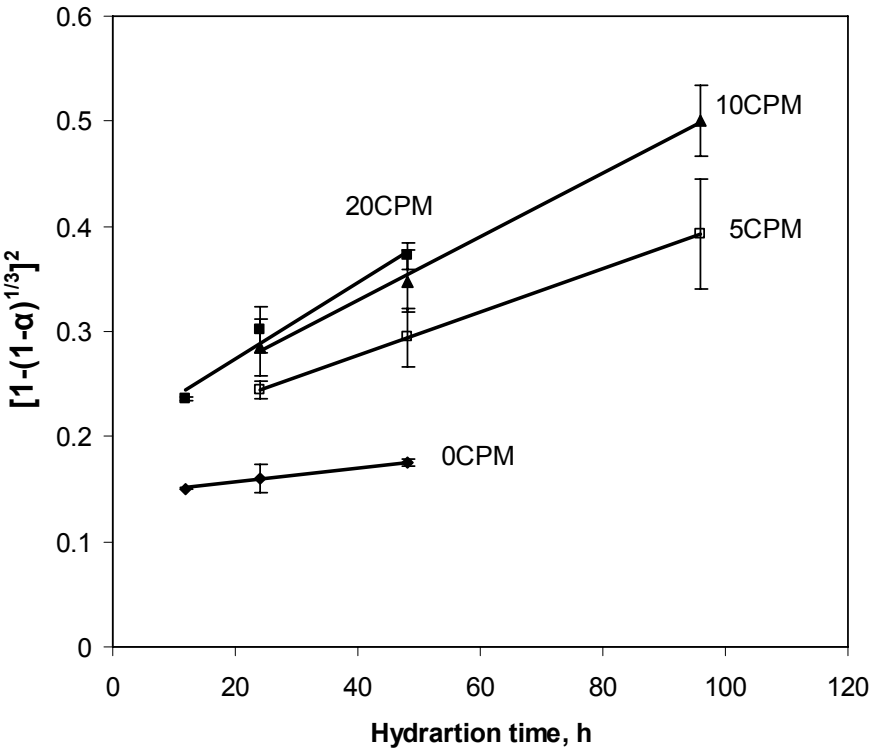

Figure 5.5 The plot of Eq. (2.3), i.e. $[1-(1-\alpha)^{1/3}]^2$ against t for the deceleration stage of the hydration of 0CPM, 5CPM, 10CPM, and 20CPM. α is the degree of hydration, % and t is the hydration time, h.

For the deceleration stage, the hydration data of 0CPM, 5CPM, 10CPM, and 20CPM fitted Eq. (2.3) very well (Figure 5.5), indicating that the kinetics of the deceleration stages of these cements were diffusion-control processes. The rate constants of the hydration of 0CPM, 5CPM, 10CPM, and 20CPM are listed in Table 5.5. The observation by SEM (Section 6.2) demonstrated that the particles of C_3S were covered by hydrates on the all surfaces during the deceleration stage.

Table 5.5 The rate constants for the deceleration stage of the hydration of 0CPM, 5CPM, 10CPM, and 20CPM

	k_d, h^{-1}	R squared
0CPM	$6.91 \pm 0.36 \times 10^{-4}$	0.9972
5CPM	$2.06 \pm 0.02 \times 10^{-3}$	0.9999
10CPM	$3.02 \pm 0.14 \times 10^{-3}$	0.9979
20CPM	$3.65 \pm 0.66 \times 10^{-3}$	0.9685

From the data above, it is clear that the hydration of CPSC was different from that of pure C_3S. For the acceleration stage, the values of q for the hydration of 5CPM, 10CPM, and 20CPM were greater than one, indicating that the acceleration stages of hydration were phase boundary controlled with deceleration of nucleation rates. In this case, the parameters of Eq. (5.2b) $u = 1$ (needle-shaped hydrates, one dimension), $v = 1$ (phase boundary control), and w was between 0 and 1 (deceleration of nucleation rates). The deceleration of nucleation rates indicated that

nucleation took place to some extent during the acceleration stage of the hydration of CPSC. As demonstrated in Section 6.2, the development of the microstructure of 0CPM pastes showed that the hydrates grew and developed into needle-shapes distributed evenly on the surfaces of C_3S grains. However, the hydration products formed during the hydration of CPSC, for example, 10CPM, distributed unevenly (Figure 6.3b), and the surfaces of the hydration products were the favourite sites to grow. The hydration products grown on the isolated hydrates were evidently displayed in Figure 6.3(b). After certain time (e.g. 12 h for 10CPM) the hydration products covered the whole surface of the particles (Figure 5.6) indicating that the surface area uncovered by hydration products would also provide nucleation sites for new hydrates after further dissolution of C_3S with the hydration process.

The CPSC with more CPM was faster in hydration (i.e. nucleation and growth of hydrates) than the one with lower content of CPM due to the acceleration effect of CPM on the hydration process. The nucleation sites on the unhydrated grain surfaces would be consumed faster and the nucleation sites diminished more noticeably for the CPSC with a higher content of CPM. For example, it took 12 h for 10CPM to cover the whole particles by hydration products, but only 2 h for 20CPM (Figures 5.6 and 6.2c). The value of q decreased in the order of 5CPM > 10CPM > 20CPM (Table 5.4). The increase in reaction constant k_r with the content of CPM in CPSC, i.e. 5CPM < 10CPM < 20CPM (Table 5.4), revealed that the acceleration effect of CPM was more evident when the content of CPM was higher in CPSC. The reaction constants for 5CPM, 10CPM, and 20CPM were lower than that of 0CPM probably due to different nucleation and growth mechanisms of the hydration products for the two kinds of cements.

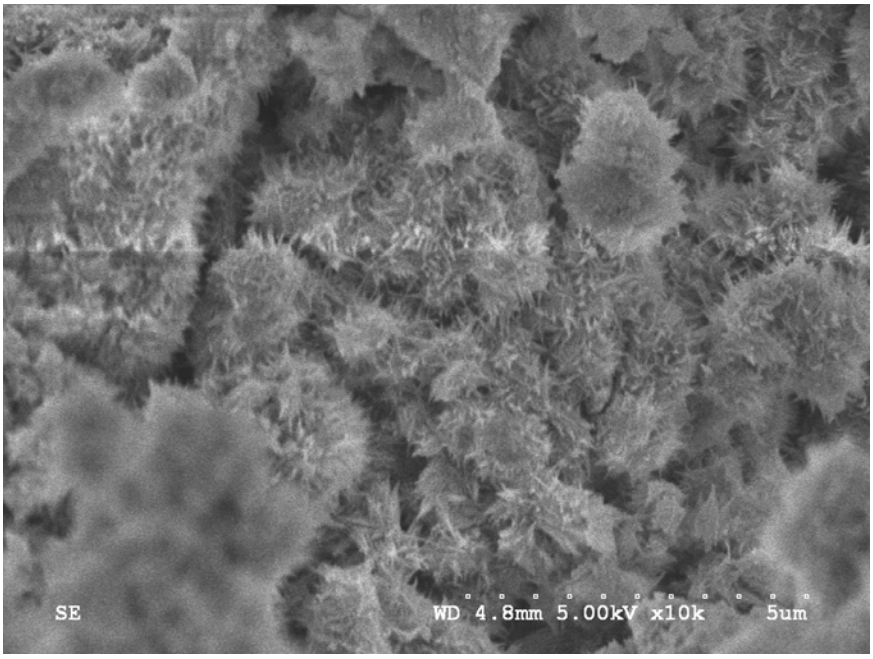

Figure 5.6 SEM micrographs of the fracture surfaces of 10CPM paste hydrated for 12 h at 37ºC.

The deceleration stage of hydration of 5CPM, 10CPM, and 20CPM was a diffusion-controlled process, the same as that for 0CPM, and the hydration data were fitted Eq. (2.3) very well (Figure 5.5). The reaction constant k_d in this stage increased with the content of CPM in CPSC and the values of k_d for CPSC were also higher than that of 0CPM (Table 5.5). The reason was probably due to the increase in porosity with the content of CPSC (Section 6.3), i.e. the high porosity could provide more surfaces to hydrate. In addition, during the hydration of CPSC, HAP precipitated accompanied by the formation of extra water, which increased with the content of CPM (Section 5.3 and Figure 1.1). This extra water could form pores, voids, or channels in set cements, which facilitated transport of reactants, hence resulting in the higher rate of hydration. However further studies are needed to understand the nucleation behaviour of the hydration products of CPSC.

It was interesting to see that the period of high hydration rates was divided into two sub-periods by a relatively low hydration rate for the CPSC in Figure 5.2 (b), but the hydration of 0CPM showed only one period of high hydration rate. The periods with high hydration rates were very close to the acceleration periods for the hydration of CPSC (Table 5.2). The beginning of the second sub period for 10CPM and 20CPM was, respectively, at the hydration of 4 h and 2 h, which were coincidently the same times when DCPD disappeared from the system. It is expected that DCPD precipitated in less than 10 min after CPM dissolved into water when the cement was mixed with water.

The first sub-period of high hydration rate was probably due to the precipitation of DCPD and/ or HAP, which would provide more nucleation sites for the C-S-(P-)H phase to accelerate the hydration of C_3S, and the second one might be attributed to the formation of more C-S-(P-)H. The data of the solubility product constants of HAP [$Ca_5(PO4)_3(OH)$, pK_{sp} = 58.6 at 37 ºC [94]] and C-S-H (pK_{sp} = 11.22 – 11.28 at 22 ºC [162]) indicate that the concentration of Ca^{2+} to reach saturation with respect to HAP at 37 ºC around pH 11.5 is much lower than that for C-S-H hydrate. XRD analysis showed that DCPD disappeared first, likely converting into HAP or incorporating into hydrates C-S-(P)H. These two sub-periods of acceleration together increased the duration of the acceleration period of the CPSC hydration therefore increased its hydration degree, although the maximum hydration rates of the two sub-periods were lower than that of the acceleration period of 0CPM. After the total acceleration periods, the hydration degree of 20CPM (86.4 ± 2.1 %) was statistically significantly higher than that of 0CPM ($p < 0.001$), and the hydration degrees of 5CPM (66.1 ± 3.8 %) and 10CPM (69.9 ± 8.0%) were not statistically significantly different from that of 0CPM (67.9 ± 3.1 %) ($p > 0.05$), Table 5.2.

Table 5.2 shows that the acceleration period started relatively early (e.g. 30 min for 20CPM, 1 h for 10CPM, and 2 h for 5CPM) and lasted a longer time (e.g. 11.5 h for 20CPM, 11 h for 10CPM, and 10 h for 5CPM) for the CPSC with high CPM. It is expected that CPSC with more CPM would produce more HAP, which would in turn produce more nucleation sites for hydrates C-S-(P-)H and result in a better acceleration effects. In addition the formation of HAP was accompanied by the production of water (i.e. refer to Eq. 5.7), and as such would produce pores and voids, which would provide the diffusion channels to continue hydration. However, the acceleration period of 0CPM started early (about 30 min) and lasted a short time (about 3.5 h) in comparison with the CPSC (10 to 11.5 h), see Table 5.2. For more than 20 wt%, CPM increased the duration of the acceleration period and the degree of hydration, instead of having an accelerating effect on the hydration rate of C_3S; but for smaller amounts (5 and 10 wt%) CPM did not show deceleration effect on the hydration in terms of the hydration degree at the end of acceleration period. These results do not agree with the traditional concept that phosphate is a retarder for the hydration of C_3S [54]. The quantitative XRD results showed that certain compositions of CPSC, for example, 10CPM have about 90% of C_3S hydrated after 1 d and more than 97% of C_3S hydrated after 4 d. This could provide some information how much C_3S would remain unhydrated after the cement was implanted for a certain time.

5.3 CaO/SiO_2 and H_2O/SiO_2 in the Hydrates

The DTA curves of the hydrated cements of 0CPM, 10CPM, and 20CPM for the preset periods of time are shown in Figure 5.7 and the weight changes during the thermal analysis are in Figure 5.8. For 0CPM a weak endotherm was observed below 200 ºC accompanying with a mass loss for each hydration period [Figures 5.7 (a) and 5.8 (a)]. After the hydration for 10 min, the peak between 400 – 500 ºC was not discernible and after 30 min a tiny endothermal peak appeared at 420 ºC. After 1 h and longer time of hydration, the sharp endothermal peaks became

more evident at around 400 – 500 ºC and their intensities became enhanced. The loss of mass could be noticed at around 400 – 500 after 30 min of hydration. The relatively broad endothermal peaks between 640 – 760 ºC were shown on the DTA curves, accompanied by weight losses for all hydration times. Two endothermal peaks at 921 and 982 ºC were observed for the hydration up to 12 h, but there were no mass changes for these thermal effects. For hydration from 12 h to 28 d, exothermal peaks at around 864 ºC were noticed, accompanied by no discernible changes in mass.

Previous studies suggested that it was difficult, maybe impossible, to obtain C-S-H free from calcium carbonate [163]. In DTA-TG analysis, both the dehydration of CH and the decomposition of $CaCO_3$ have endothermal effects. Due to different experimental conditions, such as the sample size, the state of sample and the rate of heating, DTA curves for the same compound may be also different. Biffen [163] reported that the dehydration of CH and the decarbonation of calcium carbonate took place in the ranges of 425 – 534 ºC and of 650 – 830 ºC, respectively. For comparison, Ramachandran et al. [164] gave their ranges as 450 – 550 ºC and of 750 – 900 ºC and El-Jazairi ad Illston [87] defined the ranges as 440 – 580 ºC and 580 – 1007 ºC, respectively. In the present work, the dehydration of CH and the decomposition of $CaCO_3$ took place in the ranges of 400 – 500 ºC and 640 – 760 ºC, respectively. The CH peaks appeared after a longer hydration time in comparison with C_3S, starting at 4 h for both 10CPM and 20CPM. It was reported that dehydration reactions of calcium silicate hydrates occurred in the range of 105 – 440 ºC by El-Jaairi and Illston [87]; more specifically, four dehydration temperatures (around 100, 180, 350, and 400 ºC) were indicated by Fordham and Smalley [165].

The temperatures of these thermal effects and the corresponding mass changes for 0CPM, 10CPM and 20CPM at different periods of hydration are listed in Tables 5.6, 5.7 and 5.8,

respectively. The preparation procedures in this experiment followed Taylor's suggestion that the specimen prepared by pumping with a rotary pump for 1 h to remove excess water is suitable for thermal analysis [54]. Some unduly drastic drying procedures, e.g. heating at 105 ºC or equilibration to constant weight in atmospheres of low relative humidity, such as "D-drying", partially dehydrated the C-S-H phase [54]. The second column in Table 5.6 is the first peak temperature, which was due to the dehydration of C-S-H hydrates [165]. The third column lists the percentage of the total dehydration of hydrates C-S-H to the ignited weight (i.e. the sample weight after heating to 1100 ºC); all the percentages in these tables are given in relation to the ignited weight. The column "Dehydroxylation of CH" shows that the peak temperature of CH decomposition and the corresponding percentage of the weight loss. "Decarbonation of $CaCO_3$" shows the decomposition temperature of $CaCO_3$ during the experiment and the corresponding percentage of the weight loss. The last two columns are the transformation temperatures of C-S-H to wollastonite and the transition temperature between C_3S polymorphisms, which are discussed below. Tables 5.7 and 5.8 have one column more than Table 5.6, which is named "2^{nd} endo peak" and gives the temperature of the second endothermal peak. This peak is due to the decomposition of DCPD and the TG curve missed showing its change because the amount of DCPD was small (discussed below).

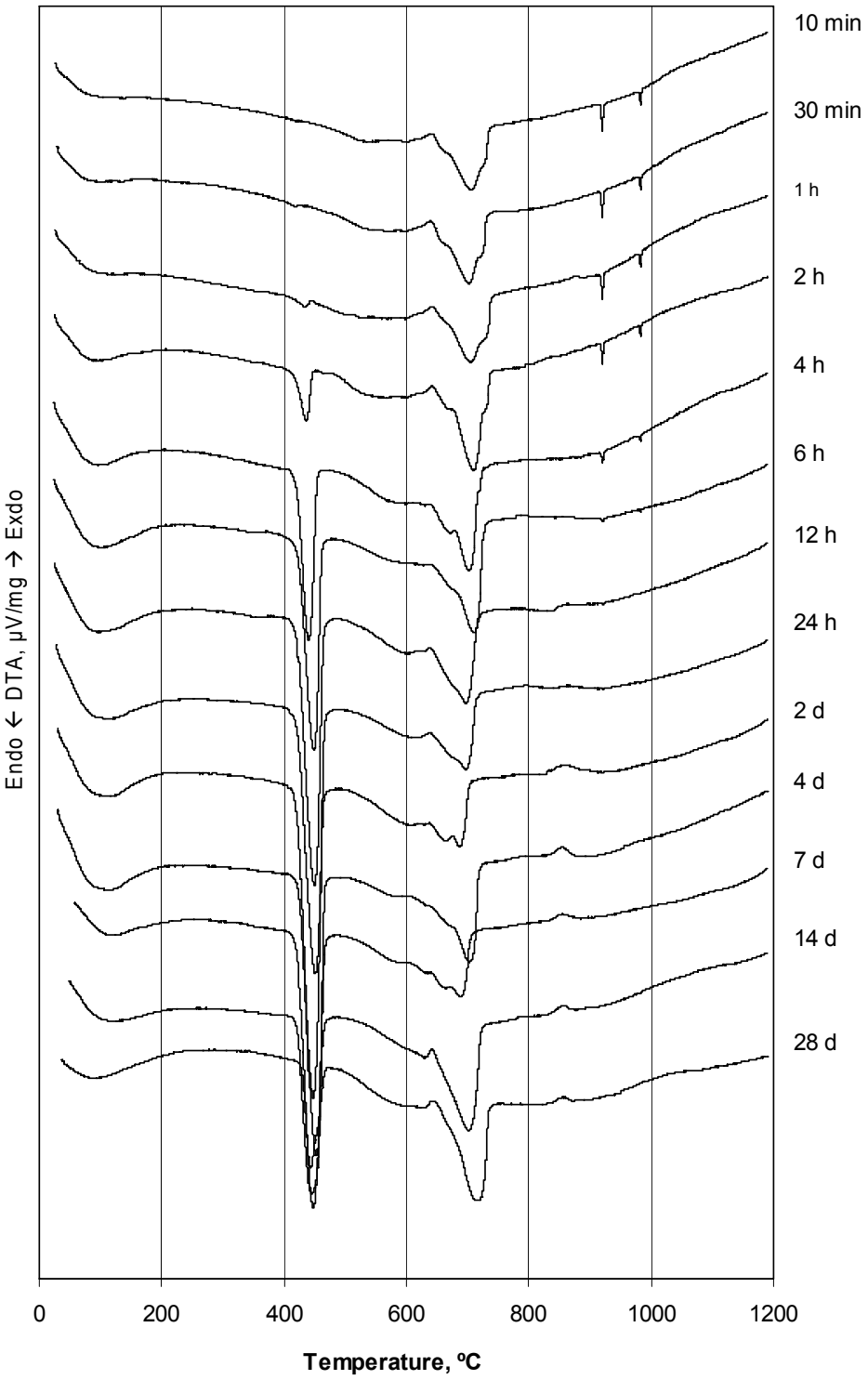

(a) 0CPM

Figure 5.7 DTA curves of the cements hydrated for different periods of hydration times, (a) 0CPM, (b) 10CPM, and (c) 20CPM. The peaks between 400 and 500 ºC are for the decomposition of CH and those between 600 and 800 ºC are for the decomposition of $CaCO_3$.

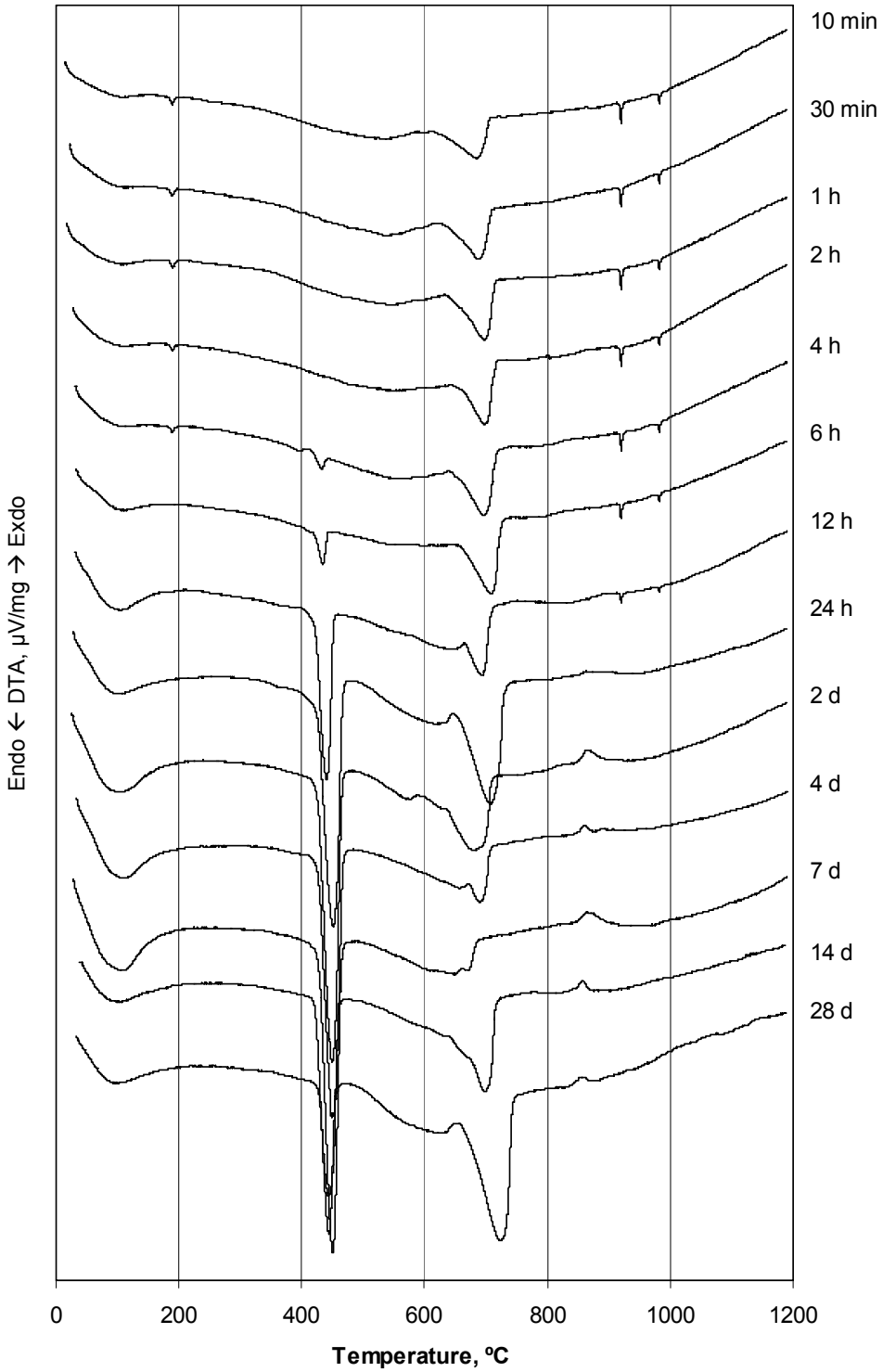

Figure 5.7 – continued: (b) 10CPM

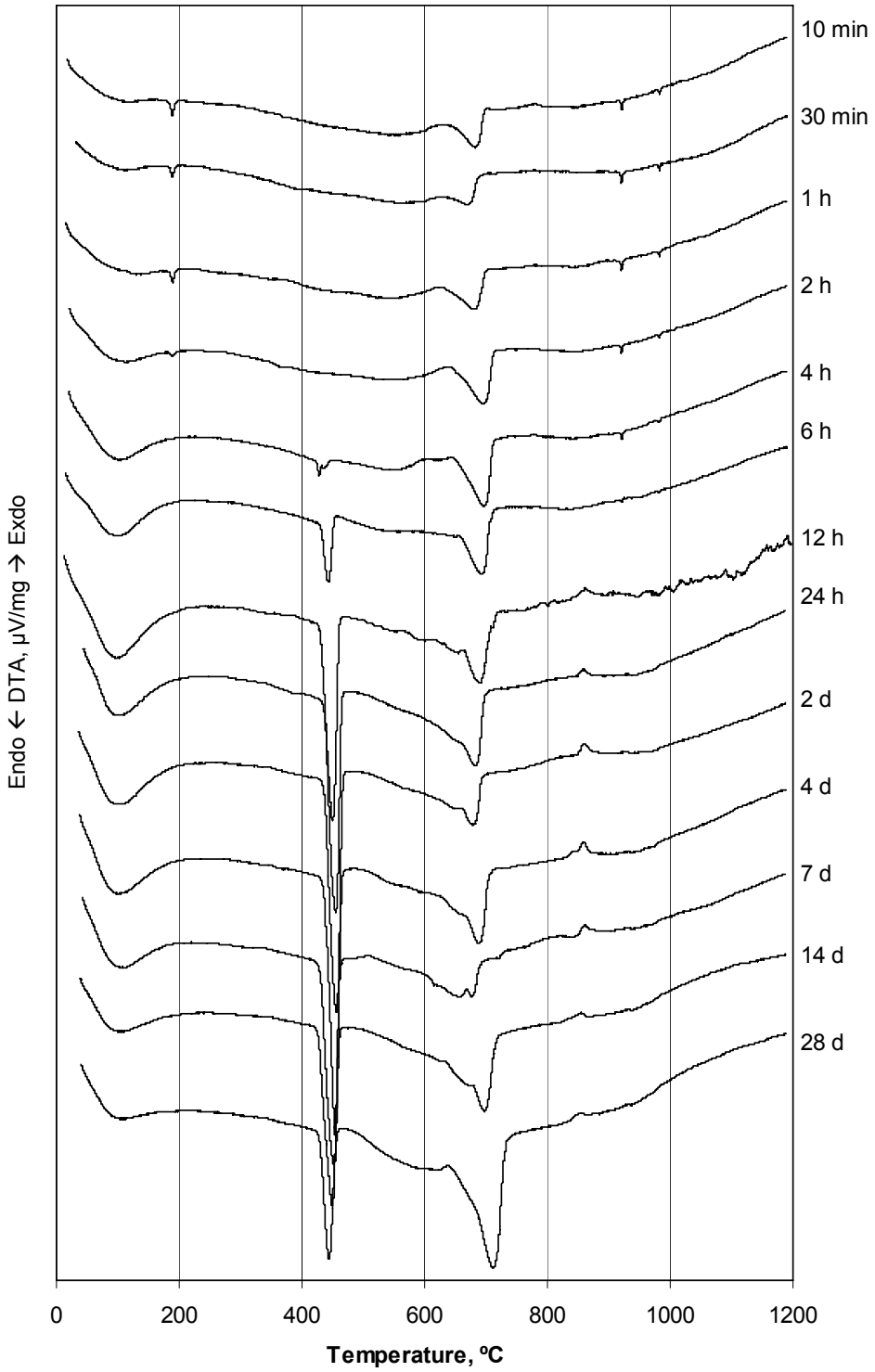

Figure 5.7 – continued (c) 20CPM

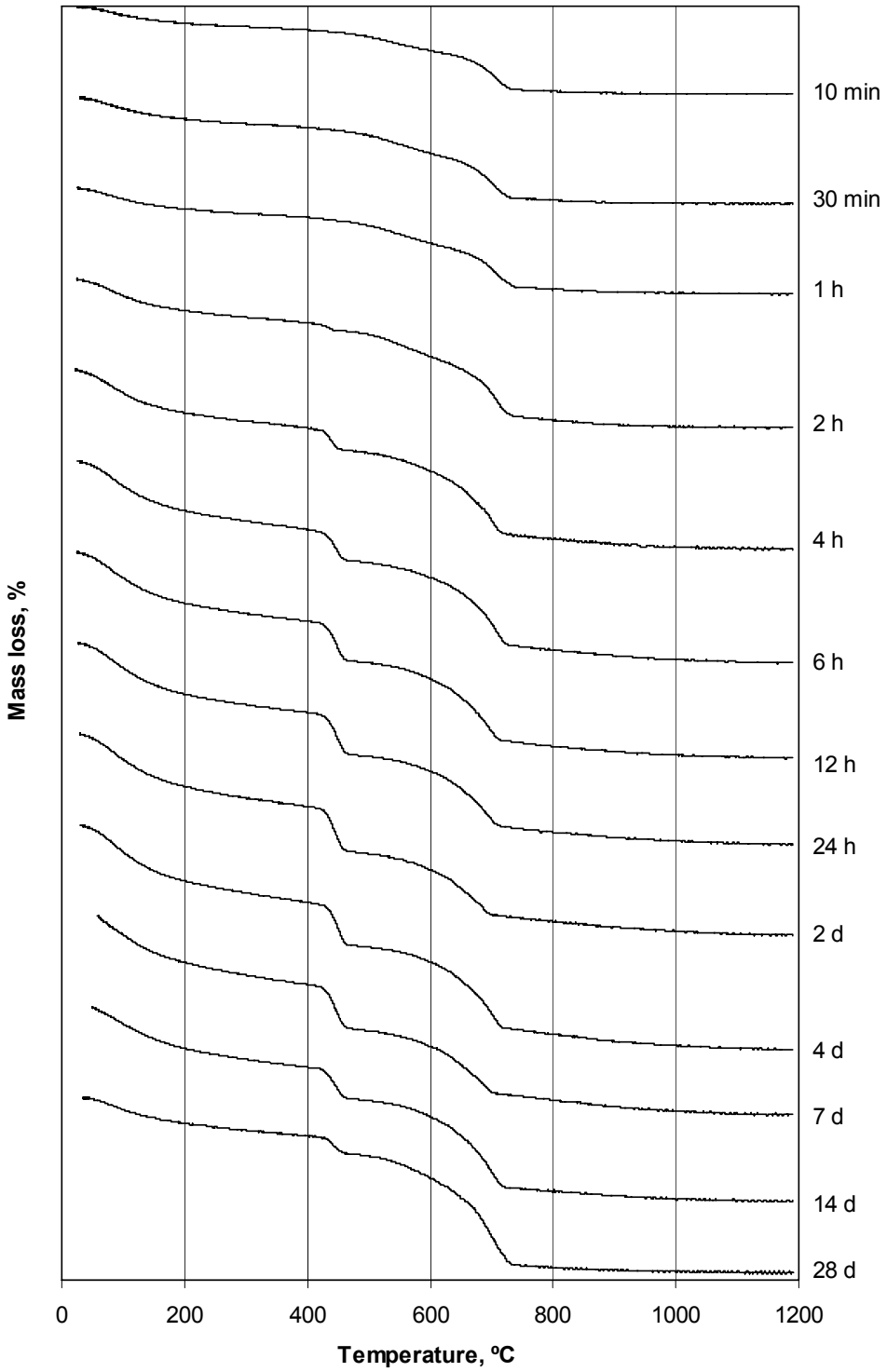

(a) 0CPM

Figure 5.8 Thermograms of the cements hydrated for different periods of hydration times, (a) 0CPM, (b) 10CPM, and (c) 20CPM. The mass losses between 400 and 500 ºC are for the decomposition of CH and those between 600 and 800 ºC are for the decomposition of $CaCO_3$.

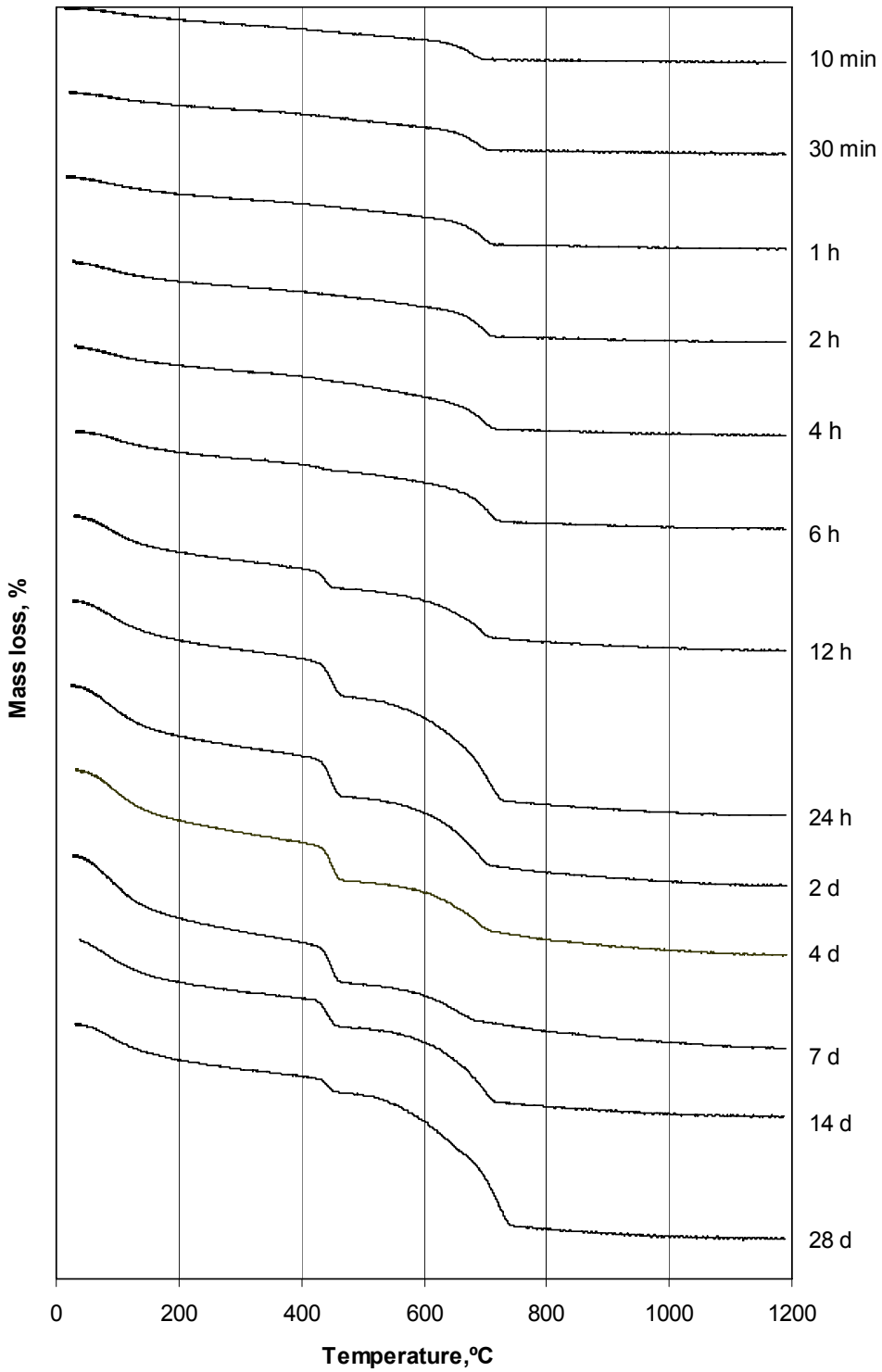

Figure 5.8 – continued (b) 10CPM

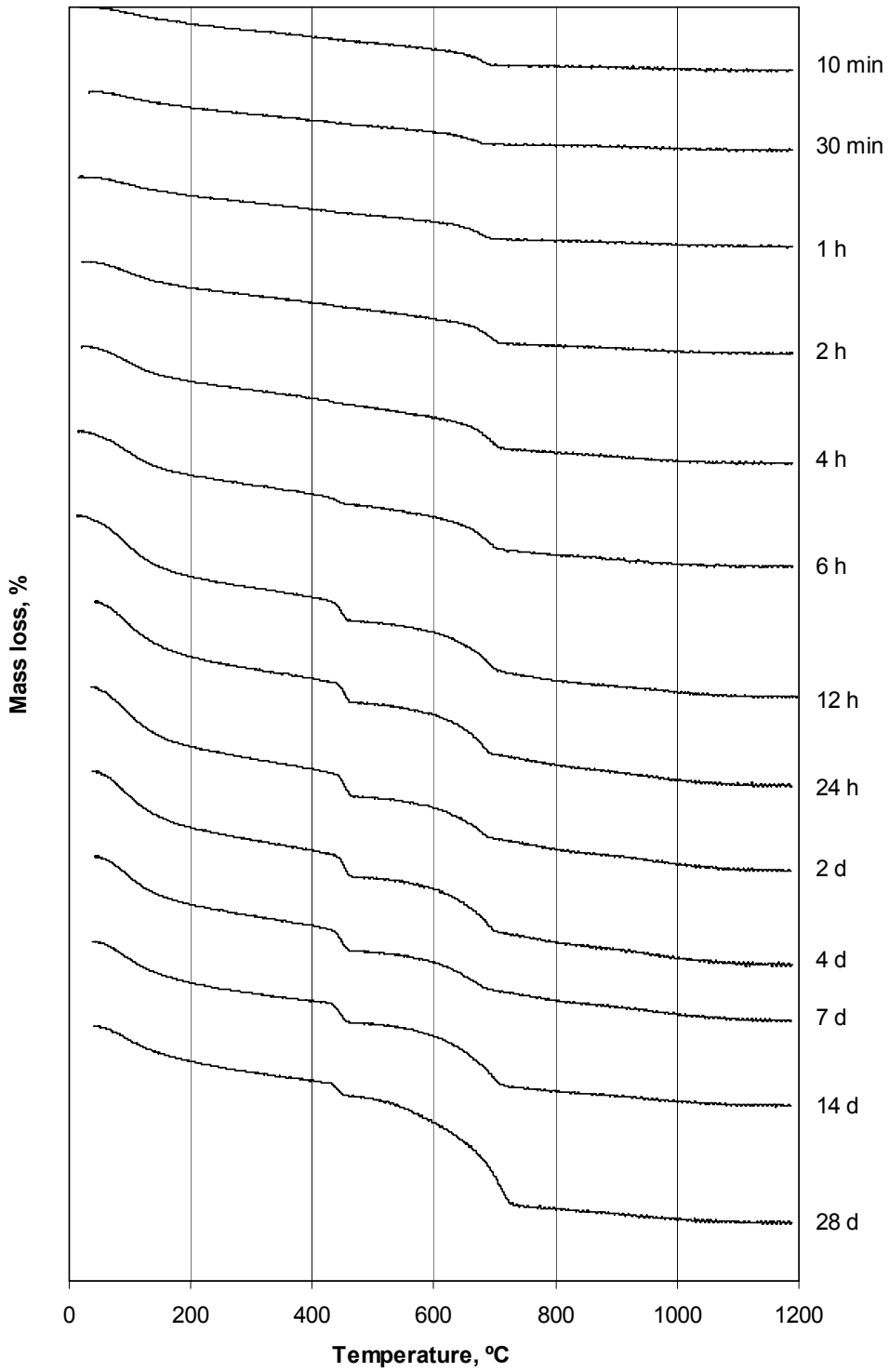

Figure 5.8 – continued (c) 20CPM

Table 5.6 The temperature of thermal effects and the corresponding weight loss of 0CPM for different periods of hydration*

Hydration Period	1st endo peak	ΔW_{dh}	Dehydroxylation of CH		Decarbonation of $CaCO_3$		Temperature of C-S-H to wollastonite	Temperature of phase conversion of C_3S	
	ºC	%	Temp,ºC	ΔW_{dx},%	Temp,ºC	ΔW_{dc},%	ºC	ºC	ºC
10 min	137	-3.0	-	-	705	-7.1	-	920	983
30 min	132	-3.8	418	-0.1	702	-8.6	-	920	983
1 h	130	-3.7	435	-0.4	704	-8.3	-	921	983
2 h	98	-5.9	437	-0.9	710	-11.3	-	920	982
4 h	102	-8.1	441	-2.9	703	-11.6	-	920	982
6 h	100	-9.9	449	-4.2	710	-12.0	862	921	982
12 h	100	-10.0	450	-5.5	697	-11.3	864	921	982
24 h	109	-10.0	451	-5.7	697	-10.2	864	-	-
2 d	110	-10.4	448	-6.2	686	-8.9	864	-	-
4 d	116	-11.4	452	-6.2	703	-12.1	853	-	-
7 d	117	-9.7	448	-6.2	688	-9.1	855	-	-
14 d	122	-9.5	445	-4.4	701	-12.3	856	-	-
28 d	87	-5.3	444	-2.4	714	-15.1	857	-	-

*ΔW_{dh}, ΔW_{dx}, and ΔW_{dc} are the percentages of the weight losses due to dehydration of hydrates, dehydroxylation of CH, and decarbonation of $CaCO_3$, respectively. The percentage of weight loss relates to the ignited weight at 1100 ºC.

Table 5.7 The temperature of thermal effects and the corresponding weight loss of 10CPM for different periods of hydration

Hydration Period	1st endo peak Temp,ºC	2nd endo peak Temp,ºC	ΔW_{dh} %	Dehydroxylation of CH Temp,ºC	ΔW_{dx},%	Decarbonation of $CaCO_3$ Temp,ºC	ΔW_{dc},%	Temperature of C-S-H to wollastonite ºC	Temperatures of phase conversion of C_3S ºC	ºC
10 min	109	189	-2.8	-	-	681	-3.5	864	920	982
30 min	109	189	-2.8	-	-	690	-4.2	864	920	982
1 h	115	189	-3.1	-	-	697	-4.8	864	920	982
2 h	114	189	-4.0	-	-	699	-5.5	864	920	982
4 h	115	189	-4.1	432	-0.1	696	-6.5	864	920	982
6 h	113	-	-4.7	434	-0.5	708	-7.0	864	920	982
12 h	104	-	-7.3	440	-2.6	693	-7.0	864	920	982
24 h	103	-	-9.1	440	-6.1	707	-16.6	864	-	-
2 d	104	-	-11.1	450	-6.0	678	-10.8	864	-	-
4 d	111	-	-11.0	448	-5.7	690	-7.6	864	-	-
7 d	106	-	-10.8	450	-5.7	669	-5.8	864	-	-
14 d	104	-	-8.8	443	-4.2	698	-11.2	857	-	-
28 d	102	-	-8.3	444	-2.4	724	-21.1	857	-	-

ΔW_{dh}, ΔW_{dx}, and ΔW_{dc} are the percentages of the weight losses due to dehydration of hydrates, dehydroxylation of CH, and decarbonation of $CaCO_3$, respectively. The percentage of weight loss relates to the ignited weight at 1100 ºC.

Table 5.8 The temperature of thermal effects and the corresponding weight loss of 20CPM for different periods of hydration

Hydration Period	1st endo peak Temp,ºC	2nd endo peak Temp,ºC	ΔW_{dh} %	Dehydroxylation of CH Temp,ºC	ΔW_{dx},%	Decarbonation of $CaCO_3$ Temp,ºC	ΔW_{dc},%	Temperature of C-S-H to wollastonite ºC	Temperature of phase conversion of C_3S ºC	ºC
10 min	121	189	-4.2	-	-	682	-3.2	779	921	982
30 min	111	189	-3.9	-	-	668	-2.7	778	921	982
1 h	130	189	-4.2	-	-	682	-3.4	780	921	982
2 h	117	189	-5.5	-	-	695	-4.8	780	921	982
4 h	104	-	-7.3	427	-0.5	697	-6.1	780	921	982
6 h	108	-	-9.1	443	-1.1	693	-6.5	780	921	982
12 h	100	-	-12.4	450	-3.2	689	-7.8	862	-	-
24 h	103	-	-12.0	455	-3.2	681	-7.8	860	-	-
2 d	101	-	-12.9	456	-3.6	679	-6.3	861	-	-
4 d	101	-	-12.5	454	-3.6	689	-8.4	860	-	-
7 d	105	-	-10.4	451	-3.4	677	-5.7	861	-	-
14 d	104	-	-8.9	449	-2.9	697	-9.4	855	-	-
28 d	108	-	-8.6	444	-2.2	711	-16.6	855	-	-

ΔW_{dh}, ΔW_{dx}, and ΔW_{dc} are the percentages of the weight losses due to dehydration of hydrates, dehydroxylation of CH, and decarbonation of $CaCO_3$, respectively. The percentage of weight loss relates to the ignited weight at 1100 ºC.

The phase transitions of C_3S polymorphisms were responsible for the endothermal effects at 921 and 982 ºC [54, 166]. When the hydration was not complete, the unhydrated C_3S caused phase transitions during the heating in DTA experiments, but there were no mass changes. The peaks of the phase transitions were not noticeable when the hydration was longer than 24 h for 0CPM, at which the degree of hydration was about 78.4 ± 7.8 % (seen as the curve of 24 h in Figure 5.7a). For 10CPM and 20CPM, the peaks of the C_3S phase transitions (seen as the curve of 24 h in Figure 5.7b and the curve of 12 h in Figure 5.7c) disappeared after 24 h and 12 h of hydration, respectively, and the hydration degree was 89.9 ± 7.2 % and 86.4 ± 2.1 %, respectively. The intensities of the peaks became smaller with the hydration time for all the cements, confirming that the amounts of un-hydrated C_3S reduced with the hydration process.

The weak exothermal peak at about 800 – 900 ºC was attributed to the formation of crystalline wollastonite from C-S-H [85]. For 0CPM the exothermal peak at 864 ºC disappeared after the hydration for 12 h, at which the hydration degree was 77.1 ± 1.7 %. For less than 6 h of hydration, however, no peaks occurred in the range of 800 – 900 ºC, suggesting that at least two compositions of C-S-H hydrates would exist.

One type of C-S-H formed mainly in the early and middle hydration stage (< 67.9 ± 3.1 % of the degree of hydration) and did not decompose at around 864 °C; and the other formed in the middle and later hydration (> 67.9 ± 3.1 % of the degree of hydration) and decomposed to wollastonite at around 864 °C (Figure 5.7a and Table 5.6). Many researches reported that two forms of C-S-H hydrates might result from hydration of Ca_3SiO_5 [83, 155, 167]. The CaO/SiO_2 and H_2O/SiO_2 molar ratios of C-S-H hydrates with the hydrated process were calculated using Eqs. (3.3b) and (3.4b), respectively, from the DTA-TG data and plotted against the hydrated degree of C_3S in Figures 5.9 and 5.10.

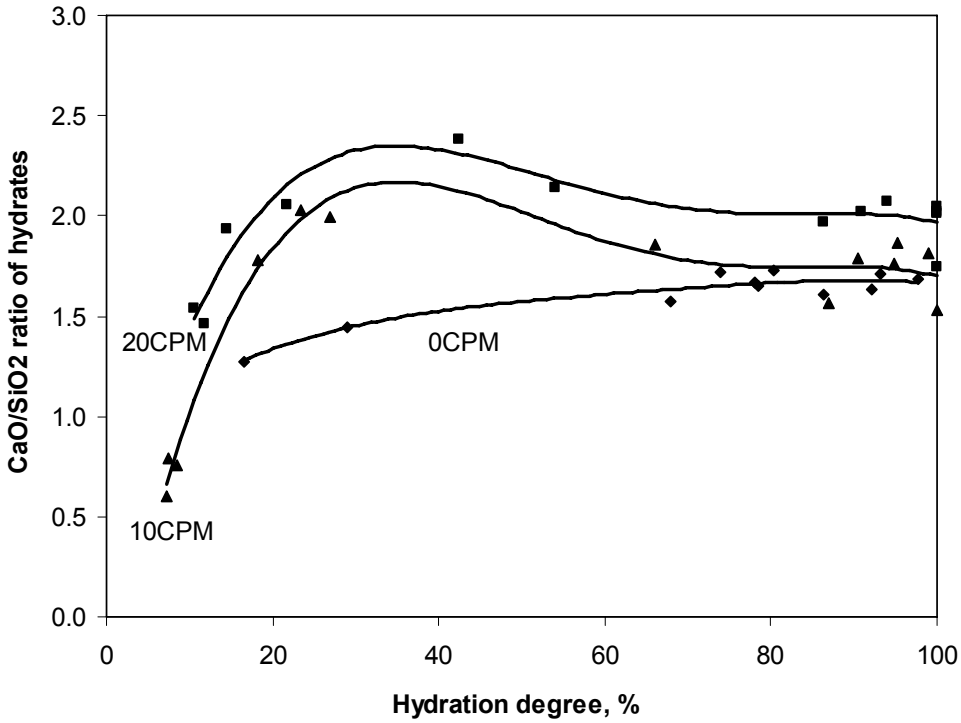

Figure 5.9 CaO/SiO_2 ratio of C-S-H hydrates plotted against hydration degree of C_3S for 0CPM, 10CPM and 20CPM.

The CaO/SiO_2 ratio of C-S-H hydrates from C_3S had a range of 1.3 to 1.7 (Figure 5.9), somewhat lower (and with lower average) than that of 1.6 to 2.0 reported in literature [54]. The literature showed that there was no general agreement among the previous results in terms of the CaO/SiO_2 ratio, especially at low degrees of hydration [167-170]. Some studies [56, 170] showed that the CaO/SiO_2 ratio was 1.5 to 2.2 below 20% of the hydration degree followed by decreasing to 1.4 to 1.8 with no consistent changes with further hydration. Other studies gave the

CaO/SiO_2 ratio of 0.8 to 1.5 below 20% of the hydration degree and the ratio rose to 1.4 to 1.9 with progressive hydration [167, 168], which our results were consistent with. The variations of the CaO/SiO_2 ratio might be due to the differences of tricalcium silicate reactivity, the hydration conditions and the analytical methods [167]. The CaO/SiO_2 ratio of the hydrates was 1.3 – 1.5 between 10 to 30 % hydration and 1.5 – 1.7 between 30 to 90% hydration (Figure 5.9); and the latter did not vary much and the corresponding exothermal peaks at 853 – 864 ºC in DTA curves were due to the conversion from the C-S-H hydrate to wollastonite [85]. This C-S-H could be called middle stage C-S-H or C-S-H (M) in here and the early stage C-S-H could be called C-S-H (E). The higher CaO/SiO_2 ratio from longer hydration would cause a relatively low conversion temperature due to polymerization of silicate ions [85]. Figure 5.10 showed that the H_2O/SiO_2 molar ratios in the hydrates of 0CPM were about 2.2 – 5.3 at 10 to 30% hydration and 1.6 – 2.2 at 30 to 90 % hydration. The stoichiometry of the C-S-H produced from pure C_3S at w/c = 10 and at 37 ºC could be therefore represented by the formula $(1.3 – 1.5)CaO{\cdot}SiO_2{\cdot}(2.2 – 5.3)H_2O$ at the hydration degree of 10 – 30 % and $(1.5 – 1.7)CaO{\cdot}SiO_2{\cdot}(1.6 – 2.2)H_2O$ at the hydration degree of 30 – 90 %. In comparison with the late stage of hydration (i.e. the hydration degree > 30 %), the low hydration degree (< 30 %) resulted in a relatively low CaO/SiO_2 ratio in the hydrates and relatively high water content as confirmed in a previous study [83]. The results of this work for C_3S (0CPM) at 30 – 90% hydration are thus consistent with the previous study, in which the C-S-H hydrates were represented by $1.7CaO{\cdot}SiO_2{\cdot}2.1H_2O$ resulting from the C-S-H equilibrated in an atmosphere of 11% RH [70]. This water, so called chemically-bound water, is only present in the interlayer space and its content is much lower than that in the hydrates of $1.7CaO{\cdot}SiO_2{\cdot}4.0H_2O$, which resulted from a saturated paste with the pores totally filled with water [54]. The preparation procedure of the specimens for the measurement of DTA-TG, i.e. air-drying followed by vacuum drying for one hour, had probably removed all the water from the pores of the hydrates.

The 10CPM and 20CPM cements had some differences in thermal behaviour from 0CPM (Figures 5.7 b & c and 5.8 b & c). DTA curves of 10CPM and 20CPM at about 189 ºC show new (i.e. absent for 0CPM) small endothermal peaks in the early hydration of up to 4 h for 10CPM and 2 h for 20CPM. The respective weight changes for these endothermal effects were not discernible in TG curves. The XRD analysis showed that DCPD peaks occurred in the hydrated 10CPM and 20CPM corresponding to the hydration periods, i.e. 10 min to 4 h for 10CPM and 10 min to 2 h for 20CPM, respectively (Figure 5.11).

Previous study [131] on the formation of HAP from the reaction of MCPM, TTCP, and CH in dilute suspensions showed that the dissolution of MCPM was very fast (finished in only 2 min) and resulted in the formation of DCPD even though pH was in the range wherein HAP is the most stable phase. The authors believed that DCPD formation was favoured kinetically, although thermodynamically HAP was the most favoured phase; the subsequent process included however consumption of DCPD and formation of HAP [131]. Another explanation may relate to the fast dissolution of CPM in the environment of hydrated C_3S which could cause decrease in the local pH to the range in which DCPD is the stable phase, although the bulk pH was in the range that was favourable for HAP. When the hydration was almost complete, the hydration products of 10CPM and 20CPM were HAP, CH, and C-S-(P-)H (also calcium carbonate, which probably formed during sample storage). DCPD was dehydrated to DCPA at around 180 ºC [171] and HAP did not decompose up to 1350 ºC [93]. Therefore the peak at 189 ºC was attributed to the decomposition of DCPD.

The above presented facts indicate that the following chain of events could be taking place during hydration of CPSC bio-cements: (1) CPM in the environment of C_3S + water transforms

into DCPD, and then (2) DCPD reacts with CH to form HAP, while (3) the hydration of C_3S is taking place for the whole period. This scenario is consistent with the relationship between the species of phosphates and pH (Figure 2.5 on Page 28), i.e. in the pH 11 to 12 (Figure 4.5 on Page 68), the dominant phosphate ion was HPO_4^{2-}. During the whole range of hydration of 10CPM and 20CPM, the XRD results did not show any peaks at 4.7 º (2 theta), which is the characteristic peak of OCP, indicating that OCP did not form, at least within detection limit of XRD (Figure 5.12).]

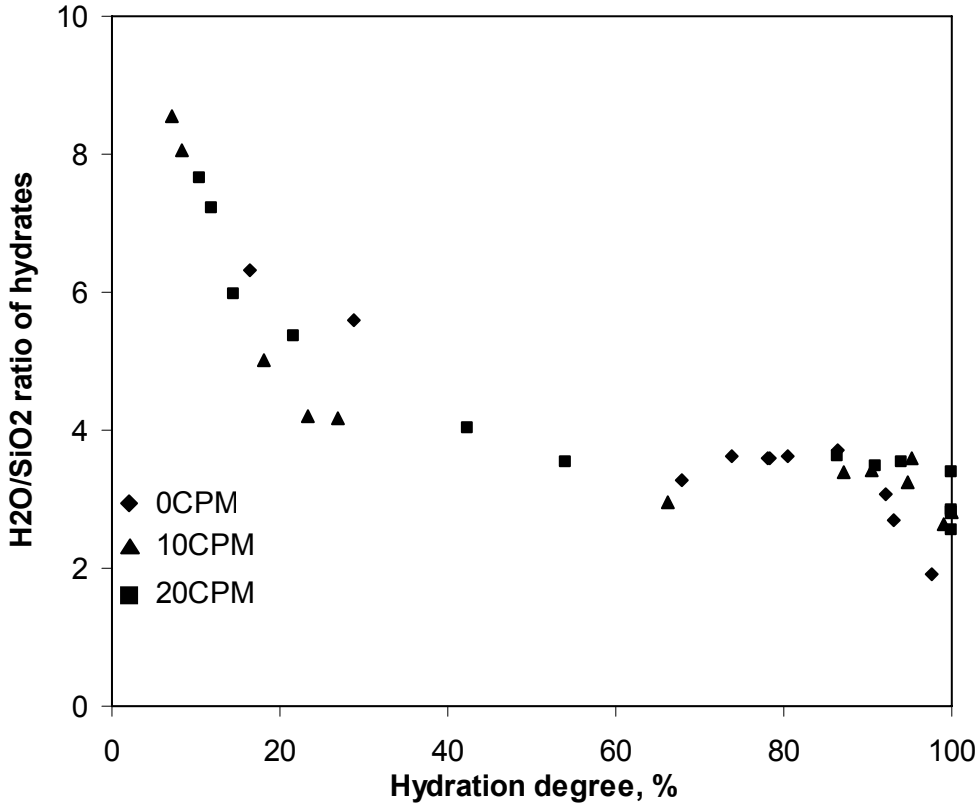

Figure 5.10 H_2O/SiO_2 ratio of C-S-H hydrates plotted against hydration degree of C_3S for 0CPM, 10CPM and 20CPM.

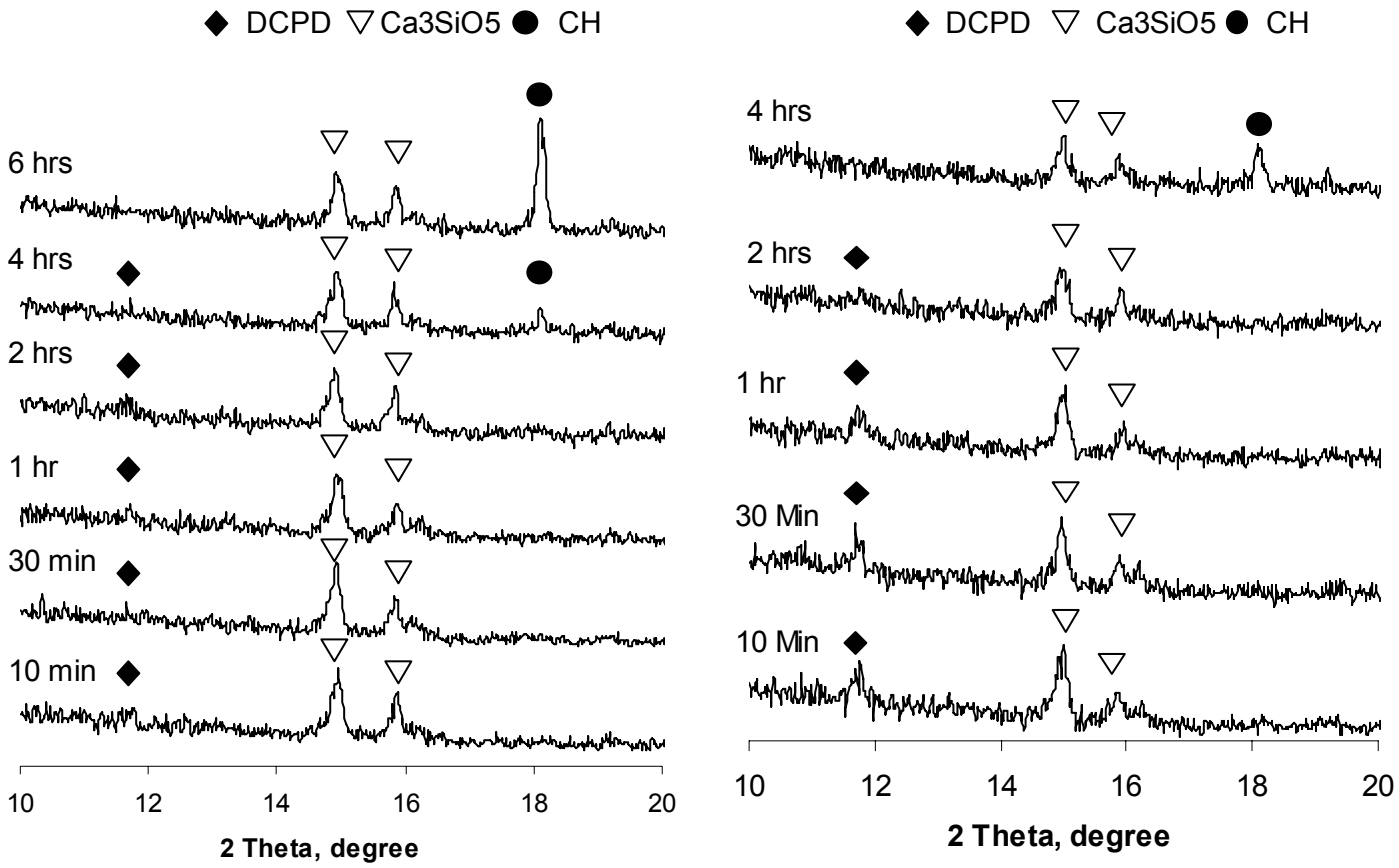

(a) (b)

Figure 5.11 XRD patterns of 10CPM (a) and 20CPM (b) in the early hydration. DCPD occurred in 10CPM up to 4 h and in 20CPM up to 2 h. CH appeared in both 10CPM and 20CPM after hydration for 4 h.

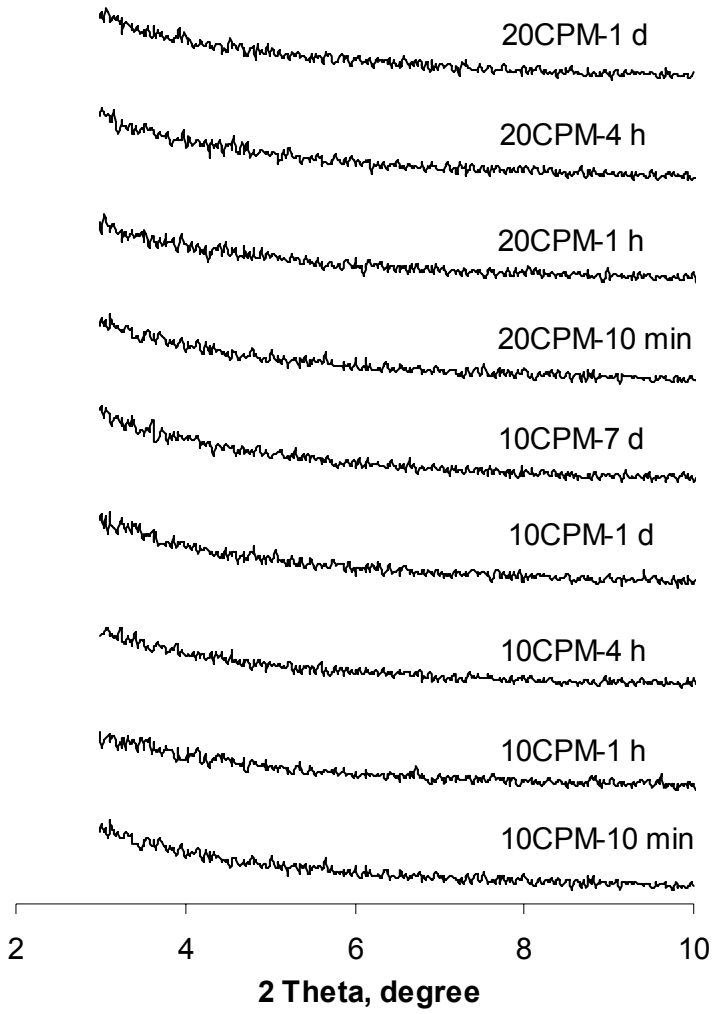

Figure 5.12 XRD patterns of 10CPM and 20CPM for the hydration periods selected randomly in the range of 2 theta of 3 to 10 degree. No peaks showing at 4.7 º (2 theta) indicates that no OCP formed during the hydration of CPSC.

The CaO/SiO_2 ratios of the hydrates from 10CPM and 20CPM showed a similar trend with a rapid increase of the ratio in the first 30% of hydrated C_3S followed by a slight decrease from 30 to 60 % and stabilized thereafter, Figure 5.9. As compared to the pure C_3S, the ratios for 10CPM and 20CPM were higher than that from pure C_3S and the higher the content of CPM, the higher the CaO/SiO_2 ratio. The CaO/SiO_2 ratios were 0.6 – 2.1 at the hydration degree of 10 – 30% and 1.8 – 2.1 at the hydration degree of 30 – 90 % for 10CPM and 1.5 – 2.3 at the hydration degree of 10 – 30% and 2.0 – 2.3 at the hydration degree of 30 – 90 % for 20CPM, respectively.

Although no indication of the formation of C-S-P-H phase could be seen directly in the XRD patterns (Figures 4.7 and 4.8), the different morphologies (discussed in Section 6.2) of the hydrates of 10CPM and 20CPM from those of pure C_3S would infer that the changes in morphology of hydrate products were caused by the presence of CPM, either by the formation of HAP and / or C-S-P-H hydrates. For 10CPM and 20CPM, the hydrates which transformed to wollastonite formed for almost the whole hydration periods. The transformation temperatures of the hydrates of 10CPM for the whole hydration period and of the hydrates of 20CPM for the hydration period longer than 12 h (equivalent to $\geq 86.4 \pm 2.1$ % of the degree of hydration) (Figure 5.7 and Tables 5.7 and 5.8) to the completion of hydration were close to that temperature of the hydrate C-S-H (M) of C_3S i.e. between 857 – 864 ºC. Although the XRD analysis did not show any evidence of the new phase of C-S-P-H, the CaO/SiO_2 ratios for 10CPM and 20CPM were very different (higher than) from those of the C-S-H hydrates from C_3S, e.g. 1.5 to 1.7 for the hydrates of C_3S at the hydration degree of 30 – 90%, and 1.8 – 2.1 and 2.0 – 2.3 for those of 10CPM and 20CPM at the hydration degree of 30 -90%, respectively. The possible explanations are: (1) ACP formed and incorporated into the C-S-H hydrates and decomposed during heating in the DTA-TG experiment because HAP does not decompose up to 1350 ºC [93]; (2) phosphate ions incorporated into the hydrates and C-S-P-H formed, and the XRD reflection of C-S-P-H

were the same as that of C-S-H, i.e. at 2 theta of 29.5, 32.8 and 50.1 degrees. The hydrates of 20CPM at the early hydration (i.e. ≤ 6 h, equivalent to ≤ 54.1 ± 1.8% of the degree of hydration) had the transformation temperatures of 778 – 780 ºC and were about 80 ºC lower than those of C-S-H (M); it could be assumed therefore that the hydrates of 20CPM at the early hydration (≤ 6 h) were C-S-P-H. The above analysis indicates that the addition of CPM in CPSC promoted the formation of C-S-H (M) and the addition of 20 % of CPM would form C-S-P-H in the early hydration (≤ 6 h).

After studying the hydration phases in the system CaO-SiO_2-P_2O_5-H_2O, Hu and Roy [133, 134] showed that both gel and crystalline phases of C-S-P-H existed and were important phases to produce high-strength to chemically bonded ceramics in the system CaO-SiO_2-P_2O_5-H_2O. The C-S-P-H gel was similar to C-S-H gel in terms of morphology and functions to serve as bond between hydrate crystals and to provide strength to cement pastes [133, 134]. Their results showed that the C-S-P-H phase had the atomic ratio of Ca:Si:P near 1:1:0.5 and usually formed in the samples whose compositions were close to the composition of silicocarnotite ($5CaO{\cdot}SiO_2{\cdot}P_2O_5$), with whose composition the chemically bonded ceramics demonstrated highest strength [133, 134]. In the present work the hydrate C-S-P-H was not identified, but the differences of microstructures between 0CPM (C_3S) and 10CPM and 20CPM provided information that CPM affected the microstructure development of C_3S. It would be reasonable to assume that the hydrates for late stage of hydration would incorporate less (or no) phosphate ions, especially after the phosphate ions were consumed by the precipitation of HAP. Further investigation on this topic is needed to better understand the incorporation of phosphate into C-S-H and the formation and structure of C-S-P-H.

The H_2O/SiO_2 ratios for the hydrates of 0CPM, 10CPM, and 20CPM are shown in Figure 5.10. It can be seen that there is no apparent differences in the ratios for the three cements, indicating that the content of CPM does not significantly affect the H_2O/SiO_2 ratio for the hydrates. However, the progress of the hydration process affects the ratio, i.e. at the low degree of hydration (10 – 30%), the H_2O/SiO_2 ratio for both of 10CPM and 20CPM was 2.2 – 5.3 at the and for higher degree of hydration (30 - 90%) the ration was 1.6 – 2.2 (see also Section 3.2.3 for the calculation of the H_2O/SiO_2 ratios). It was assumed that the maximum content of P_2O_5 in the hydrates was the same as in the starting materials. Therefore the hydrates for 10CPM and 20CPM could be written as:

For 10CPM

$(0.6 – 2.1)CaO{\cdot}SiO_2\ xP_2O_5{\cdot}(2.2 – 5.3)H_2O$, in which $0 \leq x \leq 0.11$ for $\alpha = 10 – 30$ %,

$(1.8 – 2.1)CaO{\cdot}SiO_2\ xP_2O_5{\cdot}(1.6 – 2.2)H_2O$, in which $0 \leq x \leq 0.11$ for $\alpha = 30 – 90$ %;

For 20CPM

$(1.5 – 2.3)CaO{\cdot}SiO_2\ yP_2O_5{\cdot}(2.2 – 5.3)H_2O$, in which $0 \leq y \leq 0.24$ for $\alpha = 10 – 30$ %,

$(2.0 – 2.3)CaO{\cdot}SiO_2\ yP_2O_5{\cdot}(1.6 – 2.2)H_2O$, in which $0 \leq y \leq 0.24$ for $\alpha = 30 – 90$ %;

On the basis of the results above, the hydration process of CPSC in water is proposed to involve the following reactions {Reaction (5.3) was taken from Reference [55]}:

$$Ca_3SiO_5 + H_2O\ (excess) \rightarrow 3Ca^{2+}(aq.) + 4OH^-(aq.) + H_2SiO_4^{2-}(aq.) \quad (5.3)$$

$$Ca(H_2PO_4)_2 + excess\ water \rightarrow Ca^{2+}(aq.) + 2H^+(aq.) + 2HPO_4^{2-}(aq.) \quad (5.4)$$

$$Ca^{2+} + HPO_4^{2-} + 2H_2O \rightarrow CaHPO_4{\cdot}2H_2O \quad (5.5)$$

$$Ca_3SiO_5 + H_2O \rightarrow C\text{-}S\text{-}H + Ca(OH)_2 \quad (5.6a)$$

Or $$Ca_3SiO_5 + H_2O + PO_4^{3-} \rightarrow C\text{-}S\text{-}P\text{-}H + Ca(OH)_2 \quad (5.6b)$$

$$6CaHPO_4.2H_2O + 4Ca(OH)_2 \rightarrow Ca_{10}(PO_4)_6\ (OH)_2 + 18H_2O \quad (5.7)$$

$$Ca_3SiO_5 + H_2O \rightarrow \text{C-S-H} + Ca(OH)_2 \quad (5.8)$$

(Note: The reactions (5.6a), (5.6b), and (5.8) cannot be balanced because the C-S-H and C-S-P-H phases are not stoichiometric and have variable compositions; therefore there were no specific formulas available for C-S-H and C-S-P-H.)

5. 4 Summary

Based on the results of quantitative XRD with quartz as an internal standard and DTA-TGA studies of the hydrating CPSC, which was fabricated by the process routine described in Chapter 3, the following observations are made:

1. It is proposed that the following steps were involved in the hydration of CPSC:

i) tricalcium silicate and CPM dissolved into the liquid phase and hydrolyzed;

$$Ca_3SiO_5 + H_2O \text{ (excess)} \rightarrow 3Ca^{2+}(aq.) + 4OH^-(aq.) + H_2SiO_4^{2-}(aq.)$$

$$Ca(H_2PO_4)_2 + \text{excess water} \rightarrow Ca^{2+}(aq.) + 2H^+(aq.) + 2HPO_4^{2-}(aq.)$$

ii) CPM converted to DCPD immediately from such solution;

$$Ca^{2+} + HPO_4^{2-} + 2H_2O \rightarrow CaHPO_4 \cdot 2H_2O$$

iii) C_3S continuously hydrated to produce CH and C-S-H gel, and such C-S-H gel incorporated the phosphate ions available in the solution to result in calcium-silicate-phosphate-hydrate (C-S-P-H) gel.

$$Ca_3SiO_5 + H_2O \rightarrow \text{C-S-H} + Ca(OH)_2$$

$$Ca_3SiO_5 + H_2O + PO_4^{3-} \rightarrow \text{C-S-P-H} + Ca(OH)_2$$

iv) DCPD subsequently reacted with CH produced from the hydration of C_3S to precipitate HAP

$$6CaHPO_4.2H_2O + 4Ca(OH)_2 \rightarrow Ca_{10}(PO_4)_6(OH)_2 + 18H_2O$$

v) Finally C_3S hydrated completely and the above processes ceased. The hydration-stop point for the cements studied in this work was typically about 28 days.

$$Ca_3SiO_5 + H_2O \rightarrow C\text{-}S\text{-}H + Ca(OH)_2$$

2. The final hydration products of CPSC were HAP, CH, and C-S-H / C-S-P-H. The content of each product in the set cement depended on the starting composition of CPSC. The composition of the hydrates C-S-(P-)H also varied with the starting composition of CPSC and the hydration process. Based on the experimental data in this work, the compositions of the hydrates C-S-(P-)H were estimated to be as follows:

For 10CPM

$(0.6 – 2.1)CaO{\cdot}SiO_2\ xP_2O_5{\cdot}(2.2 – 5.3)H_2O$, in which $0 \leq x \leq 0.11$ for $\alpha = 10 – 30$ %,

$(1.8 – 2.1)CaO{\cdot}SiO_2\ xP_2O_5{\cdot}(1.6 – 2.2)H_2O$, in which $0 \leq x \leq 0.11$ for $\alpha = 30 – 90$ %;

For 20CPM

$(1.5 – 2.3)CaO{\cdot}SiO_2\ yP_2O_5{\cdot}(2.2 – 5.3)H_2O$, in which $0 \leq y \leq 0.24$ for $\alpha = 10 – 30$ %,

$(2.0 – 2.3)CaO{\cdot}SiO_2\ yP_2O_5{\cdot}(1.6 – 2.2)H_2O$, in which $0 \leq y \leq 0.24$ for $\alpha = 30 – 90$ %;

The composition of the hydrates C-S-H for pure C_3S was estimated to be

$(1.3 – 1.5)CaO{\cdot}SiO_2{\cdot}(2.2 – 5.3)H_2O$ for $\alpha = 10 – 30$ %

$(1.5 – 1.7)CaO{\cdot}SiO_2{\cdot}(1.6 – 2.2)H_2O$ for $\alpha = 30 – 90$ %.

3. CPM influenced the kinetics of the hydration of C_3S. The hydration rate of such CPSC was reduced in comparison with that of pure C_3S. However, the duration of the hydration acceleration period increased for CPSC in comparison with that of pure C_3S. It has been determined that in the acceleration stage, the kinetics of CPSC hydration is phase boundary controlled with deceleration of the nucleation rates and follows the Avrami equation, which is

$-\ln(1 - \alpha) = k_r t^q$. For the deceleration stage, the kinetics is diffusion-controlled and follows the Jander equation, $[1 - (1 - \alpha)^{1/3}]^2 = k_d t$. At a higher amount of CPM (20 wt%) in CPSC, the hydration degree of C_3S in CPSC was higher than that in pure C_3S cement; but at a smaller amounts of CPM (5 and 10 wt%) in CPSC, the hydration degree of C_3S in CPSC was similar to that in pure C_3S cement. It was noted that this result does not agree with the traditional concept that phosphate is a retarder of the hydration of C_3S.

4. It is proposed that the calcium silicate phosphate hydrate (C-S-P-H) is one type of the hydrates resulting in set CPSC although its detailed composition is not clear at present. It appears, however, that the C-S-P-H provided strength to set cements, similarly as C-S-H.

6. EXPERIMENTAL RESULTS AND DISCUSSION 3: MICROSTRUCTURES AND MECHANICAL PROPERITES OF CPSC

6.1 Introduction

This chapter describes the microstructural evolution of 0CPM, 10CPM and 20CPM with hydration time, and also describes the results of apparent porosity and the compressive and flexural strengths measurements for CPSC for different curing times. The effects of CPM in CPSC on the strengths are also discussed.

Of the three components of the hardened cement, i.e. hydrated material, non-hydrated residual cement and pores, the first constituent is mainly responsible for the attained strength [53]. Since the hydration products of hardened CPSC pastes are the phases of C-S-(P-)H, HAP, and CH, the properties of hardened CPSC paste depend on the individual phases present and also of the overall assembly of phases, i.e the texture of the phases. The term “texture” includes the size and form of individual phase as well as the way they are packed together and the nature of the porosity (shape and volume-size distribution). The hydration products, such as C-S-(P-)H and HAP, especially which grow within the capillary pore space, are critical for the cement integrity; and they form the continuous phase and bind the cement together and provide the strength for the hardened cements. Therefore it is important to understand the microstructure evolution of the cements with the hydration process.

6.2 Microstructures

Microstructure evolution of 0CPM, 10CPM and 20CPM pastes with time was recorded using SEM following the hydration process at 37 ºC. Figures 6.1 – 6.8 contain micrographs of set 0CPM, 10CPM and 20CPM pastes.

After 1 h hydration of 0CPM paste, the hydrates appeared on the surfaces of the original C_3S grains [Figure 6.1(a)]. The hydrates were round button-shaped and lay on the C_3S surfaces or embedded in the particles. The size of the hydrates was about 0.2 to 0.6 μm. On smaller C_3S particles the hydrate particles were much closer to each other than on larger C_3S particles, indicating that there were more nucleation sites on the surfaces of smaller particles than on those of larger C_3S particles.

For 10CPM paste [Figure 6.1 (b)], the hydration products were narrow oval-shaped and their size was about 0.4 to 1 μm in length and 0.1 to 0.4 μm in width and about two to four times bigger than the hydrates from 0CPM. The narrow oval-shaped hydrates were either individual or grew together. The number of the hydrate particles per unit area of cement particle was much smaller than that from 0CPM paste. For 20CPM paste [Figure 6.1 (c)], the hydration products had a similar shape to those from 10CPM, but their surfaces were not as smooth as those from 10CPM. The clusters of hydrates seemed to consist of smaller particles which were near the limit of SEM resolution. The size of the clusters was about 0.2 to 0.6 μm in length and about 0.2 μm in width and smaller than the hydrates from 10CPM.

The number of the hydrate particles for 20CPM was greater than that for 10CPM, indicating that 20CPM had a faster nucleation rate than 10CPM. Almost all the hydrates from 10CPM and 20CPM were lying on the original C_3S grains. The irregularly distribution of the hydrates suggested that the hydrates from 10CPM and 20CPM had favourite sites to nucleate. It was obvious that the smaller particles of C_3S grains had more favourite sites than bigger ones [Figure 6.1 (b) & (c)].

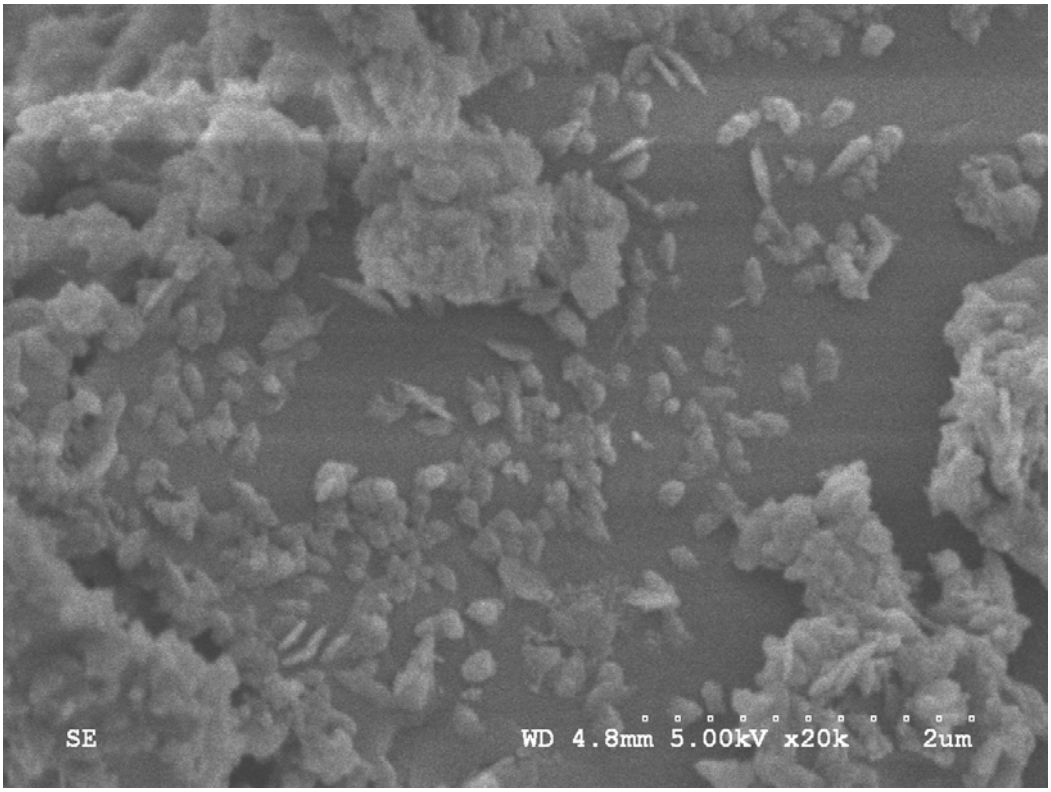

(a)

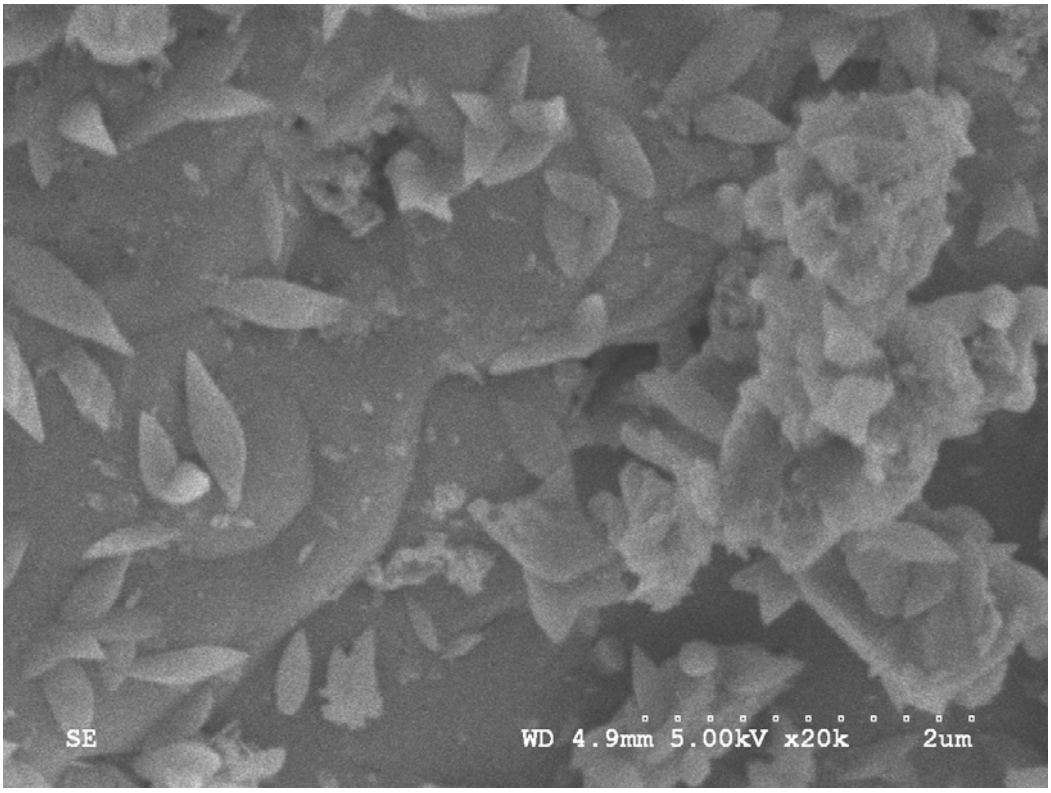

(b)

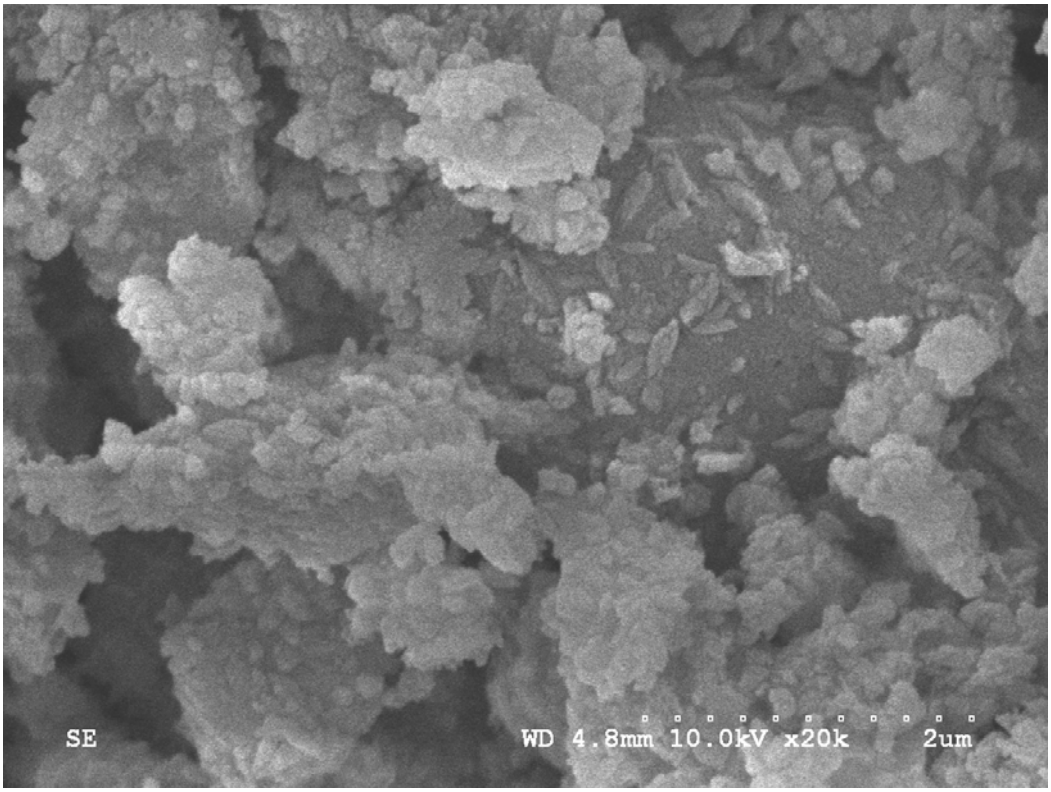

(c)

Figure 6.1 SEM micrographs of the fracture surfaces of 0CPM (a), 10CPM (b), and 20CPM (c) pastes hydrated at 37 ºC for 1 h.

After 2 h hydration, the hydrate particles of 0CPM continued growing on the surfaces of the original cement particles and also the number of the hydrates increased [Figure 6.2 (a)]. All the hydrates were acicular shape (type I hydrate C-S-H [81]) radiating from particles and uniformly distributed on the surfaces of anhydrous C_3S grains. The size of hydrates remained almost the same, i.e. 0.2 to 0.6 μm long and not more than 0.1 μm thick, and the round button-shaped hydrates disappeared. During this period of hydration, the number of hydrates increased conspicuously but it seemed that the size of the hydrates was almost not changed. The edges of anhydrous C_3S grains were still the favourite sites for the hydrates to nucleate as observed in Figure 6.2 (a).

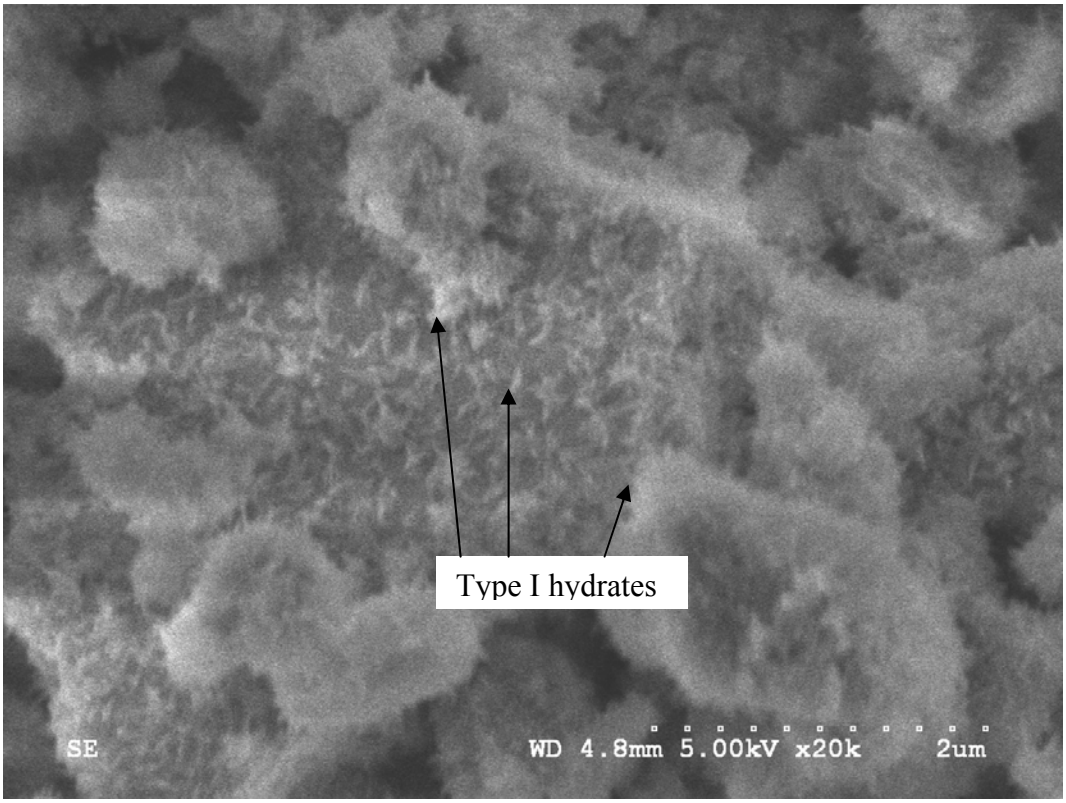
Type I hydrates
SE
WD 4.8mm 5.00kV x20k
2um

(a)

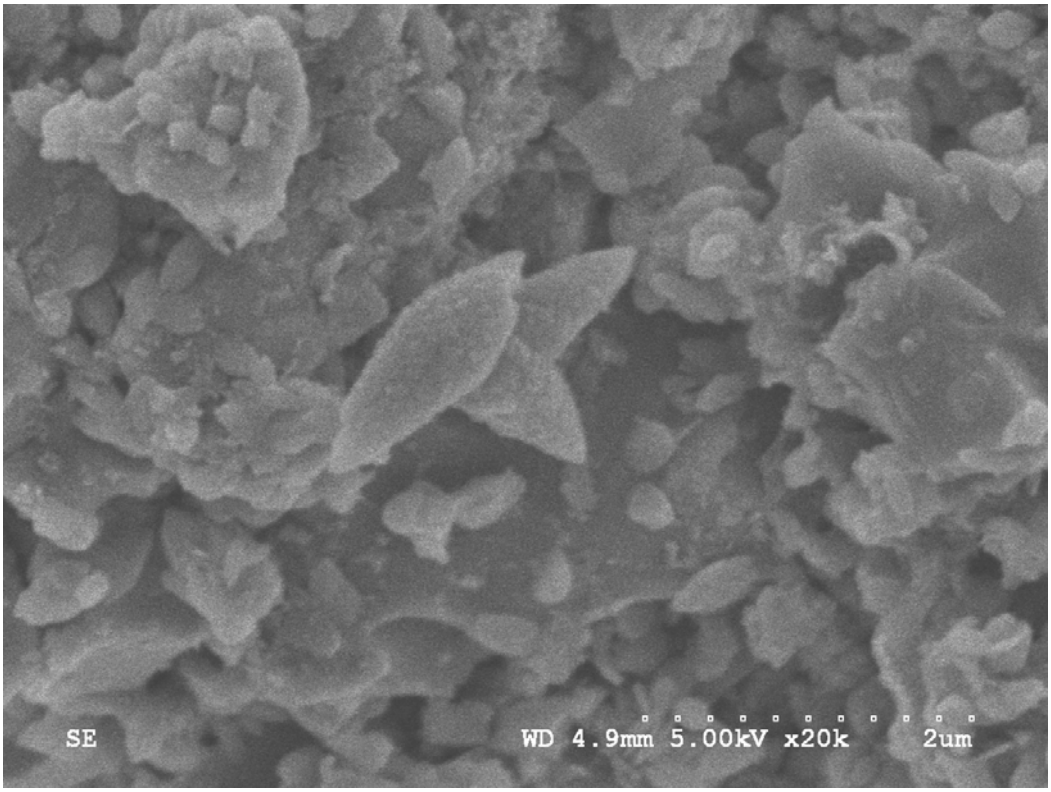
SE
WD 4.9mm 5.00kV x20k
2um

(b)

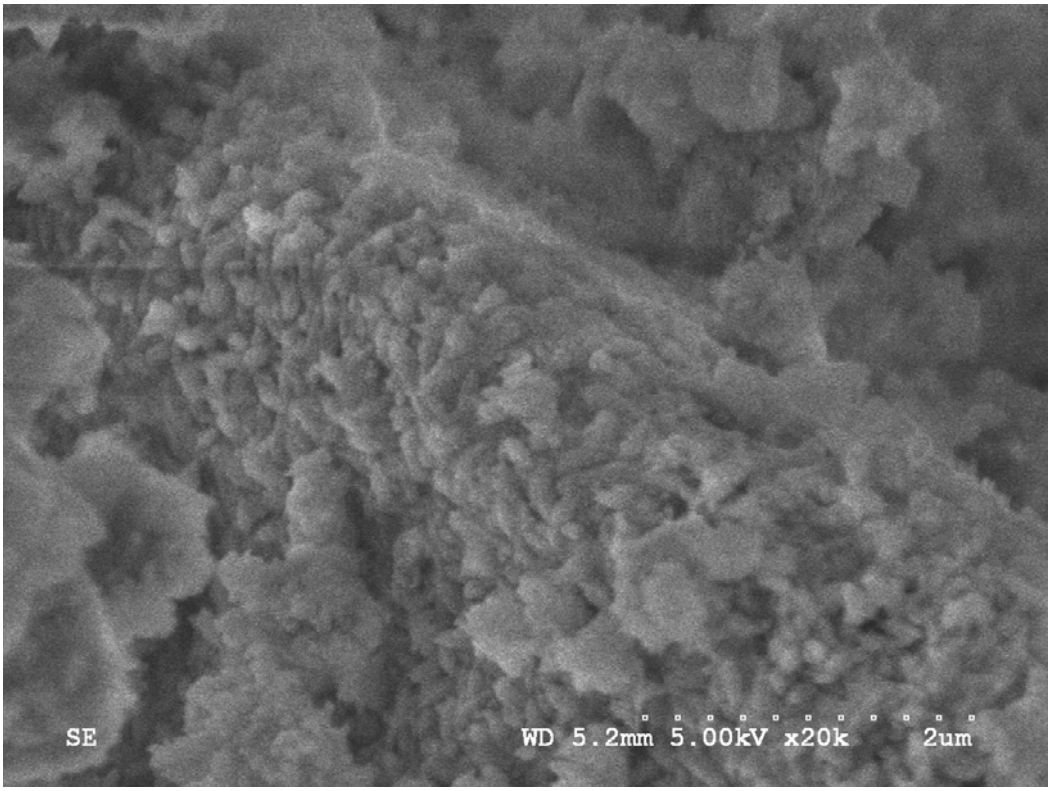

(c)

Figure 6.2 SEM micrographs of the fracture surfaces of 0CPM (a), 10CPM (b), and 20CPM (c) pastes hydrated for 2 h at 37 ºC.

10CPM had a different scenario: the hydrates of 10CPM grew bigger and the size of some hydrates reached about 2 μm long and 0.6 μm wide, but the number of the hydrate clusters did not increase noticeably [Figure 6.2 (b)], and this might be caused by the exhaustion of the favourite sites for nucleation. The hydrates of 20CPM were substantially increased in number and some of the original anhydrous C_3S particles were covered by hydrates, the size of which did not change markedly [Figure 6.2(c)] and remained 0.2 to 0.6 μm long and 0.1 to 0.2 μm wide with almond-like shapes. The HAP phase produced from the hydration of 20CPM would be the favourite sites for the hydrates C-S-(P)-H to nucleate.

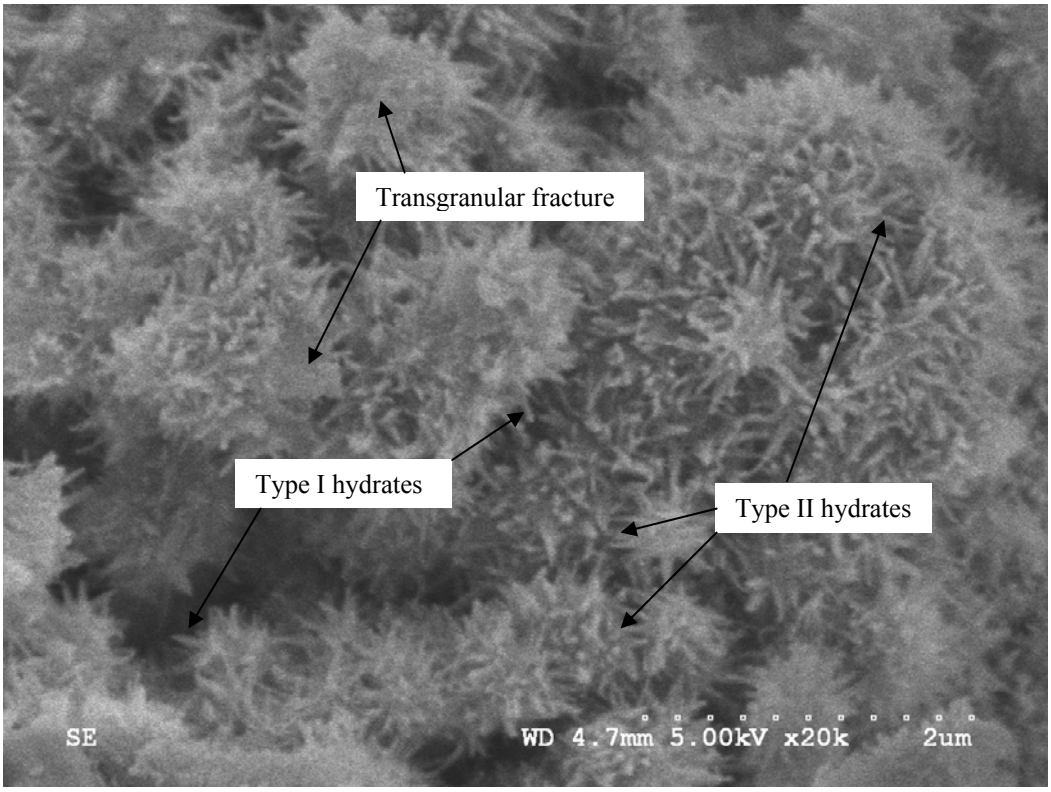
Transgranular fracture
Type I hydrates
Type II hydrates
SE
WD 4.7mm 5.00kV x20k
2um

(a)

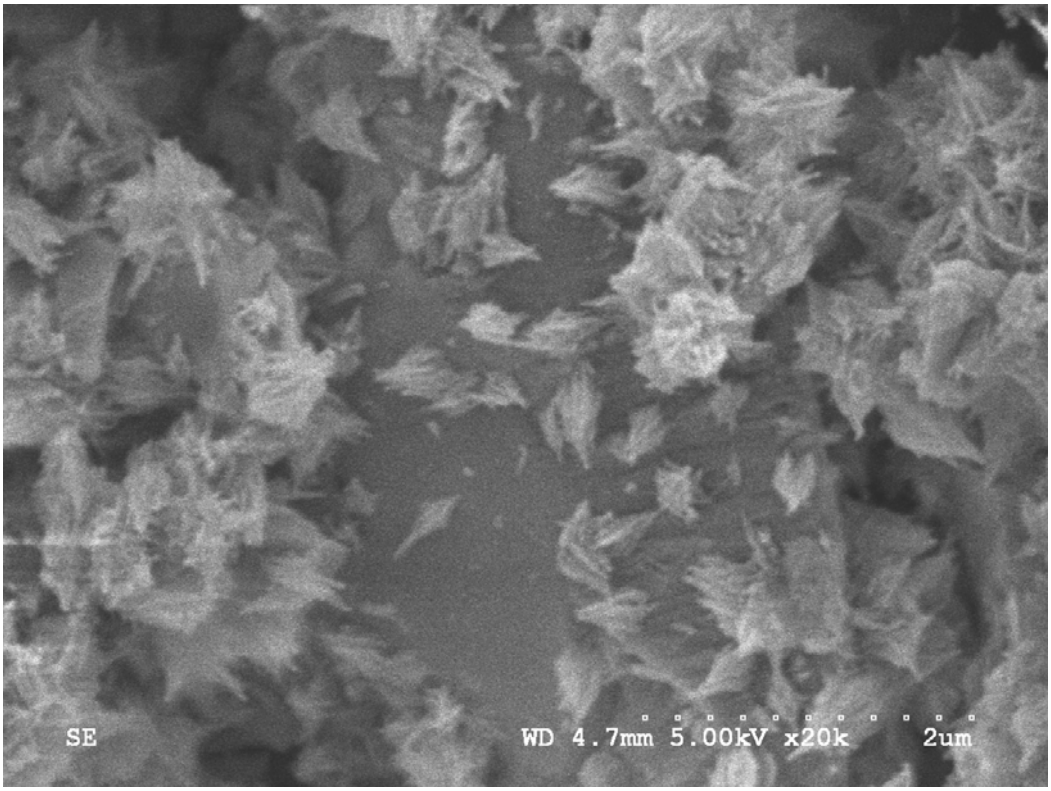
SE
WD 4.7mm 5.00kV x20k
2um

(b)

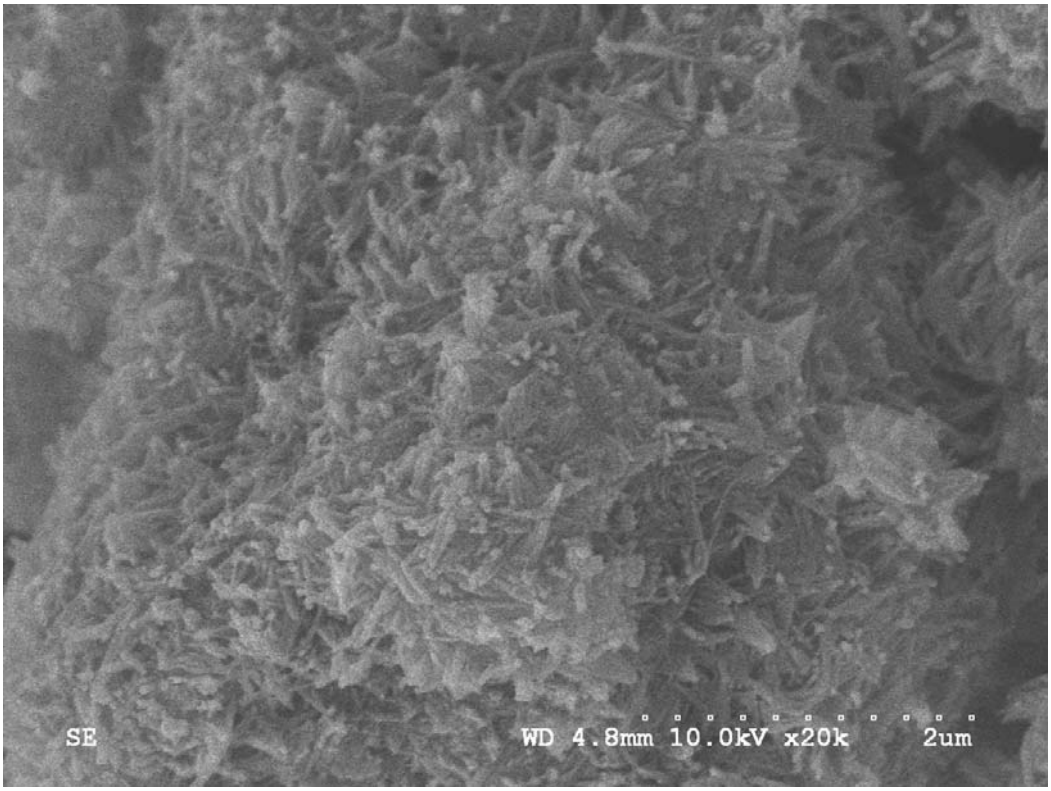

(c)

Figure 6.3 SEM micrographs of the fracture surfaces of 0CPM (a), 10CPM (b), and 20CPM (c) pastes hydrated for 4 h at 37 ºC.

After 4 h hydration, the number of the hydration product particles (type I) from 0CPM increased evidently and the fibrous hydrates covered whole C_3S grains [Figure 6.3 (a)]. The fibres from neighbouring particles touched each other and some entangled and interlocked together to form type II hydrate (reticular network) [81]. The sizes of the fibrous hydrate particles increased and most of the fibres were about 0.6 to 1 μm long. Figure 6.3 (a) showed that some hydrate particles fractured transgranularly, indicating that strong interconnection of the fibrous hydrates formed between some of hydrating particles.

The morphology of 10CPM paste after 4 h of hydration was different from that of 0CPM [Figure 6.3 (b)]. The hydration products were not uniformly distributed, but they continued growing on the isolated hydrates, instead of the whole surfaces of C_3S grains. This provided further information that the hydrates C-S-(P-)H from 10CPM had favourite nucleation sites, which would be the calcium phosphate phases, i.e. DCPD and/ or HAP. The fibrous hydrates bundled together along radial direction and formed clusters of the sizes of 1 – 2 μm long and about 1 μm thick. The clusters "radiated" from the surfaces of anhydrous particles at angles, rather than erectly radiating from the surfaces as the hydrates in pure C_3S. The hydrates with the shape of narrow oval shown in the 2 h hydration disappeared and it seemed that the newly-formed fibrous hydrates grew on the previous ones and wrap around them.

Figure 6.3 (c) gives a SEM micrograph of 20CPM. After 4 h of hydration, the morphology of the hydration products of 20CPM was different from that after 2 h hydration. The hydrates had changed from small (0.2 to 0.6 μm long and 0.1 to 0.2 μm wide) almond-like shapes to bundles of cigar-shaped tubes (about 1.0 μm long and 0.2 μm wide). Each bundles consisted of more than two "cigars" each about 0.1 μm thick and more than 0.6 μm long. This morphology was similar to that of type E hydrates from the C_3S hydration described in a previous study [69], but the difference was that these tubes were bundled together in radial directions and piled on the surfaces of anhydrous particles rather than radiating from these particles and some of the long tubes were bent over and still lay on the surfaces. The hydrates covered the whole unhydrated particles, which could not be observed from the fracture surface [Figure 6.3(c)]. The hydrates of the cigar-shaped tubes did not seem to form a network in 20CPM as the hydrates did in 0CPM. On the fracture surface of 20CPM, it was shown that the separation of the bundled cigar-shaped tubes took place when 20CPM fractured. This less cohesive morphology of 20CPM cement is supported by their lower compressive and bending strength (discussed later in this chapter).

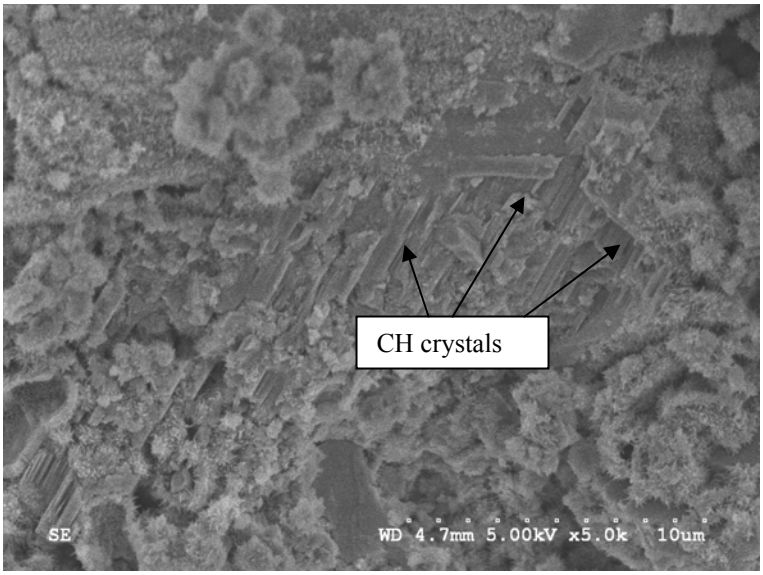

Figure 6.4 SEM micrograph of 0CPM showing that CH crystals appeared after hydration at 37 ºC for 4 h. Arrow shows CH crystals.

Another feature for 0CPM paste was that CH crystals appeared and meshed together with the original cement grains and C-S-H (Figure 6.4). However, no CH crystals could be observed in 10CPM and 20CPM pastes at this stage of hydration.

The differences in the morphology of the hydrates and their arrangement affected the cement strength (also see Section 6.4). For 0CPM, the hydrates were individual fibres and radiated from the anhydrous grains. The hydrates grew and entangled and a network formed with the hydration process. In contrast, 10CPM had the bundled hydrates, which grew and entangled although the hydrates deposit at angles with the surfaces of anhydrous grains; and moreover the network with these hydrates would be stronger than that with the individual fibres. However, for 20CPM, because the bundled hydrates piled on the grain surfaces, the hydrates might grew together with the hydration process, but they would not form a network as in 0CPM and 10CPM. The smooth and layered structure of the fracture surfaces of 20CPM in Figures 6.5 (c) & (c-1) and 6.6 (c) & (c-1) give evidence for the discussion above.

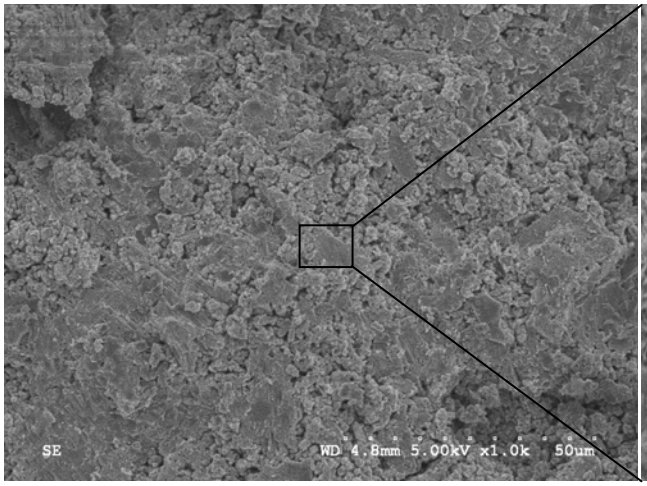

(a)

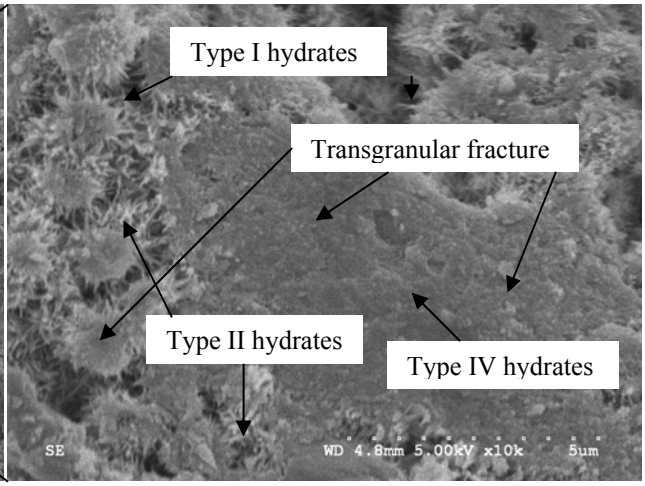

(a-1)

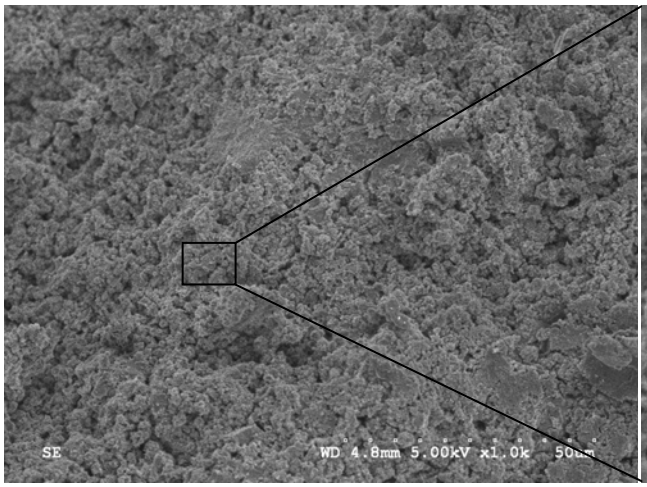

(b)

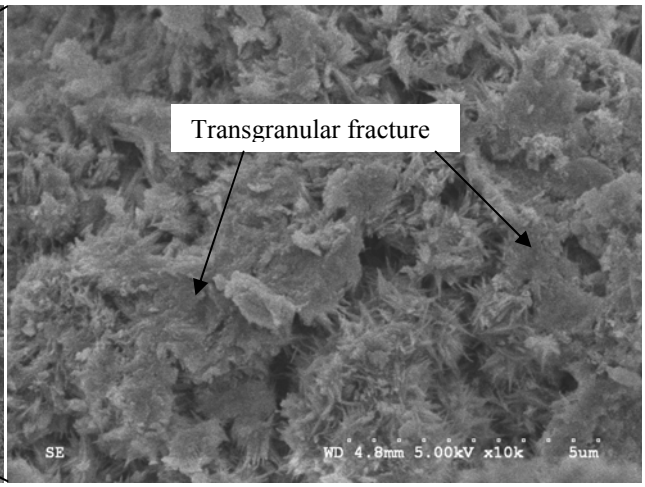

(b-1)

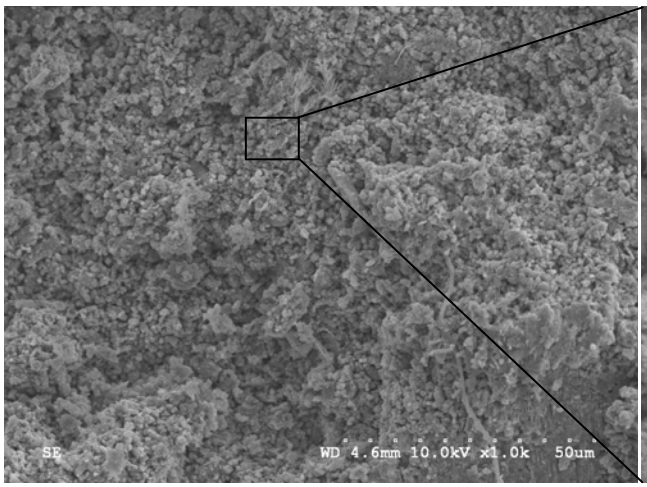

(c)

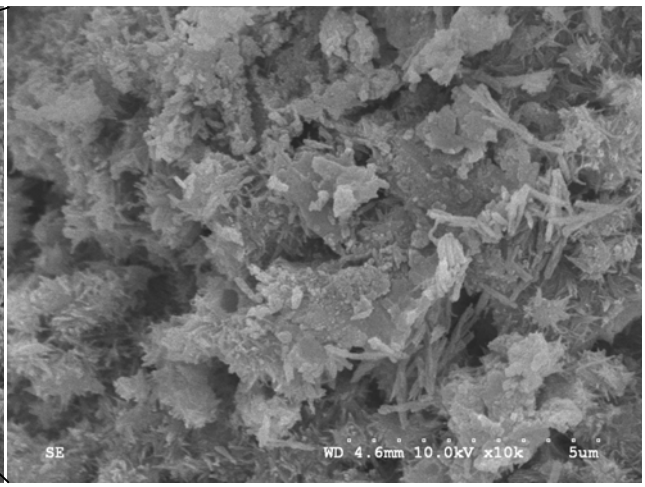

(c-1)

Figure 6.5 – SEM micrographs of the fracture surfaces of 0CPM (a) & (a-1), 10CPM (b) & (b-1), and 20CPM (c) & (c-1) pastes hydrated for 24 h at 37 ºC.

After 1 d hydration, the morphologies of the three cement pastes showed some changes in comparison with those for the first 4 h of hydration. 0CPM paste developed more networks of the hydrate fibres (type II hydrate) between neighbouring particles, leading to transgranular fracture through the hydrates. The hydrate agglomerates (type IV hydrate) appeared in the microstructure. CH crystals and C-S-H hydrates were comprised of the monolithic matrix of the paste and the anhydrous C_3S grains were hardly seen on the fracture surface [Figure 6.5 (a) & (a-1)], at the stage the QXRD results showed that about 80% of C_3S had hydrated [Figure 5.2(a)].

For 10CPM, the hydration products developed well and covered over all the original cement grains during the first day of hydration. The fibrous hydrates formed bundles and interlocked with each other between neighbouring particles; this led to transgranular fracture in most particles. CH crystals appeared in the microstructure and formed a compact structure with hydrates. The original cement grains hydrated about 90% [Figure 5.2 (a)] and were not easily noticed on the fracture surfaces [Figure 6.5 (b) & (b-1)].

For 20CPM hydrated after one day, the hydration products covered all the cement grains and entangled with each other, but the micrographs showed that 20CPM had a lower degree of transgranular fracture than 0CPM and 10CPM [Figure 6.5 (c) & (c-1)]. The broken surfaces were relatively smooth and demonstrated some layered structure, hinting of a weaker connection (not a strong network) between the hydrates. Like 0CPM and 10CPM, 20CPM did not show any unhydrated cement grains on the fracture surfaces. Figure 6.5 (c-1) showed that some single cigar-shaped hydrates formed, for which the molar ratios of elements were Ca/Si = 3.53 and Ca/P = 5.27 (Ca: Si: P = 67.9 : 19.2 : 12.9).

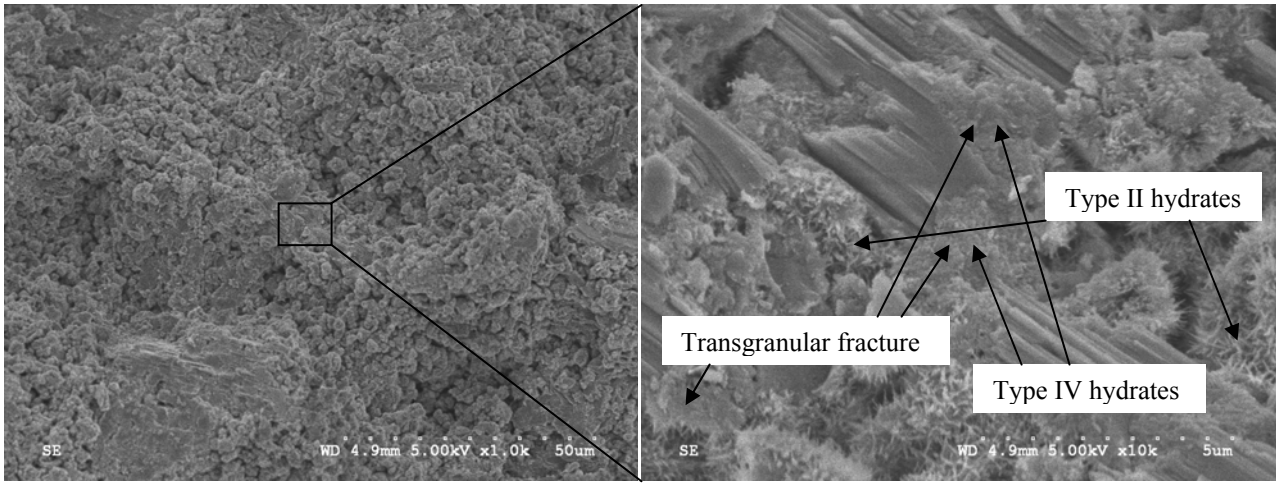

(a) (a-1)

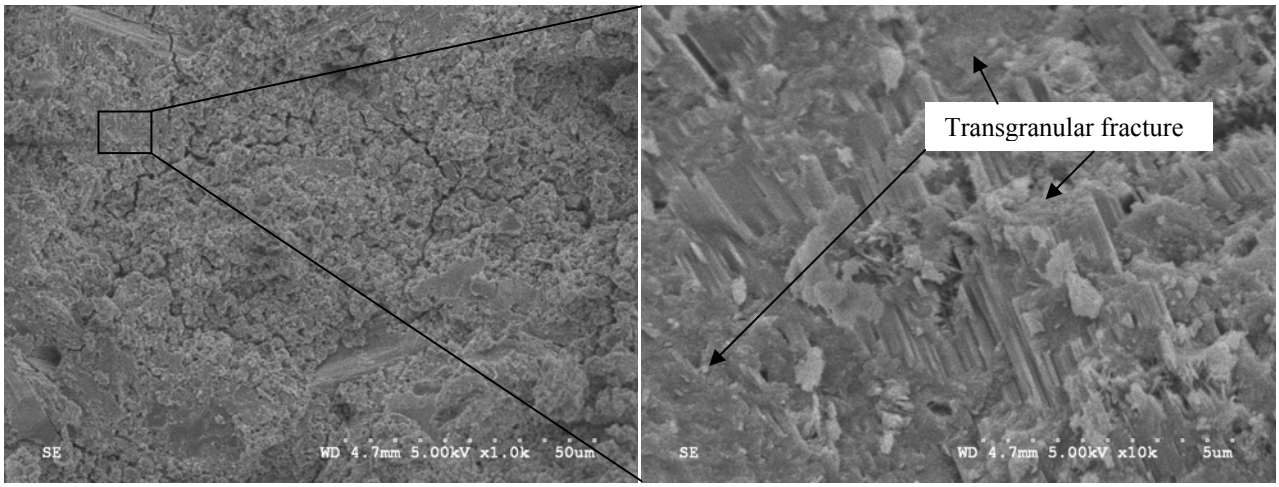

(b) (b-1)

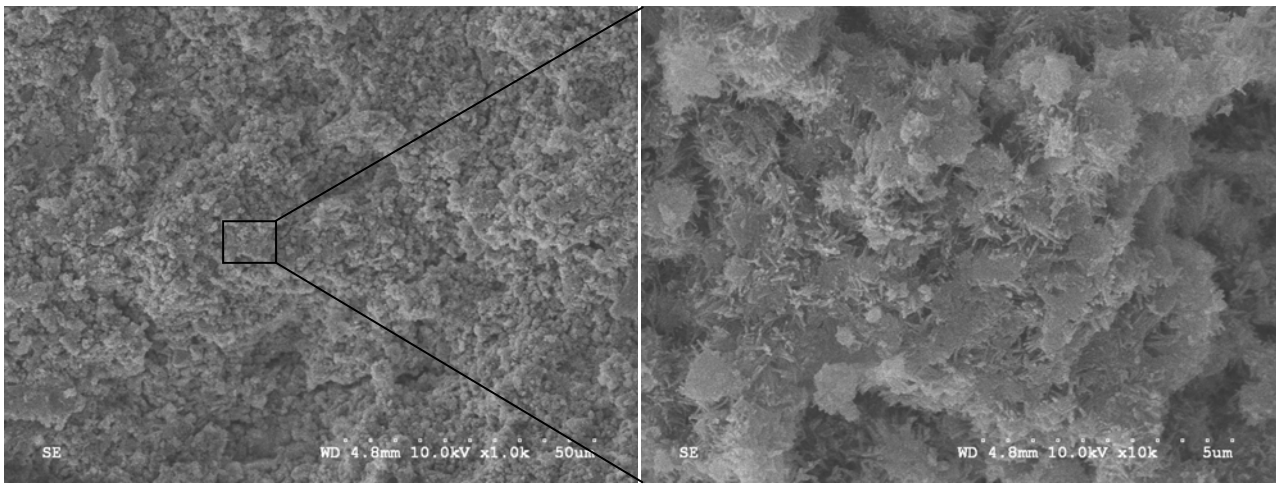

(c) (c-1)

Figure 6.6 – SEM micrographs of the fracture surfaces of 0CPM (a) & (a-1), 10CPM (b) & (b-1), and 20CPM (c) & (c-1) pastes hydrated for 4 d at 37 ºC.

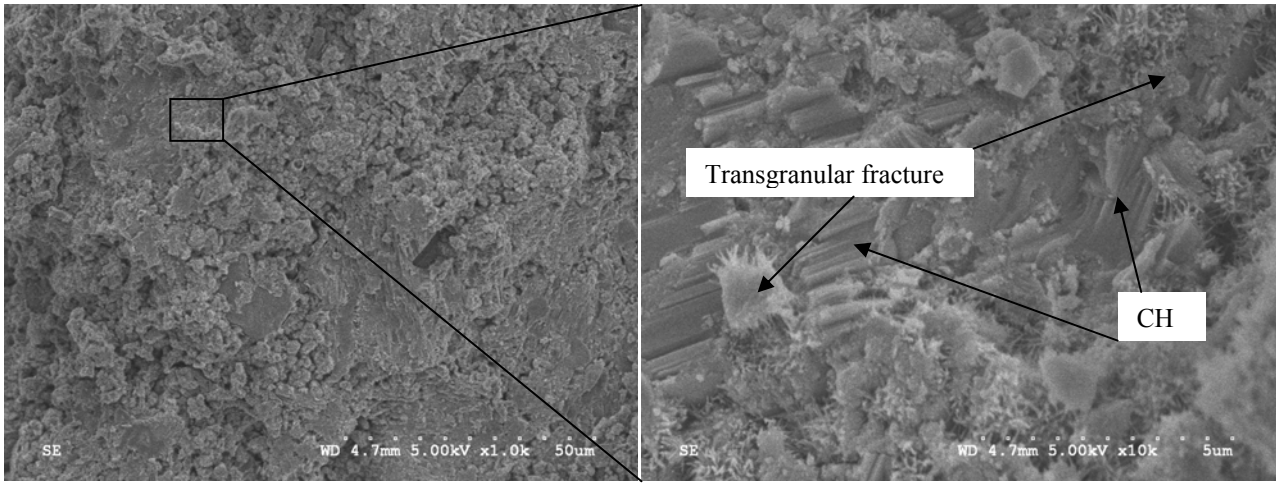

(a) (a-1)

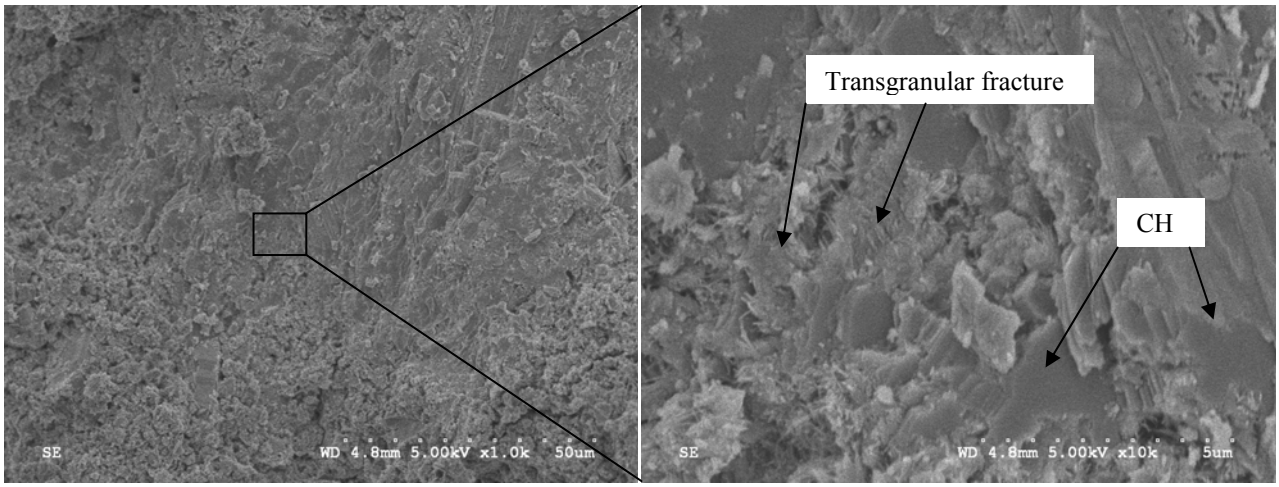

(b) (b-1)

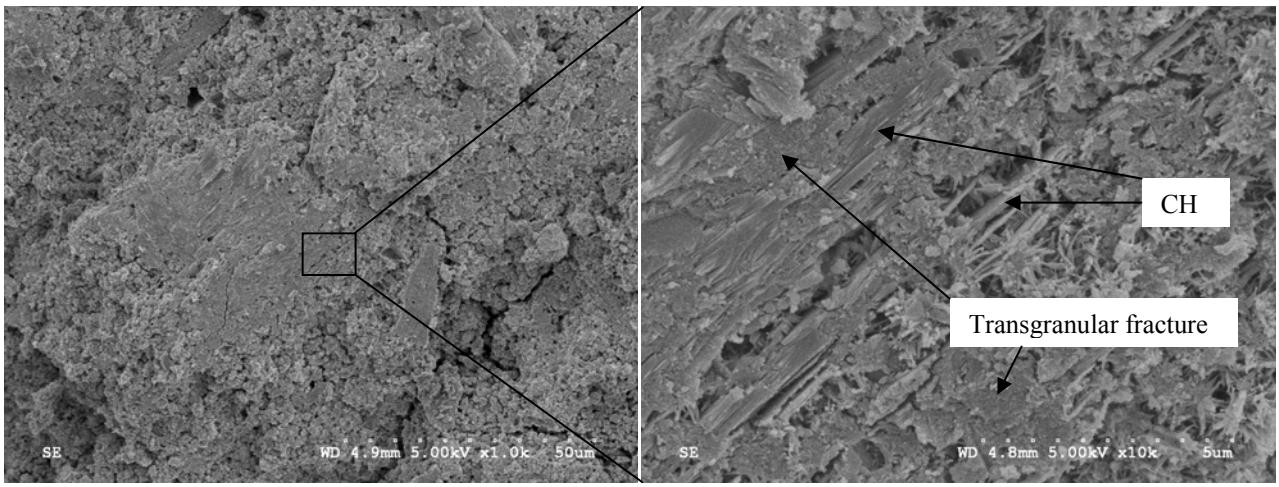

(c) (c-1)

Figure 6.7 – SEM micrographs of the fracture surfaces of 0CPM (a) & (a-1), 10CPM (b) & (b-1), and 20CPM (c) & (c-1) pastes hydrated for 7 d at 37 ºC.

After hydration for 4 d and 7 d, the microstructure of 0CPM, 10CPM and 20CPM pastes consisted of the hydrates and CH (Figures 6.6 and 6.7). The observation from the fracture surfaces showed that 0CPM and 10CPM pastes became less porous (more packed) than those for the shorter hydration times, but 20CPM paste did not change much and was more porous in comparison with 0CPM and 10CPM. For all three cements, the fractures took place transgranularly, but it seemed that 20CPM after 4 d of hydration broke at connecting areas between the hydrates of the neighbouring particles. In the fracture surfaces of all three cements, reticular networks (type II) and dense gel (type IV) hydrates co-existed with CH. The hydrates and CH connected well, except for 20CPM, in which some pores existed in between. The discussion above suggested that 20CPM might have lower strength than 0CPM and 20CPM. In all the cements, no anhydrous cement grains were observed on the fracture surfaces.

After 28 d of hydration, CH crystals grew and engulfed the hydrate particles, and the hydrates and CH crystals tightly connected. In this case, the fracture went through hydration products, the hydrates and CH. All the different morphological types of hydrates, including fibrous hydrates, reticular networks, irregular hydrate grains, and dense gel hydrates, were present in all the cements. However, the different morphologies of the hydrates and their different organization in the different cements could still be easily noticed. 0CPM paste had tapered C-S-H hydrates, which grew and entangled together to form reticular network and further grew to form dense gel. 20CPM paste had "cigar-shaped" hydrates, which piled on one another and preferred to bundle together in the radial direction of the “cigars”, and formed dense gel with the hydration process. The microstructure of 20CPM paste was more porous than 0CPM. For 10CPM, the morphology of the hydrates and their organization were between those of 0CPM and 20CPM. The hydrates were less tapered than those of 0CPM and bundled together in the radial direction of hydrates and grew in length direction.

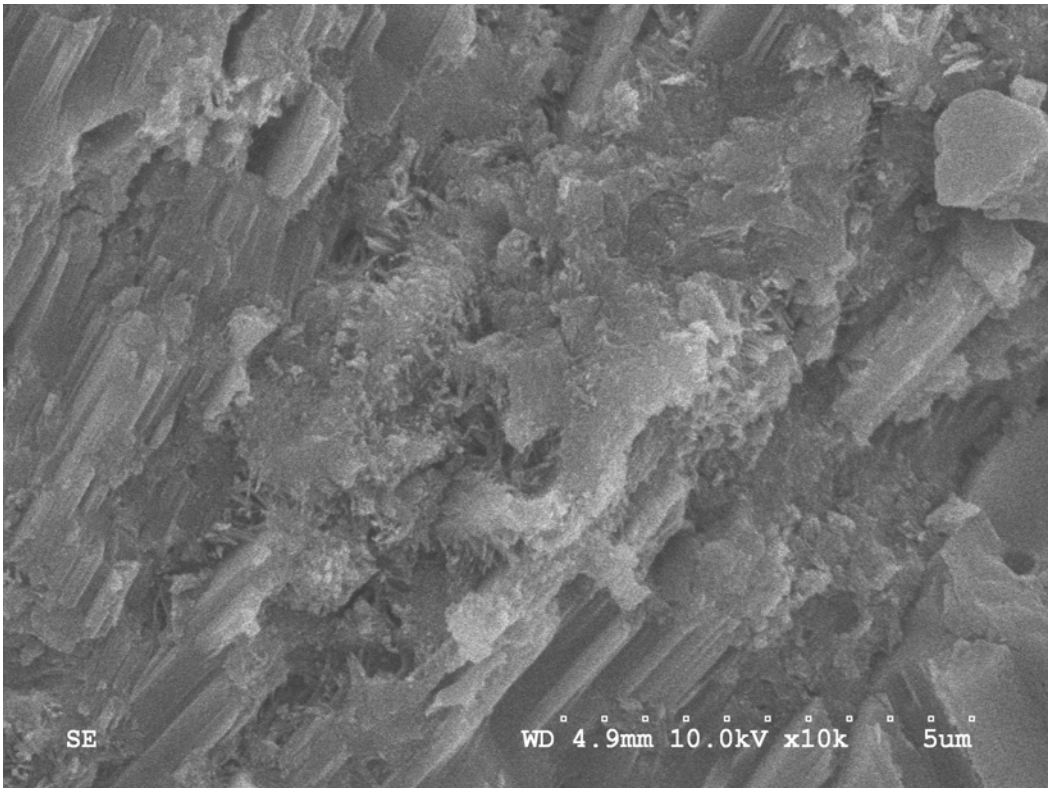

(a)

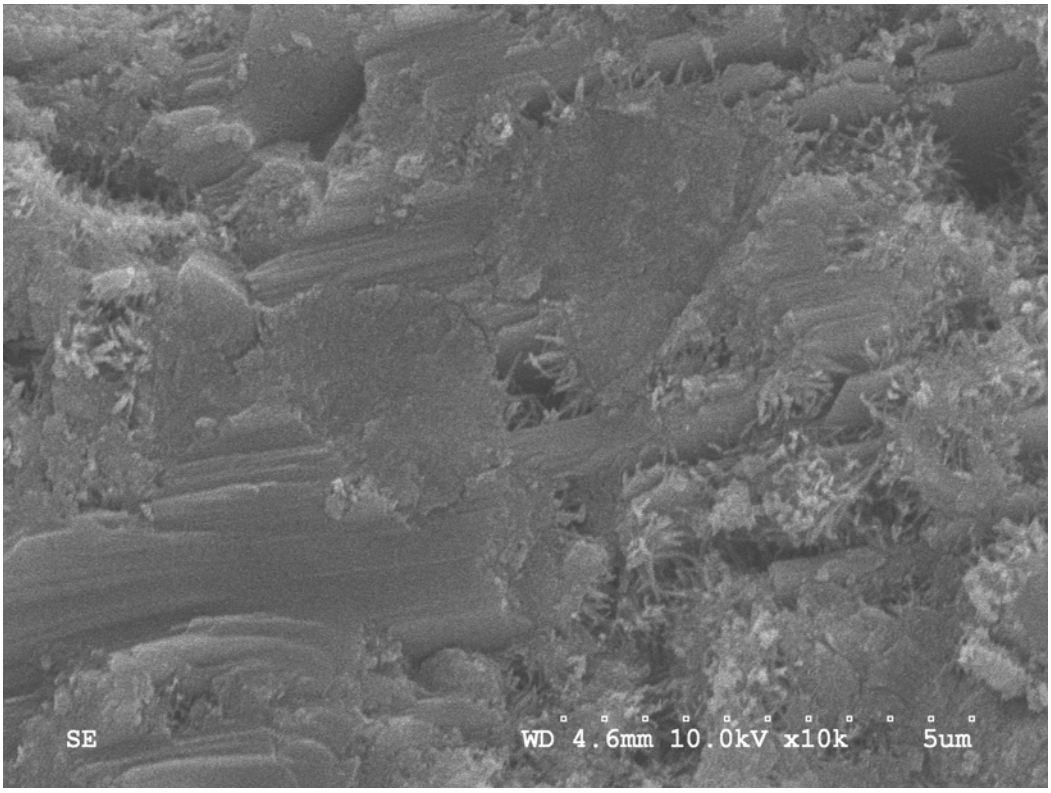

(b)

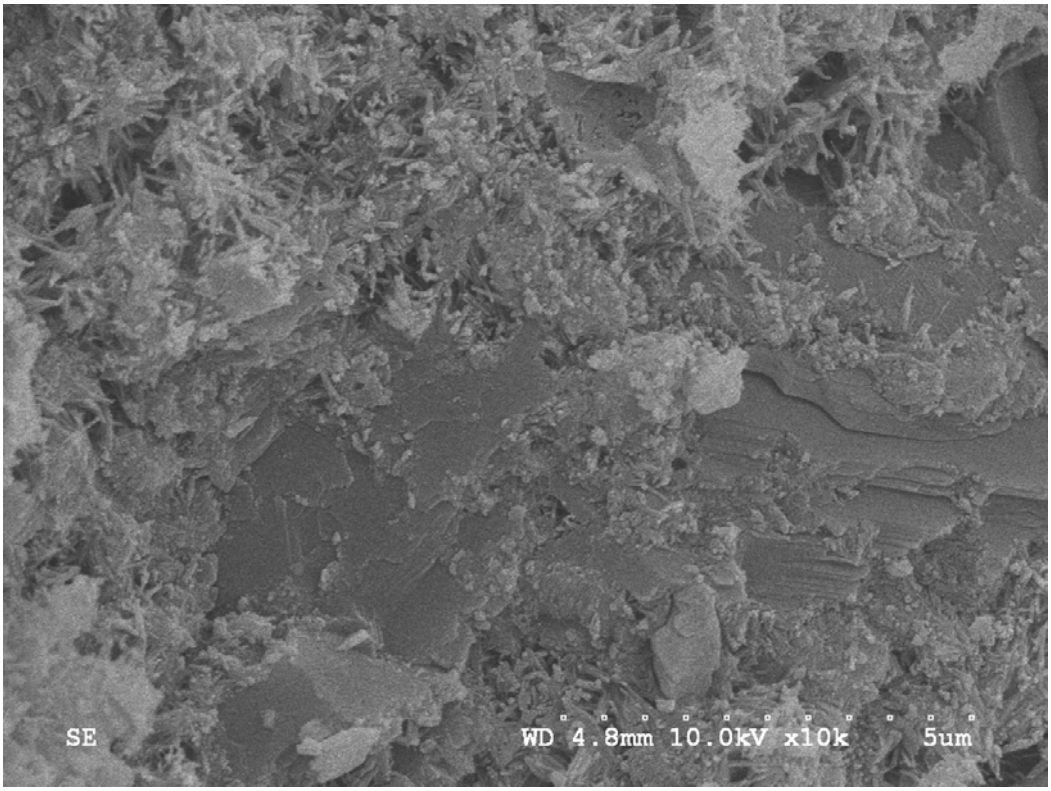

(c)

Figure 6.8- SEM micrographs of the fracture surfaces of 0CPM (a), 10CPM (b), and 20CPM (c) pastes hydrated for 28 d at 37 ºC.

6.3 Apparent Porosity

The fractured specimens used to measure the mechanical properties were collected to determine the apparent porosities of all the cements for different curing times. Table 6.1 lists the apparent porosities for different CPSC and different curing periods.

Table 6.1 The apparent porosities of CPSC cements cured in 37 ºC distilled water for different times, vol%

	0CPM	5CPM	10CPM	15CPM	20CPM	25CPM
4 d	22.9 ± 2.6	28.3 ± 1.2	22.6 ± 0.9	30.8 ± 0.4	35.2 ± 1.3	37.7 ± 3.4
7 d	22.7 ± 1.5	23.8 ± 2.7	24.3 ± 1.3	28.3 ± 0.8	35.0 ± 3.8	39.9 ± 2.1
14 d	23.1 ± 1.1	23.5 ± 1.0	24.5 ± 0.4	29.3 ± 1.1	33.3 ± 1.9	34.3 ± 1.9
28 d	26.1 ± 1.6	29.0 ± 4.2	27.7 ± 1.7	29.5 ± 3.2	33.4 ± 2.3	36.0 ± 0.5

*The data is in the form of average of three measurements ± standard deviation.

From Table 6.1, it is clearly seen that the apparent porosities of the cements increased with the amount of CPM in CPSC. For small amount of CPM in CPSC, such as 5CPM and 10CPM, its porosity was not increased significantly but when the amount of CPM was more than 15 wt% in CPSC, the porosity increased considerably. For example, after hydration for 7 d, the porosity of 0CPM was 22.7 ± 1.5 %, and the porosities of 5CPM and 10CPM were 23.8 ± 2.7 % and 24.3 ± 1.3 %, respectively, but the porosities of 15CPM, 20CPM, and 25CPM were 28.3 ± 0.8%, 35.0 ± 3.8 % and 39.9 ± 2.1 % respectively. Figure 6.9 shows the plot of apparent porosity vs. the content of CPM in CPSC.

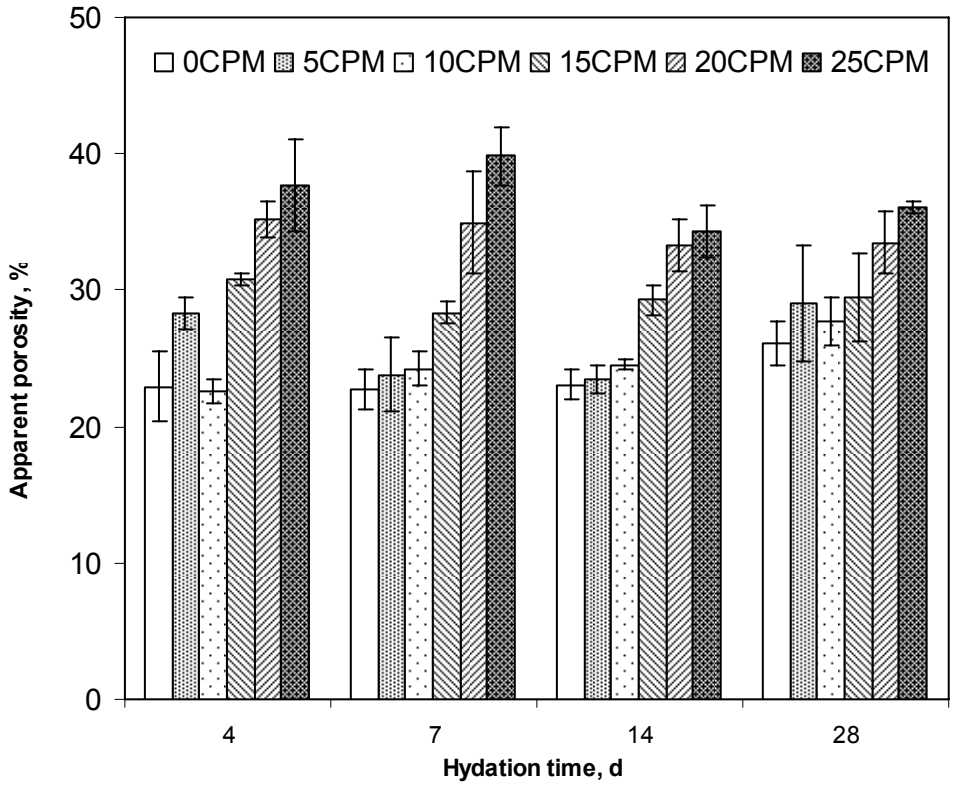

Figure 6.9 The apparent porosities of 0CPM, 5CPM, 10CPM, 15CPM, 20CPM, and 25CPM for different curing times.

During preparing the specimens for testing of mechanical properties, it was noticed that more liquid was needed for the CPSC cement with a high content of CPM in order to obtain a proper consistency of the cement e.g. to properly fill the mould. For example, a preliminary experiment showed that the water-to-cement ratio needed to obtain proper workability of the cements was 0.40 for 0CPM, 0.47 for 10CPM, and 0.62 for 20CPM The high specific surface area of the CPSC with a high content of CPM might be responsible for the requirement of more liquid to wet the cement particles and to provide the necessary workability. The BET results showed that the specific surface areas of CPSC cements increased considerably after each 5 wt%

of CPM was added to the cement, indicating that the average particle sizes of the CPSC containing more CPM were much smaller than those with less CPM (Table 4.1). The XRD analysis and DTA results showed that CPM converted to DCPD within 10 min of hydration, suggesting that the reactions (5.3) through (5.5) might take place rapidly and the water required for the conversion from CPM to DCPD might be adsorbed immediately during mixing the cement with water. Besides, the reaction (5.7) indicated that more water would be produced if CPSC contained a high content of CPM, and the produced water could form voids in the hardened cements, resulting in higher porosity. The calculations based on the reaction (5.7) demonstrate that each addition of 5 wt% of CPM would produce about 1.5 wt% more water in set CPSC cement.

While this phenomenon could be detrimental for CPSC cements admixed with sufficient amount of water at the outset of the hydration (e.g. providing excessive porosity), it could be a desirable feature of the systems setting in the environments deficient in water. This particular situation takes place for CPSC used in endodontic applications, i.e. as ready-made injectable dental root canal sealers, for example, Endosequence BC Sealer [172]. Such sealers are prepared with non-water carriers to make them easily injectable, and set only by adsorbing water from the environment, e.g. from the dental root canal walls through the dental tubules. In such unique case, the system resembles an auto-catalytic reaction wherein once the initial setting starts, it will self-propel due to in-situ generation of water (i.e. through reaction 5.7). It is anticipated that the phenomenon described above is at least partially responsible for the staggering success of CPSC-based dental sealers throughout world markets [172].

Other similar applications of such water-generating ready-mixed CPSC with long shelf-life could be envisaged outside of the medical or dental fields. For example, concrete repair kits

with easily injectable mix of CPSC with water-soluble polymeric carrier could be used to fill the defects, with the setting initiated by surface water spray or simply environmental factors (i.e. humidity or rain).

6.4 Mechanical Properties

The mechanical properties measurement for CPSC cements included compressive strength tests and three-point flexural strength tests. The strengths were determined on the specimens of all the cements with different amount of CPM for the pre-set curing times at 37 ºC. The measurement details were provided in Section 3.3.

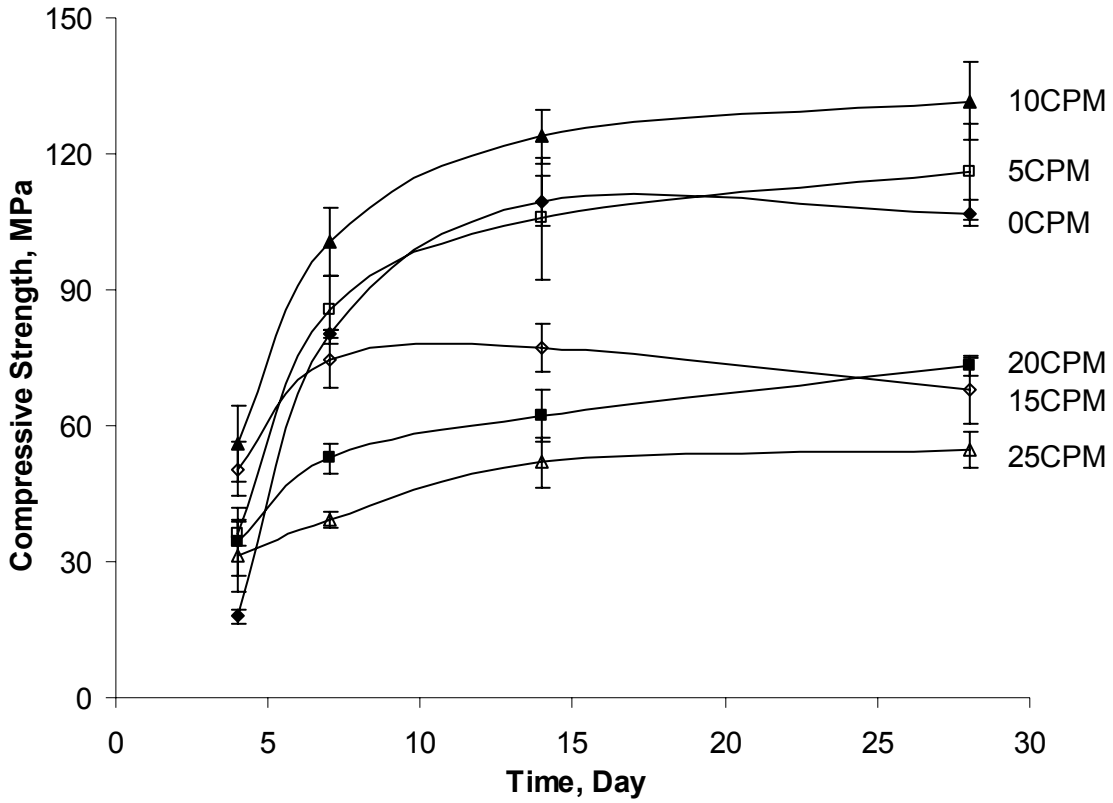

Figure 6.10 The compressive strength of C_3S (0CPM) and CPSC vs. curing time in 37 ºC distilled water.

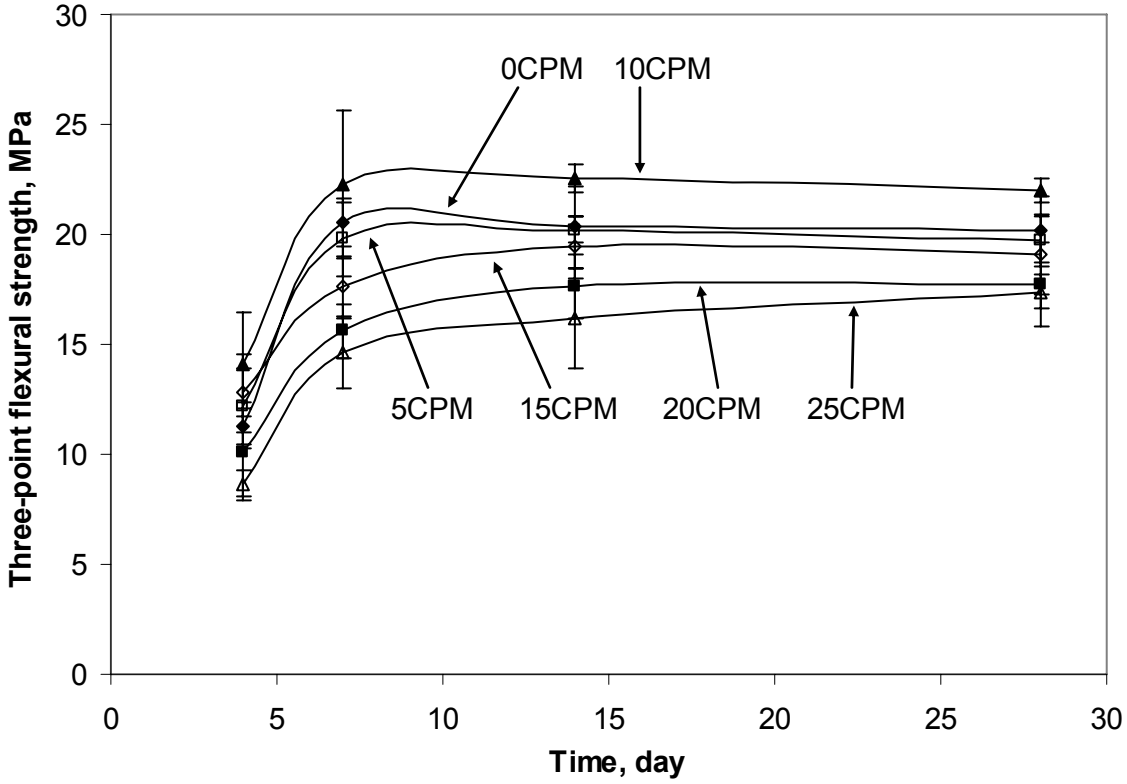

Figure 6.11 The three-point flexural strength of C_3S (0CPM) and CPSC vs. curing time in 37 ºC distilled water.

The compressive strengths of the cements for different curing times are shown in Figure 6.10. The compressive strengths for all cements increased with curing time and the increasing rate decreased with time, as clearly seen for early hydration. For hydration longer than 14 d, the increase in compressive strength was not obvious. 10CPM had the highest compressive strengths during the whole range of curing up to 28 d. 5CPM and 0CPM had very close values from 7 to 28 d, but 0CPM was the lowest in compressive strength (17.9 ± 3.2 MPa) for 4 d in comparison

with all CPSC. 15CPM, 20CPM and 25 CPM had lower compressive strengths than 0CPM when curing time was longer than 7 d, at the same time the strength decreased with the increase in the amount of CPM in the CPSC. The statistical analysis showed that the compressive strengths of 10CPM were significantly higher than those of 0CPM during the whole time range of 4 to 28 d ($p < 0.0001$).

The three-point flexural strengths of the cements for different curing times are shown in Figure 6.11. The flexural strengths of all the cements increased with curing time and the increase was fastest when the curing time was shorter than 7 d. After 7 d of hydration, the flexural strengths for all the cements did not increase significantly. For the whole range of curing time up to 28 d, the flexural strengths of 10CPM were the highest. The flexural strengths of 0CPM and 5CPM were close to each other for the curing time longer than 7 d. For 15CPM, 20CPM and 25CPM, the strengths decreased with the content of CPM in the cements, for example, the flexural strengths after 7 d of hydration were 16.6 ± 2.7 MPa for 15CPM, 15.6 ± 2.4 MPa for 20CPM, and 14.6 ± 3.1 MPa for 25CPM, respectively.

It is proposed that the hydration process of CPSC followed the reactions (5.3) to (5.8) and the formation and growth of the hydrates C-S-H and /or C-S-P-H phases entangled and polymerized to form a solid network as time proceeded to obtain strength. After the hydration for 4 d, the hydration degree for the cements reached 86.3 ± 7.5 % for 0CPM, i.e. C_3S, 94.8 ± 6.8 % for 5CPM, 97.5 ± 2.8 %, for 10CPM, and 100 ± 4.9 % for 20CPM respectively [Figure 5.2(a) on Page 75]. As the hydration proceeded, the hydration degree increased and the strengths of the cements increased. After a 14-d hydration, all the cements almost reached to the completion of hydration and the strengths did not increase obviously. The degree of polymerization of C-S-H

(C-S-P-H) hydrates continued even after the hydration completed, and this could provide more strength [54].

As discussed in Section 6.2, the content of CPM in CPSC affected the morphology of the hydrates and their arrangement, i.e. microstructure, which in turn affected the mechanical properties. The hydrates in C_3S cement had fibrous morphology and the individual fibers individually "radiated" from the surfaces of the anhydrous C_3S particles. With the progress of the hydration process, the hydrates formed a network and further tightly packed grains, which is expected to provide the mechanical strength for the hydrated C_3S. However, the addition of phosphates to C_3S modified the hydration process and hydrates morphology. For example, although the hydrates in the samples 10CPM were also fibre-shaped, they bundled together to form clusters, and these hydrate clusters deposited on the surfaces of anhydrous C_3S particles. With the progress of the hydration process, the hydrate clusters formed the denser-packed network, which is expected to provide higher mechanical strength than the network consisting of the individual fibres (e.g. as in pure C_3S). Although the hydrates of 20CPM also bundled together to form the clusters, these hydrate clusters piled on the unhydrated C_3S particles [Figure 6.3 (c)] without forming a network as in 0CPM and 10CPM. This less cohesive morphology resulted in lower compressive and flexural strength of 20CPM cement.

During the hydration of CPSC, CPM converted to DCPD first and then formed HAP by reacting with CH produced from the hydration of C_3S. In this process, CH was consumed by reacting with calcium phosphate and the "weak link" points reduced. Due to the relatively small particle size of CPM (the specific surface areas showed in Table 4.1), the particle size of HAP is also expected to be relatively small and thus act as a filler in the hardened cement microstructure. Additionally, the small particle size resulted in a reduction in the size of the individual pores and

voids in the hardened cement, although the total porosity of CPSC increased slightly, such as 10CPM. In comparison of the micrographs in Figures 6.6 (a) and (b) and 6.7 (a) and (b), it can clearly be seen that the pores in 0CPM pastes were larger than those in 10CPM pastes. Therefore the addition of CPM into pure C_3S cement is expected to improve its mechanical properties. However, the more CPM was added, the more liquid phase (water) was needed to mix with the cement [plus more pores produced through water released in the reaction (5.7)], and this resulted in more pores in the hardened cement, for example, 20CPM (refer to Table 6.1 for compilation of all porosity data). Therefore, it is concluded that the optimal amount of CPM is about 10 wt% of CPM in CPSC.

The results showed that after hydration for 28 days in distilled water at 37 ºC, the apparent porosities for all the cements of 0CPM, 5CPM, 10CPM, and 20CPM increased slightly, Figure 6.9, but the compressive and bending strengths were not significantly affected, Figures 6.10 and 6.11. At present, the reason for this is not clear. Future work is needed to clarify weather some components of the set cements dissolve into water, and also to investigate the degradability and durability *in vivo*.

Mechanical properties, such as compressive strength and flexural (bending) strength are very important to biomaterials. For example, mineral trioxide aggregate (MTA), a calcium silicate-based dental material, is widely used in dental applications, such as root canal filling, pulp capping and restorative base [173, 174]. The mechanical properties should be taken into consideration when a material is placed into a cavity that bears occlusal pressure [50]. The compressive strength of 10CPM increasing from 56.1 MPa (4 d) to 123.9 MPa (14 d) was equivalent or better than that of MTA, which increased from 40 MPa (24 h) to 67 MPa (21 d)

[50]. Therefore, 10CPM, the main component of a dental material, BioAggregate, has been commercially available as a root-filling, pulp capping, or restorative material [175-178].

Mechanical properties are more important for biocements used in orthopaedic applications than in dental field. 10CPM hydrated for 7 d (reaching compressive strength of 100.5 MPa) has an equivalent compressive strength to PMMA bone cement (93.0 MPa [46]), but the bending strength for 10CPM (19.8 MPa after hydration for 7 d) is much lower than that of PMMA bone cement (64.2 MPa). Further studies are needed to determine how other mechanical properties, such as tensile strength, shear strength, and fracture toughness for 10CPM compare to those of PMMA bone cement.

6.5 Summary

1. The morphology of the hydration products depended on the progress of hydration and composition of CPSC. At the early stages of hydration, the hydration products formed “almond-shaped” particles 0.1 - 0.4 μm by 0.4 – 1.0 μm large. It is expected that these particles subsequently served as a nucleation site for C-S-H / C-S-P-H, to eventually cover the whole surface of the C_3S grains. The morphology of the C-S-H / C-S-P-H hydrates varied, e.g. they took shape of "cigars" or tubes, which tended to form bundles along the radial direction of the tubes and to form an angle with the deposited surfaces. The angle formed between the hydrate bundles to their depositing surfaces seemed to vary, i.e. the angle became smaller with the content of CPM. The morphology of the "cigar-shaped" tubes of the hydrates was more common for the higher content of CPM in CPSC. The hydration process of CPSC was different from that of pure C_3S, in which the hydrates nucleated and grew on the surfaces of unhydrated C_3S grains and its hydrates had fibre-shape morphology. These fibres grow and further form networks and dense hydrate particles.

2. CPM increased porosity of set CPSC and this effect was particularly prominent when the content of CPM in CPSC was relatively high, i.e. 20 - 25 wt%. The reasons for this effect were proposed to be the following: i) due to the relatively high specific surface area of CPM, (21.4 to 25.6 m^2/g), more liquid was needed to mix with it in order to obtain proper workability of the cements. For example, the water to cement ratio (w/c) needed to obtain proper workability of the cements was 0.40 for 0CPM, 0.47 for 10CPM, and 0.62 for 20CPM cement samples. ii) during hydration of CPSC, water formed (along with HAP), from the reaction of CPM and CH produced from the hydration of C_3S; thus the higher the content CPM, the more water (accompanying more HAP) forms. It was expected that the extra water produced more pores and voids in the set cement.

3. CPM affected the mechanical properties of set CPSC. It was observed that due to the increasing porosity, strength of CPSC decreased for the higher content of CPM. On the other hand, CPM also reacted with the CH, which is the "weak link" within the structure of set CPSC, to form the finely dispersed HAP phase. Such dispersed phase might act as reinforcing filler, resulting in an increase of strength of CPSC. As a compromise between the two effects, the optimal content of CPM appears to exist at about 10 wt% of CPM in CPSC. The mechanical properties of such 10CPM cement improved in comparison with those of pure C_3S. The compressive strength of 10CPM cement after 7 days of hydration has been determined at 100.5 ± 14.7 MPa vs. 80.4 ± 1.9 MPa for pure C_3S.

7 EXPERIMENTAL RESULTS AND DISCUSSION 4: *IN VITRO* BIOACTIVITY AND BIOCOMPATIBILITY OF CSC AND CPSC[1]

7.1 Introduction

This chapter describes the results of *in vitro* bioactivity after the set CSC and CPSC cements were immersed in SBF and of the biocompatibility test including: cytotoxicity assay and cell adhesion assay against human gingival fibroblast.

7.2 *In Vitro* Bioactivity

The phase compositions of the surfaces of 0CPM and 10CPM paste samples immersed in SBF for 7 d were analyzed by XRD (Figure 7.1). The characteristic (002) and (211) reflections of HAP were observed at 2θ of ~ 26.1 º and ~ 32.7 º and the peaks of C-S-H were also noted at 2θ of ~ 29.3 º on both 0CPM and 10CPM sample surfaces, confirming the previous study [121]. On the surface of 0CPM, more and sharper peaks of calcium carbonate ($CaCO_3$) were identified than on that of 10CPM. In the SEM micrographs (Figure 7.2), $CaCO_3$ crystals were barely distinguishable from HAP is due to the similarity of their combined atomic numbers (thus similar contrast grayscale). Neither CH nor Ca_3SiO_5 was detected on the surfaces of the set cements exposed to SBF. The XRD analysis revealed, however, that $CaCO_3$ content decreased as the content of CPM increased. The SEM analysis of the sample surfaces of C_3S (0CPM) and 10CPM after immersion in SBF solution for 7 d [Figure 7.2 (a), (b), (d), and (e)] showed that the cement surfaces after exposure to SBF had a contiguous spherulite deposit, the morphology of which was similar to the apatite layer reported to form on silica gel [179]. Figure 7.2 (c) and (f) showed clearly that the HAP layer formed on each of the sample surfaces after immersion in SBF for 7 d.

[1] This chapter is based on the publication: Zhou S, Ma J, Shen Y, Haapasalo M, Ruse ND, Yang Q, Troczynski T. *In vitro* studies of calcium phosphate silicate bone cements. J Mater Sci: Mater Med. 2013;24:355-64.

In comparison to that on 0CPM cement, the HAP layer on the 10CPM surface appeared more homogeneous, thicker, and smoother, and the HAP crystals formed on 10CPM were smaller than that on 0CPM i.e. C_3S. The thickness of HAP layers formed on the sample surfaces of 0CPM, 5CPM, 10CPM, and 20CPM were 3.8 ± 0.2 μm, 6.3 ± 1.5 μm, 6.6 ± 1.3 μm, and 5.9 ± 0.6 μm, respectively (the micrographs for 5CPM and 20CPM are not shown here). The HAP layer formed on C_3S was much thinner than those on CPSC while the layers for 5CPM, 10CPM, and 20CPM were essentially the same as each other.

In general, a bioactive material forms a layer of apatite on its surface to bond to living bone in physiological environment, and this in vivo apatite formation can be reproduced in SBF [137]. The apatite formation in SBF, therefore, is the indicator of the in vivo bone bioactivity for a material. In the present study, the results of XRD and SEM characterizations (Figures 7.1 and 7.2) verified that both of pure C_3S and CPSC cement pastes induced formation of HAP layers after immersion in SBF for 7 d and the layers on CPSC were thicker than on pure C_3S. When pure C_3S paste sample was immersed in SBF, CH dissolved into the solution and the silanol (Si-OH) groups on the layer of hydrated silicate ions provided favorable sites and induced HAP nucleation [179, 180]. SBF is supersaturated with respect to HAP and the dissolution of more CH, which hydrolyzed into Ca^{2+} and OH^- ions, increased the ionic activity product of apatite in SBF [181]. Once HAP nuclei are formed on the surface of cements, they can grow spontaneously by consuming the ions of Ca^{2+}, PO_4^{3-} and OH^- from SBF. The HAP layer continued growing until it inhibited the CH dissolution or the concentration of phosphate ion was too low. The difference between the reactions of CPSC and pure C_3S with SBF can be explained as follows. In addition to the dissolution of CH, phosphate ions on the surfaces of CPSC paste sample might dissolve into the solution as well, and this would further increase the degree of the supersaturation of the surrounding fluid with respect to HAP, and therefore increase the rate of apatite nucleation. The

availability of more phosphate ions in the solution might be the reason why the HAP layers on CPSC were thicker than that on pure C_3S. The HAP formed in CPSC could also act as seeds to accelerate the rate of HAP nucleation and precipitation in SBF [182]. A previous study confirmed that the rate of apatite nucleation on the surfaces of P_2O_5-containing CaO-SiO_2 glass in SBF was greater than that on P_2O_5-free CaO-SiO_2 glass [180]. The formation of $CaCO_3$ on the surfaces of cements is due to the reaction between cement pastes and SBF and the high pH of the cement paste might be responsible for the formation of $CaCO_3$ [138]. However, further in vivo studies are required to confirm that CPSC could bond to bone tissue in vivo.

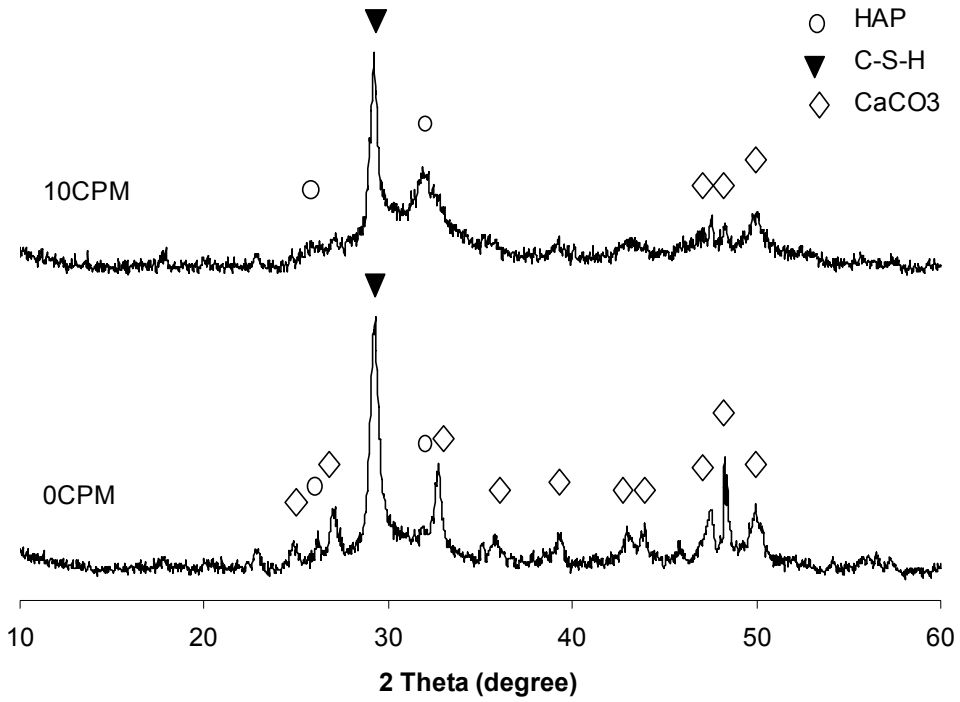

Figure 7.1 XRD patterns of the surfaces of 0CPM and 10CPM samples after immersion in SBF for 7 d.

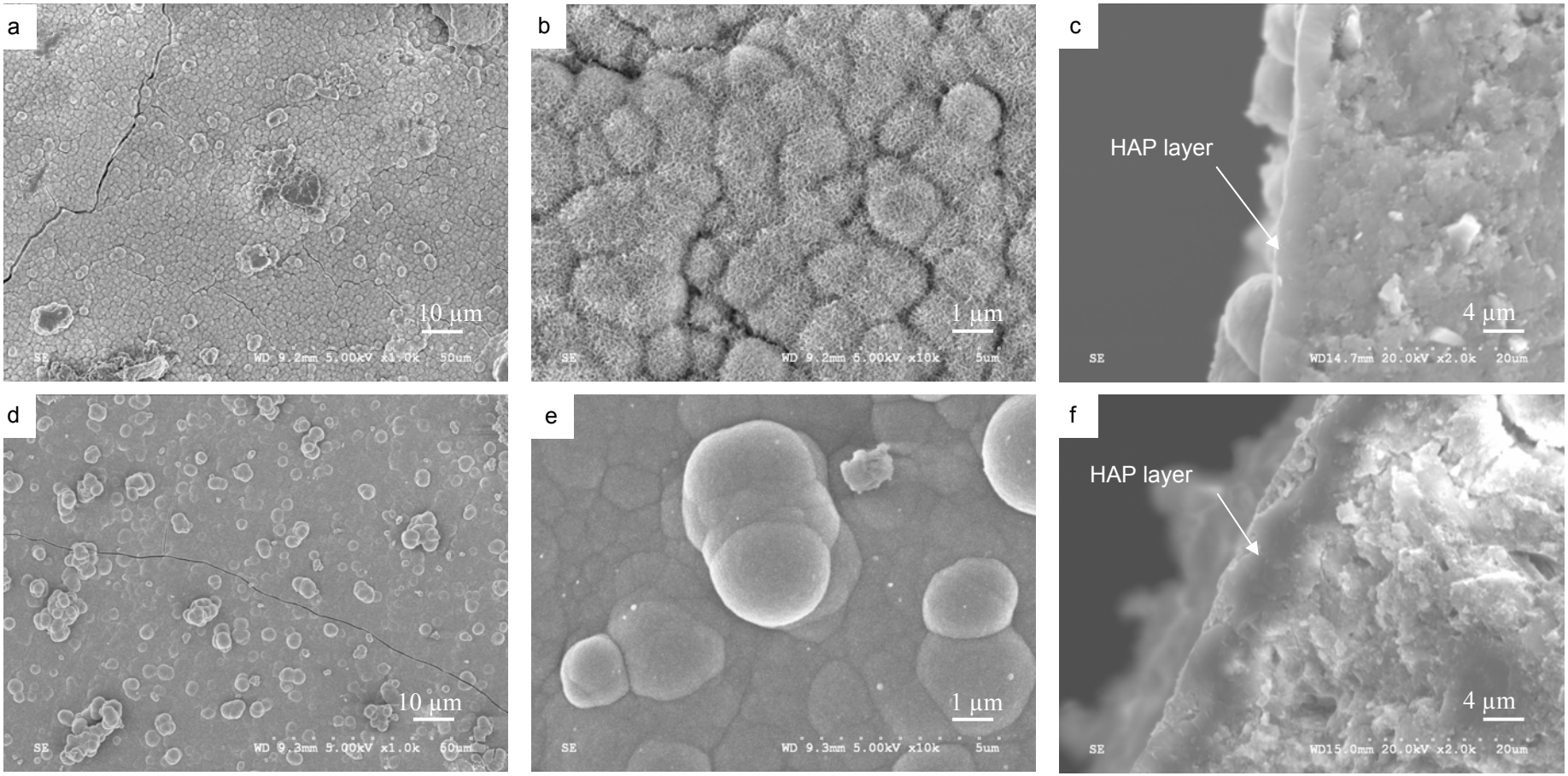

Figure 7.2 SEM micrographs of 0CPM and 10CPM paste samples after immersion in SBF for 7 d: (a) & (b), the surface morphology of 0CPM; (d) & (e), the surface morphology of 10CPM; (c) & (f), the layer thickness of the apatite on cross-section of a 0CPM sample (c) and 10CPM (f).

7.3 *In Vitro* Biocompatibility

7.3.1 Cytotoxicity assay

The viability of human gingival fibroblast cells after exposure to the 24 h and 3 d extracts of freshly mixed C_3S and CPSC pastes for 3 d was assessed. Cell viability (Figure 7.3) was strongly affected by cement composition ($p < 0.001$ for all factors), but all materials behaved in a similar way. An initial cytotoxic inhibition was apparent in the undiluted extracts, which decreased continuously with increasing the dilution of extracts. For the diluted extracts, such as the eighth and sixteenth dilutions, the cement cytotoxicity was not significantly different ($p > 0.05$); however, for the undiluted extracts, all the cements revealed significantly different cytotoxicity ($p < 0.001$). The duration of extraction also affected cell viability: the longer the extraction time, the more severe the cytotoxicity. The different contents of CPM in CPSC resulted in significantly different cytotoxicity ($p < 0.001$) against human gingival fibroblasts and the cements with increasing CPM content were less cytotoxic, i.e. 20CPM<10CPM<5CPM <0CPM.

The ionic concentrations of Ca, Si, and P in DMEM (also as the blank medium or the negative control) and the extracts from all the cements after extraction for 24 h and 3 d and their pH are shown in Table 7.1. It was found that the ionic concentrations of Ca, Si, and P were different among all the cements and from the blank medium. The Si ionic concentrations from 0CPM, 5CPM, 10CPM, and 20CPM for both incubation periods were 85 to 138 times higher than the blank medium while their Ca and P ionic concentrations were lower. The extracts from CPSC cements were higher in Ca and P concentrations than those from 0CPM, and Ca and P ionic concentrations increased with the content of CPM in the cement, except for 20CPM after 24 h extraction. The mismatch of the release kinetics of Ca and Si ions from 0CPM into cell culture medium was due to the Ca-P layer deposition on the surface of the cements during the

extracting process. The extracts from all the cements had higher pH than the blank medium and showed a slowed decreasing in pH with the content of CPM in the cements, indicating that CPM had an effect to reduce the pH of cement pastes. Due to the buffer effect of DMEM, the pH values of the extracts were lower than those of the cement pastes setting in distilled water.

Table 7.1 pH and ion concentration of the extract from 0CPM, 5CPM, 10CPM, and 20CPM in the culture medium after 24 h and 3 d incubation*.

Extraction time	Materials	Element concentration, $mmolL^{-1}$			pH
		Ca	Si	P	
	Blank**	1.84±0.15	0.03±0.00	1.18±0.06	7.30±0.02
24 h	0CPM	0.09±0.01	3.34±0.10	0.05±0.00	8.28±0.02
	5CPM	0.14±0.01	4.16±0.12	0.33±0.02	8.14±0.03
	10CPM	0.52±0.04	2.83±0.08	0.48±0.02	7.81±0.04
	20CPM	1.70±0.14	3.03±0.09	0.30±0.02	7.82±0.03
3 d	0CPM	0.06±0.00	2.63±0.08	0.04±0.02	8.23±0.03
	5CPM	0.10±0.01	2.72±0.08	0.48±0.02	8.16±0.03
	10CPM	1.05±0.08	2.55±0.08	0.63±0.03	7.88±0.04
	20CPM	1.37±0.14	2.78±0.08	0.67±0.03	7.87±0.03

* 0CPM is C_3S; 5CPM is C_3S + 5%CPM; 10CPM is C_3S + 10%CPM; 20CPM is C_3S + 20%CPM.

** Blank medium is DMEM used as the negative control.

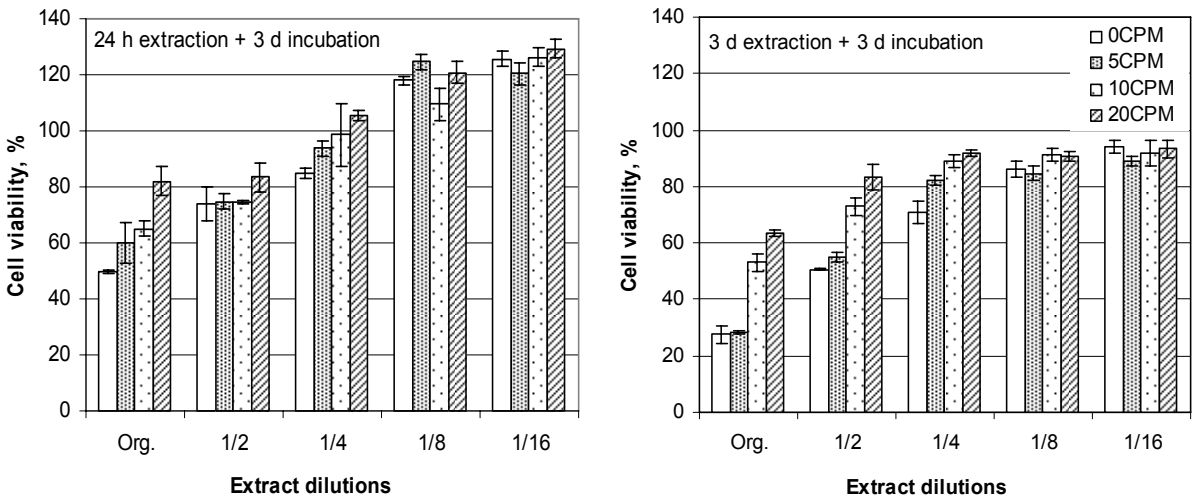

(a) (b)

Figure 7.3 Viabilities of human gingival fibroblasts after exposure to (a) 24 h and (b) 3 d extracts from freshly prepared cement pastes. Serial two-fold dilutions of the extracts were done.

In this study, the *in vitro* biocompatibility of 0CPM, 10CPM, 15CPM and 20CPM was assessed by MTT assay and cell adhesion assay using cultured human gingival fibroblasts, because the amount and nature of leachable components and the surface structure and characteristics of the material play a key role in the biocompatibility of biomaterials. The pH values of the extracts from all cements were in the range of 7.81 to 8.28, which were much higher than that of the control (7.30). The cytotoxicity effect of the extracts from the cements on the cells appeared to be correlated to the pH values. Cells, including fibroblasts, are sensitive to change in extracellular pH and the ideal pH of cell cultures is 7.2 -7.4 [183]. Studies have shown that cell growth declined precipitously on the alkaline side although the optimal pH ranges for maximum growth differed slightly from each other for different cells [184, 185]. A high pH

value of a material induces the denaturation of adjacent cells and culture medium proteins of fibroblasts directly contacting the material [186]. The higher the pH, the lower the cell viability.

It was also noticed that more cells survived in the undiluted extracts from 20CPM than in 10CPM at the same pH, and this might be attributed to the higher concentrations of Ca and Si ions in the corresponding extracts. Ca ion plays an essential role to maintain the growth and functions of living cells and extracellular Ca is a potent regulator of cell behavior and has significant effect on the proliferation and differentiation of cells (osteoblast) [187]. The presence of Ca ion may also activate adenosine triphosphatase (ATP) activity and increase in the concentration of Ca ion results in an increased rate of DNA (Deoxyribonucleic acid) synthesis and accelerates the mineralization of a hard tissue such as dentine or bone [188]. The concentration of Si ion in the medium has been shown to shorten the human cell (osteoblast) growth cycle, to enhance proliferation, differentiation and collagen production, and to have dose dependent effects on the remodeling process and osteoclast development and resorption activities. The osteogenesis expression in primary human osteoblast increased 1.4 times that of control treatments when treated with additional Si (50 μM) [189]. In addition, phosphate is an essential component of DNA and RNA (Ribonucleic acid) and necessary to produce ATP. Inorganic phosphate stimulates differentiation, resulting in type X collagen expression and acts as a signal to initiated mineral deposition in cultures of rat calvarial osteoblasts [190]. However, the previous studies also showed that there exist the optimal Si and P ionic concentrations to benefit cell function and growth, and if their concentrations were excess the range, the excess Si and P ions induce cell apoptosis and necrosis [191, 192]. For examples, the Si ionic concentration greater than 4 mM may cause osteoblast-like cells (MG63) dysfunction and even apoptosis [191]. Therefore, it is important to take the cellular effect of Ca, Si and P into consideration when designing new biomaterials.

The differences of cell viabilities for the diluted extracts (e.g. 1/8 and 1/16 dilution) were not significantly different ($p > 0.05$), indicating that the pH of the extracts might be the most important factor to influence the cell viability. The over 100% of cell viability indicated that the diluted extracts (e.g. 1/8 and 1/16 dilution) of the cements stimulated the cell proliferation and this result was consistent with a previous study [138], which showed that certain concentrations of Ca^{2+} and Si^{4+} ions significantly promoted cell proliferation. Comparing the effect of the extraction duration of 24 h and 3 d, a time-dependent decrease in the cell viability was noticed, however, the mechanisms are not fully understood at present.

Our results revealed that the C_3S cement was the most cytotoxic against human gingival fibroblasts when undiluted extract was used. This may be due to the highest pH in the extract. With an increase in the content of CPM, the pH of the extracts from CPSC was reduced, which may explain the reduced cytotoxicity of CPSC. The results of the investigated cements demonstrated 20CPM<10CPM<5CPM<0CPM in terms of cytotoxicity. However, further in vivo studies are required to confirm the cytotoxicity of these cements.

7.3.2 Cell adhesion assay

After setting for 3 d, all cements presented similar surface morphology under SEM. Irregular “dark” and “bright” areas and pores on sample surfaces were observed and the surface texture of the “dark” area was smoother than that of the “bright” area (Figure 7.4). Based on EDX analysis, the “dark” area had a higher amount of Ca (approximately 2-4x higher) as compared to the “bright” area (Table 7.2). After 3 d cell culture, the irregular “dark” and “bright” areas on the cement surfaces were still observed (Figure 7.5) and their compositions were analyzed again by EDX; and the results showed that there were higher concentrations of P and Ca in these areas, compared to the cement samples before cell culture (Table 7.3).

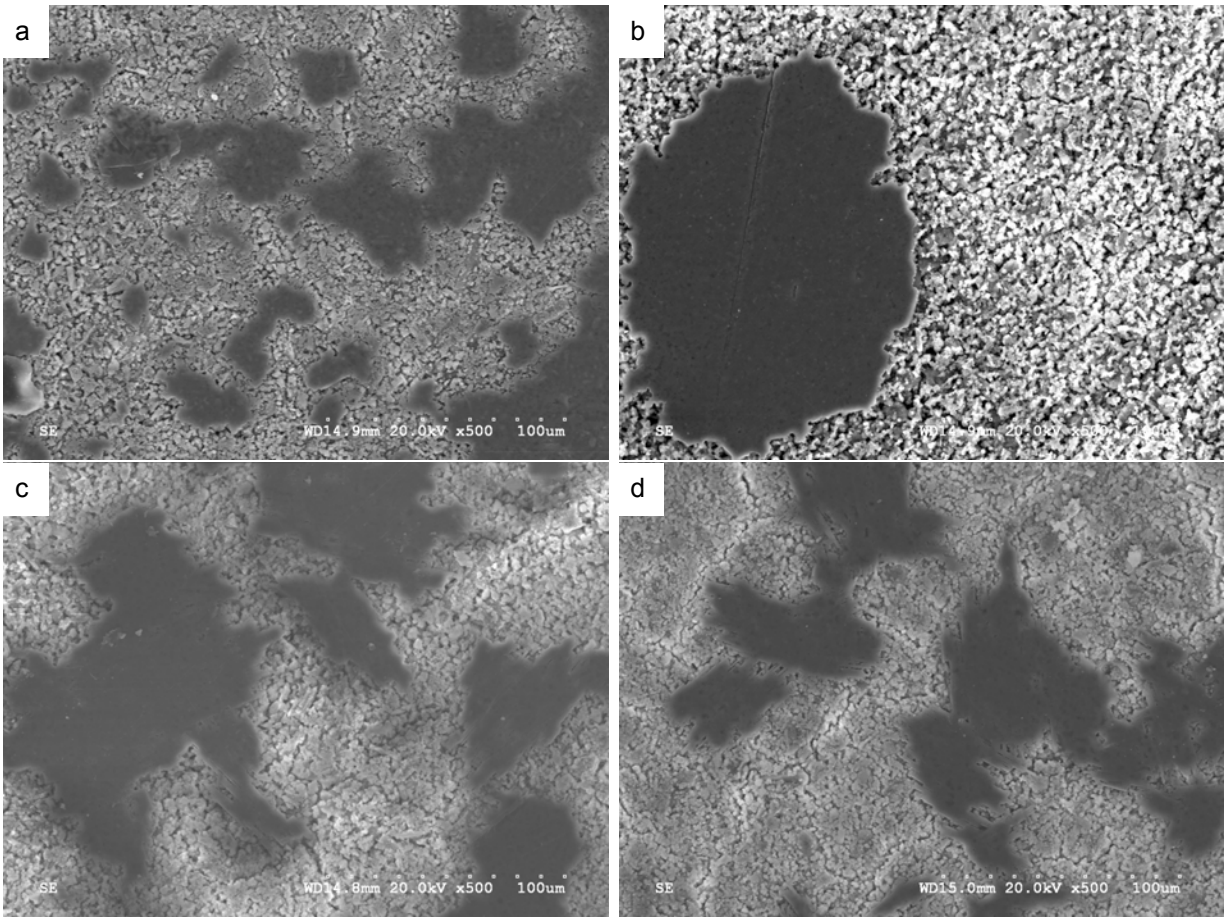

Figure 7.4 SEM micrographs of cement surfaces of (a) 0CPM, (b) 5CPM, (c) 10CPM, and (d) 20CPM set for 3 d.

Table 7.2 The atomic ratio of elements Si, P, and Ca in "dark" and "bright" areas for set samples (as Si = 1.00)

	0CPM		5CPM		10CPM		20CPM	
	Dark	Bright	Dark	Bright	Dark	Bright	Dark	Bright
P	0.00	0.00	0.11±0.00	0.07±0.00	0.21±0.02	0.16±0.02	0.36±0.07	0.38±0.01
Ca	5.68±1.56	2.46±0.15	10.46±4.30	2.26±0.06	10.28±0.20	2.56±0.26	8.70±0.05	2.52±0.10

* 0CPM is C_3S; 5CPM is C_3S + 5%CPM; 10CPM is C_3S + 10%CPM; 20CPM is C_3S + 20%CPM. ** Results represent Mean ± SD for 3 measurements.

Table 7.3 The atomic ratio of elements Si, P, and Ca in "dark" and "bright" areas after 3 d incubation (as Si = 1.00)

	0CPM		5CPM		10CPM		20CPM	
	Dark	Bright	Dark	Bright	Dark	Bright	Dark	Bright
P	0.45±0.36	0.81±0.31	0.39±0.12	2.13±1.46	0.45±0.23	5.96±3.78	0.97±0.41	4.26±1.25
Ca	5.57±1.25	4.59±1.13	13.72±3.67	7.79±3.63	6.29±1.88	16.52±7.53	11.16±4.36	8.77±2.43

* 0CPM is C_3S; 5CPM is C_3S + 5%CPM; 10CPM is C_3S + 10%CPM; 20CPM is C_3S + 20%CPM.

** Results represent Mean ± SD for 3 measurements.

After 3 d exposure of the fibroblasts to the test samples of 0CPM, most of the fibroblasts on the sample surface were round in shape and detached on both "dark" and "bright" surfaces and no cell spreading had occurred [Figure 7.5 (a)]. On the surface of 5CPM, the cells on the "dark" area still showed a small and round shape without spreading [Figure 7.5 (b)], while most of the cells in the "bright" area were spindle-shaped and showed good attachment to the cement and were spread out to a certain degree. For 10CPM [Figure 7.5 (c)] and 20CPM [Figure 7.5 (d)], similar cell morphologies on the two cements were detected and the cells were seen spreading and attaching on the surfaces of both the "dark" and "bright" areas in these two cements. The

cells had irregular shapes: some were long and slender and some were polygonal. It was also noticed that more cells survived on the surface of 20CPM than on the surface of 10CPM.

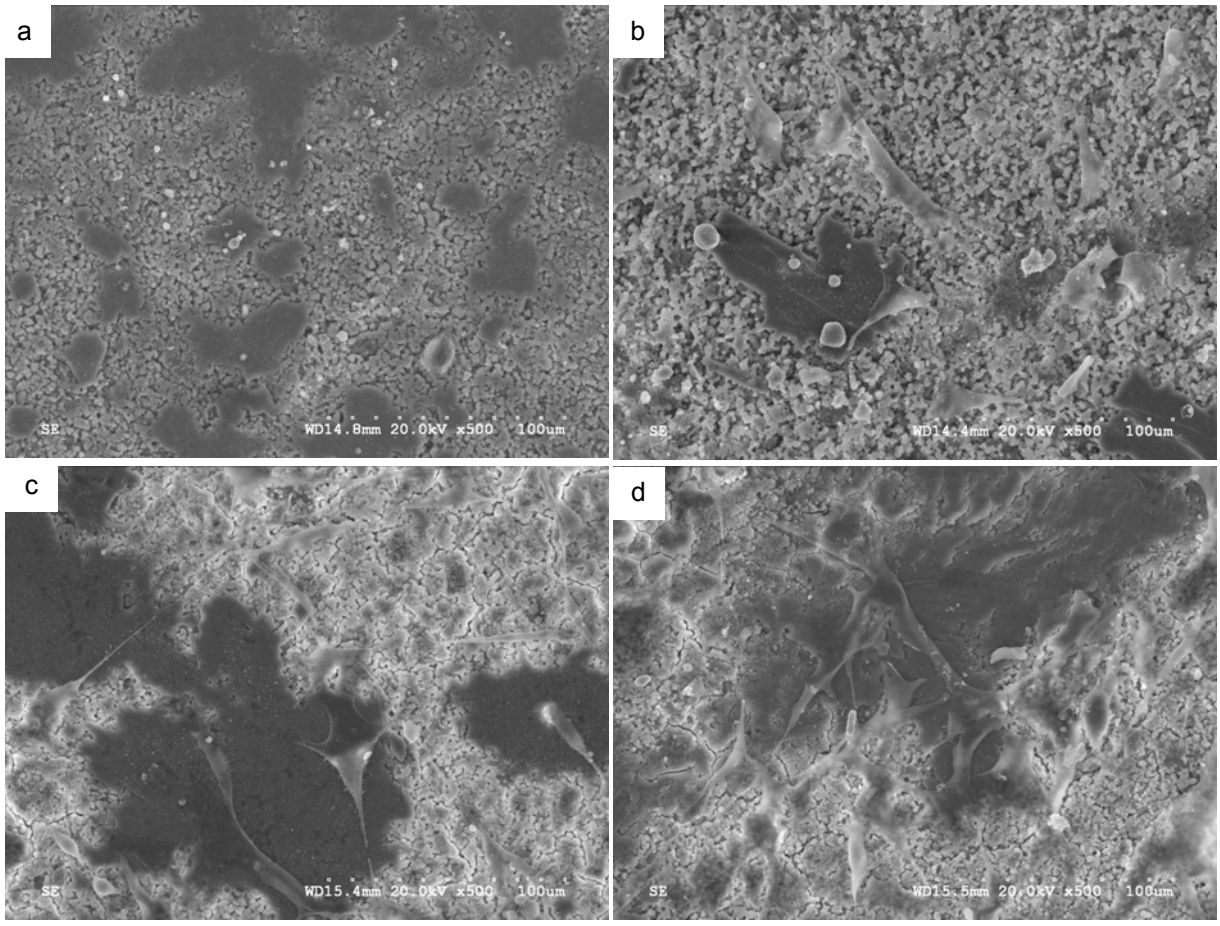

Figure 7.5 SEM micrographs of human gingival fibroblast adhesion on cement surfaces after 3 d incubation; (a): 0CPM, cells are round without spreading; (b): 5CPM, cells are round without spreading on "dark" area and spindle-shaped with good attachment on "bright" area; (c): 10CPM and (d): 20CPM, cells polygonal with spreading and attaching on both "bright" and "dark" areas (original mag. ×500).

The surface characteristics were examined under SEM/EDX for all the cement pastes after setting for 3 d in this study. Surface composition showed that the concentration of Ca in "dark" areas was higher than that in "bright" areas (Table 7.2). This was attributed to the non-uniform distribution of CH [193], which was present in higher concentrations in the "dark" areas. Consequently, it indicated that the "dark" areas would have a higher local pH than the "bright" areas in the culture medium. When the culture medium (DMEM) contacts cement samples, PO_4^{3-} in DMEM could participate in a reaction to precipitate HAP because HAP ($Ca_{10}(PO_4)_6(OH)_2$) (pK_{sp} = 117.2 at 37 ºC) is the most stable calcium phosphate in an aqueous solution in the pH range above 4.2 [94]. After incubation with fibroblasts for 3 d, more HAP precipitated in "bright" areas, resulting in the higher concentrations of P in these areas (Table 7.3). It was expected that phosphorus (presumably from HAP) was present on the surfaces of the C_3S samples after cell culture for 3 d in DMEM. Cell behavior, including cell adhesion, spreading, proliferation, and differentiation, is sensitive to the chemistry and morphology of the substratum [194]. Previous studies revealed that smooth or homogeneous roughness with micro-excavation surfaces favors human oral fibroblast attachment and soft tissue growth [195, 196]. The present results demonstrated that the "bright" area was the favorite site for cell attachment. Cell attachment and spreading on biomaterial surfaces are critical phenomena for a successful tissue-biomaterial interaction because the attachment and spreading of cells dominate normal cell growth and protein synthesis, and poor adhesion and lack of spreading will lower the cell proliferation rate. The fact that the cell could spread as well on the "dark" areas of 10CPM and 20CPM surfaces [Figure 7.5 (c) and (d)] suggested that the entire surface of 10CPM and 20CPM samples was friendly to cells. Moreover, more cells survived on the surface of 20CPM than on the surface of 10CPM. The results of the cell adhesion experiment indicated that the increasing order of *in vitro* biocompatibility in terms of cell adhesion was 0CPM<5CPM <10CPM<20CPM, which confirmed the results from MTT assay.

7.4 Summary

After immersion in SBF, the surface of the set sample of CPSC, consisting of C_3S and CPM, formed a layer of HAP, indicative of CPSC being *in vitro* bioactive. HAP, resulting from the reaction between CPM and CH produced from the hydration of C_3S, acted as seeds to accelerate the rate of HAP nucleation and precipitation on the surface of CPSC. In addition, the dissolved phosphate ions from CPSC increased the degree of the supersaturation of the surrounding solution with respect to HAP and facilitated HAP nucleation and precipitation. Compared to pure C_3S, the biocompatibility of CPSC was significantly enhanced in terms of cell adhesion and proliferation and cell cytotoxicity. This is attributed to reduced CH content (resulting in pH reduction) in set CPSC cement. The order of biocompatibility was 0CPM<5CPM<10CPM<20CPM. With its good *in vitro* bioactivity, biocompatibility, and low or no cytotoxicity, in comparison to pure C_3S, CPSC is a potential candidate as biomedical cement.

8 CONCLUSIONS

This dissertation reports on the exploratory research of the novel family of CPSC, co-invented by the author of this dissertation. Several variants of CPSC consisting of C_3S and CPM were successfully synthesized through a sol-gel and planetary ball-mill processes and thoroughly characterized. The major portion of this dissertation focuses on studies of hydration of CPSC, including evaluation of pH variations during hydration, determining the phase compositions of the cement with hydration time using quantitative XRD and DTA-TG, examining the microstructure evolution with SEM/EDX, and investigating the mechanical properties of set CPSC. In addition to these materials-engineering oriented studies, *in vitro* bioactivity and biocompatibility of CPSC using SBF environment and human gingival fibroblast cells have been explored. All these results were obtained on the materials synthesized in this work.

The principal conclusion of this work is that CH resulting from the hydration of C_3S reacted with CPM and precipitated HAP, removing CH from the set cement and reducing the pH of the cement paste. The CPSC with 10 wt% of CPM, coded 10CPM, was bioactive *in vitro*, had enhanced biocompatibility and improved compressive and flexural strengths in comparison to the pure C_3S, confirming the research hypotheses.

The following are the specific conclusions drawn form this work:

1. The “best-practice" process to prepare CPSC includes the following steps:

i) Synthesize the precursor for C_3S through a sol-gel process,

ii) Fabricate high purity C_3S powder by sintering the precursors at 1550 ºC,

iii) Obtain CPSC powder by planetary ball milling the mixture of C_3S with various amounts of CPM.

2. The following steps are proposed to be involved in the hydration of CPSC:

i) C_3S and CPM dissolve into the liquid phase and hydrolyze;

ii) CPM converts to DCPD immediately;

iii) C_3S continuously hydrates to produce CH and C-S-H gel. It is proposed that such C-S-H gel will incorporate the phosphate ions available in the solution to result in C-S-P-H gel.

iv) DCPD subsequently reacts with CH to precipitate HAP,

v) Finally, C_3S hydrates completely and above processes cease. The hydration-stop point for the cements studied in this work was typically within 28 d.

3. The final hydration products of CPSC are HAP, CH, and C-S-H / C-S-P-H. The content of each product in the set cement depends on the starting composition of CPSC. The composition of the hydrates C-S-(P-)H also varies with the starting composition of CPSC and the hydration process. In the present work the compositions of the hydrate C-S-(P-)H are estimated to be as follows:

For 10CPM

$(0.6 – 2.1)CaO{\cdot}SiO_2\ xP_2O_5{\cdot}(2.2 – 5.3)H_2O$, in which $0 \le x \le 0.11$ for $\alpha = 10 – 30$ %,

$(1.8 – 2.1)CaO{\cdot}SiO_2\ xP_2O_5{\cdot}(1.6 – 2.2)H_2O$, in which $0 \le x \le 0.11$ for $\alpha = 30 – 90$ %;

For 20CPM

$(1.5 – 2.3)CaO{\cdot}SiO_2\ yP_2O_5{\cdot}(2.2 – 5.3)H_2O$, in which $0 \le y \le 0.24$ for $\alpha = 10 – 30$ %,

$(2.0 – 2.3)CaO{\cdot}SiO_2\ yP_2O_5{\cdot}(1.6 – 2.2)H_2O$, in which $0 \le y \le 0.24$ for $\alpha = 30 – 90$ %;

4. The morphology of the hydration products depends on the progress of hydration and composition of CPSC. At the early stages of hydration, the hydration products form “almond-shaped” particles 0.1 - 0.4 μm by 0.4 – 1.0 μm large. It is expected that these particles subsequently serve as nucleation sites for C-S-H / C-S-P-H, to eventually cover the entire surface

of the C_3S grains. The morphology of the C-S-H / C-S-P-H hydrates varies, e.g. they take shape of "cigars" or tubes, which tend to form bundles along the radial direction of the tubes and to form angles with the deposited surfaces. The angle becomes smaller with the increase in CPM. The morphology of the "cigar-shaped" tubes of the hydrates is more common for the higher content of CPM in CPSC.

5. CPM influences the kinetics of the hydration of C_3S. In the acceleration stage, the kinetics of CPSC hydration is phase-boundary controlled with deceleration of nucleation rates and follows the Avrami equation: $-\ln(1 - \alpha) = k_r t^q$. For the deceleration stage, the kinetics is diffusion-controlled and follows the Jander equation: $[1 - (1 - \alpha)^{1/3}]^2 = k_d t$. The hydration rate of such CPSC is reduced in comparison with that of C_3S; however, the duration of the hydration acceleration period increases. It is noted that this result does not agree with the traditional concept that phosphate is a retarder of the hydration of C_3S.

6. At the early hydration, within the first ~ one hour, CPM presence slightly reduces pH of C_3S cement paste and the effect increases with the content of CPM.

7. CPM increases porosity of set CPSC and this effect is particularly prominent when the content of CPM in CPSC is relatively high, e.g. 20 - 25 wt%. The reasons for this effect are proposed to be the following:

i) due to the relatively high specific surface area of CPM (21.4 to 25.6 m^2/g), more liquid is needed to mix with it in order to obtain proper workability of the cements.

ii) during hydration of CPSC, water forms (along with HAP) from the reaction of CPM and CH produced from the hydration of C_3S; thus the higher the CPM content, the more water (and more HAP) forms. It is expected that the extra water produces more pores and voids.

8. CPM affects the mechanical properties of CPSC. Due to increasing porosity with increasing CPM content, strength of CPSC decreases. On the other hand, CPM also reacts with CH, which is the "weak link" within the structure of set CPSC, to form finely dispersed HAP phase. Such dispersed phase may act as reinforcing filler, resulting in an increase of strength of CPSC. As a compromise between the two effects, the optimal content of CPM appears to exist at about 10 wt% of CPM in CPSC.

9. CPSC is bioactive *in vitro*. After immersion in SBF, the surface of CPSC induces the formation of a layer of HAP from the solution, and this is indicative of CPSC being bioactive *in vitro*.

10. Compared to pure C_3S, CPSC is of significantly enhanced biocompatibility in terms of cytotoxicity and cells adhesion against human gingival fibroblasts. The results showed that more cells survived when cultured with the extracts of CPSC and more cells survived and touched on the samples with higher content of CPM than those with lower content of CPM.

With its good *in vitro* bioactivity, biocompatibility, and low or no cytotoxicity, the CPSC-based material has been used in the dental field, especially as a root canal filling material. Besides the good bio-properties of CPSC, the compressive strength of 10CPM is equivalent to that of PMMA bone cement, which is the commonly used bone cement for total joint replacements. Therefore, after improving other mechanical properties, 10CPM has potential to be used in total joint replacement as biocement.

9. FUTURE WORK

Although CPSC has been successfully synthesized through a sol-gel process and the hydration and mechanical properties and *in vitro* bio-properties of CPSC have been extensively investigated, this work is still of preliminary nature if CPSC is to be widely introduced into the medical field, e.g. orthopaedic and dental applications beyond dental root-canal sealers. It should be also emphasized that the hydration studies of calcium silicates, and generally Portland cement, continue for nearly 100 years and there still are many controversial results and theories on this topic, driving further research. CPSC has been known only for the last ~9 years and therefore we are only at the beginning of the route to fully understand this material (despite the fact that the material experiences a staggering commercial success as dental root canal filler). Consequently, there are many research directions and opportunities that need to be further explored to better understand this new bio-cement and widen its application base. We consequently propose the following several directions for the immediate future research of both fundamental and applied nature:

1. This study showed that the microstructure of hydrated CPSC paste was substantially different from that of the pure C_3S paste and this variation was attributed to the effects of phosphates on the hydration products morphology, although the exact mechanism was not clearly understood. The difference of the hydrates formed in CPSC paste from that formed in C_3S paste was noticed in DTA-TG analysis as well, and the new hydrate present in CPSC is believed to be C-S-P-H (it also appears to be amorphous since it was not found by XRD analysis). Since C-S-P-H may serve as a bond between other hydrated phases, like C-S-H [133], the detailed composition and structure of the hydrates C-S-P-H would be of interest to study.

Although the tentative composition of C-S-P-H was proposed in this work, the detailed composition would need to be determined in future studies, including the mechanisms through which phosphate ions incorporate into the hydrates C-S-H and the positions of the phosphate ions in C-S-H. As the composition of C-S-P-H appears to vary with the composition of CPSC and with the hydration process, the exact change of the C-S-P-H composition and morphology with the hydration progress should also be a subject of future studies. The important stoichiometric parameters would be the molar ratios of CaO to SiO_2 and P_2O_5 to SiO_2 within C-S-P-H. The amount of water and its state are also important characteristic of C-S-P-H.

2. The microstructure of CPSC pastes showed that bundles of the fibre-shaped hydration products formed during the middle and late stages of hydration. The fibre bundles might comprise of HAP, C-S-P-H and / or C-S-H phases. In order to understand the microstructure of C-S-P-H, and in turn the properties of CPSC, one should know the structure of the hydrates and hydration products at nano-level. The formation of nano-composite between HAP and C-S-P-H / C-S-H was an un-verified hypothesis of the current work. The study of this subject would result in better understanding of the microstructure development of CPSC during hydration and how and why the composition of CPSC affects the composition and structure of hydration products.

3. The present work showed that phosphates did not decelerate the hydration of C_3S in CPSC up to 20 wt% of CPM, and this was not consistent with the traditional concept that phosphate is a retarder for calcium silicates hydration. Further careful studies need to be done to verify what type and content of phosphate salts would retard hydration of C_3S.

4. CPSC is *in vitro* bioactive and biocompatible, but as a potential bone cement its safety to use *in vivo* must be demonstrated. Therefore extensive, multi-level *in vivo* studies on CPSC are

necessary (initially including various animal models, and finalizing with human trials) for the cement to be admitted and accepted in clinical practice. This research should also include studies of its resorption kinetics and the possibility of using CPSC for controlled drug delivery.

5. The CPSC studied in this work consisted of tricalcium silicate and CPM; the optimal composition based on the limited studies performed in this work was determined to be at 10 wt% CPM and 90 wt% C_3S. CPSC consisting of other hydraulic calcium silicates and other calcium phosphates could also be promising bone cements and the investigation on their compositions, hydration mechanisms, and mechanical and bio-properties would be necessary.

6. Like any ceramic cement CPSC is quite brittle - although measurements of its fracture toughness were beyond the scope of the current research. The issue of brittleness of CPSC needs to be addressed to enlarge the potential scope of its applications, e.g. in hip or vertebrae fixation, or other orthopaedic applications experiencing tensile or bending stresses. The search for suitable reinforcements of these cements, possibly through dispersion of biocompatible fibers, should continue.

REFERENCES

1. Brown WE, Chow LC. A new calcium phosphate, water-setting cement. In: Brown PW, editor. Cements Research Progress. Westerville, OH: American Ceramic Society; 1986. pp 351-79.

2. Chow LC, Takagi S, Constantino PD, Friedman CD. Self-setting calcium phosphate cements. In: Scheetz BE, Landers AG, Odler L, Jennings H, editors. Specialty Cements with Advanced Properties. Mater Res Soc Symp Proc 179. 1991. p 3-24.

3. Bohner M. Calcium orthophosphates in medicine: from ceramics to calcium phosphate cements. Injury Int J Care Injured. 2000;31:S-D37-47.

4. Driessens F, DeMaeyer E, Fernandez E, Boltong M, Berger G, Verbeeckugent R, et al. Amorphous calcium phosphate cements and their transformation into calcium deficient hydroxyapatite. Bioceramics. 1996;9:231-4.

5. Constantz BR, Ison IC, Fulmer MT, Poser RD, Smith ST, VanWagoner M, et al. Skeletal repair by in situ formation of the mineral phase of bone. Science. 1995;267:1796-9.

6. Suchanek W, Yoshimura M. Processing and properties of hydroxyapatite-based biomaterials for use as hard tissue replacement implants. J Mater Res. 1998;13:94-117.

7. Chohayeb, AA, Chow LC, Tsaknis PJ. Evaluation of calcium phosphate as a root canal sealer-filler material. J Endod. 1987;13:384-7.

8. Hong YC, Wang JT, Hong CY, Brown WE, Chow LC. The periapical tissue reactions to a calcium phosphate cement in the teeth of monkeys. J Biomed Mater Res. 1991:25:485-98.

9. Sugawara A, Nishiyama M, Kusama K, Moro I, Nishimura S, Kudo I, et al. Histopathological reactions of calcium phosphate cement. Dent Mater J. 1992;11:11-6.

10. Hirakata LM, Kon M, Yuasa T, Miyamoto Y, Asaoka K. Influences of crystal phases on bioactivity of calcium phosphate cements. Key Eng Mater. 2002;218-220:343-6.

11. Fujikawa K, Sugawara A, Murai S, Nishiyama M, Takagi S, Chow LC. Histopathological reaction of calcium phosphate cement in periodontal bone defect. Dent Mater J. 1995;14:45-57.

12. Boyde A, Corsi A, Quarto R, Cancedda R, Bianco P. Osteoconduction in large macroporous hydroxyapatite ceramic implants: evidence for a complementary integration and disintegration mechanism. Bone. 1999;24:579-89.

13. Ooms EM, Wolke JG, van de Heuvel MT, Jeschke B, Jansen JA. Histological evaluation of the bone response to calcium phosphate cement implanted in cortical bone. Biomaterials. 2003;24:989-1000.

14. Jackson IT, Yavuzer R. Hydroxyapatite cement: an alternative for craniofacial skeletal contour refinements. Brit J Plast Surg. 2000;53:24-9.

15. Costantino PD, Friedman CD, Jones K, Chow LC, Sisson GA. Experimental hydroxyapatite cement cranioplasty. Plast Reconstr Surg. 1992;90:174-85.

16. Brown GD, Mealey BL, Nummikoski PV, Bifano SL, Waldrop TC. Hydroxyapatite cement implant for regeneration of periodontal osseous defects in humans. J Periodontol. 1998;69:146-57.

17. Yoshikawa M, Toda T. Reconstruction of alveolar bone defect by calcium phosphate compounds. J Biomed Mater Res B Appl Biomater. 2000;53:430-7.

18. Xu HHK, Takagi S, Quinn JB, Chow LC. Fast-setting calcium phosphate scaffolds with tailored macropore formation rates for bone regeneration. J Biomed Mater Res A. 2004;68A:725-34.

19. Fukase Y, Eanes ED, Takagi, S, Chow LC, Brown WE. Setting reactions and compressive strengths of calcium phosphate cements. J Dent Res. 1990;69:1852-6.

20. Troczynski T. Bioceramics: a concrete solution. Nat Mater. 2004;3:13-4.

21. Smirnov VV, Egorov AA, Barinov SM, Shvorneva LI. Composite calcium phosphate bone cements reinforced by particulate titanium. Dokl Chem. 2007;413:82-5.

22. Zhang Y, Xu HHK, Takagi S, Chow LC. In-situ hardening hydroxyapatite-based scaffold for bone repair. J Mater Sci Mater Med. 2006;17:437-45.

23. Ambard AJ, Mueninghoff L. Calcium phosphate cement: review of mechanical and biological properties. J Prosthodont. 2006;15:321-8.

24. Xu HHK, Eichmiller FC, Giuseppetti AA. Reinforcement of a self-setting calcium phosphate cement with different fibres. J Biomed Mater Res. 2000;52:107-14.

25. Barralet JE, Hofmann M, Grover LM, Gbureck U. High-strength apatitic cement by modification with α-hydroxy acid salts. Adv Mater. 2003;15:2901-4.

26. Aeinehchi M, Eslasmi B, Ghanbariha M, Saffar AS. Mineral trioxide aggregate (MTA) and calcium hydroxide as pulp-capping agents in human teeth: a preliminary report. Int Edod J. 2003;36:225-31.

27. Maroto M, Barberia E, Planells P, Garcia Godoy F. Dentin bridge formation after mineral trioxide aggregate (MTA) pulpotomies in primary teeth. Am J Dent. 2005;18:151-4.

28. Main C, Mirzayan N, Shabahang S, Torabinejad M. Repair of root perforations using mineral trioxide aggregate: a long-term study. J Endod. 2004;30:80-3.

29. Chong BS, Pitt Ford TR, Hudson MB. A prospective clinical study of Mineral trioxide Aggregate and IRM when used as root-end filling materials in endodontic surgery. Int Endod J. 2003;36:520-6.

30. Islam I, Chng HK, Yap AU. Comparison of the physical and mechanical properties of MTA and Portland cement. J Endod. 2006;32:193-7.

31. Camilleri J, Montesin FE, Papaioannou S, McDonald F, Pitt Ford TR. Biocompatibility of two commercial forms of mineral trioxide aggregate. Int Endod J. 2004;37:699-704.

32. de Morais CA, Bernardineli N, Garcia RB, Duarte MA, Guerisoli DM. Evaluation of tissue response to MTA and Portland cement with iodoform. Oral surg Oral Med Oral Pathol Oral Radiol Endod. 2006;102:417-21.

33. Guo Z, Chang J. Synthesis and *in vitro* bioactivity of dicalcium silicate powders. J Eur Ceram Soc. 2004;24:93-9.

34. Zhao W, Chang J. Sol-gel synthesis and *in vitro* bioactivity of tricalcium silicate powders. Mater Lett. 2004;58:2350-3.

35. Knovel critical tables (2008). Section: pKsp of low solubility inorganic solutes (2nd Ed). http://www.knovel.com/web/portal/browse/display?_EXT_KNOVEL_DISPLAY_bookid=761&VerticalID=0. Accessed Dec 2010.

36. Mindess S. The strength and fracture of concrete: the role of the calcium hydroxide. In: by Skalny J, Gebauer J, Odler I, editors. Calcium Hydroxide in Concrete. Westerville, OH: American Ceramic Society; 2001. p 143-54.

37. Silica Fume Association. Silica Fume Manual. 38860 Sierra Lane, Lovettsville, VA 20180, USA; 2005.

38. Mitchell DRG, Hinczak I, Day RA. Interaction of silica fume with calcium hydroxide solutions and hydrated cement pastes. Cem Concr Res. 1998;28:1571-84.

39. Odler I, Zurz A. Structure and bond strength of cement-aggregate interfaces. MRS Proceedings. 1987;114:21-7.

40. Lu D, Zhou S (2006). Hydraulic cement compositions and methods of making and using the same. WO Patent 099748, Sep 28, 2006.

41. Lu D, Zhou S (2007). High strength biological cement composition and using the same. WO Patent 051290, May 10, 2007.

42. Lu D, Zhou S (2006). Hydraulic cement compositions and methods of making and using the same. US Patent 0213395, filing date Mar 27, 2006 and issued Sep 28, 2006.

43. Lu D, Zhou S (2007). High strength biological cement composition and using the same. US Patent 0098811, filing date Oct 20, 2006 and issued May 3, 2007.

44. Lewis G. Alternative acrylic bone cement formulations for cemented arthroplasties: present status, key issues, and future prospects. J Biomed Mater Res B Appl Biomater. 2008;84B:301-19.

45. Lewis G. Properties of acrylic bone cement: state of the art review. J Biomed Mater Res B Appl Biomater. 1997;38B:155-82.

46. Clive Lee. Properties of bone cement: the mechanical properties of PMMA bone cement. In: Breusch S, Makchau H. eds. The Well-Cemented Total Hip Arthroplasty. Heidelberg: Springer Mediin Verlag. 2005. p 60-6.

47. Young JF. Tricalcium silicate hydration: a historical overview. In: Young JF, Skalny JP, editors. Material Science of Concrete VII. Wiley; 2006. p 101-17.

48. Bogen G, Kim JS, Bakland LK. Direct pulp capping with mineral trioxide aggregate: an observational study. J Am Dent Assoc. 2008;139:35-15.

49. Ravichandra PV, Jayaprada RS, Harikumar V, Kavita A. Mineral trioxide aggregate. Indian J Dental Advancements. 2011;3:593-7.

50. Torabinejad M, Hong CU, McDonald F, Pitt Ford TR. Physical and chemical properties of a new root-end filling material. J Endod. 1995;21:349-53.

51. Parirokh M, Torabinejad M. Mineral trioxide aggregate: a comprehensive literature review – part I: chemical, physical, and antibacterial properties. J Endod. 2010;36:16-27.

52. Dorozhkin SV. Calcium orthophosphates in nature, biology and medicine. Materials. 2009;2:399-498.

53. Odler I. Hydration, setting and hardening of Portland cement. In: Hewlett PC, editor. Lea's Chemistry of Cement and Concrete (4th Ed.). Elsevier; 1998. p 241-312.

54. Taylor HFW. Cement Chemistry, 2nd edition, Thomas Telford 1997.

55. Gartner EM, Young JF, Damidot DA, Jawed I. Hydration of Portland cement. In: Bensted J, Barnes P (editors). Structure and Performance of Cements, 2nd edition. Spon Press. London and New York, 2002. p 57 -113.

56. Kondo R, Ueda S. Kinetics and mechanisms of the hydration of cement. Proc 5th ICCC, Vol. II, Hydration of Cements, Tokyo (1969) p.203-47.

57. Skalny JP, Young JF. Mechanisms of Portland cement hydration. Proc 7th ICCC, Paris Vol. I (1980), p. II 1/3–II 1/45 part II

58. Brown PW, Franz E, Frohnsdorff G, Taylor HFW. Analyses of the aqueous phase during early C_3S hydration. Cem Concr Res. 1984;14:257-62.

59. Stein HN, Stevels JM. Influence of silica on the hydration of $3CaO{\cdot}SiO_2$. J Appl Chem 1964;14:338-246.

60. Grutzeck MW, Ramachandran AR. An integration of tricalcium silicate hydration models in light of recent data. Cem Concr Res. 1987;17:164-70.

61. Regourd M, Thomassin JH, Baillif P, Touray JC. Study of the early hydration of Ca_3SiO_5 by X-ray photoelectron spectrometry. Cem Concr Res. 1980;10:223-30.

62. Jennings HM. Aqueous solubility relationships for two types of calcium silicate hydrate. J Am Ceram Soc. 1986;69:614-8.

63. Tadros ME, Skalny J, Kolyocu RS. Early hydration of tricalcium silicate. J Am Ceram Soc. 1976;59:344-7.

64. Young JF, Tong HS, Berger RL. Compositions of solutions in contact with hydrating tricalcium silicate pastes. J Am Ceram Soc. 1977;60:193-8.

65. Wu ZQ, Young JF. Formation of calcium hydroxide from aqueous suspensions of tricalcium silicate. J Am Ceram Soc. 1984;67:48-51.

66. Taylor HFW, Barret P, Brown PW, Double DD, Frohnsdorff G, et al. The hydration of tricalcium silicate. Materiaux et Constructions. 1984;17:457-68.

67. Odler I, Dorr H. Early hydration of tricalcium silicate II. the induction period. Cem Concr Res. 1979;9:277-84.

68. Sierra R. Contribution to the kinetic study of hydration of tricalcium silicate. Proc 6th ICCC, Vol II, Moscow, 1974, Part 1:138-43.

69. Jennings HM, Dalgleish BJ, Pratt PL. Morphological development of hydrating tricalcium silicate as examined by electron microscopy techniques. J Am Ceram Soc. 1981;64:567-72.

70. Young JF, Hansen W. Volume relationships for C-S-H formation based on hydration stoichiometries. Mat Res Soc Symp Proc 1987;85:313-22.

71. Copeland LE, Hayes JC. Determination of nonevaporable water in hardened Portland cement pastes. ASTM Bull. 1953;194:70-4.

72. Taylor HFW. Proposed structure for calcium silicate hydrate gel. J Am Ceram Soc 1986;69:464-7.

73. Glasser FP, Lachowaski EE, Macphee DE. Compositional model for calcium silicate hydrate (C-S-H) gels, their solubilities and free energies of formation. J Am Ceram Soc. 1987;70:481-5.

74. Richardson IG, Groves GW. Models for the composition and structure of calcium silicate hydrate (C-S-H) gel in hardened tricalcium silicate pastes. Cem Concr Res 1992;22:1001-10.

75. Cong X, Kirkpatric RJ. ^{29}Si MAS NMR study of the structure of calcium silicate hydrate. Adv Cem Based Mater 1996;3:144-56.

76. Grutzeck MW. A new model for the formation of calcium silicate hydrate (C-S-H). Mater Res Innov. 1999;3:160-70.

77. Nonat A, Lecoq X. The structure, stoichiometry and properties of C-S-H prepared by C_3S hydration under controlled conditions. In: Grimmer P, Grimmer AR, Zanni H, Sozzani P, editors. Nuclear Magnetic Resonance Spectroscopy of Cement-Based Materials. Springer, Berlin, 1998, p197-207.

78. Chen JJ, Tomas JJ, Taylor HFW, Jennings HM. Solubility and structure of calcium silicate hydrate. Cem Concr Res. 2004;34:1499-519.

79. Taylor HFW. Nanostructure of C-S-H: current status. Adv Cem Based Mater. 1993;1:38-46.

80. Mohan K, Taylor HFW. A trimethylsilylation study of tricalcium silicate pastes. Cem Concr Res. 1982;12:25-31.

81. Diamond S. Cement paste microstructure - an overview at several levels. In: Maxell-Cook PV, editor. Hydraulic Cement Pastes: Their Structure and Properties. Cement and Concrete Association, London, 1976, p 2-30.

82. Jenkins R, Snyder R. Introduction to X-ray Powder Diffractometry. John Wiley & Sons. New York, 1996.

83. Odler I, Dorr H. Early hydration of triclacium silicate I. Kinetics of the hydration process and the stoichiometry of the hydration products. Cem Concr Res. 1979;9:239-48.

84. Valenti GL, Sabatelli V, Marchese B. Hydration kinetics of tricalcium silicate solid solutions at early ages. Cem Concr Res. 1978;8:61-72.

85. Ramachandran VS. Application of Differential Thermal Analysis in Cement Chemistry. Chemical Publishing Company. New York, 1969.

86. Ramachandran VS. Kinetics of hydration of tricalcium silicate in the presence of calcium chloride by thermal methods. Thermochim Acta. 1971;2:41-55.

87. El-Jazairi B, Illston JM. A simultaneous semi-isothermal method of thermogravmetry and derivative thermogravimetry, and its application to cement pastes. Cem Concr Res. 1977;7:247-58.

88. El-Jazairi B, Illston JM. The hydration of cement paste using the semi-isothermal method of derivative thermogravimetry. Cem Concr Res. 1980;10:361-6.

89. Ramachandran VS, Zhang CM. Dependence of fineness of calcium carbonate on the hydration behaviour of tricalcium silicate. Durability Build Mat. 1986;4:45-66.

90. Ramachandran VS. Differential thermal method of estimating calcium hydroxide in calcium silicate and cement phases. Cem Concr Res. 1979;9:677-84.

91. Fernandez E, Gil FJ, Ginebra MP, Driessens CM, Planell JA, Best SM. Calcium phosphate bone cements for clinical applications Part II: precipitate formation during setting reactions. J Mater Sci Mater Med. 1999;10:177-83.

92. Wang L and Nancollas GH. Calcium orthophosphate: crystallization and dissolution. Chem Rev. 2008;108:4628-69.

93. Liao CJ, Lin FH, Chen KS, Sun JS. Thermal decomposition and reconstitution of hydroxyapatite. Biomaterials. 1999;20:1807-13.

94. Chow LC. Development of self-setting calcium phosphate cements. J Ceram Soc Jpn. 1991;99:954-64.

95. Lynn AK, Bonfield W. A novel method for the simultaneous, titrant-free control of pH and calcium phosphate mass yield. Acc Chem Res. 2005;38:202-7.

96. LeGeros RZ. Calcium Phosphate in Oral Biology and Medicine. Karger: Basel, Switzerland. 1991.

97. Biostelle R and Lopez-Valero I. Growth unit and nucleation: the case of calcium phosphate. J Cryst Growth. 1990;102:609-17.

98. Brown WE, Mathew M, Tung MS. Crystal chemistry of octacalcium phosphate. Prog Crys Growth Charact. 1981;4:59-87.

99. Brown WE. Octacalcium phosphate and hydroxyapatite: crystal structure of octacalcium phosphate. Nature 1962;196:1048-50.

100. Brown WE, Lehr JR, Smith JP, Frazier AW. Crystallgrophy of octacalcium phosphate. J Am Chem Soc. 1957;79:5318-9.

101. Brown WE. Crystal growth of bone mineral. Clin Orthop. 1966;44:205-20.

102. Bodier-Houlle P, Steuer P, Voegel JC, Cuisinier FJG. First experimental evidence for human dentine crystal formation involving conversion of octacalcium phosphate to hydroxyapatite. Acta Crytallogr D Biol Crystallogr. 1998;54:1377-81.

103. Miake Y, Shimoda S, Fukae M, Aoba T. Epitaxial overgrowth of apatite crystals on the tine-ribbon precursor at early stages of porcine enamel mineralization. Calcif Tiss Int. 1993;53:249-56.

104. Boskey AL. Amorphous calcium phosphate: the contention of bone. J Dent Res. 197;76:1433-6.

105. Bosley AL and Posner AS. Formation of hydroxyapatite at low supersaturation. J Phys Chem. 1976;80:40-5.

106. Meyer JL Eanes ED. A thermodynamic analysis of the amorphous to crystalline calcium phosphate transformation. Calcif Tiss Res. 1978;25:59-68.

107. Eanes ED, Termine JD, Nylen MU, An electron microscopic study of the formation of amorphous calcium phosphate and its transformation to crystalline apatite. Calcif Tiss Res. 1973;12:143-58.

108. Boskey AL, Posner AS. Conversion of amorphous calcium phosphate to microcrystalline hydroxyapatite. A pH-dependent, solution-mediated, solid-solid conversion. J Phys Chem. 1973;77:2313-7.

109. Kay MI, Young RA, Posner AS. Crystal structure of hydroxyapatite. Nature 1964;204:1050-2.

110. Posner AS, Betts F. Synthetic amorphous calcium phosphate and its relation to bone mineral structure. Acc Chem Res. 1975;8:273-281.

111. Onuma K, Ito A. Cluster growth model for hydroxyapatite. Chem Mater. 1998;10-3346-51.

112. Markoic M, Fowler BO, Tung MS. Preparation and comprehensive characterization of a calcium hydroxyapatite reference material. J Res Natl Inst Stand Technol. 2004;109:553-68.

113. Pilliar RM, Kandel RA, Grynpas MD, Hu Y. Porous calcium polyphosphate as load-bearing bone substitutes: In vivo study. J Biomed Mater Res B Appl Biomater. 2013;101B:1-8.

114. Griffith EJ. Phosphate Fibres. Plenum Press. New York, 1995.

115. Wang K, Chen FP, Liu CS, Russel C. The effect of polymeric chain-like structure on the degradation and cellular biocompatibility of calcium polyphosphate. Mater Sci Eng C. 2008;28:1572-8.

116. Grynpas MD, Pilliar RM, Kandel RA, Renlund R, Filiaggi M, Dumitriu M. Porous calcium polyphosphate scaffolds for bone substitute application in vivo studies. Biomaterials. 2002;23:2063-70.

117. Qiu, K, Wan CX, Zhao CS, Chen X, Tang CW, Chen YW. Fabrication and characterization of porous calcium polyphosphate scaffolds. J Mater Sci. 2006;41:2429-34.

118. Ding YL, Chen YW, Qin YJ, Shi GQ, Yu XX, Wan CX. Effect of polymerization degree of calcium polyphosphate on its microstructure and in vitro degradation performance. J Mater Sci Mater Med. 2008;19:1291-5.

119. Pilliar RM, Filiaggi MJ, Wells JD, Grynpas MD, Kandel RA. Porous calcium polyphosphate scaffolds for bone substitute application – in vitro characterization. Biomaterials. 2001;22:963-72.

120. Nurse RW. The effect of phosphate on the constitution and hardening of Portland cement. J App Chem. 1952;2:708-16.

121. Huan Z, Chang J. Novel tricalcium silicate/monocalcium phosphate monohydrate composite bone cement. J Biomed Mater Res B Appl Biomater. 2007;82B:352-9.

122. Wang X, Ye J, Wang Y, Chen L. Self-setting properties of a β-dicalcium silicate reinforced calcium phosphate cement. J Biomed Mater Res B Appl Biomater. 2007;82B:93-9.

123. Huan Z, Chang J. Calcium-phosphate-silicate composite bone cement: self-setting properties and *in vitro* bioactivity. J Mater Sci Mater Med. 2009;20:833-41.

124. Cardenas LJ, Takeuchi A, Tsuru K, Matsuya S, Ishikawa K. Synthesis and *in vitro* cell compatibility of α-tricalcium phosphate-based apatite cement containing tricalcium silicate. IFMBE Proceedings. 2010;27:207-10.

125. Morejon-Alonso L, Ferreira OJB, Carrodeguas RG, dos Santos LA. Bioactive composite bone cement based on α-tricalcium phosphate/tricalcium silicate. J Biomed Mater Res B Appl Biomater. 2012;100B:94-102.

126. Michailesco P, Kouassi M, Briak HE, Armynot A, Boudeville P. Antimicrobial activity and tightness of a DCPD-CaO-based hydraulic calcium phosphate cement for root canal filling. J Biomed Mater Res B Appl Biomater. 2005;74B:760-7.

127. Wang X, Ma J, Wang Y, He B. Bone repair in radii and tibias of rabbits with phosphorylated chitosan reinforced calcium phosphate cements. Biomaterials 2002;23:4167-76.

128. Boudeville P, Serral S, Leloup JM, Margerit J, Pauvert B, Terol A. Physical properties and self-setting mechanism of calcium phosphate cements from calcium bis-dihydrogenophosphate monohydrate and calcium oxide. J Mater Sci Mater Med. 1999;10:99-109.

129. Bermudez O, Boltong MG, Driessens FCM, Planell JA. Optimization of a calcium orthophosphate cement formulation occurring in the combination of monoclacium phosphate monohydratie with calcium oxide. J Mater Sci Mater Med. 1994;5:67-71.

130. Mirtchi AA, Lemaitre J, Terao N. Calcium phosphate cement: study of the β-tricalcium phosphate – monocalcium phosphate system. Biomaterials. 1989;10:475-80.

131. Fulmer MT, Martin RI, Brown PW. Formation of calcium deficient hydroxyaptite at near – physiological temperature. J Mater Sci Mater Med. 1992;3:299-305.

132. Alge DL, Cruz GS, Goebel WS, Chu TMG. Characterization of dicalcium phosphate dihydrate cements prepared using a novel hydroxyapatite-based formulation. Biomed Mater. 2009;4:025016.

133. Hu J, Agrawal DK, Roy R. Investigation of hydration phases in the system CaO-SiO_2-P_2O_5-H_2O. J Mater Res 1988;3:772-80.

134. Hu J, Agrawal DKI, Roy R. Studies of strength mechanism in newly developed chemically bonded ceramics in the system CaO-SiO_2-P_2O_5-H_2O. Cem Concr Res. 1988;18:103-8.

135. Steinke RA, Silabee MR, Agrawal DK, Roy R, Roy DM. Development of chemically boned ceramics in the CaO-SiO_2-P_2O_5-H_2O system. Cem Concr Res. 1991;21:66-72.

136. Ma W, Brown PW. Effect of phosphate additions on the hydration of Portland cement. Adv Cem Res. 1994;6:1-12.

137. Kokubo T, Takadama H. How useful is SBF in predicting in vivo bone bioactivity? Biomaterials. 2006;27:2907-15.

138. Zhao W, Wang J, Zhai W, Wang Z, Chang J. The self-setting properties and *in vitro* bioactivity of tricalcium silicate. Biomaterials. 2005;26:6113-21.

139. Kokubo T, Yoshihara S, Nishimura N, Yamamuro T, Nakamura T. Bioactive bone cement based on CaO-SiO2-P_2O_5 glass. J Am Ceram Soc. 1991;74:1739-41.

140. Kokubo T. Apatite formation on surfaces of ceramics, metals and polymer in body environment. Acta Mater. 1998;46:2519-27.

141. Huang X, Jiang D, Tan S. Apatite formation on the surface of wollastonite/tricalcium phosphate composite immersed in simulated body fluid. J Biomed Mater Res B Appl Biomater. 2004;69B:70-2.

142. Kim HM, Himeno T, Kokubo T, Nakamura T. Process and kinetics of bonelike apatite formation on sintered hydroxyapatite in a simulated body fluid. Biomaterials 2005;26:4366-73.

143. Duan YR, Zhang ZR, Wang CY, Chen JY, Zhang XD, Dynamic study of calcium phosphate formation on porous HA/TCP ceramics. J Mater Sci Mater Med. 2004;15:1205-11.

144. Williams DF. Williams Dictionary of Biomaterials. Liverpool University Press. 1999.

145. Lai YL, Chen YT, Lee SY, Shieh TM, Hung SL. Cytotoxic effect of dental resin liquids on primary gingival fibroblasts and periodontal ligament cells in vivo. J Oral Rehabil. 2004;31:1165-72.

146. Mosmann T. Rapid colorimetric assay for cellular growth and survival: application to proliferation and cytotoxicity assays. J Immunol Methods. 1983;65:55-63.

147. Folkman J, Moscona A. Role of cell shape in growth control. Nature 1978;273:345-349.

148. Ben-Zeev A, Farmer SR, Penman S. Protein synthesis requires cell surface contact while nuclear events respond to cell shape in anchorage dependent fibroblasts. Cell 1980;21:211-236.

149. Yule JW, Chardwick RD. The determination of free CaO in cement and clinker. In Gebhardt RF, editor. Rapid Methods for Chemical Analysis of Hydraulic Cement. ASTM; 1988. p 55-77.

150. American Society for Testing and Materials International. Standard test methods for apparent porosity, liquid absorption, apparent specific gravity, and bulk density of refractory shapes by vacuum pressure. ASTM Standard C830-00.

151. Somerman MJ, Archer SY, Imm GR, Foster RA. A comparative study of human periodontal ligament cells and gingival fibroblasts *in vitro*. J Dent Res. 1988;67:66-70.

152. Shen QY, Sun J, Wu J, Liu CS, Chen FP. An in vitro investigation of the mechanical-chemical and biological properties of calcium phosphate/calcium silicate/bismutite cement for dental pulp capping. J Biomed Mater Res B Appl Biomater. 2010;94B:141-8.

153. Pierre AC. Introduction to Sol-Gel Processing. Kluwer Academic Publishers. Boston, 1998.

154. Li S, Roy DM. Preparation and characterization of high and low CaO/SiO2 ratio “pure” C-S-H for chemically bonded ceramics. J Mater Res. 1988;3:380-6.

155. Ramachandran AR, Grutzeck MW. Effect of pH on the hydration of tricalcium silicate. J Am Ceram Soc. 1993;76:72-80.

156. Odler I, Schuppstuhl J. Early hydration of tricalcium silicate III. Control of the induction period. Cem Concr Res. 1981;11:765-74.

157. Berger RL, McGregor JD. Effect of temperature and water-solid ratio on growth of $Ca(OH)_2$ crystals formed during hydration of Ca_3SiO_5. J Am Ceram Soc. 1973;56:73-9.

158. McCury KG and Stein HN. Suspension hydration of C_3S at constant pH. I. Variation of particle size and C_3S content. Cem Concr Res. 1973;3:247-62.

159. Bamford CH, Tipper CFH. Comprehensive Chemical Kinetics: Reaction in Solid State. Vol. 22. Elsevier, Amsterdam, 1980.

160. Avrami M. Kinetics of phase change. I and II. J Phys Chem. 1939;7:1103 and 1940;8:212.

161. Brown PW, Pommersheim J, Frohnsdorff G. A kinetic model for the hydration of triclacium silicate. Cem Concr Res. 1985;15:35-41.

162. Rothstein D, Thomas JJ, Christensen BJ, Jennings HM. Solubility behaviour of Ca-, S-, Al-, and Si-bearing solid phases in Portland cement pore solutions as a function of hydration time. Cem Concr Res. 2002;32:1663-71.

163. Biffen FM. Determination of free lime and carbonate in calcium silicate hydrates by thermobalance. Anal Chem. 1956;28:1133-6.

164. Ramachandran VS, Paroli RM, Beaudoin JJ, Delgado AH. Handbook of Thermal Analysis of Construction Materials. Noyes Publications /William Andrew Publishing. Norwich, New York; 2002.

165. Fordham CJ, Smalley IJ. A simple thermogravimetric study of hydrated cement. Cem Concr Res. 1985;15:141-4.

166. Mazieres C. Micro and semimicro differential thermal analysis (μDTA). Anal Chem. 1964;36:602-5.

167. Dent Glasser LS, Lachowski EE, Mohan K, Taylor HFW. A multi-method study of C_3S hydration. Cem Concr Res. 1978;8:733-40.

168. Locher FW. Stoichiometry of tricalcium silicate hydration. Symposium on Structure of Portland Cement Paste and Concrete, Highway Res. Board Spec. Rep. No. 90. Highway Research Board, Washington, 1966. p. 300-8.

169. Kantro DL, Weise CH, Brunauer S. Paste hydration of beta-dicalcium silicate, tricalcium silicate, and alite. *ibid.* p. 309-27.

170. Kantro DL, Brunauer S, Weise CH. Development of Surface in the hydration of calcium silicates. II. Extention of investigations to earlier and later stages of hydration. J Phys Chem. 1962;66:1804-9.

171. Elliot JC. Structure and Chemistry of the Apatites and Other Calcium Orthophosphates. Elsevier. Amsterdan, 1994.

172. Koch K, Brave Dennis. Bioceramic technology – the game changer in endodontics. Endodontic Practice US. 2009;2(2):13-7.

173. Roberts HW, Toth JM, Berzins DW, Charlton DG. Mineral trioxide aggregate material use in endodontic treatment: a review of the literature. Dent Mater. 2008;24:149-64.

174. Schwartz RS, Mauger M, Clement DJ, Walker WA III. Mineral trioxide aggregate: a new material for endodontics. J Am Dent Assoc. 1999;130:967-75.

175. Tuna EB, Dinçol ME, Gençay K, Aktören O. Fracture resistance of immature teeth filled with BioAggregate, mineral trioxide aggregate and calcium hydroxide. Dent Traumatol. 2011;27:174-8.

176. Yan P, Yuan Z, Jiang H, Peng B, Bian Z. Effect of BioAggregate on differentiation of human periodontal ligament fibroblasts. Int Endod J. 2010;43:1116-21.

177. De-Deus G, Canabarro A, Alves G, Linhares A, Senne MI, Granjeiro JM. Optimal cytocompatibility of a bioceramics nanoparticulate cement in primary human mesenchymal cell. J Endod. 2009;35:1387-90.

178. EI Sayed M, Saeed M. In vitro comparative study of sealing ability of Diadent Bioaggregate and other root-end filling materials. J Conserv Dent. 2012;15:249-52.

179. Li P, Ohtsuki C, Kokubo T, Nakanishi K, Soga N. Apatite formation induced on silica gel in a simulated body fluid. J Am Ceram Soc. 1992;75:2094-7.

180. Ohtsuki C, Kokubo T, Yamamuro T. Mechanism of apatite formation on $CaO\text{-}SiO_2\text{-}P_2O_5$ glasses in a simulated body fluid. J Non-Cryst Solids. 1992;143:84-92.

181. Kokubo T, Kushitani H, Ohtsuki C, Sakka S, Yamamuro T. Chemical reaction of bioactive glass and glass-ceramics with a simulated body fluid. J Mater Sci Mater Med. 1992;3:79-83.

182. Yang Q, Troczynski T, Liu DM. Influence of apatite seeds on the synthesis of calcium phosphate cement. Biomaterials. 2002;23:2751-60.

183. Harrison MA, Rae IF. General Techniques of Cell Culture. Cambridge University Press; 1997.

184. Mackenzie CG, Mackenzie JB, Beck P. The effect of pH on growth, protein synthesis, and lipid-rich particles of cultured mammalian cells. J Biophys Biochem Cytol. 1961; 9:141-56.

185. Froehlich JE, Anastassiades TP. Role of pH in fibroblast proliferation. J Cell Physiol. 1974;84:253-60.

186. Haglund R, He J, Jarvis J, Safavi KE, Spangberg LS, Zhu Q. Effects of root-end filling materials on fibroblasts and macropages *in vitro*. Oral Surg Oral Med Oral Pathol Oral Radiol Endod. 2003;95:739-45.

187. Nemeth EF, Carafoli E. The role of extracellular calcium in the regulation of intracellular calcium and cell function. Cell Calcium. 1990;11:319–21.

188. Abiko Y. Studies on calcium-stimulated adenosine triphosphatase in the albino rabbit dental pulp: its subcellular distribution and properties. J Dent Res. 1977;56:1558-68.

189. Reffitt D, Ogston N, Jugdaohsingh R, Cheung H, Evans B, Thompson R, et al. Orthosilicic acid stimulates collagen type I synthesis and osteoblastic differentiation in human osteoblast-like cells *in vitro*. Bone. 2003;32:127–35.

190. Bonen DK, Schmid TM. Elevated extracellular calcium concentrations induce type X collagen synthesis in chondrocyte cultures. J Cell Biol. 1991;115:1171–8.

191. Shie MY, Ding SJ, Chang HC. The role of silicon in osteoblast-like cell proliferation and apoptosis. Acta Biomaterialia. 2011;7:2604-14.

192. Meleti Z, Shapiro IM, Adams CS. Inorganic phosphate induces apoptosis of osteoblast-like cells in culture. Bone. 2000;27:359-66.

193. Kjellsen KO, Justnes H. Revisiting the microstructure of hydrated tricalcium silicate – a comparison to Portland cement. Cem Concr Compos. 2004;26:947-56.

194. Hamilton DW, Brunette DM. The effect of substratum topography on osteoblast adhesion mediated signal transduction and phosphorylation. Biomaterials. 2007;28:1806-1819.

195. Feist IS, Micheli GD, Carneiro SRS, Eduardo CP Miyagi SPH, Marques MM. Adhesion and growth of cultured human ginival fibroblasts on periodontally involved root surfaces treated by Er:YAG laser. J Periodontol. 2003;74:1368-75.

196. Cochran DL, Simpson J, Weber HP, Buser D. Attachment and growth of periodontal cells on smooth and rough titanium. Int J Oral Maxillofac Implants. 1988;3:21-4.

APPENDIX A

DATA PROCESS FOR THE QUANTITATIVE XRD ANALYSIS

The quantitative XRD data were collected on the samples of 0CPM, 5CPM, 10CPM, and 20CPM for the hydration of pre-set periods of unhydrated, 10 m (minute), 30 m, 1 h (hour), 2 h, 4 h, 6 h, 12 h, 24 h, 2 d (days), 4 d, 7 d, 14 d, and 28 d. The intensity ratios of peak areas of C_3S to quartz on the reference peaks are listed in Table A-1. The peak areas were calculated by the software MDI JADE 7, which was provided with the XRD machine. Each piece of data was derived from an average of no less than 12 measurements.

Table A-1 The intensity ratios (I_c/I_s) of peak areas of C_3S to quartz on the reference peaks for the pre-set hydration.*

Hydration period	0CPM	5CPM	10CPM	20CPM
Before hydration	0.8395 ± 0.0661	0.7975 ± 0.0777	0.7555 ± 0.0543	0.6716 ± 0.0390
10 m	0.7972 ± 0.0681	0.7551 ± 0.0508	0.7009 ± 0.0534	0.5919 ± 0.0450
30 m	0.8014 ± 0.0235	0.7551 ± 0.0448	0.6922 ± 0.0601	0.6009 ± 0.0347
1 h	0.7011 ± 0.0963	0.7658 ± 0.0576	0.6995 ± 0.0701	0.5743 ± 0.0379
2 h	0.5464 ± 0.0615	0.7633 ± 0.0867	0.6180 ± 0.0718	0.5261 ± 0.0163
4 h	0.3535 ± 0.0215	0.6677 ± 0.0433	0.5786 ± 0.0232	0.3866 ± 0.0341
6 h	0.2953 ± 0.0332	0.5833 ± 0.0565	0.5212 ± 0.0306	0.3081 ± 0.0131
12 h	0.2235 ± 0.0079	0.2701 ± 0.0183	0.2277 ± 0.0287	0.0914 ± 0.0050
24 h	0.1837 ± 0.0211	0.1033 ± 0.0076	0.0766 ± 0.0089	0.0613 ± 0.0058
2 d	0.1561 ± 0.0095	0.0761 ± 0.0072	0.0522 ± 0.0050	0.0400 ± 0.0038
4 d	0.1400 ± 0.0153	0.0414 ± 0.0057	0.0189 ± 0.0032	0.0000

7 d	0.1166 ± 0.0127	0.0378 ± 0.0051	0.0098 ± 0.0028
14 d	0.0572 ± 0.0063	0.0081 ± 0.0033	0.0057 ± 0.0028
28 d	0.0282 ± 0.0027	0.0027 ± 0.0027	0.000
60 d	0.0172 ± 0.0032	0.000	

*The data are average ± standard deviation.

The weight ratios (X_c/X_s) of C_3S to quartz in the mixed cement pastes for the pre-set hydration were calculated with the equation 4.1b and are listed in Table A-2. The degrees of hydration (α, percentage of hydrated C_3S in cements) are calculated and shown in Table A-3. The degrees of hydration (α) of C_3S, 5CPM, 10CPM, and 20CPM are plotted with the hydration time in Fig. A-1 (the same as Fig. 4.9a).

Table A-2 The weight ratios (X_c/X_s) of C_3S to quartz in the mixed cement pastes for the pre-set hydration*

Hydration period	0CPM	5CPM	10CPM	20CPM
Before hydration	8.998 ± 0.679	8.548 ± 0.804	8.098 ± 0.553	7.198 ± 0.389
10 m	8.545 ± 0.701	8.093 ± 0.516	7.512 ± 0.543	6.344 ± 0.454
30 m	8.589 ± 0.223	8.903 ± 0.451	7.419 ± 0.616	6.440 ± 0.343
1 h	7.515 ± 1.003	8.208 ± 0.588	7.497 ± 0.723	6.155 ± 0.378
2 h	5.856 ± 0.630	8.181 ± 0.900	6.624 ± 0.741	5.639 ± 0.146
4 h	3.789 ± 0.202	7.157 ± 0.435	6.202 ± 0.220	4.144 ± 0.337
6 h	3.165 ± 0.327	6.252 ± 0.577	5.586 ± 0.300	3.302 ± 0.112
12 h	2.395 ± 0.056	2.895 ± 0.168	2.440 ± 0.279	0.980 ± 0.025

24 h	1.969 ± 0.197	1.107 ± 0.052	0.821 ± 0.066	0.657 ± 0.033
2 d	1.673 ± 0.073	0.816 ± 0.048	0.559 ± 0.025	0.428 ± 0.012
4 d	1.501 ± 0.135	0.444 ± 0.032	0.203 ± 0.006	0.000
7 d	1.250 ± 0.107	0.405 ± 0.026	0.105 ± 0.002	
14 d	0.613 ±0.039	0.087 ± 0.007	0.061 ± 0.001	
28 d	0.302 ± 0.001	0.000	0.000	
60 d	0.184 ± 0.005	0.000		

*The data are average ± standard deviation.

Table A-3 The degree of hydration (α, percentage of hydrated C_3S in cements), %, of 0CPM, 5CPM, 10CPM, and 20CPM for the pre-set hydration.

Hydration period	C_3S	5CPM	10CPM	20CPM
Before hydration	0.0 ± 0.1	0.0 ± 0.1	0.0 ± 0.1	0.0 ± 0.1
10 m	5.0 ± 0.4	5.3 ± 0.3	7.2 ± 0.5	11.9 ± 0.8
30 m	4.5 ± 0.1	5.3 ± 0.3	8.4 ± 0.7	10.5 ± 0.6
1 h	16.2 ± 2.2	4.0 ± 0.3	7.4 ± 0.7	14.5 ± 0.9
2 h	34.9 ± 3.8	4.3 ± 0.5	18.2 ± 2.0	21.7 ± 0.6
4 h	57.9 ± 3.1	16.3 ± 1.0	23.4 ± 0.8	42.4 ± 3.4
6 h	64.8 ± 6.7	26.9 ± 2.5	31.0 ± 1.7	54.1 ± 1.8
12 h	73.4 ± 1.7	66.1 ± 3.8	69.9 ± 8.0	86.4 ± 2.1
24 h	78.1 ± 7.8	87.1 ± 4.1	89.9 ± 7.2	90.9 ± 4.6
2 d	81.4 ± 3.5	90.5 ± 5.3	93.1 ± 4.1	94.1 ± 2.5
4 d	83.3 ± 7.5	94.8 ± 6.8	97.5 ± 2.8	100.0 ± 4.9
7 d	86.1 ± 7.4	95.3 ± 6.1	98.7 ± 1.4	
14 d	93.2 ± 5.9	99.0 ± 7.4	99.2 ± 1.9	

28 d	96.6 ± 0.1	100.0 ± 4.9
60 d	98.0 ± 2.7	

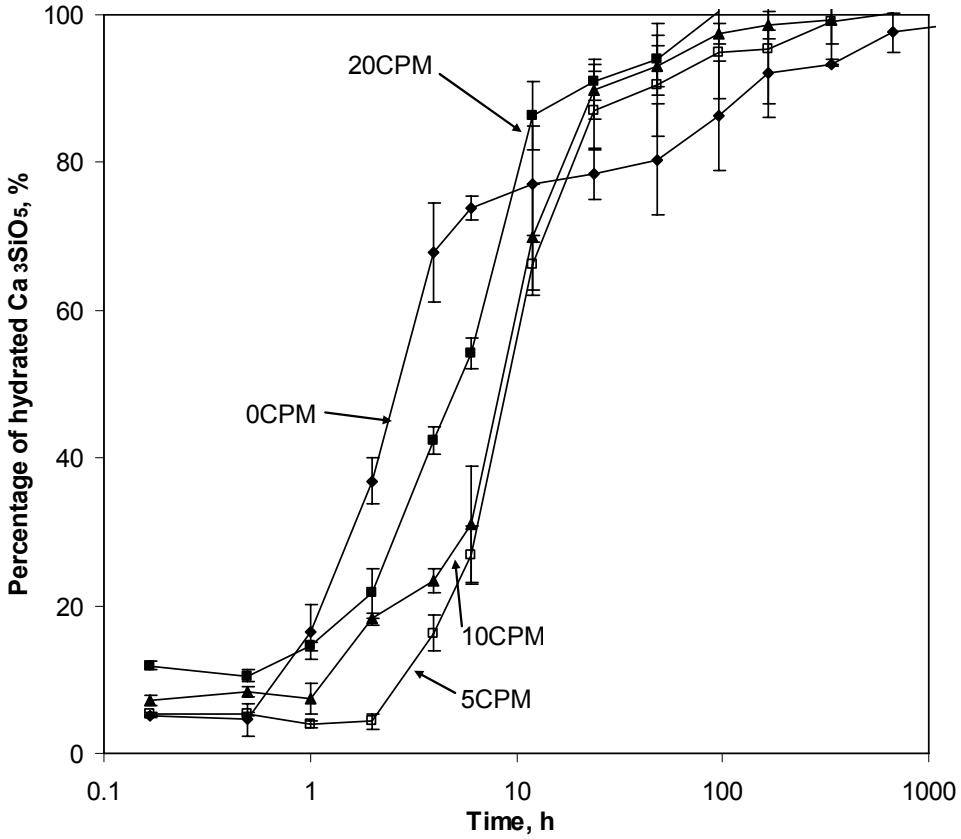

Fig. A-1 The percentage of hydrated C_3S (α) with hydration time for the cements of 0CPM, 5CPM, 10CPM, and 20CPM at w/c = 10 at 37 ºC.

The average hydration rates (the first derivative of the degree of hydration to the hydration time) of C_3S, 5CPM, 10CPM, and 20CPM are listed in Table A-4 and are plotted in Fig. A-2 (the same as Fig. 4.9b) against the hydration time. The average hydration rate for a hydration period is calculated with the following equation:

$$v = \frac{\alpha_2 - \alpha_1}{t_2 - t_1} \qquad \text{(A-1)}$$

where v = the average hydration rate for a hydration period, %/h

α_2 = the hydration degree at the end of the period, %

α_1 = the hydration degree at the beginning of the period, %

t_2 = the time at the end of the period, h

t_1 = the time at the beginning of the period, h.

Table A-4 The average hydration rate with hydration time for 0CPM, 5CPM, 10CPM, and 20CPM

Hydration period	0CPM	5CPM	10CPM	20CPM
10 m	30.2	31.9	43.4	71.2
30 m	0.0*	0.0	3.5	0.0*
1 h	23.9	0.0*	0.0*	7.9
2 h	18.4	0.3	10.8	7.2
4 h	11.5	6.0	2.6	10.4
6 h	3.5	5.3	3.8	5.9
12 h	1.4	6.5	6.5	5.4
24 h	0.4	1.7	1.7	0.4
2 d	0.1	0.1	0.1	0.1
4 d	0.0	0.1	0.1	0.1
7 d	0.0	0.0	0.0	
14 d	0.0	0.0	0.0	

28 d	0.0	0.0

*The number should not be a negative value and is changed to zero.

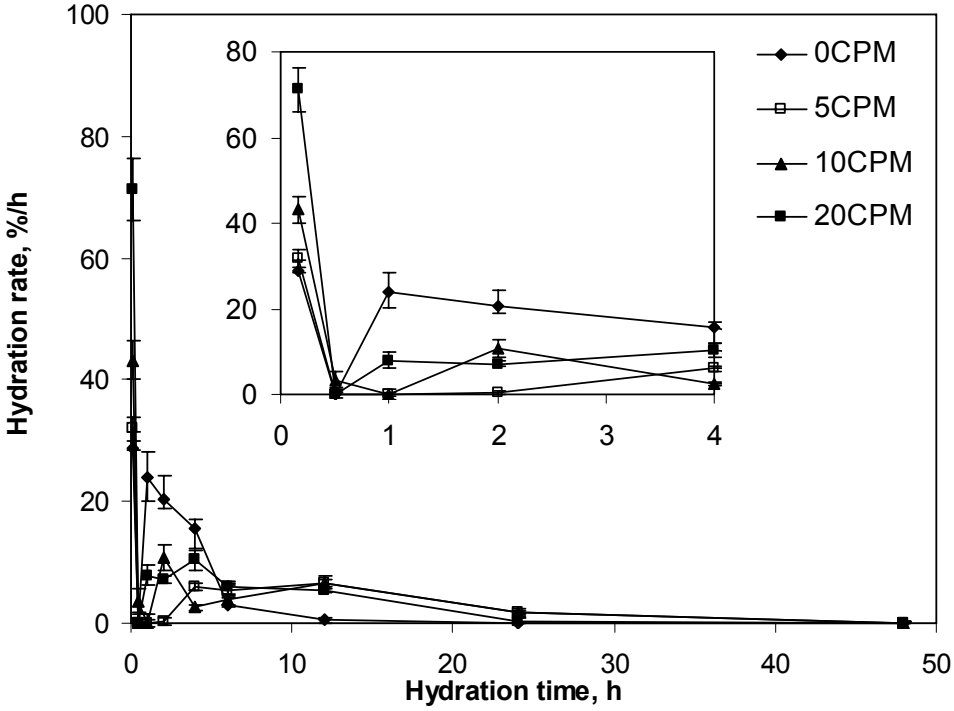

Fig. A-2 The average hydration rate (the first derivative of the hydration degree to hydration time) with hydration time for the cements of 0CPM, 5CPM, 10CPM, and 20CPM at w/c = 10 at 37 ºC.